



Josephson effect in multicomponent Bose-Einstein condensates

Marina Melé Messeguer



Aquesta tesi doctoral està subjecta a la llicència **Reconeixement- NoComercial 3.0. Espanya de Creative Commons**.

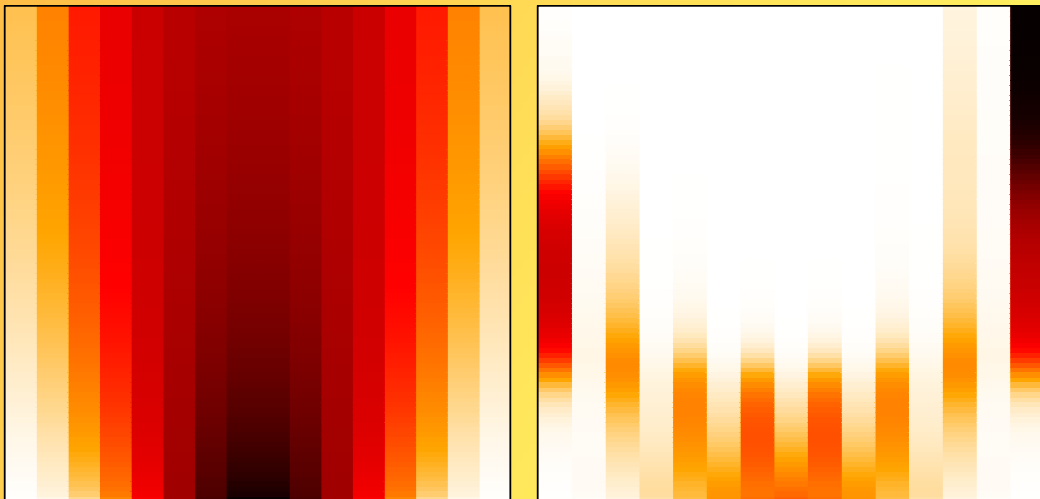
Esta tesis doctoral está sujeta a la licencia **Reconocimiento - NoComercial 3.0. España de Creative Commons**.

This doctoral thesis is licensed under the **Creative Commons Attribution-NonCommercial 3.0. Spain License**.

PhD Thesis

Josephson effect in multicomponent Bose-Einstein condensates

Marina Melé Messeguer



Universitat de Barcelona

Tesi doctoral - PhD Thesis



Josephson effect in multicomponent Bose-Einstein condensates

MARINA MELÉ MESSEGUER

Directors:

Prof. Artur Polls i Martí

Dr. Bruno Juliá Díaz

Tesi doctoral presentada a la Universitat de Barcelona, dins del programa de doctorat de Física. Curs 2012/13.

Doctoral thesis presented at the University of Barcelona, within the PhD program of Physics. Academic year 2012/13

*Per l'Armacenda Domitila
i la Filomena Anastàcia*

Contents

Agraiments	iii
Resum	v
Abstract	vii
1 Introduction	1
2 Mean-field theory of Bose-Einstein Condensates	11
2.1 The Gross-Pitaevskii equation	11
2.1.1 Variational approach	12
2.1.2 Stationary Gross-Pitaevskii equation	13
2.1.3 Time-dependent Gross-Pitaevskii equation	14
2.1.4 Thomas-Fermi limit	14
2.2 1-dimensional reductions	15
3 Josephson effect in scalar condensates	17
3.1 Experimental realization of an external BJJ	18
3.2 Two-mode approximation	19
3.2.1 Standard two-mode	22
3.2.2 Improved two-mode	24
3.2.3 Regimes for a scalar condensate	24
3.3 Numerical solutions of the TDGPE	29
3.3.1 TDGPE results	30
3.3.2 TDGPE, 1D reductions and two-mode approximations	33
3.4 Beyond the two-mode approximation	36
4 Josephson effect in binary mixtures	41
4.1 Gross-Pitaevskii equation for a binary mixture	42
4.2 Two-mode approximation for a binary mixture	43
4.2.1 Standard two-mode model for a binary mixture	43
4.2.2 Improved two-mode model for a binary mixture	45
4.2.3 Dynamical regimes in a binary mixtures	47
4.3 Numerical solutions of the TDGPE for a binary mixture	50
4.3.1 TDGPE calculations: phase coherence and localization	52
4.3.2 Small oscillations around $z_{a,b}^0$ and $\delta\phi_{a,b}^0 = 0$	53

4.3.3	Small oscillations around $z_{a,b}^0$, $\delta\phi_a^0 = 0$ and $\delta\phi_b^0 = \pi$	55
4.3.4	Small oscillations around $z_{a,b}^0$ and $\delta\phi_{a,b}^0 = \pi$	56
4.3.5	Effects beyond two-mode	57
5	Josephson effect beyond mean field	61
5.1	Second quantization	62
5.2	Two-site Bose-Hubbard Hamiltonian	63
5.3	Static properties	64
5.3.1	Variational ansatz for the ground state	67
5.4	Dynamical properties	70
5.5	$1/N$ approximation to the BH model	72
6	Josephson effect in spinor condensates	77
6.1	Spinor condensates	78
6.2	Josephson effect: mean-field description	80
6.2.1	Population transfer in the Josephson regime	83
6.2.2	Numerical simulations	84
6.3	Bose-Hubbard model for $F = 1$ spinors in a double well	88
6.4	Ground state properties	90
6.4.1	Single well	90
6.4.2	Double well	91
6.4.3	Spin driven symmetry breaking	93
7	Temperature effects in spinor BEC	99
7.1	$F = 1$ spinor BEC	100
7.1.1	Homogeneous condensate	101
7.1.2	Confined condensate: local density approximation	104
7.2	Dipolar $F = 3$ spinor BEC	105
7.2.1	Dipolar scalar BEC	106
7.2.2	Spin-3 dipolar condensate	108
7.2.3	Homogeneous condensate	109
7.2.4	Confined condensate: local density approximation	111
8	Summary and conclusions	113
A	Imaginary time step method	117
B	Scalar BH: estimation of the bifurcation point	119
	List of publications	121
	Bibliography	122

Agraïments

Primer de tot, m'agradaria donar les gràcies a l'Artur i el Bruno, els meus directors de tesi, per haver-me donat l'oportunitat de fer el doctorat amb ells i introduir-me al món de la ciència. Durant els darrers anys, m'han ensenyat moltes coses i m'han proporcionat tots els recursos per poder-me formar a escoles i congressos arreu del món. Especialment, m'agradaria agrair-los l'esforç que han fet durant els últims mesos, al llegir-se críticament aquesta tesi.

També m'agradaria agrair a tota la gent que m'ha ensenyat i ajudat al llarg d'aquests últims quatre anys: gent del departament, col·laboradors i companys durant les estades a l'estranger. Especialment al Simone Paganelli, al Luis Santos, al Lincoln Carr, a la Montserrat Guilleumas, al Joan Martorell i a l'Anna Sanpera.

Als meus pares, l'Enric i la Quima, m'agradaria agrair-los el suport incondicional que m'han donat durant tots aquest anys. També m'agradaria felicitar-los perquè aquesta tesi és, en gran part, mèrit seu: si avui estic aquí escrivint-la, és perquè s'han esforçat dia a dia, des de la guarderia fins a la carrera, a ensenyar-me a gaudir aprenent coses. Moltíssimes gràcies per tot el que heu fet per mi.

A la Maria, la meva super-cangur i pseudo-mare, li vull agrair tot el que ha fet per mi durant aquests anys. Ella també ha tingut un paper molt gran en la meva educació, i ha dedicat molt temps a escoltar-me i ajudar-me.

A la meva germana, la Marta, li he dedicat aquesta tesi. Perquè l'admiro i perquè l'estimo. Ha estat un gran suport i una gran amiga durant tots aquests anys, i sempre té una solució amagada a casi tots els meus problemes.

També m'agradaria agrair el suport i companyia que m'han donat els meus amics, companys de despatx, de pis, de pàdel i de viatge, Axel i Cris.

I als meus companys de carrera, de laboratoris, de menjadors universitaris, de festa, de creuer i de viatges. Especialment a la Lena, la Laia, l'Edgar, la Lidia, el Miquel, l'Albert i el Bartrés.

Escriure aquesta tesi suposa el final de la meva vida d'estudiant. Per això, m'agradaria agrair també a tota l'altra gent que ha estat amb mi durant tot aquest temps, i que m'ha acompanyat i ajudat fins aquí. Familiars, companys d'escola, d'institut, de carrera, de jazz, de volei, de feines d'estiu i de simulacions d'hivernacles.

Finalment, i especialment, m'agradaria agrair-li al Marc que hagi estat al meu costat durant aquests anys. Ell és amb qui més he compartit aquesta tesi, i qui m'ha ajudat i animat dia a dia. Set per tres vint-i-una, t'estimo.

This work was supported by an FPI PhD grant of the Ministerio de Ciencia e Innovación (Spain).

Resum

La coherència de fase és una propietat característica dels condensats de Bose-Einstein que porta a fenòmens macroscòpics fascinants, com els efectes d'interferència o les oscil·lacions tipus Josephson. Aquestes últimes es produeixen en una junció bosònica de Josephson (*bosonic Josephson junction - BJJ*), que esquemàticament consisteix en dos condensats dèbilment acoblats on idealment 1) els àtoms només ocupen dos estats monoparticulars diferents i 2) les interaccions atòmiques són de contacte. Aquestes junccions poden ser externes o internes: la BJJ externa està formada per un condensat que es troba confinat en una trampa tipus doble pou, on la barrera intermèdia es suficientment alta com per assegurar un lligam dèbil entre els condensats de cada banda. En canvi, la BJJ interna consisteix en un condensat on els àtoms que el formen poden estar en dos estats diferents de spin. Un làser extern és el responsable d'acoblar dèbilment aquests dos estats atòmics. D'aquesta manera, les oscil·lacions de Josephson són oscil·lacions de densitat de partícules d'un mode a un altre, on els modes són esquerra i dreta pel doble pou, i els dos estats de spin per la BJJ interna. A més a més, l'efecte de les interaccions entre partícules produeix altres efectes a part de les oscil·lacions, com ara el que es coneix com a autoconfinament (*self-trapping*), que és un regim dinàmic on la major part dels àtoms roman atrapada en un dels dos modes.

En aquesta tesi s'estudia i es caracteritza el comportament dels condensats de Bose-Einstein en una BJJ, tot utilitzant dos formalismes teòrics diferents: l'aproximació de camp mig (amb l'equació de Gross-Pitaevskii) i càlculs de molts cossos (basats en models de Bose-Hubbard). Primer s'estudia el cas més simple, format per un condensat d'una sola component, i després es passa a estudiar la barreja de dues components. Finalment, també s'estudia un cas espinorial, format per àtoms que tenen grau de llibertat de spin, i on es permet l'intercanvi de spin.

En condensats d'una sola component, ens hem centrat en l'estudi de l'estructura de l'estat fonamental en funció dels paràmetres del sistema, com la interacció entre àtoms, el número d'àtoms o l'alçada de la barrera. Hem identificat estats altament correlacionats que no es poden descriure amb teories de camp mig, i hem proposat una funció d'ona variacional que captura l'estructura de l'estat fonamental en un ampli ventall de valors d'aquests paràmetres. També hem estudiat els efectes no lineals de l'equació de Gross-Pitaevskii, visibles quan les interaccions entre àtoms són fortes. Hem vist com, degut a la no linealitat, el sistema surt de la descripció bimodal i s'exciten modes superiors. Conseqüentment, hem analitzat els nous acoblaments entre els estats més poblats.

Per condensats formats per dues components hem fet un estudi intensiu dels diferents règims que es poden formar i en quines condicions. L'aproximació bimodal estàndard (*standard two-mode approximation*) és una de les més utilitzades en l'estudi de l'efecte

Josephson, ja que proporciona unes equacions analítiques senzilles que capturen, en gran mesura, el comportament del sistema. Quan la connexió entre condensats no és suficientment dèbil, s'ha de considerar una correcció a aquesta aproximació, anomenada aproximació bimodal millorada (*improved two-mode approximation*). En aquesta tesi hem derivat aquesta última aproximació per la barreja i hem comprovat la seva validesa tot comparant-la amb simulacions numèriques de l'equació de Gross-Pitaevskii tridimensional. A més a més, com que la dinàmica Josephson es quasi unidimensional, hem considerat les reduccions més usals de la dimensionalitat de l'equació Gross-Pitaevskii. En aquest cas, també hem comparat mitjançant simulacions, aquestes reduccions unidimensionals amb l'equació tridimensional.

També hem estudiat condensats espinorials en una BJJ externa. Ens hem centrat en condensats formats per àtoms amb spin $F = 1$, que poden estar en qualsevol dels tres estats interns $m_F = 0, \pm 1$. A més a més, a diferència de la barreja, també s'hi introdueix l'intercanvi de spin entre partícules, de manera que la població de cada una de les tres components passa a ser una variable dinàmica. Primer, hem estudiat aquest sistema dins la teoria de camp mig, tot utilitzant l'equació de Gross-Pitaevskii. Hem derivat les equacions de l'aproximació bimodal, i ens hem centrat en estudiar com es desacobla l'efecte Josephson de la dinàmica d'intercanvi de partícules. En aquest cas, també comparem els resultats amb les simulacions numèriques de l'equació tridimensional de Gross-Pitaevskii. Segon, hem estudiat la BJJ espinorial utilitzant el formalisme de Bose-Hubbard, ja que algunes propietats de les fluctuacions quàntiques estan més ben capturades que amb el formalisme de camp mig. Hem caracteritzat l'estat fonamental, fixant-nos especialment en les regions on aquest està fortament correlacionat. Hem vist com la creació de singlets (estat molt correlacionat entre dues partícules) afecta en l'estructura de l'estat fonamental.

Finalment, hem estudiat l'efecte de temperatura finita en condensats de Bose-Einstein espinorials en presència d'un camp magnètic, per dos casos ben diferenciats. En primer lloc, hem agafat un condensat format per partícules amb spin $F = 1$ i amb interaccions atòmiques de contacte. Hem considerat que el condensat està format per àtoms en l'estat intern $m_F = 0$, i hem estudiat la dependència de les fluctuacions de les altres dues components $m_F = \pm 1$ en funció de la temperatura. Hem utilitzat el formalisme de Bogoliubov aplicat a un sistema homogeni, i després hem generalitzat el resultat a una trampa harmònica tot utilitzant l'aproximació de densitat local (*local density approximation*). En segon lloc, hem estudiat un condensat format per partícules amb spin $F = 3$, amb interaccions atòmiques de contacte i a més a més, interaccions dipolars. Aquestes noves interaccions, degudes als dipols magnètics dels àtoms, són de llarg abast i anisòtropes: dos dipols orientats iguals, si estan situats un a continuació de l'altre s'atrauen, mentre que si estan un al costat de l'altre es repelen. De manera similar al cas anterior, aquí considerem que el condensat està format per partícules amb $m_F = -3$ i estudiem les fluctuacions en les altres components degut a la temperatura. A primer ordre, només tenim fluctuacions en $m_F = -2$ i $m_F = -3$. En tots dos casos, hem realitzat simulacions numèriques per veure la dependència de les fluctuacions amb la temperatura, utilitzant rubidi-87 pel primer cas amb $F = 1$ i crom-52 pel segon cas, dipolar amb $F = 3$.

Abstract

Phase coherence is a characteristic property of Bose-Einstein condensates that yields fascinating macroscopic phenomena, like interference effects or Josephson oscillations. The latter ones are produced in a bosonic Josephson junction (BJJ), that schematically consists of two condensates weakly coupled where ideally 1) atoms only occupy two different single-particle states and 2) atom-atom interactions are contact-like. These junctions can be external or internal: the external BJJ is formed by a condensate confined in a double-well trap, where the intermediate barrier is large enough in order to ensure a weak link between condensates at each side of the double well. In contrast, the internal BJJ consists of a condensate in which the atoms can be in two different internal spin states. An external laser couples weakly these two atomic states. Consequently, Josephson oscillations are particle density oscillations from one mode to the other, where the modes are left and right for the double well, and the two internal spin states for the internal BJJ. Furthermore, atom-atom interactions yield more interesting phenomena, like what is called self-trapping, which is a dynamical regime where most of the atoms remain trapped in one of the two modes.

In this thesis we study and characterize the behavior of Bose-Einstein condensates in a BJJ, using two different theoretical formalisms: the mean-field approximation (with the Gross-Pitaevskii equation) and many-body calculations (based on Bose-Hubbard models). First we study the simplest case, which consists of a single-component condensate and then, we consider a mixture of two different components. Finally, we also study a spinor BJJ, in which atoms have a spin degree of freedom, and spin exchange is allowed.

With single-component Bose-Einstein condensates, we have focused on the study of the structure of the ground state as a function of the system parameters, like the atom-atom interaction strength, the number of atoms or the barrier height. We have looked for strongly correlated states, that cannot be described with mean-field theories, and we have proposed a variational wave function that captures the structure of the ground state for a broad interval of the system parameters. We have also studied the nonlinear effects of the Gross-Pitaevskii equation, visible when atom-atom interactions are strong. We have seen how, due to the nonlinearity, the system abandons the bimodal description and more modes get excited. Consequently, we have analyzed the new couplings between the highest populated states.

In the case of binary mixtures of Bose-Einstein condensates we have performed an intensive study of the different regimes that can arise and in which conditions. The standard two-mode approximation is one of the most used in the study of the Josephson effect, as it gives simple analytic equations that capture, to a great extent, the behavior of the system. When the link between condensates is not weak enough, one has to consider a correction

to this approximation, namely, the improved two-mode approximation. In this thesis, we have derived this last approximation for the binary mixture and we have checked its validity comparing it with numerical simulations of the three-dimensional Gross-Pitaevskii equation. Moreover, as the Josephson dynamics is almost one-dimensional, we have considered the two most common reductions of the dimensionality of the Gross-Pitaevskii equation. In this case, we have also compared, using simulations, these one-dimensional reductions with the three-dimensional equation.

We have also studied spinor condensates in an external BJJ. We have focused on condensates formed by atoms with spin $F = 1$, which can be in any of the three internal states $m_F = 0, \pm 1$. Furthermore, in contrast to the binary mixture, spin interchange is allowed, so that the number of particles of each component becomes a dynamic variable. First, we have studied this system within the mean-field framework, using the Gross-Pitaevskii equation. We have derived the two-mode approximation equations and we have focused in studying the decoupling of the Josephson effect and the population transfer dynamics. In this case, we also compare the results with numerical simulations of the three dimensional Gross-Pitaevskii equation. Second, we have studied the spinor BJJ using the Bose-Hubbard formalism, because some features of quantum fluctuations are better captured than with the mean-field. We have characterized the ground state, paying special attention to the regions where it is strongly correlated. We have seen how the spin singlet formation (strongly correlated state between two particles) affects the structure of the ground state.

Finally, we have studied finite temperature effects on spinor Bose-Einstein condensates in the presence of a magnetic field, for two different cases. First, we have analyzed a condensate formed by $F = 1$ atoms with contact interactions. We have considered that the condensate was formed by atoms in the internal state $m_F = 0$ and we have studied the dependence of the fluctuations of the other two components $m_F = \pm 1$ as a function of temperature. We have used the Bogoliubov formalism applied to an homogeneous system, and then, we have generalized the result to an harmonic trap by using the local density approximation. Second, we have studied a condensate formed by particles with $F = 3$ with contact interactions and moreover, dipolar interactions. The latter ones, which are due to the atom magnetic dipoles, are long-ranged and anisotropic: two dipoles oriented equally attract to each other when are head-to-tail and repel to each other if they are parallel. In a similar way as the previous case, we consider that the condensate is formed by particles with $m_F = -3$ and we study the fluctuations in the other spin components. At first order, we only have fluctuations in $m_F = -2$ and $m_F = -3$. With both cases, we have performed numerical simulations in order to see the dependence of fluctuations with temperature, using rubidium-87 for the case with $F = 1$, and chromium-52 for the dipolar case with $F = 3$.

Chapter 1

Introduction

Bose-Einstein condensation is a phenomenon that occurs when a gas of bosonic particles is cooled below a certain critical temperature T_c , and a large fraction of the atoms condense in the lowest energy single-particle state. It was first predicted by A. Einstein in 1924 [1, 2] based in a previous work of S. N. Bose on the quantum statistics of photons [3]. Basically, S. N. Bose considered the thermal black-body radiation as a gas of indistinguishable particles. The main idea was to count the number of microscopic states of light quanta compatible with a macroscopic state, and maximize the entropy of the system for a given total energy. As a result, he re-derived Planck's law for black-body radiation.

Based on this result, A. Einstein extended this way of counting the number of microscopic states to the case of an ideal Bose gas of indistinguishable particles. He derived the following expression for the number of particles n_i populating an individual state characterized by the energy ε_i

$$n_i = \frac{1}{e^{\beta(\varepsilon_i - \mu)} - 1}, \quad (1.1)$$

where $\beta = 1/k_B T$, k_B is the Boltzmann constant, T is the temperature, and μ is the chemical potential. From this distribution one can calculate all the thermodynamic properties of an ideal gas composed of particles that satisfy Bose-Einstein statistics. To get physical insight, it is useful to define the fugacity $z = e^{\beta\mu}$, which turns out to be restricted to the domain $z \in [0, 1)$. The chemical potential μ is obtained by imposing that the sum of all occupations is equal to the total number of particles N ,

$$N = \sum_i n_i = \sum_i \frac{z}{e^{\beta\varepsilon_i} - z}. \quad (1.2)$$

When the number of particles N is low or the temperature T is high, this equation gives a very small fugacity $z \ll 1$. Consequently, Eq. (1.1) becomes $n_i \simeq z e^{-\beta\varepsilon_i}$, approaching the classical Maxwell-Boltzmann distribution.

On the other hand, by increasing N or decreasing T the fugacity approaches its upper limit $z = 1$. If we write Eq. (1.2) separating the number of particles occupying the lowest energy state, which has $\varepsilon_0 = 0$, we get

$$N = n_0 + \sum_{i>0} n_i = \frac{z}{1 - z} + \sum_{i>0} \frac{z}{e^{\beta\varepsilon_i} - z}. \quad (1.3)$$

When $z \simeq 1$, n_0 becomes large and the number of particles in excited states becomes bounded by:

$$N_{\text{exc}} \leq N_{\text{max}} = \sum_{i>0} \frac{1}{e^{\beta\varepsilon_i} - 1}. \quad (1.4)$$

The key point is that when the number of particles is larger than N_{max} , the excess of particles $N - N_{\text{max}}$ must be accommodated by the single-particle lowest energy state. Particles occupying the lowest energy single-particle state form the condensate, and particles on the single-particle excited states form the thermal cloud. Notice that the upper bound N_{max} also depends on temperature. Thus, one can define the critical temperature for which N becomes of the order of N_{max} and particles start to condense.

The thermal de Broglie wavelength $\lambda_{\text{dB}} = \sqrt{2\pi\hbar^2/Mk_B T}$ is the average de Broglie wavelength of the Bose gas particles, of mass M , at temperature T ¹. In terms of λ_{dB} , the critical condition reads [4]

$$\rho\lambda_{\text{dB}}^3(T_c) = \zeta(3/2), \quad (1.5)$$

where $\rho = N/V$ is the density of the gas and $\zeta(x)$ is the Riemann zeta function, with $\zeta(3/2) \simeq 2.6124$. From this equation we can see that when $T \simeq T_c$, the thermal de Broglie wavelength becomes comparable to the interparticle distance. Below the transition temperature, the number of particles in the condensate is given by² $N_0 = N[1 - (T/T_c)^{3/2}]$.

In order to better understand Bose-Einstein condensation, there are a few things to mention:

- For an ideal Bose gas trapped in a 3D-harmonic trap one can derive similar expressions as the ones obtained for the uniform ideal Bose gas, see for example Ref. [4]. The critical temperature is $k_B T_c = \hbar\bar{\omega}N^{1/3}[\zeta(3)]^{-1/3}$, where $\bar{\omega} = \sqrt[3]{\omega_x\omega_y\omega_z}$ and ω_i are the trap frequencies along the different axis. Below this temperature, the number of particles in the condensate is $N_0 = N[1 - (T/T_c)^3]$.
- A thermodynamic system can undergo, under some conditions, through a phase transition. One signature of such transition is the appearance of a discontinuity in a derivative of the free energy \mathcal{F} with respect to some thermodynamic variable. The lowest order of the derivative at which the discontinuity appears defines the order of the phase transition.

For an ideal Bose gas trapped in a 3D-harmonic trap, one finds that the heat capacity at constant volume, $C_V = -T \left. \frac{\partial^2 \mathcal{F}}{\partial T^2} \right|_V$, has a discontinuity at T_c [4]. This is a direct signature that Bose-Einstein condensation in such conditions is a second order phase transition.

The order parameter characterizing the phase transition, which vanishes in the non-condensed state and becomes nonzero in the condensed state, can be identified with the macroscopic wave function of the condensate.

¹The de Broglie wavelength establishes a relation between the momentum and the wavelength of a particle, reflecting the wave-particle duality of matter. It is defined as $\lambda = h/p$, where h is the Planck constant and p the momentum of the particle.

²For further reading in Bose-Einstein condensation theory, see for example Refs. [4, 5]

- Dimensionality has critical effects on condensation. For example, for a uniform ideal Bose gas in two dimensions, condensation only occurs at zero temperature [4]. However, if the same gas is confined by an harmonic bi-dimensional potential, condensation can occur at nonzero temperature [4].
- The value of T_c in real experiments is extremely low. For example, for the case of a rubidium gas with $\rho = 10^{14}$ atoms/cm³, the transition temperature is $T_c \simeq 350$ nK [6].

The first Bose-Einstein condensate

When Einstein presented the results for the ideal Bose gas described above, experimentalists didn't try to achieve a Bose-Einstein condensate (BEC) in their laboratories [6]. They were skeptic because of two reasons: (1) the predicted temperature T_c was very low and was not achievable at that time [6], and (2) this prediction was done for an ideal gas, without considering interactions, and thus without taking into account the more than probable solidification of the gas [6].

In 1938 P. Kapitza, J. F. Allen and D. Misener reported the observation of superfluidity in ⁴He below the λ temperature (2.17K) [7, 8]. Shortly after, F. London suggested that despite the strong interatomic interactions present in helium, BEC was indeed occurring and was responsible for the superfluid properties that were observed [5, 9, 10]. In the following years, many experimental efforts were devoted to the measurement of the condensed fraction in liquid ⁴He [11], which turned out to be of only $\sim 10\%$.

To avoid the effects of correlations, new efforts were addressed to look for the presence of BEC in weakly-interacting Bose gases. In 1959 C. E. Hecht proposed that spin-polarized hydrogen would be a good candidate for a weakly-interacting Bose gas [12]. Interactions between two hydrogen atoms that have their spin aligned was then estimated to be so weak that no bound state should exist [4]. W. C. Stwalley and L. H. Nosanow, in 1976, confirmed Hecht's conclusions and also argued that the system would be both superfluid and Bose-Einstein condensed [13]. Their predictions stimulated the quest to achieve BEC with hydrogen atoms [4].

The first spin-polarized hydrogen gas was stabilized in 1980 by I. F. Silvera and J. T. M. Walraven [14]. Hydrogen atoms were confined by a high magnetic field gradient against a cryogenically cooled surface. However, interactions between hydrogen atoms and the surface limited the density achieved in the experiments [4]. This promoted the study of novel methods of confining atoms using only magnetic fields [15].

On the other hand, in 1975 the first proposal that laser light could be used for cooling atoms was presented by T. W. Hänsch and A. L. Schawlow [16]. When an atom is moving towards a resonant laser beam and absorbs a photon, it also absorbs its momentum. The subsequent spontaneous emission occurs in an arbitrary direction. Therefore, after this process is repeated many times, atoms slow down [4]. By using the Doppler shift, one can achieve that atoms absorb only the photons that are coming towards them, and not the ones that come from behind. For instance, with a 3-dimensional configuration of laser beams, atoms can be cooled down. C. Cohen-Tannoudji, S. Chu and W. D. Phillips were some of the pioneer researchers in developing methods to cool and trap atoms with laser light. For their achievements, they won the Nobel Prize in physics in 1997 [17].

However, these techniques were not applicable for cooling hydrogen atoms because the strong Lyman- α lines were not in resonance with any convenient laser source [18]. Alkali atoms in contrast, have a single valence electron that couples with the nuclear spin to give several hyperfine levels, which can be coupled by a resonant laser source. As a result, alkali atoms became candidates for achieving Bose-Einstein condensation [4]. However, the densities required to avoid the solidification of the gas are very low and therefore, T_c is extremely low.

In the usual experiments [19], atoms are confined in a magneto-optical trap (MOT) [20], which uses a combination of magnetic and optical forces to cool and trap the gas. The temperatures attained by the atoms, $\sim 40\mu\text{K}$ [21], are limited by the recoil energy, which is the energy acquired by an atom at rest when it absorbs a photon with a given momentum [4]. Further cooling of the gas is obtained by first transferring the atoms to a pure magnetic trap and then using evaporative cooling [15]. This technique consists of decreasing the depth of the confining trap, letting the most energetic atoms to escape. The mean energy decreases and the gas is rethermalized to a lower temperature [4].

More than 70 years after its prediction, in 1995, the first condensate was experimentally produced E. Cornell, C. Wieman and co-workers at JILA (USA) [22]. They cooled ~ 2000 ^{87}Rb atoms below 170nK by using a MOT followed by evaporative cooling. Four months later, the group of W. Ketterle at MIT created a condensate made of ^{23}Na that had about a hundred times more atoms [23]. This allowed to observe important effects, such as the coherence wave behavior of the condensates. E. Cornell, C. Wiemann and W. Ketterle won the Nobel Prize in Physics in 2001 for their achievements [19, 24]. Interestingly, there was another experiment one month after the JILA work, carried out by the group of R. G. Hulet at Rice University. They reported the creation of a condensate of lithium atoms [25], which in contrast to ^{87}Rb and ^{23}Na , presents attractive atom-atom interactions. This kind of interaction produces the collapse of the gas and therefore, prevents the gas from reaching condensation. However, in their experiment they demonstrated that when the gas is confined in a trap, the zero point energy can compensate the attractive interaction and prevent the collapse [25].

The particle density at the center of a BEC atomic cloud is typically $10^{13} - 10^{15} \text{ cm}^{-3}$, much smaller than the typical densities found in liquids and solids $\sim 10^{22} \text{ cm}^{-3}$ [4]. At these low densities, solidification of the gas induced by three-body collisions is slowed down (\sim seconds or minutes) [26]. The thermalization of the gas due to elastic binary collisions takes $\sim 10\text{ms}$, which means that one obtains a metastable BEC for a few seconds [26]. In a dilute gas at low temperature, atoms interact mainly through s-wave binary collisions. A common approach to simplify the many-body problem is to consider that each atom experiences an average interaction cast by the presence of the rest of the atoms [21]. The strength of this mean-field interaction depends on the local atomic density and the s-wave scattering length [21]. This model yields the well-known Gross-Pitaevskii equation [27, 28], which is a nonlinear Schrödinger equation.

Information about the BEC is obtained by projecting its wave function onto real-space (density distribution) or onto momentum space (velocity distribution) [29]. To measure the density, particles are illuminated with a resonant light and a camera is placed at the other side of the gas [29]. As particles absorb light, they create a shadow in the image detected by the camera. For the momentum distribution, the external confinement is

turned off and particles are released from the trap [29]. The gas expands due to its kinetic energy, and when its size is much greater than the initial cloud, the density is measured using an absorption image. Notice that by measuring the density after expansion, one actually is accessing the initial velocity distribution of the ultracold gas. This second method is called time-of-flight measurement.

Recent developments with ultra-cold gases

The first experimental groups were concentrated in increasing the number of atoms in the condensate. In this way, the wave phenomena associated to the fact of having many particles in the same quantum state would be observable at macroscopic scales. This opened the possibility of examine two characteristic properties of the wave behavior: the interference phenomena [30], and the superfluidity or vortex formation [31, 32, 33].

Immediately after the condensation of hydrogen in 1998 [34], many experimental efforts were devoted to obtain condensates of different elements, with different properties and atom-atom interactions³. Moreover, a crucial point has been the possibility to control the strength of the interaction between the atoms. The so called Feshbach resonances [49] occur when the total energy of a pair of colliding atoms is equal to the molecular bound state energy [21]. Close to the resonance, the effective s-wave scattering length of the atoms changes dramatically [21]. Furthermore, the different magnetic moments of the atomic and molecular states can be shifted using magnetic fields, and therefore, one can bring colliding atoms into or out of resonance. As a result, one can take advantage of the Feshbach resonances to change the strength of the interaction through several orders of magnitude and from attractive to repulsive [50].

Moreover, an important effect arises when condensing atoms with high magnetic moment, like chromium, dysprosium or erbium. Apart from the usual contact atom-atom interaction, these atoms also interact through sizeable magnetic dipole-dipole interactions. This interaction has two important differences with respect to contact interactions. First, it has a long range, and second, it is anisotropic: two parallel dipoles repel each other whereas two dipoles oriented head-to-tail attract each other. This interaction can also be tuned, using a rotating polarizing field [51]. For a recent review on dipolar gases we refer to [52].

The ability to confine atoms with pure optical traps opened the possibility of trapping different internal states of the same atoms. This allowed studies with spinor condensates [53, 54, 55], in which more than one hyperfine state is condensed. Interestingly, in these systems the number of particles in each component is not conserved, as spin-changing collisions or dipole-dipole interactions might couple the different internal states. Another possibility is to create mixtures of BECs [56], where different species are condensed. Notice that in this case the nature of the species is more general than in a spinor condensate. In a binary mixture for example, the two species can be two different elements [57], two different isotopes [58] or two different internal states of the same isotope [59]. Furthermore, the existence of Feshbach resonances can be used to change both intra- and inter-species interactions, increasing the number of configurations that one can

³Up to now, the elements condensed are ^{85}Rb [35], $^4\text{He}^*$ [36, 37], ^{41}K [38], ^{133}Cs [39], ^{174}Yb [40], ^{52}Cr [41], ^{170}Yb [42], ^{176}Yb [43], ^{40}Ca [44], ^{84}Sr [45, 46], ^{164}Dy [47] and ^{168}Er [48].

experimentally achieve [49].

After the first realization of BEC, the field of cold atom physics has been continuously expanding, and it has become an interdisciplinary branch of physics, relating statistical mechanics, atomic physics, photonics, solid state physics, nonlinear physics, condensed matter physics, and high energy physics. For example, the observation of solitons [60, 61], which are objects that can travel over long distances without changing its shape, merges cold atom physics with nonlinear physics and photonics. Optical lattices, as a second example, merge the fields of cold atoms, condensed matter physics and high energy physics. This is because ultracold atomic vapors trapped in optical lattices have recently been proposed as possible simulators of dynamical gauge fields [62]. For a general overview on the advances in atomic physics we refer to the recent book of C. Cohen-Tannoudji and D. Guéry-Odelin [6].

The Josephson effect

One interesting phenomenon that has been observed with BECs is an analog of the Josephson effect in condensed matter systems. Schematically, a bosonic Josephson junction (BJJ) consists of two weakly coupled BECs in which ideally 1) atoms can populate only two different single-particle states, and 2) atoms interact with each other only locally, through contact atom-atom interactions. As we have seen at the beginning of this chapter, a condensate is described by an order parameter, corresponding to the single-particle wave function that each atom populates, φ . This wave function, can be written in terms of its modulus $|\varphi|$ and its global phase $\phi(t)$, that evolves in time. In a BJJ scheme, there are two weakly coupled condensates, each of them with a modulus and a phase. Interestingly, the presence of a phase difference between them, yields the appearance of an oscillatory coherent tunneling of particles from one condensate to the other, through the weak link. This is what is known as Josephson effect in BEC.

This effect was predicted in 1962 by B. D. Josephson [63] in the context of superconductivity. When two superconductors are separated by a thin insulating barrier, forming what is called a Josephson junction, there exists a finite current between them. This current is the macroscopic observation of tunneling of particles through a barrier, and is related to the phase difference between the two superconductors⁴. This phenomenon is called direct current (d.c.) Josephson effect [63] and was experimentally observed in 1963 by P. L. Anderson and J. W. Rowel [64]. Moreover, if a constant voltage is applied to the junction, an alternating current appears. This is the alternating current (a.c.) Josephson effect, and was experimentally demonstrated in 1963 by S. Saphiro [65]. Because of the relevance and importance of the Josephson effect, B. D. Josephson won the Nobel prize in Physics in 1973.

The idea of the manifestation of the Josephson effect in cold atoms was proposed by J. Javanainen in 1986 [66], long before the first experimental BEC was created. One way of preparing a BJJ experimentally is by confining a single BEC in a double-well potential [67]. In such system, the Josephson junction consists in the two localized matter wave packets in each well, that are weakly coupled via tunneling of particles through a potential barrier.

⁴Superconductors can also be described by a macroscopic wave function, characterized by a modulus and a phase.

This configuration presents analogous a.c. and d.c. Josephson effects, but interestingly, it also presents what is called macroscopic quantum self-trapping (MQST) [68]. The MQST was predicted by A. Smerzi and collaborators [68], and consists of the suppression of the tunneling between condensates as a consequence of atom-atom interactions. Notice that this effect is not present in a superconducting Josephson junction.

In 2001, a few years after the first experimental realization of a BEC, the Josephson effect was observed in an array of bosonic Josephson junctions [69]. In 2005 the first single bosonic Josephson junction was experimentally achieved in M. K. Oberthaler's group in Heidelberg [70], where they observed both Josephson and self-trapped dynamics. Two years later, the a.c. and d.c. Josephson effects were also experimentally observed by the group of J. Steinhauer [71].

A common theoretical approach to study the dynamics of a bosonic Josephson junction within a mean-field approach was proposed by A. Smerzi et al. [68]. As we will discuss in more detail in this thesis, under some conditions this system can be described using only the first two lowest energy modes. As a result, one obtains a couple of simple equations relating the phase difference between condensates and their population imbalance [68, 72, 73]. The latter is the difference on the number of particles between the two condensates.

However, a mean-field description fails to fully capture correlations between atoms, and therefore, there are certain quantum effects that cannot be described. In contrast, the two-site Bose-Hubbard model [74], which can be mapped into the Lipkin-Meshkov-Glick model [75] is a two-mode approximation in the second quantization formalism. It can be used to describe correlated many-body quantum states, such as entangled states [76, 77, 78] or squeezed states [79, 80, 81, 82]. This model, allowed to study in detail the transition between Josephson and self-trapped regimes [83, 84], as well as the study of the ground state, which presents a strongly correlated structure for some ranges of the atom-atom interactions [85].

Outline of the thesis

The aim of this thesis is to combine the Josephson effect with the rich phenomenology present in binary mixtures and spinor condensates. We will be particularly interested in the novel effects that appear due to the additional degrees of freedom, as well as the role of interactions, which now one can distinguish between intra- and inter-species atom-atom interactions. Moreover, spinor BJJs introduce a population transfer between the different hyperfine states, and therefore, one expects new regimes that are not present neither in the single-component nor the binary mixture BJJs.

Both the binary mixture and the spinor BJJs will be studied within a mean-field framework, using the Gross-Pitaevskii equation. Moreover, for a better understanding of the quantum correlations present in a spinor BJJ we will also analyze this system from a quantum approach, using a generalization of the well-known Bose-Hubbard model [74]. We will pay special attention to the ground state properties, and we will discuss the effects of singlet formation in the structure of the ground state.

Finally, we will consider temperature effects on spinor BEC. We will be interested in the spin fluctuations created via spin-changing collisions or spin relaxation, that depend strongly on temperature. This dependence, will allow to propose a new protocol to measure temperature.

The thesis is organized as follows:

In **chapter 2** we present the theoretical basis to describe a BEC within a mean-field framework. It is a short chapter with well-known theoretical material, but very important for the understanding of the following developments. We recall the derivation of the Gross-Pitaevskii equation (GPE) [27, 28], the time-dependent Gross-Pitaevskii equation (TDGPE), the Thomas-Fermi limit and the two most common reductions of the dimensionality of the GPE: 1D Time-dependent Gross-Pitaevskii equation (1D-TDGPE) [86] and non-polynomial nonlinear Schrödinger equation (NPSE) [87].

Chapter 3 is devoted to the Josephson effect with a single component condensate, within the mean-field framework. In section 3.1, we introduce the external Josephson effect through its first experimental realization [70]. We review the two-mode approximations of the GPE in section 3.2, both the standard two-mode (S2M) [68] and the improved two-mode (I2M) [88], and recall the different regimes that can arise in the BJJ. In section 3.3 we compare the numerical solution of the TDGPE with both the two-mode approximations and the one-dimensional reductions of the GPE. Finally, in section 3.4 we also study the validity of the two-mode approximation when atom-atom interactions are increased. The results obtained are published in Ref. [89].

In **chapter 4** we extend the mean-field description to a binary mixture BJJ. In section 4.1 we recall the corresponding GPE for the binary mixture and its one-dimensional reductions. In section 4.2 we review the S2M approximation for the mixture [90] and derive the equations of the I2M approximation. The different dynamical regimes are also discussed. Section 4.3 shows a comparison of the numerical simulation of the TDGPE with both the two-mode approximations and the one-dimensional reductions. These results are published in Refs. [91, 92, 93].

A full quantum description of a single component BJJ is presented in **chapter 5**. First, we introduce the second quantization notation in section 5.1 and the two-site Bose-Hubbard (BH) Hamiltonian in section 5.2. The static properties of the system are reviewed in section 5.3, paying special attention to the ground-state structure. A variational ansatz to describe the ground state is also proposed. This study appeared in Ref. [94]. Moreover, the dynamics is briefly described in section 5.4, together with a comparison with the mean-field S2M approximation, discussed in chapter 3. Finally, an approximation to the BH model is reviewed in section 5.5, and is compared to the results obtained with the BH model.

Chapter 6 is dedicated to the study of a spin-1 BJJ. In section 6.1 we introduce both the many-body Hamiltonian in second quantization [95], and the mean-field GPEs [53, 54]. We start by deriving, in section 6.2, the S2M equations for a spin-1 BEC confined in a symmetric double-well potential, and compare them with the numerical solution of the TDGPEs. In section 6.3 we recall the extended two-site Bose-Hubbard model describing a spin-1 BJJ [96]. The ground state properties are described in section 6.4. We discuss the importance of the spin-singlet formation in the characterization of the ground state. The results are published in Refs [97, 98].

In **chapter 7** we explore temperature effects in spinor condensates in the presence of a magnetic field. Section 7.1 is devoted to the study of a spin-1 BEC that is stable in the $m = 0$ hyperfine state. We focus on the thermally activated spin fluctuations that appear due to spin-changing collisions. On the other hand, in section 7.2, we consider a spin-3

dipolar condensate stable in the $m = 3$ hyperfine state. To this end, we first introduce the Hamiltonian of a dipolar condensate, and the description of a dipolar spinor condensate. Then, we analyze the thermally activated spin fluctuations arising from the dipole-dipole interaction. The results are published in Ref. [99].

Chapter 2

Mean-field theory of Bose-Einstein Condensates

In the introduction we have discussed the appearance of Bose-Einstein condensation for a uniform ideal Bose gas. We have seen that the atoms in the condensate occupy the same single-particle state, and therefore, the complete many-body wave function is constructed as a direct product of N identical wave functions. This picture is also true for a confined ideal Bose gas [6], in which the macroscopically-occupied state is the single-particle ground state of the external potential.

In contrast, if one considers atom-atom interactions, the ground state wave function Ψ of the condensate is a $3N$ -dimensional wave function that cannot be expressed as a direct product of single-particle wave functions [6]. However, one can find the product of N identical single-particle wave functions φ such that best reproduces the total wave function Ψ . The result of this approach is the Gross-Pitaevskii equation [27, 28]. It describes how the single-particle wave function φ is determined by the combined effect of the kinetic energy, the trapping potential and the mean field exerted on a given atom by the $N - 1$ other atoms [6].

In this chapter we introduce the basic framework to study the Josephson effect within the mean-field theory. It is a short chapter that contains well-known theory, but we considered that it was important to establish this theoretical basis, that will be used in the following chapters. In section 2.1 we review the derivation of the Gross-Pitaevskii equation [27, 28]. We also discuss the time-dependent Gross-Pitaevskii equation and the Thomas-Fermi limit. In section 2.2 we recall the two most common reductions of the dimensionality of the Gross-Pitaevskii equation [86, 87].

2.1 The Gross-Pitaevskii equation

In this section we recall the derivation of the Gross-Pitaevskii equation [27, 28], which is a nonlinear Schrödinger equation that describes the order parameter of the system, i.e. the macroscopic quantum state. We follow the same approach as in Ref. [6].

We consider N identical bosons trapped in an external potential $V_{\text{ext}}(\mathbf{r})$ in equilibrium at temperature $T = 0\text{K}$. If atoms do not interact, all of them are in the same single-particle state $|\varphi_0\rangle$, which is the ground state of the external potential $V_{\text{ext}}(\mathbf{r})$. The N -body state

is the direct product $|\Psi\rangle = |\varphi_0(1)\rangle \otimes |\varphi_0(2)\rangle \otimes \cdots \otimes |\varphi_0(N)\rangle$.

When atom-atom interactions are considered, the total N -body wave function Ψ is the ground state of the N -body Hamiltonian

$$H = \sum_{i=1}^N \left[\frac{\mathbf{p}_i^2}{2M} + V_{\text{ext}}(\mathbf{r}_i) \right] + \frac{1}{2} \sum_i \sum_{i \neq j} \mathcal{V}(|\mathbf{r}_i - \mathbf{r}_j|), \quad (2.1)$$

where \mathbf{r}_i and \mathbf{p}_i are the position and momentum associated to particle i , M is the mass of the particles and \mathcal{V} is the two-body interaction potential, that in a first approximation, only depends on the distance between particles. In general it is not possible to find an analytic solution to this N -body Hamiltonian and it has to be solved numerically, using for example Monte Carlo methods [100]. However, under certain conditions, one can find a good approximation to the N -body wave function.

2.1.1 Variational approach

In this section, we find an approximate solution to the ground state of the N -body Hamiltonian. We restrict the solution to the family of tensor products of N single-particle identical states

$$|\Psi\rangle = |\varphi(1)\rangle \otimes |\varphi(2)\rangle \otimes \cdots \otimes |\varphi(N)\rangle. \quad (2.2)$$

In the subspace generated by these states, one finds the best $|\varphi\rangle$ by imposing the minimization of the energy functional

$$E[\varphi, N] = \frac{\langle \Psi | H | \Psi \rangle}{\langle \Psi | \Psi \rangle}, \quad (2.3)$$

with the constraint $\langle \Psi | \Psi \rangle = 1$. Using a Lagrange multiplier μ to include this constraint, the problem reduces to minimize $\langle \Psi | H | \Psi \rangle - \mu \langle \Psi | \Psi \rangle$. The functional differentiation $\delta(\langle \Psi | H | \Psi \rangle - \mu \langle \Psi | \Psi \rangle) = 0$ gives

$$N \int d\mathbf{r} \delta\varphi^*(\mathbf{r}) \left\{ -\frac{\hbar^2}{2M} \nabla^2 \varphi(\mathbf{r}) + V_{\text{ext}}(\mathbf{r}) \varphi(\mathbf{r}) + (N-1) \left[\int d\mathbf{r}' \mathcal{V}(\mathbf{r} - \mathbf{r}') |\varphi(\mathbf{r}')|^2 \right] \varphi(\mathbf{r}) - \mu \varphi(\mathbf{r}) \right\} + \text{c.c.} = 0. \quad (2.4)$$

Since the variations of $\delta\varphi(\mathbf{r})$ and $\delta\varphi^*(\mathbf{r})$ can be considered independent, the coefficient of $\delta\varphi^*(\mathbf{r})$ must vanish [6]. Therefore

$$-\frac{\hbar^2}{2M} \nabla^2 \varphi(\mathbf{r}) + V_{\text{ext}}(\mathbf{r}) \varphi(\mathbf{r}) + (N-1) \left[\int d\mathbf{r}' \mathcal{V}(\mathbf{r} - \mathbf{r}') |\varphi(\mathbf{r}')|^2 \right] \varphi(\mathbf{r}) = \mu \varphi(\mathbf{r}). \quad (2.5)$$

This equation describes an atom trapped in the external potential V_{ext} that also feels the mean-field potential created by the other $(N-1)$ atoms¹.

¹This is similar to the Hartree-Fock approximation for electrons in the atom.

2.1.2 Stationary Gross-Pitaevskii equation

In typical experiments the condensate density is of the order of $n \sim 10^{14}$ particles/cm³, and the effective range of the particle-particle interaction, described by the s-wave scattering length a_s , is of the order of $a_s \sim 10^{-7}$ cm. Therefore, the interparticle distance is much larger than the range of the interaction, $na_s^3 \ll 1$. Under these assumptions, the dominant collisions are elastic two-body low energy collisions and the two-particle interaction can be well described by a delta potential:

$$\mathcal{V}(|\mathbf{r}_i - \mathbf{r}_j|) = g_{3D} \delta(\mathbf{r}_i - \mathbf{r}_j), \quad (2.6)$$

where $g_{3D} = 4\pi\hbar^2 a_s/M$ is the three-dimensional coupling constant. Using this two-particle interaction, Eq. (2.5) becomes

$$\left[-\frac{\hbar^2}{2M} \nabla^2 + V_{\text{ext}}(\mathbf{r}) + g_{3D}(N-1)|\varphi(\mathbf{r})|^2 \right] \varphi(\mathbf{r}) = \mu \varphi(\mathbf{r}). \quad (2.7)$$

This equation is the stationary Gross-Pitaevskii equation (GPE), and was developed by E. P. Gross [27, 101] and L. P. Pitaevskii [28] in 1961. It plays an important role in the study of static properties of Bose-Einstein condensates in the dilute limit [102].

In order to relate the Lagrange multiplier μ to a physical quantity, we replace the delta potential Eq. (2.6) into the energy functional Eq. (2.3):

$$E[\varphi, N] = N \int d\mathbf{r} \varphi^*(\mathbf{r}) \left[-\frac{\hbar^2}{2M} \nabla^2 + V_{\text{ext}}(\mathbf{r}) + \frac{(N-1)}{2} g_{3D} |\varphi(\mathbf{r})|^2 \right] \varphi(\mathbf{r}). \quad (2.8)$$

The total derivative of this functional with respect to the number of particles is

$$\frac{dE[\varphi, N]}{dN} = \int d\mathbf{r} \varphi^*(\mathbf{r}) \left[-\frac{\hbar^2}{2M} \nabla^2 + V_{\text{ext}}(\mathbf{r}) + \left(N - \frac{1}{2} \right) g_{3D} |\varphi(\mathbf{r})|^2 \right] \varphi(\mathbf{r}), \quad (2.9)$$

where we have used the minimization condition $\delta E[\varphi, N]/\delta\varphi = 0$. Using the GPE (2.7) we find an integral expression for the Lagrange multiplier μ :

$$\mu = \int d\mathbf{r} \varphi^*(\mathbf{r}) \left[-\frac{\hbar^2}{2M} \nabla^2 + V_{\text{ext}}(\mathbf{r}) + (N-1)g_{3D} |\varphi(\mathbf{r})|^2 \right] \varphi(\mathbf{r}). \quad (2.10)$$

If we compare Eq. (2.8) with Eq. (2.10), in the limit of large N , one deduces that [6]

$$\mu(N) = \frac{\partial E[\varphi, N]}{\partial N} = E[\varphi, N] - E[\varphi, N-1], \quad (2.11)$$

where $\mu(N)$ is the chemical potential, which is the variation of the energy when N varies by one unit.

Usually, the number of particles in the condensate is large, $N \gg 1$, and therefore we can replace $N-1$ by N . The GPE (2.7) becomes

$$\left[-\frac{\hbar^2}{2M} \nabla^2 + V_{\text{ext}}(\mathbf{r}) + g_{3D} N |\varphi(\mathbf{r})|^2 \right] \varphi(\mathbf{r}) = \mu \varphi(\mathbf{r}), \quad (2.12)$$

and the energy functional (2.8)

$$E[\varphi, N] = N \int d\mathbf{r} \left[\frac{\hbar^2}{2M} |\nabla\varphi(\mathbf{r})|^2 + V_{\text{ext}}(\mathbf{r}) |\varphi(\mathbf{r})|^2 + \frac{N}{2} g_{3D} |\varphi(\mathbf{r})|^4 \right]. \quad (2.13)$$

2.1.3 Time-dependent Gross-Pitaevskii equation

To find the time-dependent Gross-Pitaevskii equation, one proposes the N -particle wave function as a product of N identical time-dependent single-particle functions [6]

$$\Psi(\mathbf{r}_1, \dots, \mathbf{r}_N, t) = \varphi(\mathbf{r}_1, t)\varphi(\mathbf{r}_2, t) \dots \varphi(\mathbf{r}_N, t). \quad (2.14)$$

Like in the time-independent case, this solution neglects some quantum correlations between the atoms. Inserting this ansatz into a least-action principle approach yields the time-dependent Gross-Pitaevskii equation (TDGPE) [6]

$$i\hbar \frac{\partial \varphi(\mathbf{r}, t)}{\partial t} = \left[-\frac{\hbar^2}{2M} \nabla^2 + V_{\text{ext}}(\mathbf{r}, t) + g_{3D} N |\varphi(\mathbf{r}, t)|^2 \right] \varphi(\mathbf{r}). \quad (2.15)$$

If the external potential is time-independent, one can find stationary solutions of the TDGPE of the form $\varphi(\mathbf{r}, t) = \varphi(\mathbf{r})e^{-i\mu t/\hbar}$, and recover the time-independent GPE (2.12).

Along this thesis, we will be consistent with the notation: $\Psi(\mathbf{r})$ describes the total wave function of the condensate, and thus is normalized to the total number of particles N , whereas $\varphi(\mathbf{r})$ describes a single-particle wave function, normalized to 1.

2.1.4 Thomas-Fermi limit

Let us consider a condensate confined in a harmonic trap. When the number of atoms becomes large enough, interactions dominate over the kinetic energy and $a_s N / a_{\text{h.o.}} \gg 0$, where $a_{\text{h.o.}} = \sqrt{\hbar/(M\omega)}$ is the length associated to the harmonic trap. Then, the kinetic term in the GPE can be neglected, and Eq. (2.12) simplifies to [103]:

$$V_{\text{ext}}(\mathbf{r}) + g_{3D} n(\mathbf{r}) = \mu, \quad (2.16)$$

where $n(\mathbf{r}) = N|\varphi(\mathbf{r})|^2$ is the density of the condensate. In the case of an axially symmetric harmonic potential $V_{\text{ext}}(\mathbf{r}) = M\omega_{\perp}^2(r^2 + \lambda^2 z^2)/2$, with $r^2 = x^2 + y^2$ and $\lambda = \omega_z/\omega_{\perp}$, the density distribution is:

$$n(\mathbf{r}) = \begin{cases} \frac{\mu}{g_{3D}} \left[1 - \frac{r^2}{R_{\perp}^2} - \frac{z^2}{R_z^2} \right] & \text{for } r \leq R_{\perp} \text{ and } z \leq R_z \\ 0 & \text{otherwise,} \end{cases} \quad (2.17)$$

which is an inverted parabola. The radial dimensions of the condensate are $R_{\perp} = \sqrt{2\mu/M\omega_{\perp}^2}$ and $R_z = R_{\perp}/\lambda$. The chemical potential is obtained by imposing the normalization condition $\int n(\mathbf{r}) d\mathbf{r} = N$, which gives

$$\mu = \left(\frac{15}{8\pi} N \lambda g_{3D} \right)^{2/5} \left(\frac{M\omega_{\perp}^2}{2} \right)^{3/5}. \quad (2.18)$$

This approximation gives in most cases analytical results, which are very useful in order to understand and predict the behavior of the system.

2.2 1-dimensional reductions

In many experiments, the confining potential is an elongated harmonic trap that causes the condensate to adopt the shape of a cigar. In such cases, dynamical effects occur mostly in the elongated dimension, simulating a quasi 1D system. Therefore, it is convenient to review the two most common dimensionality reductions of the TDGPE (2.15), which simplify the complexity of the problem. These approximations will be used in chapters 3 and 4.

We consider the 3-dimensional harmonic trapping potential

$$V_{\text{ext}}(\mathbf{r}) = \frac{1}{2}M\left(\omega_x^2 x^2 + \omega_\perp^2 r_\perp^2\right), \quad (2.19)$$

where $r_\perp^2 = y^2 + z^2$, $\omega_\perp = \omega_y = \omega_z$, and ω_i are the trap frequencies. We are interested in the strongly anisotropic case, where $\omega_\perp \gg \omega_x$, and the condensate has a cigar shape.

When the chemical potential is much smaller than the energy of the transverse modes, $\mu \ll \hbar\omega_\perp$, we can assume that the particles populate the ground state of the transverse effective potential (recall that we are considering a weakly interacting gas, so that the effect of interactions is small). Then, the wave function can be factorized as $\Psi(x, r_\perp, t) = \Psi(x, t)\varphi(r_\perp)$, and only the longitudinal modes, with $\hbar\omega_x \lesssim \mu$ are excited.

If the effect of interactions is small, the transverse wave function $\varphi(r_\perp)$ will preserve the shape of the single-particle ground state of the transverse harmonic oscillator:

$$\varphi(r_\perp) = \frac{1}{\sqrt{2\pi\sigma^2}} e^{-\frac{r_\perp^2}{2\sigma^2}}, \quad (2.20)$$

where σ^2 is the variance of the distribution. There are two common reductions of the GPE, the first one assumes that $\varphi(r_\perp)$ is equal to the single-particle ground state of the transverse potential $V_{\text{ext}}(r_\perp)$ [86], and the second one takes σ as a variational parameter in order to take into account interactions [87]. We discuss these two approximations in the following subsections.

1D Time-dependent Gross-Pitaevskii equation

First, we consider that the transverse wave function $\varphi(r_\perp)$ is well approximated by the single-particle ground state of the transverse harmonic potential [86]:

$$\varphi(r_\perp) = \frac{1}{\sqrt{2\pi a_\perp^2}} e^{-\frac{r_\perp^2}{2a_\perp^2}}, \quad (2.21)$$

where the oscillator length $a_\perp = \sqrt{\hbar/(M\omega_\perp)}$ plays the role of σ . Inserting this factorization into the TDGPE (2.15), integrating over r_\perp and rescaling the energy a factor $\hbar\omega_\perp$, we get the one-dimensional time-dependent Gross-Pitaevskii equation (1D-TDGPE) [86]:

$$i\hbar \frac{\partial \Psi(x, t)}{\partial t} = \left[-\frac{\hbar^2}{2M} \frac{\partial^2}{\partial x^2} + V_{\text{ext}}(x) + g_{1D} |\Psi(x, t)|^2 \right] \Psi(x, t), \quad (2.22)$$

where the reduced one-dimensional coupling constant is $g_{1D} = g_{3D}/(2\pi a_\perp^2)$.

Non-polynomial nonlinear Schrödinger equation

The previous approximation does not include the effect of interactions in the shape of the transverse ground state, or the possibility of a transverse dynamics. Therefore, in order to capture part of these effects, one can consider $\varphi(r_\perp)$ to be time-dependent: $\varphi(r_\perp, t)$. The transverse wave function is considered a Gaussian but with a variational $\sigma(x, t)$, that depends on the position and time, and which value is determined by minimizing the energy functional. The TDGPE (2.15) becomes the non-polynomial nonlinear Schrödinger equation (NPSE) [87]:

$$i\hbar \frac{\partial \Psi(x, t)}{\partial t} = \left[-\frac{\hbar^2}{2M} \frac{\partial^2}{\partial x^2} + V_{\text{ext}}(x) + g_{1D} \frac{|\Psi(x, t)|^2}{\sqrt{1 + 2a_s |\Psi(x, t)|^2}} + \frac{\hbar\omega_\perp}{2} \left(\frac{1}{\sqrt{1 + 2a_s |\Psi(x, t)|^2}} + \sqrt{1 + 2a_s |\Psi(x, t)|^2} \right) \right] \Psi(x, t), \quad (2.23)$$

where the transverse wave function $\varphi(r_\perp, t)$ is characterized by

$$\sigma^2(x, t) = a_\perp^2 \sqrt{1 + 2a_s |\Psi(x, t)|^2}. \quad (2.24)$$

Chapter 3

Josephson effect in scalar condensates

The Josephson effect in Bose-Einstein condensates is a macroscopic quantum effect that enables to enlighten one of the most subtle aspects of quantum mechanics: the quantum phase. From the previous chapter, we know that a BEC can be accurately represented by the order parameter $\varphi(\mathbf{r})$, corresponding to the single-particle wave function in which atoms condense. Moreover, we have also seen that the chemical potential μ of the condensate governs the time-evolution of its global phase, as $\varphi(\mathbf{r}, t) = \varphi(\mathbf{r})e^{-i\mu t/\hbar}$. Therefore, the time-evolution of the phase difference between two independent BECs is proportional to the difference in their chemical potentials. The effects of this phase difference were experimentally measured for the first time in the experiment performed by M. R. Andrews and collaborators [30]. They made two independent BECs overlap by expanding them freely, and studied the interference pattern that was produced [30]. They observed high-contrast matter-wave fringes, with an spacing much smaller than the length of the condensates. This was a clear evidence of the large spatial coherence of the phase along each condensate.

The Josephson effect is observed when two BECs are coupled, allowing particles to transfer from one condensate to the other. The link between them has to be weak in order to ensure the preservation of the phase coherence in each condensate. When initially, there is a phase difference between the two condensates, appears a current of particles across the link as a signature of the d.c. Josephson effect [71, 104]. The exchange of particles modulates the chemical potential of each condensate and therefore, the evolution of the phase difference is affected. As a result, one obtains oscillations of particles from one condensate to the other, called Josephson oscillations. As we will see, the frequency of these oscillations depends on the strength of the atom-atom interactions.

There are two setups which have already been used to create a bosonic Josephson junction (BJJ). The first one, that we will study extensively, is the external BJJ. In this case, the two condensates are spatially separated. This can be achieved by condensing the ultracold atomic cloud on a double-well potential [67]. The weakly linked condition can be controlled with the potential barrier between the two wells, that allows particles to tunnel from one side to the other. The second one is the internal BJJ [105], in which the two BECs are not spatially separated. Instead, the two condensates are made of two

different internal states of the same atom. The link is obtained by coupling a laser beam in resonance with the transition from one internal state to the other. In this case, the intensity of the laser controls the strength of the link.

A seminal theoretical study of BJJ was done by A. Smerzi et al. in 1997 [68]. In their paper, they considered a BEC confined in a double-well potential described by the mean-field Gross-Pitaevskii equation [27, 28], discussed in Chapter 2. They realized that under certain conditions, the system can be described using only the two lowest energy modes. As we will see in the following, with this two-mode approximation, they derived a simple system of differential equations relating the phase difference between condensates and their population imbalance (difference in the number of particles between the two condensates). Moreover, they predicted what is called macroscopic quantum self-trapping (MQST) [68]. This is a dynamical regime in which the atoms remain mostly trapped in one well, and the tunneling through the barrier is mostly suppressed. This is a novel effect of BJJ which depends crucially on atom-atom interactions, and that was not present in the superconducting analog.

In section 3.1, we describe in more detail the first experimental realization of a single external BJJ, made in the group of M. K. Oberthaler in 2005 [70]. The aim is 1) to give some insight into the Josephson dynamics, and 2) to introduce the setup parameters of the experiment, that will be used in the numerical results of Sec. 3.3. In section 3.2 we review the two-mode approximation [68, 88] and describe the dynamics and different regimes that can take place within this approximation. In section 3.3 we show a comparison between the numerical calculations of the TDGPE (2.15) with both the two-mode descriptions [68, 88] and the 1-dimensional reductions described in the previous chapter, 1D-TDGPE [86] and NPSE [87].

Finally, in section 3.4 we focus in a quasi 1-dimensional system described by the 1D-TDGPE (2.22). We explore the validity of the two-mode approximation when the interactions are increased. Contrary to the two-mode predictions, the numerical simulations of the 1D-TDGPE (2.22) show a revival on the tunneling when interactions become even stronger. However, we show that in this situation the dynamics of the system can still be described using a bimodal picture, involving higher energy modes.

3.1 Experimental realization of an external BJJ

The first experimental realization of a single external BJJ was done by M. Albiez et al. [70, 104], in the Heidelberg group of M. K. Oberthaler. There, a condensate of 1150 ^{87}Rb atoms was loaded to an external effective double-well potential. This potential was the combination of a 3-dimensional harmonic trap of frequencies $\omega_x = 2\pi \times 78$ Hz, $\omega_y = 2\pi \times 66$ Hz and $\omega_z = 2\pi \times 90$ Hz, and a 1-dimensional optical lattice in the x direction, of spacing $q_0 = 5.2\mu\text{m}$ and potential depth $V_0 = 413$ hHz, where h is the Planck constant. The resulting effective potential is [70]

$$V_{\text{ext}}(\mathbf{r}) = \frac{1}{2}M(\omega_x^2(x - \Delta x)^2 + \omega_y^2 y^2 + \omega_z^2 z^2) + V_0 \cos^2 \frac{\pi x}{q_0}, \quad (3.1)$$

where Δx is the relative position shift of the two potentials and M is the mass of the atoms. The interactions between the ^{87}Rb atoms are described by the s-wave atom-atom

scattering length $a_s = 100.87a_B$, with a_B the Bohr radius, that yields an interaction strength $g_{3D} = 4\pi\hbar^2 a_s/M = 48.78 \hbar \mu\text{m}^3\text{Hz}$.

In the experiment [70], the system is initially prepared with a different amount of particles in each well. This is achieved by condensing the ultracold gas in the ground state of an asymmetric double-well potential [104], obtained by taking $\Delta x \neq 0$ in Eq.(3.1). Notice that the phase is constant along the condensate and therefore, the initial phase difference between the matter-wave packets localized in each well is zero.

At $t = 0$ the asymmetry is quickly removed, $\Delta x = 0$, and the ultracold atomic cloud is no longer in the ground state solution of the double-well potential. The subsequent dynamics can be understood by considering two weakly linked BEC, each one localized in one well. From the GPE (2.12) one can see that the chemical potential μ of a condensate depends on the number of particles N in the condensate. Therefore, condensates with different number of particles have different phase evolutions. This results in the appearance of a phase difference between the two sides of the well, which translates into a current of particles between sides.

The results obtained by M. Albiez et al. are plotted in Fig. 3.1. The experimental measurements are density plots taken after time-of-flight expansion of the condensate¹. The initial conditions of panel (a) consist in a small difference in the number of particles and zero phase difference between the condensates. One can see that the density at each side oscillates indicating that the atoms go from one side to the other of the potential barrier, performing Josephson oscillations. The frequency of the oscillation is usually called plasma frequency, in analogy with the superconducting Josephson junctions [104]. In panel (b), the starting phase difference between condensates is again zero, but initially most of the particles are in the left well. This gives rise to a self-trapped dynamics [68], in which particles remain mostly trapped on one well during time-evolution. There are small oscillations in the density, but always with more particles on the left well.

In the following section we review the most common approximation that captures the dynamics of a BJJ: the two mode approximation.

3.2 Two-mode approximation

We have seen that an external BJJ can be achieved by placing a BEC in a double-well potential, and that the central barrier has to be high enough in order to ensure a weak link between condensates at each side. As we will describe in more detail, in this situation the many-body ground and first excited states are very close in energy, and well separated from the other excited states. This allows for a two-mode approximation in which the system is described using only the two lowest energy modes.

The two-mode approximation was introduced by Smerzi et al. [68], and allows, under certain conditions, to study the dynamics of two weakly linked BEC without solving the full TDGPE, Eq. (2.15), or without reducing its dimensionality. Moreover, it provides analytical expressions that predict the different regimes that can occur. When the system does not fulfill the weakly linked condition, multi-orbital theories like those discussed

¹Notice that time-of-flight expansion is a destructive technique, and therefore, the experiment has to be repeated many times.

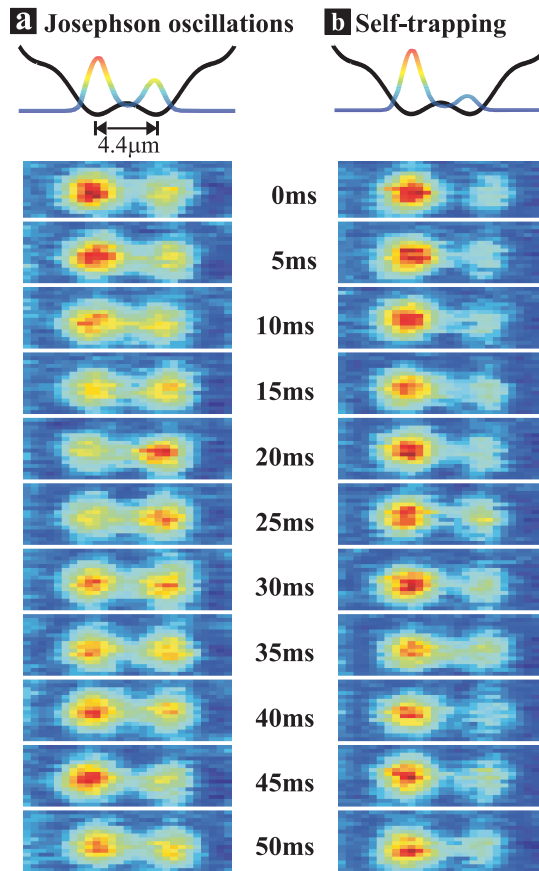


Figure 3.1: Figure taken from Ref. [70]. Observation of the tunneling dynamics of two weakly linked Bose-Einstein condensates in a symmetric double-well potential. Panel (a) shows plasma oscillations, in which the initial number of particles differs only slightly between wells. Panel (b) is an example of self-trapping. Initially there are many more particles in the left well, and due to interactions, the particles remain mostly trapped on that well.

in [106, 107] have to be used.

We consider the external potential of Eq. (3.1) with $\Delta x = 0$, which consists in the superposition of a 3-dimensional harmonic trap and a barrier in the x direction, that creates a symmetric double well. As an example, we plot in Fig. 3.2 the external double-well potential in the x direction, $V_{\text{ext}}(x) = M\omega_x^2 x^2/2 + V_0 \cos^2(\pi x/q_0)$, using the parameters of the Heidelberg experiment [70], see Sec. 3.1. If the atom-atom interactions are weak, which is a necessary condition for the validity of the GPE, we can consider that the lowest stationary states of the system are very similar to the non-interacting ones. Thus, in order to study the validity of the two-mode approximation, we also plot the first four eigenenergies and the corresponding eigenmodes of the single particle Hamiltonian:

$$H_{\text{sp}} = -\frac{\hbar^2}{2M}\nabla^2 + V_{\text{ext}}(x). \quad (3.2)$$

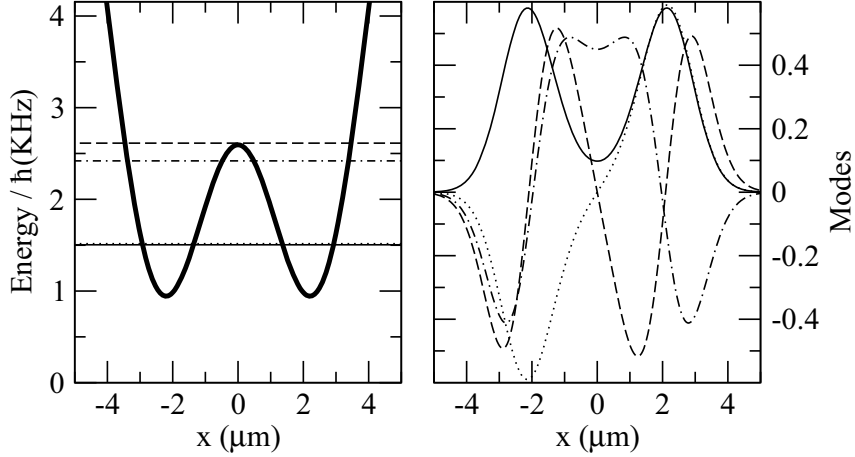


Figure 3.2: Left: External double-well potential $V_{\text{ext}}(x)$ used in the Heidelberg experiment [70] in units of \hbar , see Sec. 3.1. The horizontal lines are the first four eigenenergies of the single-particle Hamiltonian. Right: The first four single-particle eigenmodes corresponding to the eigenenergies depicted on the left.

As we can see, the first two eigenvalues, E_{sp}^0 and E_{sp}^1 , show a clear separation with respect to the other excited states, which suggests that at very low temperatures we can describe the order parameter of the condensate using only the first two eigenmodes. The relevant physical quantity is the ratio $(E_{\text{sp}}^1 - E_{\text{sp}}^0)/(E_{\text{sp}}^2 - E_{\text{sp}}^0)$, which describes how far is the second excited state with respect to the first two. When this ratio is small, the other excited states will not get populated and the dynamics will be well described by a combination of the ground state $\varphi_+^{\text{sp}}(\mathbf{r})$ and the first excited state $\varphi_-^{\text{sp}}(\mathbf{r})$ of the single-particle Hamiltonian. As this picture remains the same for a weakly interacting system, we use $\varphi_+(\mathbf{r})$ and $\varphi_-(\mathbf{r})$ of the full GP Hamiltonian in order to describe the dynamics. In Fig. 3.3 we plot the density distributions $\rho_+(\mathbf{r})$ and $\rho_-(\mathbf{r})$ associated to the states $\varphi_+(\mathbf{r})$ and $\varphi_-(\mathbf{r})$. These states have been calculated by imaginary time evolution (see Appendix A) in the conditions of the Heidelberg experiment [70]. However, due to the large degree of coherence that each condensate preserves at each side, it is more convenient to describe the dynamics using the combinations:

$$\varphi_L(\mathbf{r}) = \frac{\varphi_+(\mathbf{r}) + \varphi_-(\mathbf{r})}{\sqrt{2}}; \quad \varphi_R(\mathbf{r}) = \frac{\varphi_+(\mathbf{r}) - \varphi_-(\mathbf{r})}{\sqrt{2}}, \quad (3.3)$$

where $\varphi_L(\mathbf{r})$ is a mode that is mostly localized on the left, and $\varphi_R(\mathbf{r})$ on the right, see Fig. 3.3. Under this two-mode approximation, the total wave function can be expressed as:

$$\Psi(\mathbf{r}, t) \simeq \psi_L(t)\varphi_L(\mathbf{r}) + \psi_R(t)\varphi_R(\mathbf{r}), \quad (3.4)$$

where $\psi_{L(R)}(t) = \sqrt{N_{L(R)}(t)} e^{i\phi_{L(R)}(t)}$, and $N_{L(R)}(t)$ is the number of particles occupying the mode $\varphi_{L(R)}(\mathbf{r})$ with a phase $\phi_{L(R)}(t)$. The total number of particles is conserved $N = N_L(t) + N_R(t)$, and the modes at each side are real and normalized: $\int d\mathbf{r} \varphi_{L,R}^2(\mathbf{r}) = 1$.

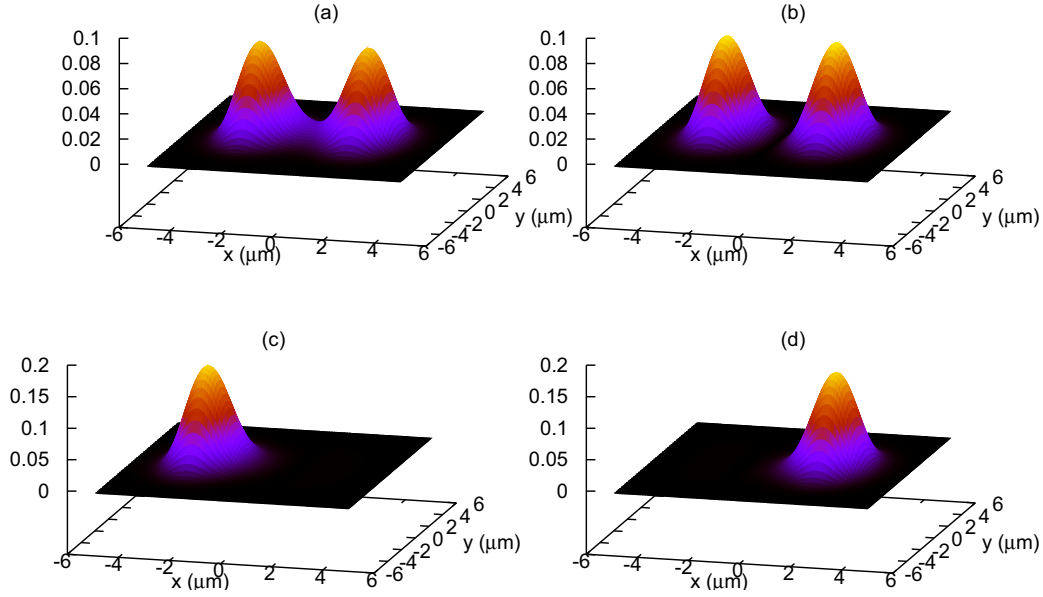


Figure 3.3: TDGPE simulations under the conditions of the Heidelberg experiments [70]. The plots correspond to the density of (a) the ground state $\rho_+(\mathbf{r})$, (b) the first excited state $\rho_-(\mathbf{r})$, (c) the left mode $\rho_L(\mathbf{r})$ and (d) the right mode $\rho_R(\mathbf{r})$. These left and right modes are the ones that we use to create the initial state, as well as the ones used to compute the different parameters in the two-mode models.

3.2.1 Standard two-mode

As a first step, we consider the standard two-mode approximation (S2M), introduced in [68]. It yields essentially the same qualitative results as the TDGPE, although it may lead to different quantitative predictions depending on the specific barrier properties [70, 73].

Inserting the two-mode ansatz Eq. (3.4) into the TDGPE Eq. (2.15), and neglecting integrals involving mixed products of $\varphi_L(\mathbf{r})$ and $\varphi_R(\mathbf{r})$ of order larger than 1, one gets the coupled system of equations:

$$\begin{cases} i\hbar \frac{\partial \psi_L(t)}{\partial t} = [E_L^0 + U_L N_L(t)] \psi_L(t) - K \psi_R(t) \\ i\hbar \frac{\partial \psi_R(t)}{\partial t} = [E_R^0 + U_R N_R(t)] \psi_R(t) - K \psi_L(t) \end{cases}, \quad (3.5)$$

where E_i^0 is the single-particle energy of a particle in the site $i = L, R$

$$E_i^0 = \int d\mathbf{r} \left[\frac{\hbar^2}{2M} |\nabla \varphi_i(\mathbf{r})|^2 + \varphi_i^2(\mathbf{r}) V_{\text{ext}}(\mathbf{r}) \right], \quad (3.6)$$

and U_i is the mean-field interaction energy of the site i :

$$U_i = g_{3D} \int d\mathbf{r} \varphi_i^4(\mathbf{r}). \quad (3.7)$$

When the atom-atom interactions are switched off, particles tunnel from one site to the other with a frequency proportional to

$$K = - \int d\mathbf{r} \left[\frac{\hbar^2}{2M} \nabla \varphi_L(\mathbf{r}) \cdot \nabla \varphi_R(\mathbf{r}) + \varphi_L(\mathbf{r}) V_{\text{ext}}(\mathbf{r}) \varphi_R(\mathbf{r}) \right]. \quad (3.8)$$

This term is also proportional to the energy difference between the single-particle ground and first excited states.

Next, we express these equations in terms of the population imbalance $z(t) = [N_L(t) - N_R(t)]/N$ and the phase difference between wells $\delta\phi(t) = \phi_R(t) - \phi_L(t)$. Taking into account that the total number of particles is conserved, $\dot{N}_L + \dot{N}_R = 0$, one gets the S2M equations [68]:

$$\begin{cases} \dot{z}(t) = -\omega_R \sqrt{1 - z^2(t)} \sin \delta\phi(t) \\ \delta\dot{\phi}(t) = \omega_R \Delta E + \omega_R \Lambda z(t) + \omega_R \frac{z(t)}{\sqrt{1 - z^2(t)}} \cos \delta\phi(t), \end{cases} \quad (3.9)$$

where $\omega_R = 2K/\hbar$ is the Rabi frequency and

$$\begin{aligned} \Delta E &= \frac{E_L^0 - E_R^0}{2K} + \frac{U_L - U_R}{4K} N \\ \Lambda &= \frac{U_L + U_R}{4K} N. \end{aligned} \quad (3.10)$$

Note that $\Lambda > 0$ and $\Lambda < 0$ correspond to repulsive and attractive atom-atom interactions, respectively.

Finally, using the two-mode ansatz (3.4) into the energy functional of the TDGPE (2.13) we can define the conserved energy per particle of the system, in units of K , as:

$$H = \frac{E - C}{NK} = \Delta E z + \frac{U_L + U_R}{8K} N z^2 - \sqrt{1 - z^2} \cos \delta\phi \quad (3.11)$$

where C is a rescaling constant. Note that the equations of motion (3.9) can be recovered using that z and $\delta\phi$ are canonical conjugate [68]:

$$\dot{z} = -\frac{\partial H}{\partial \delta\phi}; \quad \delta\dot{\phi} = \frac{\partial H}{\partial z}. \quad (3.12)$$

In the particular case of a symmetric double-well potential we have $E_L^0 = E_R^0$ and $U_L = U_R \equiv U$, so $\Delta E = 0$ and $\Lambda = NU/(2K)$. The S2M equations read:

$$\begin{cases} \dot{z}(t) = -\omega_R \sqrt{1 - z^2(t)} \sin \delta\phi(t) \\ \delta\dot{\phi}(t) = \omega_R \Lambda z(t) + \omega_R \frac{z(t)}{\sqrt{1 - z^2(t)}} \cos \delta\phi(t), \end{cases} \quad (3.13)$$

and the energy:

$$H = \frac{\Lambda}{2} z^2 - \sqrt{1 - z^2} \cos \delta\phi. \quad (3.14)$$

3.2.2 Improved two-mode

Smerzi and collaborators [88] noticed that for a symmetric double well there was no need to neglect any of the overlapping integrals to obtain a closed set of equations relating $z(t)$ and $\delta\phi(t)$. Retaining all these terms, we get the improved two-mode equations (I2M) [73]:

$$\begin{cases} \dot{z}(t) &= -B\sqrt{1-z^2(t)} \sin \delta\phi(t) + C(1-z^2(t)) \sin 2\delta\phi(t) \\ \delta\dot{\phi}(t) &= Az(t) + \frac{Bz(t)}{\sqrt{1-z^2(t)}} \cos \delta\phi(t) - Cz(t) \cos 2\delta\phi(t), \end{cases} \quad (3.15)$$

where the coefficients are:

$$A = \frac{N}{4}(10\gamma_{+-} - \gamma_{++} - \gamma_{--}) \quad (3.16)$$

$$B = 2K + \frac{N}{2}(\gamma_{--} - \gamma_{++}) \quad (3.17)$$

$$C = g_{3D}N \int d\mathbf{r} \varphi_L^2(\mathbf{r})\varphi_R^2(\mathbf{r}) \quad (3.18)$$

$$\gamma_{ij} = g_{3D} \int d\mathbf{r} \varphi_i^2(\mathbf{r})\varphi_j^2(\mathbf{r}), \quad \text{for } i, j = +, -. \quad (3.19)$$

Note that these coefficients are in terms of the left and right modes $\varphi_{L(R)}(\mathbf{r})$ and also the ground and first excited states $\varphi_{+(-)}(\mathbf{r})$. In the S2M approximation, $C = 0$, $\gamma_{ij} = \gamma = U/2$ and the system (3.15) reduces to the corresponding S2M equations (3.9).

As discussed in detail in Ref. [73], the physics arising from the I2M is similar to the one present in the S2M. However, the I2M is in much better agreement with the TDGPE for a broader set of double-well potentials, as we will see in Sec. 3.3.

3.2.3 Regimes for a scalar condensate

In this section, we review the different regimes that occur in a scalar condensate in a symmetric double-well potential [68]. We use the S2M equations instead of the I2M because they capture qualitatively the dynamics of the system, and are much simpler than the I2M equations. First, we focus in the case of repulsive interactions, and then discuss the analogies with attractive interactions.

Stability analysis

The stationary solutions $(z^0, \delta\phi^0)$ of a scalar condensate with repulsive interactions $\Lambda > 0$, can be found by solving the equations:

$$\left. \frac{\partial H}{\partial z} \right|_{z^0, \delta\phi^0} = 0; \quad \left. \frac{\partial H}{\partial \delta\phi} \right|_{z^0, \delta\phi^0} = 0, \quad (3.20)$$

where H is the S2M Hamiltonian (3.14). To assess the stability of these points, we need to study the Hessian matrix of the system, which for the possible values of the phase difference, $\delta\phi^0 = 0$ or π , is always diagonal and its eigenvalues are $\partial_z^2 H|_{z^0, \delta\phi^0}$ and $\partial_{\delta\phi}^2 H|_{z^0, \delta\phi^0}$. Depending on the sign of these eigenvalues the stationary points will be maxima, saddle

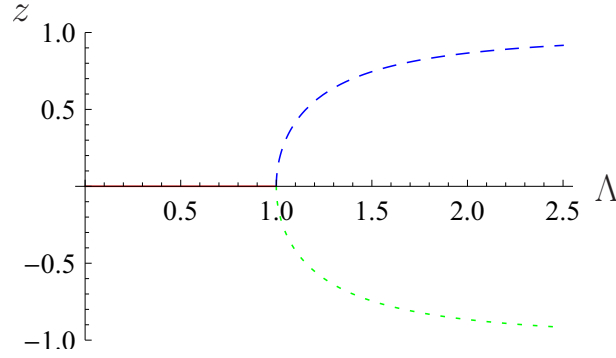


Figure 3.4: Population imbalance of the stationary points of the system that are a maximum for $\Lambda > 0$: $z^0 = 0$ (solid-red), $z^0 = \sqrt{1 - 1/\Lambda^2}$ (dashed-blue) and $z^0 = -\sqrt{1 - 1/\Lambda^2}$ (dotted-green). In all cases $\delta\phi^0 = \pi$.

points or minima. The stationary points and their stability are summarized in Table 3.1. Notice that for repulsive interactions, $\Lambda > 0$, the stationary state $(z^0, \delta\phi^0) = (0, 0)$ is always a minimum, and the stationary state with a maximum has $\delta\phi^0 = \pi$ and a bifurcation for the population imbalance at $\Lambda = 1$: for $\Lambda < 1$ the population imbalance is $z^0 = 0$ and for $\Lambda > 1$ there are two solutions, $z^0 = \pm\sqrt{1 - 1/\Lambda^2}$. This bifurcation has been experimentally observed in Ref. [105], using an internal BJJ.

The evolution of the system can be represented on a $z - \delta\phi$ plane, where the system follows trajectories with constant energy, see Fig. 3.5. Note that oscillations around a stationary point occur only if the central point is either a maximum or a minimum of the energy, but not a saddle point.

Symmetry between attractive and repulsive interactions

The stability analysis has been presented only for repulsive interactions, but from the system (3.13) we can see that if we change the interactions, $\Lambda \rightarrow -\Lambda$, we recover the same system of equations if $\delta\phi \rightarrow \pi - \delta\phi$:

$$\begin{cases} \frac{d}{dt}z(t) &= -\sqrt{1 - z^2(t)} \sin(\pi - \delta\phi(t)) \\ \frac{d}{dt}(\pi - \delta\phi(t)) &= -\Lambda z(t) - \frac{z(t)}{\sqrt{1 - z^2(t)}} \cos(\pi - \delta\phi(t)), \end{cases} \quad (3.21)$$

which means that the dynamics of the system and the different regimes are the same for both types of interactions, with a phase-shift of π . This can be seen in Fig. 3.6, that shows

$(z^0, \delta\phi^0)$	stationary	minimum	saddle	maximum
$(0, 0)$	$\forall\Lambda$	$\forall\Lambda$	—	—
$(0, \pi)$	$\forall\Lambda$	—	$\Lambda > 1$	$\Lambda < 1$
$(\pm\sqrt{1 - 1/\Lambda^2}, \pi)$	$\Lambda > 1$	—	—	$\Lambda > 1$

Table 3.1: Stationary points of the system for repulsive interactions, $\Lambda > 0$, and their stability.

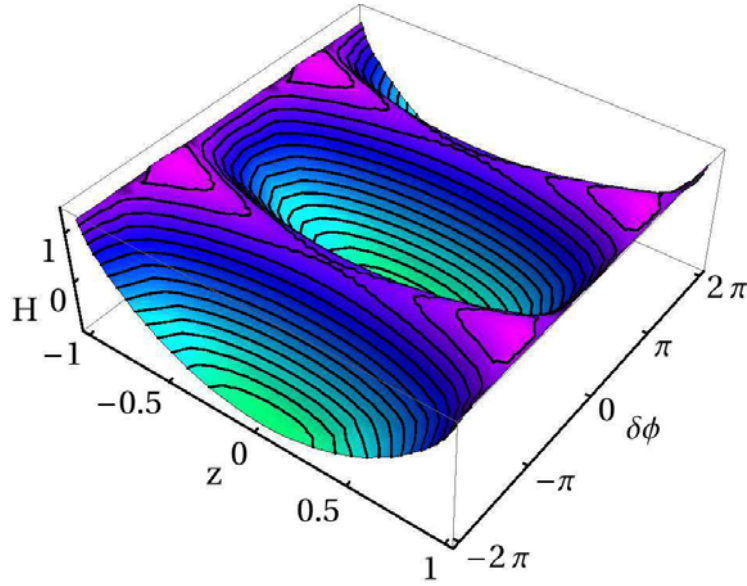


Figure 3.5: Energy surface, Eq. (3.14), for $\Lambda = 2.5$. The lines on the surface correspond to possible classical trajectories of the system, which have constant energy.

the behavior of the system for a given set of initial conditions. The upper panels are for repulsive interactions $\Lambda > 0$ and the lower ones for attractive interactions $\Lambda < 0$. The gray regions correspond to Josephson oscillations, the blue regions to zero- and π -modes, and the red regions to running phase modes, as we will discuss in the following sections.

Josephson dynamics

This regime is characterized by a fast oscillating tunneling of population across the potential barrier. Plotted in a $z - \delta\phi$ map, the system evolves following closed trajectories around a minimum or a maximum ($z^0 = 0, \delta\phi^0$) configuration, with a zero time-average of the population imbalance, $\langle z \rangle_t = 0$. The stability analysis shows that for $\Lambda > -1$, which corresponds to repulsive or slightly attractive interactions, the stationary point ($z^0 = 0, \delta\phi^0 = 0$) is a minimum permitting Josephson oscillations around it. Analogously, when $\Lambda < 1$, for either attractive or slightly repulsive interactions, the stationary point ($z^0 = 0, \delta\phi^0 = \pi$) becomes a maximum, and therefore also allows for closed orbits around it. For $|\Lambda| > 1$, there are Josephson oscillations around only one point: ($z^0 = 0, \delta\phi^0 = 0$), or ($z^0 = 0, \delta\phi^0 = \pi$). However, in the region of weak interaction, $|\Lambda| < 1$, the oscillations around both points are allowed.

In panel (a) of Fig. 3.7, $\Lambda = 0.5$, the black closed orbits around $\delta\phi^0 = 0$ or around $\delta\phi^0 = \pi$ correspond to Josephson dynamics around these points. In panel (b) however, as $\Lambda = 1.5 > 1$, only the origin can give rise to Josephson oscillations, so the closed orbits around ($z^0 = 0, \delta\phi^0 = \pi$) disappear.

It is also interesting to study the behavior of the system for small oscillations around these two stationary points of zero imbalance, i.e., smallest orbits in Fig. 3.7 (a). In this limit, the system (3.13) can be linearized giving the dynamical equation: $\ddot{z}(t) = -z(t)(1 +$

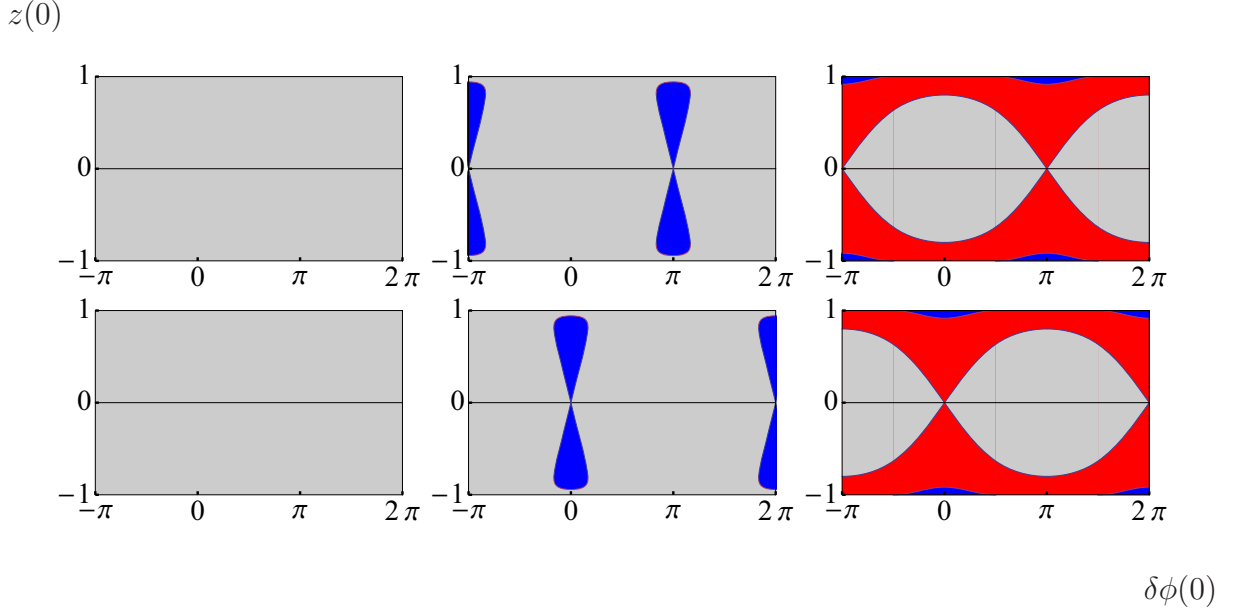


Figure 3.6: Different regimes for a set of initial conditions, imbalance $z(0)$ in the y -axis and phase difference $\delta\phi(0)$ in the x -axis. The upper panels correspond to repulsive interactions while the lower ones to attractive interactions. The values of $|\Lambda|$ are 0.5, 1.5, and 5. for the left, middle and right panels respectively. Grey regions correspond to Josephson oscillations, blue regions to π -modes (upper panels) and zero-modes (lower panels), and red regions to running phase modes.

$\Lambda \cos \delta\phi^0$) with $\cos \delta\phi^0 = \pm 1$. The population imbalance performs sinusoidal oscillations with a frequency $\omega_J = \omega_R \sqrt{1 + \Lambda \cos \delta\phi^0}$, independent of the initial population imbalance. Note that this frequency only exists when these points are either maxima or minima. The phase difference oscillates with the same frequency but with a phase-shift of $\pi/2$ with respect to the imbalance. If the initial population imbalance increases, the dynamics of the system changes substantially to non-sinusoidal oscillations, and the frequency becomes dependent on the initial conditions [68].

Macroscopic quantum self-trapping

In the case of repulsive interactions, we have seen that for $\Lambda > 1$, the stationary point ($z^0 = 0, \delta\phi^0 = \pi$) becomes a saddle point and there appear two maxima, ($z^0 = \pm\sqrt{1 - 1/\Lambda^2}, \delta\phi^0 = \pi$). A similar behavior is found for attractive interactions. These stationary points allow for oscillations around them with $\langle z \rangle_t \neq 0$. In fact, in this regime, the imbalance has the same sign during the evolution, and therefore one of the wells is always overpopulated.

This regime is called macroscopic quantum self-trapping (MQST), as the tunneling is strongly suppressed and the particles remain mostly trapped in one of the wells. This is a phenomenon arising from the atom-atom interaction, which appears as a nonlinearity

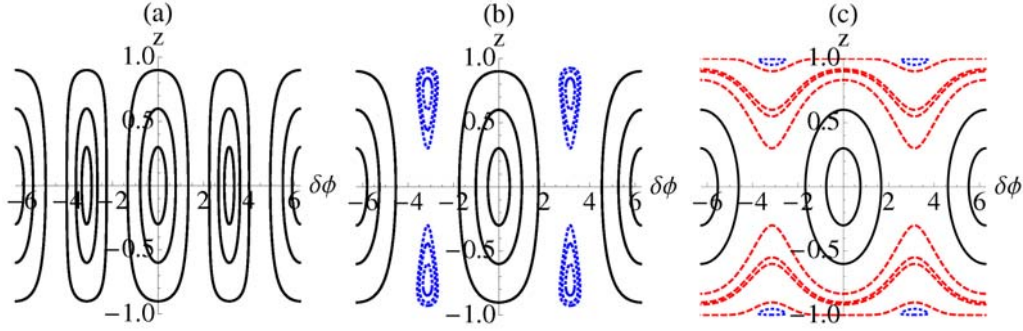


Figure 3.7: $z - \phi$ representation of different constant energy trajectories for three values of Λ : 0.5 (a), 1.5 (b), and 5 (c). Solid-black lines correspond to Josephson oscillations, dotted-blue to π -modes, and dashed-red lines to running phase modes.

in the Gross-Pitaevskii equation.

The critical condition for the existence of the MQST regime can be found by imposing that the system remains on one side of the trap [68]. For a given set of initial conditions, $z(0) \neq 0$ and $\delta\phi(0)$, the system will remain trapped if,

$$\Lambda > 2 \left(\frac{\sqrt{1 - z(0)^2} \cos[\delta\phi(0)] + 1}{z(0)^2} \right) \quad \text{for } \Lambda > 1$$

$$\Lambda < 2 \left(\frac{\sqrt{1 - z(0)^2} \cos[\delta\phi(0)] - 1}{z(0)^2} \right) \quad \text{for } \Lambda < -1, \quad (3.22)$$

where the limits of the interaction parameter are due to the fact that only when $|\Lambda| > 1$ the $(z^0 \neq 0, \delta\phi^0)$ stationary points exist.

In this regime however, there are two different kind of MQST depending on whether the phase difference evolves bounded, giving the so-called zero- and π -modes, or whether it evolves unbounded, increasing (or decreasing) always in time, giving rise to the running phase modes.

For values of the interaction parameter of $1 < |\Lambda| < 2$ the only MQST regime that one can have is the zero-mode for attractive interactions and the π -mode for repulsive interactions (which are plotted in blue dotted lines in panel (b) of Fig. 3.7). In these regimes the phase difference evolves bounded around $\delta\phi = 0$ and $\delta\phi = \pi$, respectively.

On the other hand, for values of $|\Lambda| > 2$ one can have both classes of MQST. In general however, for a given set of initial conditions, the system will evolve following a running phase mode (dashed-red lines of panel (c) of Fig. 3.7), because the values of $z^0 = \pm\sqrt{1 - 1/\Lambda^2}$, that allow closed orbits, are very close to 1 (see the small π -modes of panel (c) in blue dotted lines).

In panel (c), one can see that the broadest closed orbit around $(z^0 \neq 0, \delta\phi^0 = \pi)$, for $\Lambda > 2$, is the one that goes through $(z = \pm 1, \delta\phi = 0)$. Notice that an orbit that crosses the $\delta\phi = 0$ axis in any other point, $z \neq \pm 1$, would correspond to a running phase mode. The case of attractive interactions can be understood by taking into account the phase-shift of π in $\delta\phi$. The latter can be used to find the condition to have bounded or

running phase difference modes. For a given set of initial conditions $(z(0), \delta\phi(0))$ fulfilling the self-trapping condition (3.22), the system will evolve in a bounded phase mode only if:

$$|\Lambda| < \frac{2 \cos \delta\phi(0)}{\sqrt{1 - z^2(0)}}. \quad (3.23)$$

Moreover, in a zero- or a π -mode MQST, we can study small oscillations around the corresponding minima or maxima, $z(t) = z^0 + \delta z$ and $\delta\phi(t) = \delta\phi^0 + \hat{\delta}\phi(t)$, so the linearized system (3.13) becomes:

$$\delta\ddot{z}(t) = -\delta z(t) \left[1 + \Lambda \cos \delta\phi^0 \frac{1 - 2(z^0)^2}{\sqrt{1 - (z^0)^2}} \right], \quad (3.24)$$

which gives a sinusoidal behavior with a frequency:

$$\omega = \omega_R \sqrt{1 + \Lambda \cos \delta\phi^0 \frac{1 - 2(z^0)^2}{\sqrt{1 - (z^0)^2}}}. \quad (3.25)$$

3.3 Numerical solutions of the TDGPE

We consider the same setup and the same trap parameters as in the experiments of the Heidelberg group [70], see Sec. 3.1. However, in our numerical simulations the initial states with either $\delta\phi(0) = 0$ or π are constructed in a different way than in the experiment. We build initial states which are by construction two-mode-like. First, we obtain numerically the ground $\Phi_+(\mathbf{r})$ and first excited $\Phi_-(\mathbf{r})$ states of the condensate in the double-well potential by solving the time independent GP equation (both for the 1D reductions and the 3D case). We use these modes to build the left $\Phi_L(\mathbf{r})$ and right $\Phi_R(\mathbf{r})$ modes, see Fig. 3.3, and finally construct initial states of any given initial imbalance, z_0 , as:

$$\Psi_{z_0}(\mathbf{r}, t = 0) = \alpha \Phi_L(\mathbf{r}) + e^{il\pi} \beta \Phi_R(\mathbf{r}), \quad (3.26)$$

with $\alpha^2 + \beta^2 = 1$, $\alpha^2 - \beta^2 = z_0$, $l = 0, 1$ and $\int d\mathbf{r} |\Phi_{L(R)}(\mathbf{r})|^2 = N$. The ground and first excited states are obtained by a standard imaginary time evolution, see Appendix A of the equation from an initial state with the proper parity. The density profiles of the ground and first excited states, together with the corresponding left and right modes computed numerically are plotted in Fig. 3.3.

Noting that the number of atoms is known up to 10% in the experiment, the relevant product, $g_{3D}N/\hbar$ is in the range $[51.22, 60.98] \mu\text{m}^3\text{kHz}$. Ref. [73] uses a value of $58.8 \mu\text{m}^3\text{kHz}$ to simulate the experimental setup. This large value of $g_{3D}N$ corresponds to a situation similar to panel (c) of Fig. 3.7, where the possible dynamical situations are: Josephson oscillations, i.e. closed orbits around the stationary point $(z^0, \delta\phi^0) = (0, 0)$, and self-trapping regimes, usually running phase modes.

From these ground and first excited states we compute all the parameters entering in the S2M and I2M descriptions: $K/\hbar = 0.00799 \text{ KHz}$ and $NU/\hbar = 1.19841 \text{ KHz}$ for the S2M and $A/\hbar = 1.19372 \text{ KHz}$, $B/\hbar = 0.03683 \text{ KHz}$, and $C/\hbar = 0.0023590 \text{ KHz}$

for the I2M ². The small value of C implies that the main difference between the I2M and S2M is not due to the term proportional to C in Eq. (3.15), which would imply qualitative differences between both, but mostly to a change in the tunneling rate due to the extra overlaps included in computing B in the I2M. The values of the overlaps are: $N\gamma_{++}/\hbar = 0.581746$ KHz, $N\gamma_{+-}/\hbar = 0.59803$ KHz and $N\gamma_{--}/\hbar = 0.623769$ KHz.

In the full TDGPE simulations we define the number of atoms in the left well as: $N_L(t) = \int_{-\infty}^0 dx \int_{-\infty}^{\infty} dy \int_{-\infty}^{\infty} dz |\Psi(\mathbf{r}; t)|^2$. The number of atoms in the right well is computed as $N_R(t) = N - N_L(t)$. From these values, the population imbalance reads, $z(t) = (N_L(t) - N_R(t))/N$. Analogous definitions are used in the 1D-TDGPE and NPSE equations.

The total wave function is

$$\Psi(x, y, z; t) = \sqrt{\rho(x, y, z; t)} \exp(i \phi(x, y, z; t)), \quad (3.27)$$

where $\rho(x, y, z; t) = |\Psi(x, y, z; t)|^2$ is the local density, and $\phi(x, y, z; t)$ the local phase. We define the averaged densities

$$\rho(x, y; t) = \int_{-\infty}^{\infty} dz \rho(x, y, z; t). \quad (3.28)$$

and the averaged phases

$$\phi(x, y; t) = \frac{1}{\rho(x, y; t)} \int_{-\infty}^{\infty} dz \rho(x, y, z; t) \phi(x, y, z; t). \quad (3.29)$$

The phase on the left, $\phi_L(t)$, is defined as,

$$\phi_L(t) = \frac{1}{N_L(t)} \int_{-\infty}^0 dx \int_{-\infty}^{\infty} dy \int_{-\infty}^{\infty} dz \rho(x, y, z; t) \phi(x, y, z; t), \quad (3.30)$$

and the phase on the right is defined accordingly. Finally, $\delta\phi(t) = \delta\phi_R(t) - \delta\phi_L(t)$.

The implementation of the averages over the phase has been done in the following way,

$$\begin{aligned} \phi(x, y; t) &= \arctan \frac{\int_{-\infty}^{\infty} dz \operatorname{Im}[\Psi(x, y, z; t)] \rho(x, y, z; t)}{\int_{-\infty}^{\infty} dz \operatorname{Re}[\Psi(x, y, z; t)] \rho(x, y, z; t)}, \\ \phi_L(t) &= \arctan \frac{\int_{-\infty}^0 dx \int_{-\infty}^{\infty} dy \int_{-\infty}^{\infty} dz \operatorname{Im}[\Psi(x, y, z; t)] \rho(x, y, z; t)}{\int_{-\infty}^0 dx \int_{-\infty}^{\infty} dy \int_{-\infty}^{\infty} dz \operatorname{Re}[\Psi(x, y, z; t)] \rho(x, y, z; t)}. \end{aligned} \quad (3.31)$$

3.3.1 TDGPE results

In Figs. 3.8 and 3.9 we present full TDGPE simulations for a Josephson regime and a running phase mode self-trapped case, respectively. These figures clearly show two

²These values compare reasonably well with the ones provided in page 33 of Albiez PhD thesis [104], there they are given in units of ω_x : $A/\omega_x = 2.43572$, $B/\omega_x = 0.0751497$, $C/\omega_x = 0.0048$, and $K/\omega_x = 0.0163$.

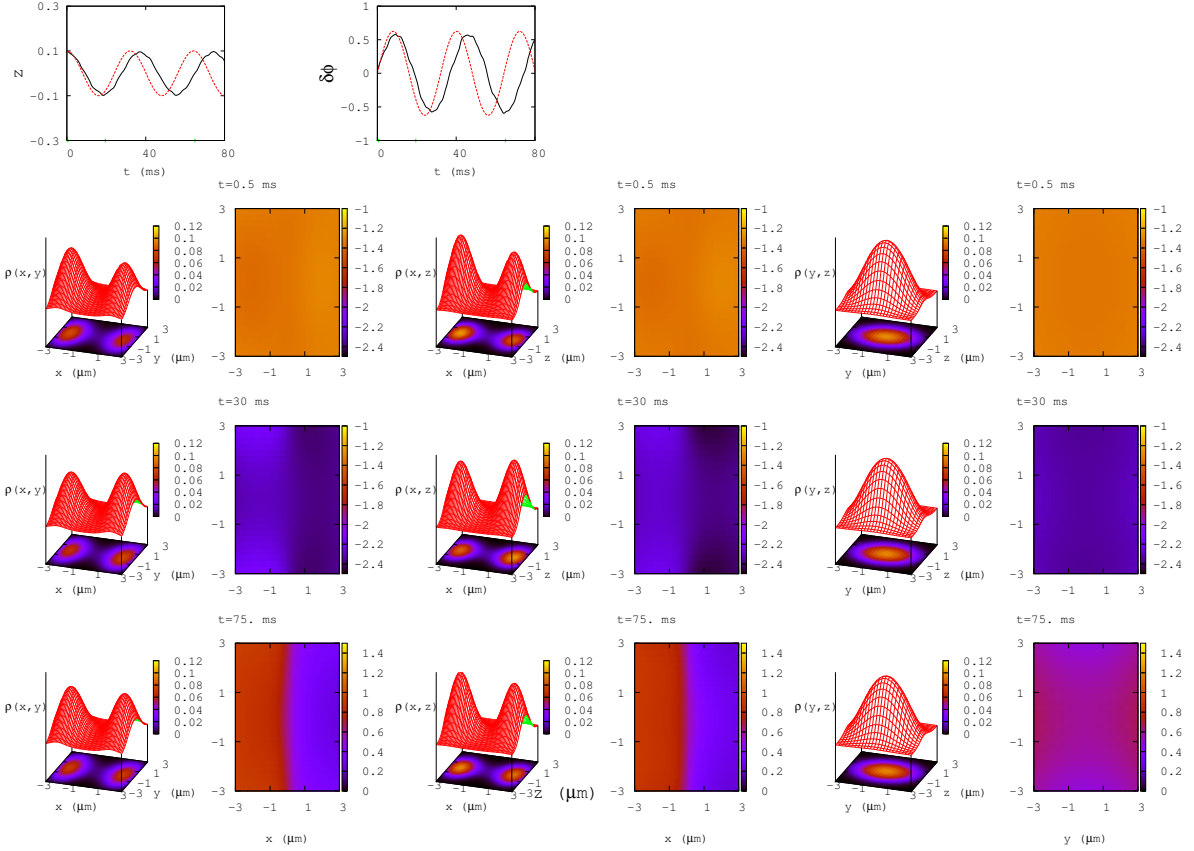


Figure 3.8: The two upper plots show in solid-black the TDGPE time evolution of z (left) and $\delta\phi$ (right), computed as explained in the text, and in dashed-red the I2M predictions. Also shown are 3D pictures complemented with contour plots, left, of $\rho(x, y; t)$, $\rho(x, z; t)$ and $\rho(y, z; t)$ at three different times, 0.5 ms (upper), 30 ms (middle) and 75 ms (lower), respectively. On the right of each plot we present a contour plot of the averaged quantum phase $\phi(x, y; t)$, $\phi(x, z; t)$ and $\phi(y, z; t)$ at the same times. They correspond to the first run presented in Fig. 3.10(a), $z(0) = 0.1$ and $\delta\phi(0) = 0$.

relevant aspects of the problem. First, it is clear that during the full time evolution, which covers up to $t = 80$ ms in the figure, the system remains mostly localized on the two minima of the potential³. Therefore, the density has a two-peaked structure over the considered time period. Secondly, the atoms in each of the two wells remain to a large extent in a coherent phase during all times. This can be seen from the uniform color, constant phase, at each side of the barrier in the right panels of the figures. These two characteristics of the time evolution of the 3D Gross-Pitaevskii equation support the use of two-mode approximations.

The modulation of the density profiles on the transverse direction is seen to be small, with a mostly constant quantum phase in the region populated by the atoms. This

³Notice that the time considered here $t = 80$ ms is larger than the time considered in the experimental results of [70], see Fig. 3.1, of $t = 50$ ms. However, it is smaller than the Rabi time $t_R = 2\pi/\omega_R$, which for this experimental setup is $t_R \simeq 400$ ms.

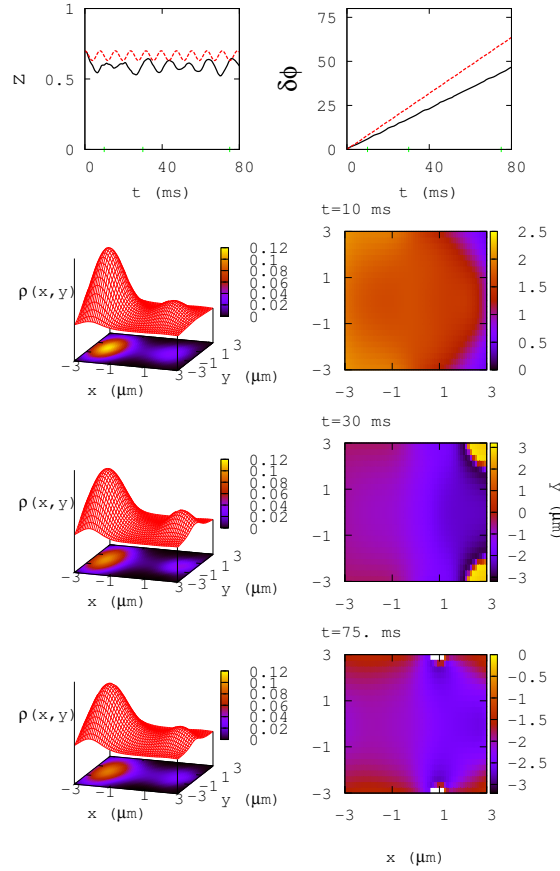


Figure 3.9: Similar to Fig. 3.8 but for a self-trapped case, $z(0) = 0.7$, $\delta\phi(0) = 0$, for three different times, 10, 30 and 75 ms and showing the averages over z . We plot $\rho(x, y; t)$ and contour plots. On the right panels we present contour plots of the averaged quantum phase, $\phi(x, y; t)$. The phase coherence of the condensates at each side of the barrier is clearly seen.

indicates that the transverse dynamics can be integrated out to a large extent, as is done in the 1D reductions discussed in Sec. 2.2.

The Josephson dynamics, Fig. 3.8, is clearly seen in the small upper panels depicting $z(t)$ and $\delta\phi(t)$. They both oscillate with the same period but with a phase-shift of $\pi/2$.

A self-trapped case is shown in Fig. 3.9. The atoms remain trapped mostly on the left side of the trap (they start with an imbalance of $z(0) = 0.7$) and remain trapped in this potential-well during the considered time evolution. The coherence of the phase at each side of the potential barrier can also be appreciated in the figure, although here we should note that the right side of the barrier, being less populated, is concentrated on a smaller (x, y) domain.

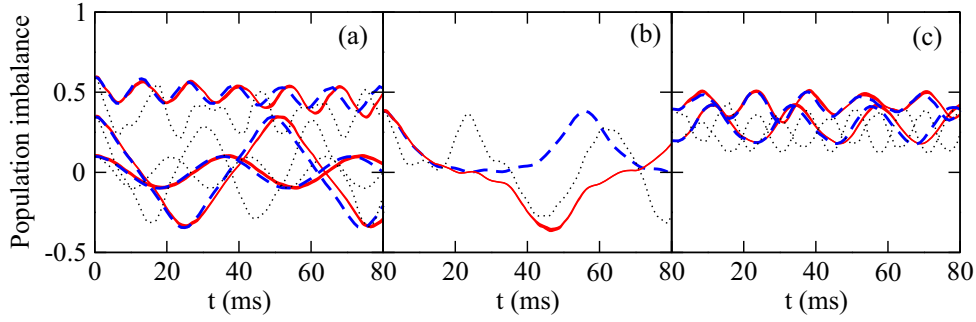


Figure 3.10: Dynamical evolution of the population imbalance, z , between both sides of the barrier for a single component condensate. Solid (red) line corresponds to the TDGPE, the dashed (blue) line to the NPSE, and the dotted (black) stands for the 1D-TDGPE. Panel (a) contains $\delta\phi(0) = 0$ cases, with $z(0) = 0.1, 0.35$, and 0.6 . (b) Corresponds to the critical value, $z(0) = 0.39$ and $\delta\phi(0) = 0$. (c) Depicts two self-trapped cases with an initial $\delta\phi(0) = \pi$, with $z(0) = 0.2$, and 0.4 .

3.3.2 TDGPE, 1D reductions and two-mode approximations

The TDGPE cases described above indicate that within the configuration considered here the two commonly employed two-mode models and 1D equations are expected to be reasonable. In this section we present comparisons between the different approaches described in the previous sections: 1D reductions (NPSE and 1D-TDGPE in Sec. 2.2) and two-mode models (S2M in Sec. 3.2.1 and I2M in Sec. 3.2.2).

TDGPE vs 1D reductions: 1D-TDGPE and NPSE

In Fig. 3.10 we present the time evolution of the population imbalance for the different dynamical regimes described in Sec. 3.2.3, i.e. Josephson, and self-trapping. We compare the full TDGPE (solid red) with the two previously described 1D reductions, 1D-TDGPE (dotted black) and NPSE (dashed blue).

First, we note that the dynamics emerging from the TDGPE is indeed similar to what was predicted by analyzing the S2M equations in Sec. 3.2.3. Qualitatively, the TDGPE simulations do follow the patterns predicted by the two-mode approximations. Let us briefly describe each of the results:

- a) The first panel, (a), contains simulations performed with zero initial phase difference, i.e. Josephson oscillations and self-trapping cases. For the Josephson cases, $z(0) = 0.1, 0.35$, the imbalance oscillates with a frequency which is mostly independent of the initial imbalance (for small imbalances). With $z(0) = 0.1$ the oscillations are almost sinusoidal, while as we increase the initial imbalance their shape becomes more involved but remaining periodic. In the self-trapped case, $z(0) = 0.6$, the atoms remain mostly on the initial side of the trap and there are short and small periodic oscillations as predicted by the two-mode models. At longer times, the imbalance is seen to decrease smoothly, implying a departure from the predicted two-mode dynamics [89].

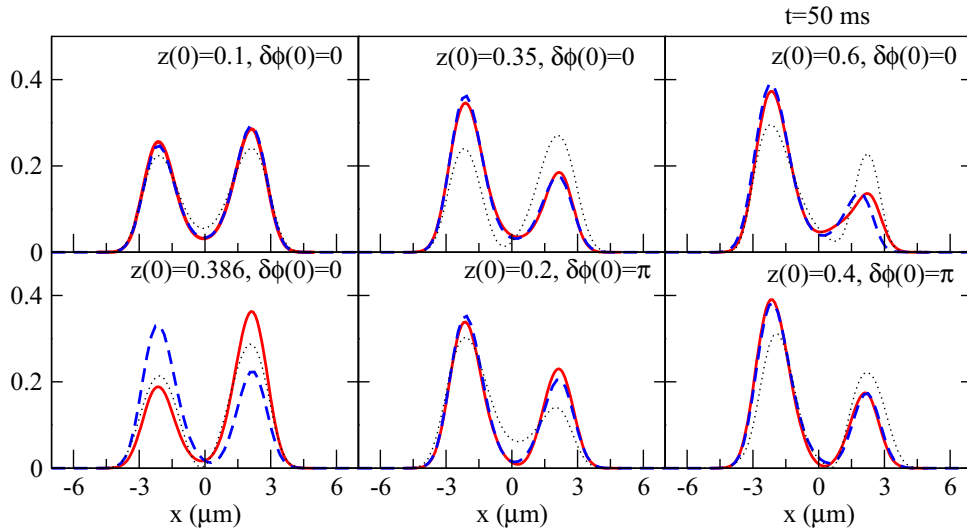


Figure 3.11: Snapshots of the axial density profiles, $\rho(x; t)$ (μm) $^{-1}$ at $t = 50$ ms calculated by means of the TDGPE evolution (solid red line), the NPSE (dashed blue line), and the 1D-TDGPE (dotted black line). The initial conditions correspond to the ones used to generate Fig. 3.10.

The two 1D reductions give qualitatively similar results in most situations to TDGPE, but the quantitative agreement worsens in some cases. The NPSE is seen to reproduce very well the TDGPE in all the runs up to times near ~ 40 ms. Above those times, the period of oscillation predicted by the NPSE is slightly shorter than the TDGPE one. The 1D-TDGPE on the contrary only captures the amplitude of oscillation in the Josephson dynamics, failing in all cases to give the same period as the TDGPE or the NPSE. Moreover, the 1D-TDGPE departs notably from two-mode for the self-trapped case. It does predict self-trapping, but more than two modes contribute to the time evolution.

- b) Panel (b) is computed very close to the critical value of the full TDGPE, $z(0) = 0.39$ for $\delta\phi(0) = 0$. The 1D-TDGPE and NPSE predict a critical initial imbalance close to the TDGPE value.
- c) Panel (c) contains two self-trapped cases obtained with an initial $\delta\phi(0) = \pi$ and $z(0) = 0.2$, and 0.4 . Notice that for $\delta\phi(0) = \pi$ the critical imbalance is smaller than for $\delta\phi(0) = 0$. The discussion is similar to the Josephson case, i.e. the NPSE captures most of the dynamical features of the TDGPE while the 1D-TDGPE only provides a qualitative understanding of the problem.

To further explore the quality of the 1D reductions, in Fig. 3.11 we plot the density profiles in the x direction after integrating over y, z , $\rho(x; t) = \int_{-\infty}^{\infty} dy \int_{-\infty}^{\infty} dz |\Psi(x, y, z; t)|^2$ at $t = 50$ ms. The agreement between the NPSE and the TDGPE is very good in most situations, except for the critical case, as expected. In all cases, the density profiles show a clear bimodal structure. The 1D-TDGPE, as could be inferred from the previous results, does not predict the correct density profiles and, as seen in the self-trapped case,

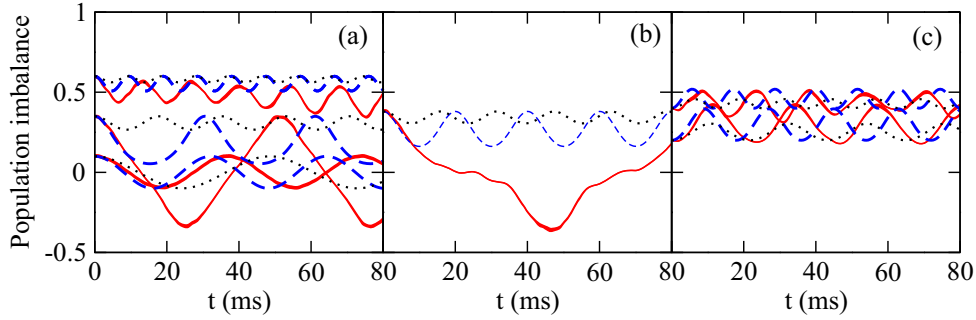


Figure 3.12: Dynamical evolution of the population imbalance between the two sides of the barrier for a single component condensate. The TDGPE (solid red) is compared to the I2M (dashed blue) and the S2M (dotted black) results. The parameters entering in the two-mode descriptions are given in the text. Panel (a) contains runs for $\delta\phi(0) = 0$, with $z(0) = 0.1, 0.35$, and 0.6 . (b) Corresponds to the critical value for $z(0) = 0.39$ and $\delta\phi(0) = 0$. (c) Depicts two self-trapped states obtained by an initial $\delta\phi(0) = \pi$, with $z(0) = 0.2$, and 0.4 .

($z(0) = 0.6, \delta\phi(0) = 0$), do show the contribution of higher modes. The critical initial imbalance starting with no phase difference that we find numerically by means of the TDGPE is the same as found in Ref. [73], $z_c = 0.39$, and differs from the one reported in Ref. [70], $z_c = 0.5$.

The agreement of the NPSE with TDGPE results justify the use NPSE in Ref. [70] to analyze their experiment.

TDGPE vs two-mode approximations, S2M and I2M

As explained above, the use of two-mode models is suggested by the TDGPE results, see Figs. 3.8 and 3.9. What is, a priori, not clear, is whether the extra assumption used in deriving the S2M (which are the most commonly employed equations) will work for each specific double-well potential. As discussed in Sec. 3.2.2, the conditions of the Heidelberg experiment are such that the S2M predictions are not good. However, this does not mean that the dynamics is not two-mode but that the overlaps involving high powers of the two localized modes are not negligible as assumed in deriving the S2M equations.

In Fig. 3.12 we compare TDGPE (solid red), the S2M (dotted black) and the I2M (dashed blue) results using the parameters calculated microscopically from the ground and first excited state of the TDGPE. Both two-mode schemes predict the same phenomenology and thus qualitatively capture the dynamics of the system. At the quantitative level, however, the I2M is clearly better. In the run with $z(0) = 0.1$ and $\delta\phi(0) = 0$ (panel (a)), both the S2M and I2M predict a similar behavior with the correct amplitude and oscillation period close to the TDGPE one. As the imbalance is increased, e.g. ([70] considers $z(0) = 0.28$), the S2M fails to describe the correct period and predicts smaller amplitudes. This is analyzed in full detail in Ref. [73]. The critical initial imbalances determined by both two-mode approaches are smaller than the TDGPE one, see panel (b). Finally, for the self-trapped cases with $\delta\phi(0) = \pi$ (panel (c)) the I2M gives similar oscillation amplitudes with shorter periods than the TDGPE. The S2M fails both in

reproducing the amplitudes and the periods.

3.4 Beyond the two-mode approximation

In the previous sections, we have studied a weakly interacting bosonic Josephson junction, where the two-mode approximations reproduced fairly well the behavior of the TDGPE. In this section, we increase the strength of the interactions and drive the system out of the validity of the two-mode approximations, but within the validity of the mean-field GPE, see Sec. 2.1. We also focus in a specific dynamical configuration, in which initially the majority of the atoms are located in one of the wells. By studying the oscillations of the population imbalance we find that increasing the atom-atom interactions the amplitude of the oscillations starts to increase, departing from the usual self-trapping behavior. We demonstrate that this dynamics can be explained when higher modes of the Gross-Pitaevskii potential are considered. Under certain conditions, the coupling between the second and third modes successfully explains the results.

We perform this study using a quasi 1D BEC, i.e. with a cigar shape, and with a double well in its longitudinal direction. This system is well described by the 1D-TDGPE (2.22), which taking $\hbar = M = 1$, reads

$$i \frac{\partial \varphi(x, t)}{\partial t} = \left[-\frac{1}{2} \frac{\partial^2}{\partial x^2} + V_{\text{eff}}[x, \varphi(x, t)] \right] \varphi(x, t), \quad (3.32)$$

where $\varphi(x, t)$ is normalized to 1, and where we have defined the time-dependent effective potential:

$$V_{\text{eff}}[x, \varphi(x, t)] = V_{\text{ext}}(x) + g_{1D} N |\varphi(x, t)|^2. \quad (3.33)$$

In order to make the S2M more accurate, we take the external double-well potential $V_{\text{ext}}(x)$ deeper than the one used in the previous sections. It is generated by connecting two parabolas with an inverted parabola:

$$V_{\text{ext}}(x) = \begin{cases} (x+2)^2 & \text{for } x \leq -1/2 \\ 3(1-x^2) & \text{for } -1/2 < x < 1/2 \\ (x-2)^2 & \text{for } x > 1/2. \end{cases} \quad (3.34)$$

Note that the relevant parameter in (3.32) is the product $\lambda \equiv g_{1D} N$, which sets the importance of the nonlinear term. Different values of N and g_{1D} produce exactly the same GP evolution provided λ is fixed.

In this analysis we consider repulsive interactions and study the dynamics for increasing values of $g_{1D} \geq 0$, going from the Rabi regime, $g_{1D} = 0$, to the Josephson and self-trapped dynamics, and further beyond the range of validity of the usual two-mode approximation. For each value of the interaction g_{1D} , we start with the initial state $\varphi(x, t=0) = \varphi_L(x)$, obtained by previously computing the ground $\varphi_+(x)$ and first excited $\varphi_-(x)$ states of (3.32). This corresponds with an initial state with all the atoms on the left well: $z(t=0) = 1$.

Moreover, we also consider the S2M equations for a symmetric double well (3.13). The parameters governing these equations are computed as described in Sec. 3.2.1, using

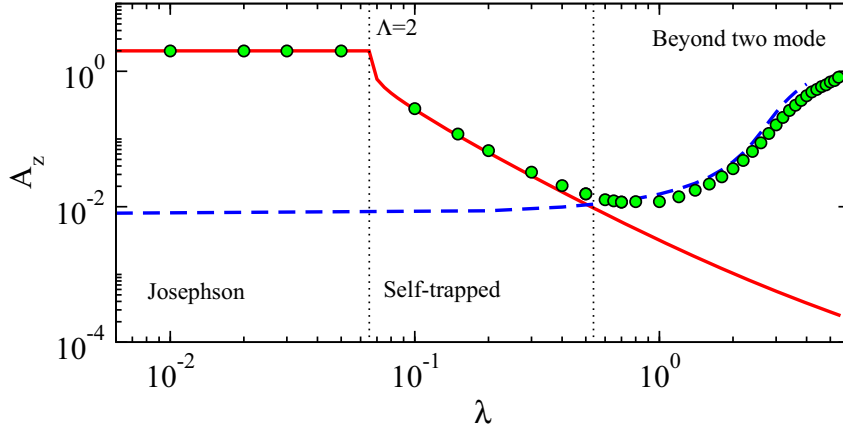


Figure 3.13: Maximum amplitude of the imbalance oscillations, $z_{\max} - z_{\min}$ computed with 1D-TDGPE (circles) as a function of g_{1D} . The solid (red) line is the classical two-mode prediction using Eqs. (3.13). The dashed (blue) line is a two-mode calculation using modes (1,2) as explained in the text.

the single-particle modes. We find a tunneling rate $K = 7.9 \times 10^{-3}$ and an interaction $U = 0.47g_{1D}$, which gives $\Lambda = NU/(2K) = 29.7\lambda$. The critical value of Λ_c to have self-trapping within this two mode approximation and for the considered initial state $\varphi_L(x)$ is $\Lambda_c = 2$, see Eq. (3.22). This translates into a critical value for $\lambda^{(0,1)} = 0.067$, where the superscript (0,1) refers to the states involved in the tunneling dynamics.

The results are shown in Fig. 3.13, where we compare the amplitudes of $z(t)$ found by solving numerically the 1D-TDGPE (3.32) with the semiclassical two-mode prediction (3.13). At $\lambda < \lambda^{(0,1)}$ there is no self-trapping and $z(t)$ oscillates between +1 and -1, thus leading to a constant maximal amplitude, $A_z \equiv z_{\max} - z_{\min} = 2$. With increasing interaction strength, near $\lambda^{(0,1)}$, self-trapping appears. The atoms become increasingly confined in the left well and A_z decreases abruptly. In all this range the semiclassical model predictions are very successful, covering the well known Josephson and self-trapped regimes. This range of λ is the one recently explored experimentally in Ref. [105].

With further increase of λ , deviations begin to appear. Whereas the semiclassical two-mode model predicts a smooth decrease of A_z , the GP calculations show a smooth reappearance of tunneling between the two wells.

Figure 3.14 shows the effective potential (3.33) for several values of λ at two different times, $t = 0$ and $t = t_{z_{\min}}$ which correspond to the time of the first minimum of the population imbalance. In this way the band covers the variation of the effective potential during the simulation. When $\lambda \lesssim \lambda^{(0,1)}$ the nonlinear contribution is fairly small, and $V_{\text{eff}}(x, t) \simeq V(x)$ at all times. This corresponds to the Rabi and Josephson regimes, with maximal oscillations of the population. Increasing λ further, $\lambda^{(0,1)} \lesssim \lambda \lesssim 3$, the value of $V_{\text{eff}}(x, t)$ in the left well is increased, but leaving the value in the right well almost unchanged. This is a direct consequence of self-trapping. In this regime, the effective potential changes very little with time, see fig. 3.14 (a). Further increasing λ , $3 \lesssim \lambda \lesssim 5$, the potential on the left well increases, and V_{eff} does begin to change appreciably with time. Still, the dynamics remains self-trapped but the oscillation amplitudes in $z(t)$

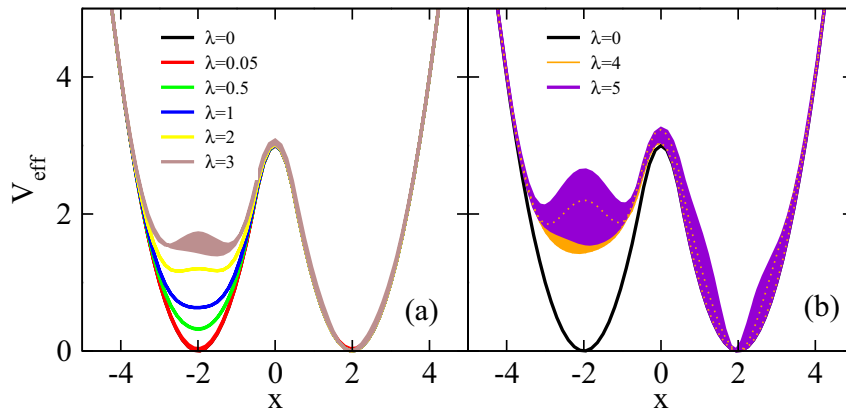


Figure 3.14: Effective potential $V_{\text{eff}}(x, t)$ for different values of λ . The bands are generated by joining $V_{\text{eff}}(x, 0)$ and $V_{\text{eff}}(x, t_{z_{\text{min}}})$, as explained in the text. The key to the various lines is shown in each panel.

departure from the S2M predictions.

In fact, as we increase the interactions, the energies of the first excited state separates from the energy of the ground state, and near $\lambda \simeq 2$ ($\Lambda \sim 60$), it becomes closer to the energy of the second excited state. As these two modes are respectively mostly localized on the left and right wells, tunneling of atoms is again allowed. This corresponds to the rise of A_z in figure 3.13 beyond $\lambda \simeq 1$.

This coupling, which is zero in absence of interaction, occurs due to the large nonlinearity: it deforms the wave functions enough to enable the coupling between the ground state of one well and the first excitation in the other. It is a large and clearly density dependent effect which requires a change in the modes used and cannot be accommodated by varying the parameters of the usual two-mode picture. This effect is different in nature from what was reported in Refs. [108, 109, 110] where the alignment takes place due to the presence of a large enough bias in the system. In our case, it is clearly a dynamical phenomenon which happens even for symmetric double-well potentials. The role played here by the nonlinear interaction in modifying the single particle states is more similar to the interaction blockade effect demonstrated for double wells with few atoms in optical superlattices [111].

Our result is also of different nature than the disappearance of self-trapping reported in Ref. [112]. There, the authors explore the population of low-energy Bogoliubov excitations in the condensates of each of the wells finding, using a schematic model, a departure from self-trapping due to excitation of such low energy modes. By using the time-dependent GP equation to determine the condensate wave function, the low energy Bogoliubov states are already incorporated into its time evolution. See Eq. (8.43) and the discussion in section VIII.E in Ref. [5]. Including them again along the lines of Ref. [112] would be redundant.

Following similar arguments to those in the derivation of Eqs. (3.9) we can write down the new two mode equations for the first $\varphi_- \equiv \varphi_1$ and second φ_2 excited states, which

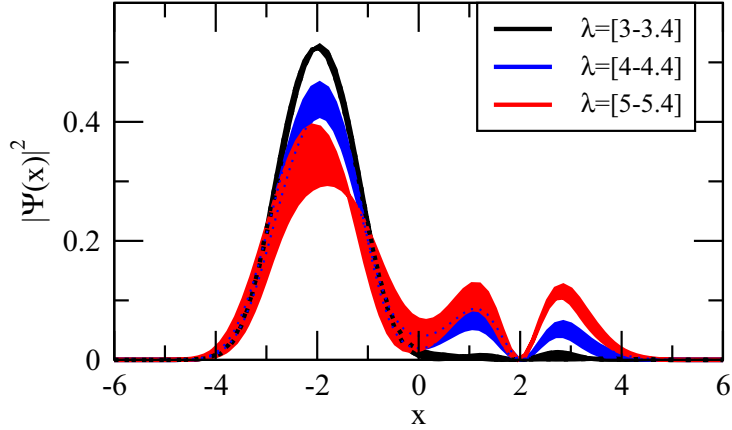


Figure 3.15: Density of atoms along the x direction at a given time $t = t_{\text{Rabi}}/10$ for several values of g_{1D} . The bands are built by joining the calculations at two different values of g_{1D} .

are mostly localized on the left and right wells, respectively:

$$\begin{cases} \dot{z}(t) = -\bar{\omega}_R \sqrt{1 - z^2(t)} \sin \delta\phi(t) \\ \delta\dot{\phi}(t) = \bar{\omega}_R \Delta \bar{E} + \bar{\omega}_R \bar{\Lambda} z(t) + \bar{\omega}_R \frac{z(t)}{\sqrt{1 - z^2(t)}} \cos \delta\phi(t), \end{cases} \quad (3.35)$$

where $\bar{\omega}_R = 2\bar{K}$ and

$$\begin{aligned} \bar{E}_{1(2)}^0 &= \int dx \left[\frac{1}{2} |\partial_x \varphi_{1(2)}|^2 + \varphi_{1(2)}^2 V_{\text{ext}}(x) \right] \\ \bar{K} &= \int dx \left[\frac{1}{2} \partial_x \varphi_1 \partial_x \varphi_2 + \varphi_1 \varphi_2 V_{\text{ext}}(x) \right] \\ \Delta \bar{E} &= \frac{\bar{E}_1^0 - \bar{E}_2^0}{2\bar{K}} + \frac{\bar{U}_1 - \bar{U}_2}{4\bar{K}} N \\ \bar{U}_{1(2)} &= g_{1D} \int dx \varphi_{1(2)}^4. \end{aligned} \quad (3.36)$$

Using $\lambda = 1.2$ to build the modes gives, $\Delta \bar{E} = -1.26$, $N\bar{U} = 0.35$, and $\bar{K} = -0.037$. The prediction of this new two-mode model is shown by the dashed (blue) lines in Fig. 3.13. As can be seen this (1,2) model works well in the range $1 \lesssim \lambda \lesssim 3.5$, giving a good account of both the dominant frequency and the amplitude of the imbalance observed in the GP simulations. The transition from (0,1) to (1,2) coupling reflects also in the appearance of the node of the $|\psi(x,t)|^2$ near $x = 2$, obtained solving the GP equations as seen in Fig. 3.15. This is an observable feature which should be looked for experimentally.

Further increasing λ , $\lambda \gtrsim 6$, our initial state has an average energy above the barrier, thus facilitating the flow of atoms between the wells. At high enough λ a certain equilibration of the imbalance can be expected, in line with Ref. [113], mostly due to the sizeable contributions from modes with energies above the barrier.

A study of the eigenenergies of the effective potential, and the frequencies involved in the population imbalance dynamics can be found in Ref. [89].

Chapter 4

Josephson effect in binary mixtures

A bosonic binary mixture is made of two different species of bosons, which for example could be two different atoms, two isotopes of the same element, or one isotope but in two different internal spin states [4]. The first experimental realization of Bose-Einstein condensation with a binary mixture was achieved in 1997 by the JILA group [59]. They condensed a mixture of ^{87}Rb atoms in the hyperfine states $F = 2$, $m_F = 2$ and $F = 1$, $m_F = 1$. In 2001 a mixture of two different isotopes of rubidium, ^{85}Rb and ^{87}Rb , was also Bose-condensed by I. Bloch and collaborators [58], and one year after, the group of M. Inguscio prepared a condensate with two different kind of atoms, ^{41}K and ^{87}Rb [57].

Nowadays, the experiments and studies with binary mixtures are more sophisticated. The group of I. B. Spielman, for example, engineers the spin-orbit coupling in a neutral atomic Bose-Einstein condensate with two different internal spin states [114]. S. B. Papp and collaborators observed the controllable phase separation in a BEC mixture of ^{85}Rb and ^{87}Rb atoms [115]. By tuning the scattering length of ^{85}Rb , they were able to control the miscibility of the two quantum fluids. Another interesting recent investigation is the study of the ground state of a binary mixture of ^{87}Rb atoms in two different hyperfine states [116], in which the formation and suppression of domain walls separating the two components is considered.

In this Chapter we extend the study of the Josephson effect within the mean-field theory to binary mixtures. The richness of the mixture and the possibility of controlling both intra- and inter-species interactions using Feshbach resonances [49], allows to explore new regimes that were not present in the one component case. For example, the presence of simultaneous self-trapping of each species in different wells.

S. Ashhab and C. Lobo considered an external BJJ with binary mixtures within the mean-field theory, and applied a two-mode approximation [90]. They derived the S2M equations, see Sec. 3.2.1, for the binary mixture and performed an extensive study characterizing the different dynamical regimes. The same theoretical framework was used for L. Wen and J. Li [117] and X-Q. Xu and collaborators [118], who studied the tunneling dynamics with a time-dependent external potential. Ref. [119] went one step further and performed a simulation of the 1D-TDGPE for a binary mixture, and compared the results with the corresponding S2M equations.

The chapter is organized as follows: in section 4.1 we recall the time-dependent Gross-Pitaevskii equation (TDGPE) for binary mixtures [56] and the corresponding 1-

dimensional reductions: 1D-TDGPE [120] and NPSE [121]. Then, in section 4.2 we review the S2M approximation for a binary mixture in a double-well potential [90], and derive the corresponding I2M equations. The derivation of the I2M equations was presented at the same time in Refs [122, 123]. Moreover, the group of C. W. Clark [122], also studied the symmetry breaking due to the inter-species interactions. We focus in the particular case of a binary mixture formed by two different hyperfine states of the same kind of atoms. Interactions are considered to be dependent on the nature of the colliding atoms, but there is no transfer of particles between different species [124, 125]. In section 4.2.3 we describe extensively the different regimes that can arise by discussing the stability of the stationary solutions of the S2M equations of the binary mixture.

In section 4.3 we consider the particular case of a binary mixture obtained by populating the two $m_F = \pm 1$ Zeeman states of $F = 1$ ^{87}Rb atoms. The confining potential is taken to be the double-well potential described in Sec. 3.1. We perform numerical simulations of the TDGPE and compare them with (1) the two-mode approaches and (2) the 1-dimensional reductions of the TDGPE. Finally, we discuss some effects present in the TDGPE simulations that the two-mode approaches do not capture, e.g. excitations of transverse modes.

4.1 Gross-Pitaevskii equation for a binary mixture

The Gross-Pitaevskii mean-field theory, see Sec. 2.1, provides a well-grounded framework for investigating Josephson dynamics in weakly interacting systems provided that (a) the number of atoms is large enough so that quantum fluctuations can be neglected and (b) the initial many-body state is of mean-field type. The TDGPE describing a binary mixture consists of a coupled system of equations [56]:

$$\begin{cases} i\hbar \frac{\partial \Psi_a(\mathbf{r}, t)}{\partial t} = \left[H_{\text{sp}}^{(a)} + g_{aa} |\Psi_a(\mathbf{r}, t)|^2 + g_{ab} |\Psi_b(\mathbf{r}, t)|^2 \right] \Psi_a(\mathbf{r}, t) \\ i\hbar \frac{\partial \Psi_b(\mathbf{r}, t)}{\partial t} = \left[H_{\text{sp}}^{(b)} + g_{ba} |\Psi_a(\mathbf{r}, t)|^2 + g_{bb} |\Psi_b(\mathbf{r}, t)|^2 \right] \Psi_b(\mathbf{r}, t), \end{cases} \quad (4.1)$$

where $H_{\text{sp}}^{(i)}$ is the single-particle Hamiltonian for the particle i

$$H_{\text{sp}}^{(i)} = -\frac{\hbar^2}{2M_i} \nabla^2 + V_{\text{ext}}(\mathbf{r}), \quad (4.2)$$

and g_{ij} describes the interaction between particles i and j .

1-dimensional reductions of the TDGPE

Like in the scalar Josephson junction, the dynamics with a binary mixture Josephson junction occurs mostly in only one direction, i.e. the direction in which the external potential has a double well. Therefore, we also review the 1-dimensional reductions of the TDGPE, see Sec. 2.2, for the coupled TDGPE (4.1).

The generalization of the 1D-TDGPE to binary mixtures may be written down readily [120], by integrating out the transverse directions assuming they are well described by the ground state of single-particle Hamiltonian,

$$\begin{cases} i\hbar \frac{\partial \Psi_a(x,t)}{\partial t} = \left[-\frac{\hbar^2}{2M_a} \partial_x^2 + V_{\text{ext}}(x) + g_{aa}^{1D} |\Psi_a(x,t)|^2 + g_{ab}^{1D} |\Psi_b(x,t)|^2 \right] \Psi_a(x,t) \\ i\hbar \frac{\partial \Psi_b(x,t)}{\partial t} = \left[-\frac{\hbar^2}{2M_b} \partial_x^2 + V_{\text{ext}}(x) + g_{ba}^{1D} |\Psi_a(x,t)|^2 + g_{bb}^{1D} |\Psi_b(x,t)|^2 \right] \Psi_b(x,t), \end{cases} \quad (4.3)$$

where, the rescaled couplings are $g_{ij}^{1D} = g_{ij}/(2\pi a_\perp^2)$.

The NPSE for a binary mixture has been addressed in Ref. [121]. The system of equations, which become rather involved, can be greatly simplified when both intra- and inter-species are equal. Taking $g \equiv g_{aa} = g_{bb} = g_{ab} = g_{ba}$, for each component $i = a, b$ the NPSE reduces to:

$$i\hbar \frac{\partial \Psi_i(x,t)}{\partial t} = \left[-\frac{\hbar^2}{2M_j} \partial_x^2 + V_{\text{ext}} + g_{1D} \frac{n(x,t)}{\sqrt{1+2a_s n(x,t)}} + \frac{\hbar\omega_\perp}{2} \left(\frac{1}{\sqrt{1+2a_s n(x,t)}} + \sqrt{1+2a_s n(x,t)} \right) \right] \Psi_i(x,t), \quad (4.4)$$

where $n(x,t) = |\Psi_a(x,t)|^2 + |\Psi_b(x,t)|^2$, and $g_{1D} = g/(2\pi a_\perp^2)$.

4.2 Two-mode approximation for a binary mixture

In this section, we review the two-mode approximations for a binary mixture, both the S2M [90] and the I2M [122]. We follow a similar procedure as the one used for the scalar condensates, see Sec. 3.2.

4.2.1 Standard two-mode model for a binary mixture

Let us recall the two-mode approximation for a weakly linked binary mixture [90, 126, 117, 118]. The total wave function of each component (a, b) is written as a superposition of two time-independent spatial wave functions localized in each well (L, R) [90]:

$$\Psi_\alpha(\mathbf{r}, t) = \psi_{\alpha L}(t) \varphi_{\alpha L}(\mathbf{r}) + \psi_{\alpha R}(t) \varphi_{\alpha R}(\mathbf{r}), \quad (4.5)$$

where $\langle \varphi_{\alpha i} | \varphi_{\beta j} \rangle = \delta_{\alpha\beta} \delta_{ij}$, with $\alpha, \beta = a, b$ and $i, j = L, R$. For a given component, the condensates in each side of the trap are weakly linked. Then, as in the scalar case, one can assume that the wave function in each side of the trap has a well defined quantum phase $\phi_{\alpha j}(t)$, which is independent of the position but which changes during the time evolution

$$\psi_{\alpha j}(t) = \sqrt{N_{\alpha j}(t)} e^{i\phi_{\alpha j}(t)}. \quad (4.6)$$

$N_{\alpha j}(t)$ corresponds to the population of the α -component on site i , with $N_\alpha = N_{\alpha L}(t) + N_{\alpha R}(t)$. Inserting the two-mode ansatz (4.5) into the coupled TDGPE equations for the

mixture (4.1), and retaining up to first order crossed terms yields the following system of coupled equations [68]:

$$\left\{ \begin{array}{l} \dot{z}_a(t) = -\frac{2K_a}{\hbar} \sqrt{1 - z_a^2(t)} \sin \delta\phi_a(t) \\ \delta\dot{\phi}_a(t) = \Delta E_{ab} + \frac{U_{aaL} + U_{aaR}}{2\hbar} N_a z_a(t) + \frac{U_{abL} + U_{abR}}{2\hbar} N_b z_b(t) + \frac{2K_a}{\hbar} \frac{z_a(t)}{\sqrt{1 - z_a^2(t)}} \cos \delta\phi_a(t) \\ \dot{z}_b(t) = -\frac{2K_b}{\hbar} \sqrt{1 - z_b^2(t)} \sin \delta\phi_b(t) \\ \delta\dot{\phi}_b(t) = \Delta E_{ba} + \frac{U_{bbL} + U_{bbR}}{2\hbar} N_b z_b(t) + \frac{U_{baL} + U_{baR}}{2\hbar} N_a z_a(t) + \frac{2K_b}{\hbar} \frac{z_b(t)}{\sqrt{1 - z_b^2(t)}} \cos \delta\phi_b(t), \end{array} \right. \quad (4.7)$$

where,

$$\begin{aligned} \Delta E_{\alpha\beta} &= \frac{E_{\alpha L}^0 - E_{\alpha R}^0}{\hbar} + \frac{U_{\alpha\alpha L} - U_{\alpha\alpha R}}{2\hbar} N_\alpha + \frac{U_{\alpha\beta L} - U_{\alpha\beta R}}{2\hbar} N_\beta \\ E_{\alpha i}^0 &= \int d\mathbf{r} \left[\frac{\hbar^2}{2M_\alpha} |\nabla \varphi_{\alpha i}(\mathbf{r})|^2 + \varphi_{\alpha i}^2 V(\mathbf{r}) \right] \\ K_\alpha &= - \int d\mathbf{r} \left[\frac{\hbar^2}{2M_\alpha} \nabla \varphi_{\alpha L}(\mathbf{r}) \cdot \nabla \varphi_{\alpha R}(\mathbf{r}) + \varphi_{\alpha L}(\mathbf{r}) V(\mathbf{r}) \Phi_{\alpha R}(\mathbf{r}) \right] \\ U_{\alpha\beta i} &= g_{\alpha\beta} \int d\mathbf{r} \varphi_{\alpha i}^2(\mathbf{r}) \Phi_{\beta i}^2(\mathbf{r}), \end{aligned} \quad (4.8)$$

with $\alpha, \beta = a, b$ and $i = L, R$. Let us consider a mixture with the same atomic mass for both components $M \equiv M_a = M_b$, which are trapped in the same symmetric double-well potential. Then, the localized modes are the same for both components but depend on the site: $\Phi_{L(R)} \equiv \varphi_{a,L(R)} = \varphi_{b,L(R)}$. Therefore, $E_{aL}^0 = E_{bL}^0 = E_{aR}^0 = E_{bR}^0 \equiv E$, $U_{aaL} = U_{bbL} = U_{aaR} = U_{bbR} \equiv U$ and $U_{abL} = U_{baL} = U_{abR} = U_{baR} \equiv \tilde{U}$, $K_a = K_b \equiv K$.

The population imbalance and phase difference between sites for each component are

$$z_\alpha(t) = \frac{N_{\alpha L}(t) - N_{\alpha R}(t)}{N_\alpha}, \quad \delta\phi_\alpha(t) = \phi_{\alpha R}(t) - \phi_{\alpha L}(t). \quad (4.9)$$

In terms of these variables, the S2M equations become

$$\left\{ \begin{array}{l} \dot{z}_a(t) = -\sqrt{1 - z_a^2(t)} \sin \delta\phi_a(t) \\ \delta\dot{\phi}_a(t) = f_a \Lambda z_a(t) + f_b \tilde{\Lambda} z_b(t) + \frac{z_a(t)}{\sqrt{1 - z_a^2(t)}} \cos \delta\phi_a(t) \\ \dot{z}_b(t) = -\sqrt{1 - z_b^2(t)} \sin \delta\phi_b(t) \\ \delta\dot{\phi}_b(t) = f_b \Lambda z_b(t) + f_a \tilde{\Lambda} z_a(t) + \frac{z_b(t)}{\sqrt{1 - z_b^2(t)}} \cos \delta\phi_b(t), \end{array} \right. \quad (4.10)$$

where $\Lambda = NU/(2K)$, $\tilde{\Lambda} = N\tilde{U}/(2K)$, $f_a = N_a/N$, $f_b = N_b/N$ and the time is rescaled as $t \rightarrow \omega_R t$, with $\omega_R = 2K/\hbar$ the Rabi frequency. The stability of this system of equations have been analyzed recently in Ref. [118].

4.2.2 Improved two-mode model for a binary mixture

As we have seen in Sec. 3.3 for the scalar condensate, when the two modes are not so well localized, then it becomes necessary to consider the I2M to have a quantitative agreement with the TDGPE results. This model provides an exact description of the dynamics in the symmetric double-well potential, with no approximations beyond the assumption of a two-mode ansatz of the total wave function $\Psi_j(\mathbf{r}, t)$, Eq. (4.5).

The resulting system of equations relating the population imbalance and phase difference for each component within the I2M approximation reads¹:

$$\begin{cases} \dot{z}_a(t) &= -\frac{2K_{ab}(t)}{\hbar} \sqrt{1-z_a^2(t)} \sin \delta\phi_a(t) \\ \dot{\delta\phi}_a(t) &= \frac{\Delta_a(t)}{\hbar} + \frac{2K_{ab}(t)}{\hbar} \frac{z_a(t)}{\sqrt{1-z_a^2(t)}} \cos \delta\phi_a(t) \\ \dot{z}_b(t) &= -\frac{2K_{ba}(t)}{\hbar} \sqrt{1-z_b^2(t)} \sin \delta\phi_b(t) \\ \dot{\delta\phi}_b(t) &= \frac{\Delta_b(t)}{\hbar} + \frac{2K_{ba}(t)}{\hbar} \frac{z_b(t)}{\sqrt{1-z_b^2(t)}} \cos \delta\phi_b(t), \end{cases} \quad (4.11)$$

with

$$\begin{aligned} \Delta_a(t) &= 2\gamma_{+-}^{aa} N_a z_a(t) + 2\gamma_{+--+}^{aabb} N_b z_b(t), \\ \Delta_b(t) &= 2\gamma_{+-}^{bb} N_b z_b(t) + 2\gamma_{+--+}^{bbaa} N_a z_a(t), \\ 2K_{ab}(t) &= (\mu_-^a - \mu_+^a) + \frac{1}{2} \left[N_a (\gamma_{++}^{aa} - \gamma_{--}^{aa}) \right. \\ &\quad + N_b (\gamma_{++}^{ab} - \gamma_{--}^{ab} - \gamma_{+-}^{ab} + \gamma_{-+}^{ab}) \\ &\quad - N_a (\gamma_{++}^{aa} + \gamma_{--}^{aa} - 2\gamma_{+-}^{aa}) \sqrt{1-z_a^2(t)} \cos \delta\phi_a(t) \\ &\quad \left. - N_b (\gamma_{++}^{ab} + \gamma_{--}^{ab} - \gamma_{+-}^{ab} - \gamma_{-+}^{ab}) \sqrt{1-z_b^2(t)} \cos \delta\phi_b(t) \right] \\ \gamma_{ij}^{\alpha\beta} &= g_{\alpha\beta} \int d\mathbf{r} \varphi_{\alpha i}^2(\mathbf{r}) \varphi_{\beta j}^2(\mathbf{r}) \\ \gamma_{+--+}^{aabb} &= \gamma_{+--+}^{bbaa} = g_{ab} \int d\mathbf{r} \varphi_{a+}(\mathbf{r}) \varphi_{a-}(\mathbf{r}) \varphi_{b+}(\mathbf{r}) \varphi_{b-}(\mathbf{r}). \end{aligned} \quad (4.12)$$

$\varphi_{\alpha+}$ and $\varphi_{\alpha-}$ are the ground and first excited single-particle states of the α component, and μ_+^α , μ_-^α the corresponding chemical potentials, that can be calculated from the time-independent GP equation for $\varphi_{\alpha\pm}$, respectively. Analogously one can define $2K_{ba}$ by exchanging the subindex a and b in the previous expression.

Notice that we have kept the full 3D dependence of the wave functions $\varphi_{j\pm}(\mathbf{r})$, instead of averaging the transverse spatial dependence as in Refs. [73, 122]. Thus, the coupling parameters $g_{\alpha\beta}$ in Eqs. (4.12) are the 3D ones and are not renormalized.

¹Our system of equations differs slightly with the previously derived ones, cf. appendix of Ref. [122]. We believe their system has some minor errors, which do not affect their discussion which is based on the S2M equations.

The equations for the I2M are essentially similar to the S2M. The main difference is that the tunneling term, $K_{ab}(t)$, is time-dependent and contains effects due to the interactions. As expected, if the localization of the modes is increased, e.g. by increasing the barrier height, $K_{ab}(t)$ approaches the constant value, $2K_{ab} \rightarrow \mu_-^a - \mu_+^a$, which equals $2K$ of Eq. (4.8). The coupled equations obtained in the I2M model reduce to well-known dynamical equations in two limiting cases:

- i) Setting to zero the overlapping integrals that involve mixed products of left and right modes of order larger than 1, the I2M equations reduce to the S2M model for the mixture, Eqs. (4.10).
- ii) Assuming a noninteracting mixture, the inter-species interaction is $g_{ab} = 0$, and the I2M equations for the mixture reduce to two non-coupled system of equations, that are the dynamical equations of the I2M for a single component, Sec. 3.2.2.

As discussed at the beginning of this section, we are interested in the particular case of a binary mixture made of atoms populating two different hyperfine states. Then, both components have the same mass M , and are trapped in the same symmetric double-well potential. We initially restrict to the case in which the inter-species interaction is also almost equal to the intra-species one, $g \equiv g_{aa} = g_{bb} \sim g_{ab}$. This is the situation for $F = 1$, $m = \pm 1$ of ^{87}Rb . This case allows straightforward comparisons between the results of the I2M and the ones obtained by solving the NPSE or 1D-TDGPE for a mixture, explained in Sec. 4.1.

The ground and first excited states in a symmetric double-well potential are the same for both components. Moreover, since $g = g_{ab}$ the overlap integrals (4.12) reduce to:

$$\begin{aligned} \gamma_{++}^{aa} &= \gamma_{++}^{bb} = \gamma_{++}^{ab} \equiv \gamma_{++} \\ \gamma_{--}^{aa} &= \gamma_{--}^{bb} = \gamma_{--}^{ab} \equiv \gamma_{--} \\ \gamma_{+-}^{aa} &= \gamma_{+-}^{bb} = \gamma_{+-}^{ab} = \gamma_{-+}^{ab} = \gamma_{+-+}^{aabb} \equiv \gamma_{+-}, \end{aligned} \quad (4.13)$$

and the chemical potentials $\mu_i^a = \mu_i^b \equiv \mu_i$ with $i = +, -$. This yields the following relations: $K_{ab} = K_{ba}$ and $\Delta_a = \Delta_b$. The I2M system reduces to:

$$\left\{ \begin{aligned} \dot{z}_a(t) &= -\frac{2K_{ab}(t)}{\hbar} \sqrt{1 - z_a^2(t)} \sin \delta\phi_a(t) \\ \dot{\delta\phi}_a(t) &= \frac{2(N_a z_a(t) + N_b z_b(t))\gamma_{+-}}{\hbar} + \frac{2K_{ab}(t)}{\hbar} \frac{z_a(t)}{\sqrt{1 - z_a^2(t)}} \cos \delta\phi_a(t) \\ \dot{z}_b(t) &= -\frac{2K_{ab}(t)}{\hbar} \sqrt{1 - z_b^2(t)} \sin \delta\phi_b(t) \\ \dot{\delta\phi}_b(t) &= \frac{2(N_a z_a(t) + N_b z_b(t))\gamma_{+-}}{\hbar} + \frac{2K_{ab}(t)}{\hbar} \frac{z_b(t)}{\sqrt{1 - z_b^2(t)}} \cos \delta\phi_b(t). \end{aligned} \right. \quad (4.14)$$

In this case both components obey the same system of coupled differential equations. Then, if the initial conditions are the same for both, $z_a(0) = z_b(0)$ and $\delta\phi_a(0) = \delta\phi_b(0)$, they will evolve with the same imbalance and phase, and no mixture effects will be observed.

4.2.3 Dynamical regimes in a binary mixtures

We proceed now to analyze the stability of the system of equations (4.10), cf. see the appendix of Ref. [90]. As in the single-component case, and in order to get analytical results that allow for a physical insight, we perform the study in the framework of the S2M approximation. First we note that an stationary point, defined by the equations: $\dot{z}_\alpha = 0$ and $\dot{\delta\phi}_\alpha = 0$, necessarily fulfills,

$$\begin{aligned}\sin \delta\phi_a = 0 &\Rightarrow \delta\phi_a^0 = 0, \pi \\ \sin \delta\phi_b = 0 &\Rightarrow \delta\phi_b^0 = 0, \pi,\end{aligned}\quad (4.15)$$

and the following system of equations,

$$\begin{aligned}z_a^0 &= -z_b^0 \left(\frac{\Lambda}{\tilde{\Lambda}} + \frac{1}{\tilde{\Lambda} f_b \sqrt{1 - (z_b^0)^2 \cos \delta\phi_b^0}} \right) \\ z_b^0 &= -z_a^0 \left(\frac{\Lambda}{\tilde{\Lambda}} + \frac{1}{\tilde{\Lambda} f_a \sqrt{1 - (z_a^0)^2 \cos \delta\phi_a^0}} \right).\end{aligned}\quad (4.16)$$

Therefore there are four different cases: $(\delta\phi_a^0 = 0, \delta\phi_b^0 = 0)$, $(\delta\phi_a^0 = 0, \delta\phi_b^0 = \pi)$, $(\delta\phi_a^0 = \pi, \delta\phi_b^0 = 0)$, $(\delta\phi_a^0 = \pi, \delta\phi_b^0 = \pi)$, noting that in all of them there is an obvious stationary point, $z_a^0 = z_b^0 = 0$. These stationary points will be referred to as ‘‘trivial stationary points’’. We need to find the conditions for non-trivial solutions in each case.

The stability of the system is analyzed by considering small variations around the stationary points for each of the four situations. Defining the displacements η_α ,

$$\begin{aligned}z_a(t) &= z_a^0 + \eta_a(t) \\ z_b(t) &= z_b^0 + \eta_b(t),\end{aligned}\quad (4.17)$$

the following system of equations for the η 's can be derived from Eqs. (4.10)

$$\begin{pmatrix} \ddot{\eta}_a \\ \ddot{\eta}_b \end{pmatrix} = -\Omega^2 \begin{pmatrix} \eta_a \\ \eta_b \end{pmatrix}\quad (4.18)$$

where,

$$\begin{aligned}\Omega^2 &= \omega_R^2 \begin{pmatrix} 1 + (f_a \Lambda z_a^0 + f_b \tilde{\Lambda} z_b^0)^2 & 0 \\ 0 & 1 + (f_a \tilde{\Lambda} z_a^0 + f_b \Lambda z_b^0)^2 \end{pmatrix} \\ &+ \omega_R^2 \begin{pmatrix} f_a \Lambda \sqrt{1 - (z_a^0)^2 \cos \delta\phi_a^0} & f_a \tilde{\Lambda} \sqrt{1 - (z_a^0)^2 \cos \delta\phi_a^0} \\ f_b \tilde{\Lambda} \sqrt{1 - (z_b^0)^2 \cos \delta\phi_b^0} & f_b \Lambda \sqrt{1 - (z_b^0)^2 \cos \delta\phi_b^0} \end{pmatrix}.\end{aligned}\quad (4.19)$$

In Table 4.1 we give the explicit values of the eigenfrequencies of Ω for the trivial stationary points, $z_i^0 = 0$, which are obtained for $\Lambda > 0$ and $\tilde{\Lambda} > 0$. Approximate simpler expressions of these eigenfrequencies can be derived when $\tilde{\Lambda} \sim \Lambda$. Defining $\tilde{\Lambda} = \Lambda(1 + \beta)$ and retaining up to terms of order β , one obtains the frequencies listed in Table 4.2.

$(\delta\phi_a^0, \delta\phi_b^0)$	ω_1^2/ω_R^2	ω_2^2/ω_R^2
(0,0)	$1 + \frac{\Lambda}{2} \left(1 + \sqrt{\Delta f^2 + 4f_a f_b (\tilde{\Lambda}/\Lambda)^2} \right)$	$1 + \frac{\Lambda}{2} \left(1 - \sqrt{\Delta f^2 + 4f_a f_b (\tilde{\Lambda}/\Lambda)^2} \right)$
(π, π)	$1 - \frac{\Lambda}{2} \left(1 - \sqrt{\Delta f^2 + 4f_a f_b (\tilde{\Lambda}/\Lambda)^2} \right)$	$1 - \frac{\Lambda}{2} \left(1 + \sqrt{\Delta f^2 + 4f_a f_b (\tilde{\Lambda}/\Lambda)^2} \right)$
$(\pi, 0)$	$1 + \frac{\Lambda}{2} \left(\sqrt{1 - 4f_a f_b (\tilde{\Lambda}/\Lambda)^2} - \Delta f \right)$	$1 - \frac{\Lambda}{2} \left(\sqrt{1 - 4f_a f_b (\tilde{\Lambda}/\Lambda)^2} + \Delta f \right)$
$(0, \pi)$	$1 + \frac{\Lambda}{2} \left(\sqrt{1 - 4f_a f_b (\tilde{\Lambda}/\Lambda)^2} + \Delta f \right)$	$1 - \frac{\Lambda}{2} \left(\sqrt{1 - 4f_a f_b (\tilde{\Lambda}/\Lambda)^2} - \Delta f \right)$

Table 4.1: Square of the frequencies of the eigenmodes of the S2M system, Eqs. (4.10), linearized around the trivial stationary points, $z_i^0 = 0$ for the four different $\delta\phi_i^0$ combinations, and with $\Delta f = f_a - f_b$.

$(\delta\phi_a, \delta\phi_b)$	ω_1^2/ω_R^2	ω_2^2/ω_R^2
(0,0)	$1 + \Lambda(1 + 2\beta f_a f_b)$	$1 - 2\Lambda\beta f_a f_b$
(π, π)	$1 + 2\Lambda\beta f_a f_b$	$1 - \Lambda(1 + 2\beta f_a f_b)$
$(\pi, 0)$	$1 - \frac{2\beta f_a f_b \Lambda}{f_a - f_b}$	$1 + (f_b - f_a)\Lambda + \frac{2\beta f_a f_b \Lambda}{f_a - f_b}$
$(0, \pi)$	$1 + (f_a - f_b)\Lambda - \frac{2\beta f_a f_b \Lambda}{f_a - f_b}$	$1 + \frac{2\beta f_a f_b \Lambda}{f_a - f_b}$

Table 4.2: Same as Table 4.1 but retaining up to the first order in β , where $\tilde{\Lambda} = \Lambda(1 + \beta)$. We assume $f_a > f_b$.

Stationary points with $(\delta\phi_a^0 = 0, \delta\phi_b^0 = 0)$

In this case, the condition for the existence of non-trivial solutions to the equations (4.16) depends on the slope at the origin of the two curves (4.16) [90]. The condition

$$\left(\frac{\Lambda}{\tilde{\Lambda}} + \frac{1}{f_b \tilde{\Lambda}} \right) \left(\frac{\Lambda}{\tilde{\Lambda}} + \frac{1}{f_a \tilde{\Lambda}} \right) < 1, \quad (4.20)$$

guarantees the existence of two additional solutions besides the trivial one. However, in the particular case $\tilde{\Lambda} \sim \Lambda > 0$, the condition (4.20) cannot be fulfilled and therefore the only stationary point is the trivial one, $z_a^0 = z_b^0 = 0$.

In this case, the insertion of the stationary point, $z_a^0 = z_b^0 = 0$ and $\delta\phi_a^0 = \delta\phi_b^0 = 0$ into Eq. (4.19) yields,

$$\Omega^2 = \omega_R^2 \begin{pmatrix} 1 & 0 \\ 0 & 1 \end{pmatrix} + \omega_R^2 \begin{pmatrix} f_a \tilde{\Lambda} & f_a \tilde{\Lambda} \\ f_b \tilde{\Lambda} & f_b \tilde{\Lambda} \end{pmatrix}, \quad (4.21)$$

which has two eigenvalues, listed in Table 4.1.

In a very polarized mixture, $f_a \sim 1, f_b \sim 0$, the population imbalance of the most populated component decouples from the less populated one and oscillates with the Josephson frequency $w_J = \omega_1$ (see Eq. (4.10)). The behavior of the less populated component is driven by the other component and follows its dynamics, thus giving rise to ‘‘anti-Josephson’’ oscillations. The smaller frequency oscillation observed in the population imbalance of the less populated component is ω_2 (Fig. 4.3(a)), which is very similar to ω_R [124].

Also interesting is the case of the non-polarized mixture, $f_a = f_b = 1/2$, then (assuming $\tilde{\Lambda} \sim \Lambda$, which is the case for ^{87}Rb),

$$\begin{aligned}\ddot{z}_a(t) &= -\Lambda/2(z_a(t) + z_b(t)) - z_a(t), \\ \ddot{z}_b(t) &= -\Lambda/2(z_a(t) + z_b(t)) - z_b(t).\end{aligned}\quad (4.22)$$

and defining $\Delta z(t) = z_a(t) + z_b(t)$, $\delta z(t) = z_a(t) - z_b(t)$ we have,

$$\ddot{\Delta z}(t) = -(\Lambda + 1)\Delta z(t), \quad \ddot{\delta z}(t) = -\delta z(t).$$

Therefore, Δz behaves as a single component, oscillating with the usual Josephson frequency, $w_J = \omega_R \sqrt{1 + \Lambda}$ while δz oscillates with the Rabi frequency, as it would do a single component in the absence of atom-atom interactions. This mode can be further enhanced by imposing that $z_a(0) = -z_b(0)$ thus forcing both imbalances to oscillate with the same frequency.

We have proposed in Ref. [124] to use these two configurations to extract the frequencies governing the dynamics of the system in order to obtain the microscopic atom-atom interaction. The idea was to profit from the fact that the difference between the inter- and intra-species interaction is small for the case of ^{87}Rb , $\tilde{\Lambda} = \Lambda(1 + \beta)$, so we can use the expressions listed in Table 4.2, $\omega_1^2 = \omega_R^2(1 + \Lambda(1 + 2\beta f_a f_b))$, and $\omega_2^2 = \omega_R^2(1 - 2\Lambda\beta f_a f_b)$. Note that in the anti-Josephson case the oscillation with larger period is $\omega_2^2 = \omega_R^2(1 + \mathcal{O}(\beta f_b))$ and the shorter is $\omega_1^2 = \omega_R^2(1 + \Lambda + \mathcal{O}(\beta f_b))$, with $\beta \ll 1$ and $f_b \ll 1$, allowing to extract both the Rabi and Josephson frequencies with good precision. The second configuration only has one frequency which is $\omega_1^2 = \omega_R^2(1 + \Lambda(1 + \beta/2))$ which allows to isolate the value of β .

Stationary points with $(\delta\phi_a^0 = \pi, \delta\phi_b^0 = 0)$

In this case, the condition for the existence of three stationary points is,

$$\left(\frac{\Lambda}{\tilde{\Lambda}} - \frac{1}{f_a \tilde{\Lambda}}\right) \left(\frac{\Lambda}{\tilde{\Lambda}} + \frac{1}{f_b \tilde{\Lambda}}\right) > 1. \quad (4.23)$$

For the case considered here, $\tilde{\Lambda} \sim \Lambda$, and, in most applications, $\Lambda > 1$. Therefore, an appropriate choice of f_a can ensure the existence of three stable points. The stability of the trivial solution is checked by studying,

$$\Omega^2 = \omega_R^2 \begin{pmatrix} 1 & 0 \\ 0 & 1 \end{pmatrix} + \omega_R^2 \begin{pmatrix} f_a \Lambda & f_a \tilde{\Lambda} \\ -f_b \tilde{\Lambda} & -f_b \Lambda \end{pmatrix}, \quad (4.24)$$

whose eigenvalues are listed in Table 4.1. The stability of the other two solutions is easy to study with the same tools. Simple analytic expressions are only attainable for the case $\tilde{\Lambda} = \Lambda$. Then we have,

$$\begin{aligned}\Omega^2 &= \omega_R^2 \begin{pmatrix} 1 + \Lambda(f_a z_a^0 + f_b z_b^0)^2 & 0 \\ 0 & 1 + \Lambda(f_a z_a^0 + f_b z_b^0)^2 \end{pmatrix} \\ &+ \omega_R^2 \Lambda \begin{pmatrix} f_a \sqrt{1 - (z_a^0)^2} & f_a \sqrt{1 - (z_a^0)^2} \\ -f_b \sqrt{1 - (z_b^0)^2} & -f_b \sqrt{1 - (z_b^0)^2} \end{pmatrix},\end{aligned}\quad (4.25)$$

whose eigenvalues are,

$$\omega_1^2 = \omega_R^2(\Lambda^2(f_a z_a^0 + f_b z_b^0)^2), \quad \omega_2^2 = \omega_R^2(1 + \Lambda^2(f_a z_a^0 + f_b z_b^0)^2). \quad (4.26)$$

Stationary points with $(\delta\phi_a^0 = \pi, \delta\phi_b^0 = \pi)$

The condition for the existence of three stationary points is in this case [90],

$$\left(\frac{\Lambda}{\tilde{\Lambda}} - \frac{1}{f_b \tilde{\Lambda}}\right) \left(\frac{\Lambda}{\tilde{\Lambda}} - \frac{1}{f_a \tilde{\Lambda}}\right) < 1. \quad (4.27)$$

The eigenvalues corresponding to small oscillations around the trivial point are listed in Table 4.1. Its dynamical stability depends on the specific values of f_i , $\tilde{\Lambda}$, Λ and ω_R . For the case $\tilde{\Lambda} = \Lambda$, it is stable provided that $\omega_R > \Lambda$.

The eigenfrequencies for the non-trivial solution are the same as for the case $(\delta\phi_a = 0, \delta\phi_b = \pi)$. In the simplest case, $\tilde{\Lambda} = \Lambda$, they are,

$$\omega_1^2 = \omega_R^2 (\Lambda^2 (f_a z_a^0 + f_b z_b^0)^2), \quad \omega_2^2 = \omega_R^2 (1 + \Lambda^2 (f_a z_a^0 + f_b z_b^0)^2). \quad (4.28)$$

4.3 Numerical solutions of the TDGPE for a binary mixture

As discussed in Refs. [124, 91], one feasible way of experimentally prepare binary mixtures of BECs is to consider a number of atoms populating the $m = \pm 1$ Zeeman components of an ^{87}Rb $F = 1$ spinor BEC². This is because the creation rate of $m_F = 0$ due to spin-changing collisions is small for short times. Therefore, the spinor condensate can be described by a binary mixture with a constant number of particles in each species.

For a binary mixture of $m_F = \pm 1$ ^{87}Rb the two components of the mixture have the same mass, $M \equiv m_a = m_b$, equal intra-species interactions, $g_{aa} = g_{bb} \equiv g$, and slightly different inter-species interaction $g_{ab} \sim g$. The explicit values are $g = c_0 + c_2$, $g_{ab} = c_0 - c_2$, with $c_0 = 4\pi\hbar^2(a_0 + 2a_2)/(3M)$, $c_2 = 4\pi\hbar^2(a_2 - a_0)/(3M)$, $a_0 = 101.8a_B$, $a_2 = 100.4a_B$ and a_B the Bohr radius [127].

We fix the total number of particles to 1150 and consider the external double-well potential used in the Heidelberg experiment [70], see Sec. 3.1. We want to investigate the Josephson-like dynamics for different number of atoms populating each component $N_a = f_a N$ and $N_b = f_b N$ and for different initial conditions $z_a(0)$, $z_b(0)$, $\delta\phi_a(0)$ and $\delta\phi_b(0)$.

The values of $\Lambda = NU/\hbar\omega_R$ and $\tilde{\Lambda} = N\tilde{U}/\hbar\omega_R$ are $\Lambda = 74.278$ and $\tilde{\Lambda} = 74.968$. With $\Lambda/\tilde{\Lambda} = 0.99$. These are obtained from the microscopic 3D parameters computed in the scalar case, with the same total number of particles, Sec. 3.3. This is reasonable for the case we are considering where $g_{aa} = g_{bb} \sim g_{ab}$, which implies that the ground state wave functions for the GP equations of the mixture do not depend on f_a and f_b for a fixed total number of particles. This would certainly not be the case if $g_{aa} = g_{bb} \neq g_{ab}$, in such case one would need to recompute the ground state wave functions for a and b for each value of f_a .

Following the discussion in Sec. 4.2.3, where the predictions of the S2M were discussed in detail, the system has the trivial equilibrium points, listed in Table 4.2 with $\beta = 0.009$. In Fig. 4.1 we show the values of the two eigenfrequencies for each of the trivial equilibrium

²See Chapter 6 for a detailed description of a spinor condensate.

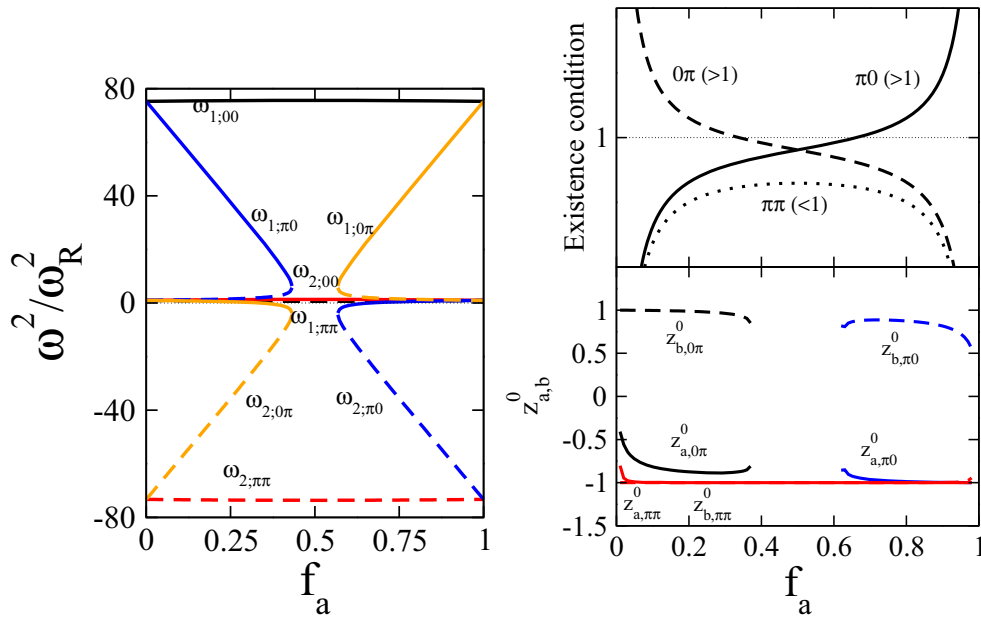


Figure 4.1: (left) Values of the frequencies, ω/ω_R , listed in Table 4.2 for the specific conditions considered in the numerical simulations as a function of the fraction of atoms in the a component, f_a . The notation is as follows, $\omega_{i;\alpha\beta}$, with $i = 1, 2$ the index of the eigenfrequency, and $\alpha, \beta = 0, \pi$ the phase difference of the stationary point for each component. (right) The conditions for the existence of the non-trivial equilibrium points given in Eqs. (4.20, 4.23, 4.27), upper panel, as function of f_a for the conditions described in the text. The lower panel contains the explicit equilibrium points z_a^0, z_b^0 as a function of f_a obtained by solving equations (4.16). Note that each equilibrium point has a trivial partner which is obtained by flipping the sign of z_a^0, z_b^0 .

points listed in Table 4.2 for the specific conditions described above. The figure shows a number of important features about the stability of the trivial equilibrium points. First, the $(z_a^0, \delta\phi_a^0, z_b^0, \delta\phi_b^0) = (0, 0, 0, 0)$ is always stable regardless of the total polarization of the system (measured by $f_b - f_a$). Second, the $(z_a^0, \delta\phi_a^0, z_b^0, \delta\phi_b^0) = (0, \pi, 0, \pi)$ mode is always unstable, as seen by the negative value taken by the square of the frequencies. Third, the $(z_a^0, \delta\phi_a^0, z_b^0, \delta\phi_b^0) = (0, 0, 0, \pi)$ mode should be stable for $f_b \lesssim 0.43$, correspondingly the $(z_a^0, \delta\phi_a^0, z_b^0, \delta\phi_b^0) = (0, \pi, 0, 0)$ is stable for $f_a \lesssim 0.43$ and therefore there is a range of polarizations, given by $0.43 \lesssim f_a \lesssim 0.57$ where the only trivial mode which is stable is the $(z_a^0, \delta\phi_a^0, z_b^0, \delta\phi_b^0) = (0, 0, 0, 0)$.

The non-trivial equilibrium points in this case can be obtained by analyzing the conditions given in Sec. 4.2.3. For $(\delta\phi_a^0, \delta\phi_b^0) = (0, 0)$ there are no equilibrium points apart from the trivial one, due to $\Lambda \sim \bar{\Lambda}$. In the other three cases there are non-trivial equilibrium points depending on the specific values of f_a . In Fig. 4.1(right) we analyze their existence. First, we note that there are non-trivial points corresponding to $(\delta\phi_a^0, \delta\phi_b^0) = (0, \pi)$ provided $f_a \lesssim 0.37$, correspondingly there are also equilibrium points for $(\delta\phi_a^0, \delta\phi_b^0) = (0, \pi)$ if $f_b \lesssim 0.37$. There is also a non-trivial equilibrium point for $(\delta\phi_a^0, \delta\phi_b^0) = (\pi, \pi)$ regardless of f_a . As can be seen in the figure, all these non-trivial equilibrium points correspond to fairly imbalanced conditions and can in most cases be understood in simple terms from

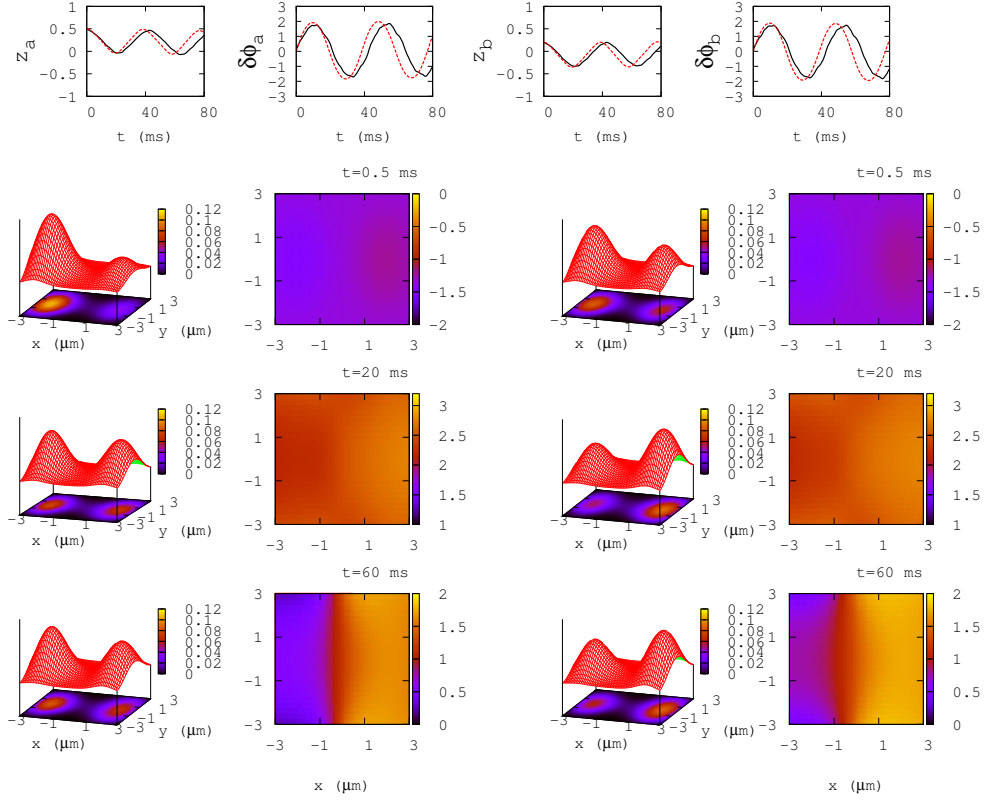


Figure 4.2: Full TDGPE calculations of the dynamics of a binary mixture with $z_a(0) = 0.5$, $z_b(0) = 0.2$, $\delta\phi_a(0) = 0$, $\delta\phi_b(0) = 0$, $f_a = 0.25$ and $f_b = 0.75$. The upper four plots depict, from left to right, $z_a(t)$, $\delta\phi_a(t)$, $z_b(t)$, and $\delta\phi_b(t)$ in solid black compared to the I2M prediction, dashed-red. Then each row contains from left to right: 3D depictions complemented by contour plots of $\rho_a(x, y; t)$, a contour plot of the averaged phase $\phi_a(x, y; t)$, 3D depictions complemented by contour plots of $\rho_b(x, y; t)$, and a contour plot of the averaged phase $\phi_b(x, y; t)$. Each row corresponds to a different time, .5 ms (upper), 20 ms (middle) and 60 ms (lower), respectively.

the analysis of the scalar case. For instance, the equilibrium point for $(\delta\phi_a^0, \delta\phi_b^0) = (\pi, \pi)$ corresponds to $z_a^0 \sim z_b^0 \sim 1$ (or -1), which can be understood as having both components locked in a π -mode. Similarly, the equilibrium points in the $(0, \pi)$ or $(\pi, 0)$ cases exist whenever the most abundant component is populated enough to drive the dynamics close to being π locked.

4.3.1 TDGPE calculations: phase coherence and localization

The numerical solutions of the TDGPE presented in Sec. 3.3 for the single-component system showed two features. First, the atoms remained mostly localized in the two minima of the potential well and secondly, each group of atoms had to a large extent the same quantum phase. This, clearly supported the picture of having two BEC, one at each side of the barrier, with a well defined phase at each side during the dynamical evolution.

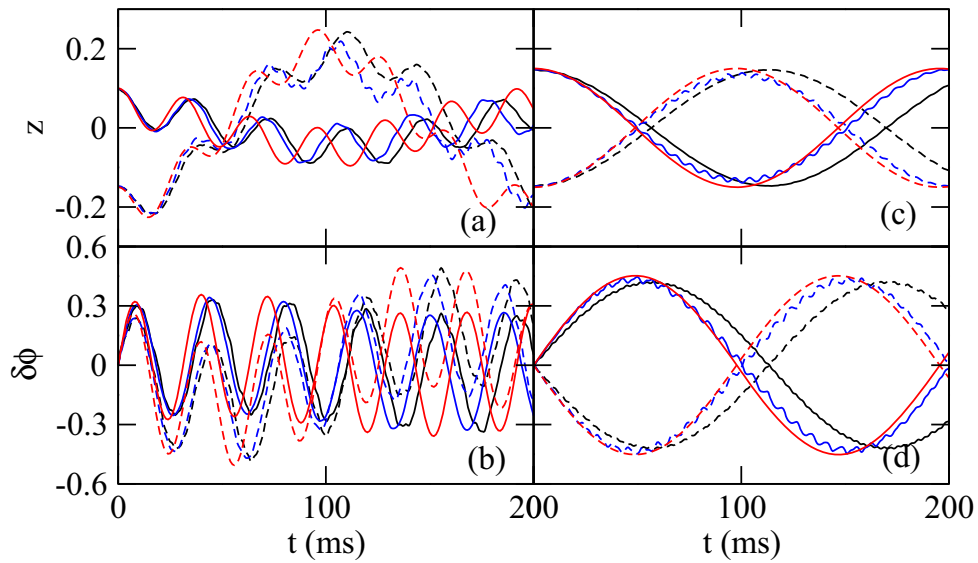


Figure 4.3: Behavior of the population imbalance, $z_a(t)$ (solid lines), and $z_b(t)$ (dashed lines), and phase difference, $\delta\phi_a(t)$ (solid lines) and $\delta\phi_b(t)$ (dashed lines), computed using TDGPE (black lines), NPSE (blue lines), and I2M (red lines) in a polarized case, $f_a = 0.8$, left, and a zero polarization case, $f_a = 0.5$, right, respectively. The initial conditions are $z_a(0) = 0.1$, $z_b(0) = -0.15$ and $\delta\phi_a(0) = \delta\phi_b(0) = 0$ for the left panels, and $z_a(0) = -z_b(0) = 0.15$ and $\delta\phi_a(0) = \delta\phi_b(0) = 0$ for the right panels.

Essentially those are the premises used to derive the two-mode models, both for single component and for binary mixtures.

As in the scalar case, our exact TDGPE numerical solutions of the dynamics of the binary mixture in several initial conditions of population imbalances and phase differences show two distinctive features, see Fig. 4.2. First, the density of atoms for each component is always bi-modal, with the two atom bunches centered around the minima of the potential well. Secondly, the phase of the wave function is mostly constant for each species at each side of the potential trap. Thus, we find that the TDGPE does predict the dynamics to be mostly bi-modal also for the binary mixture case.

At the end of the section we will consider some deviations from the bi-modal behavior that are found in very specific conditions, e.g. for very large population imbalances and also when analyzing a case with $g_{ab} \neq g_{aa} = g_{bb}$.

4.3.2 Small oscillations around $z_{a,b}^0$ and $\delta\phi_{a,b}^0 = 0$

The two predictions of the two-mode described in Sec. 4.2.3, namely the “anti-Josephson” behavior, and the enhancement of the Rabi mode, are confirmed by the NPSE and 1D-TDGPE simulations as can be seen in Fig. 4.3. In Fig. 4.3 (left panels) we consider a very polarized case, $f_a = 0.8$. As expected from the two-mode analysis the dynamics of the most populated component should to a large extent decouple from the less populated one and perform fast Josephson oscillations with a frequency close to the corresponding one for the scalar case, $\omega_J = \omega_R\sqrt{1+\Lambda}$. The TDGPE simulation is seen to confirm the above and follow closely the predictions of the I2M. The behavior of the less abundant

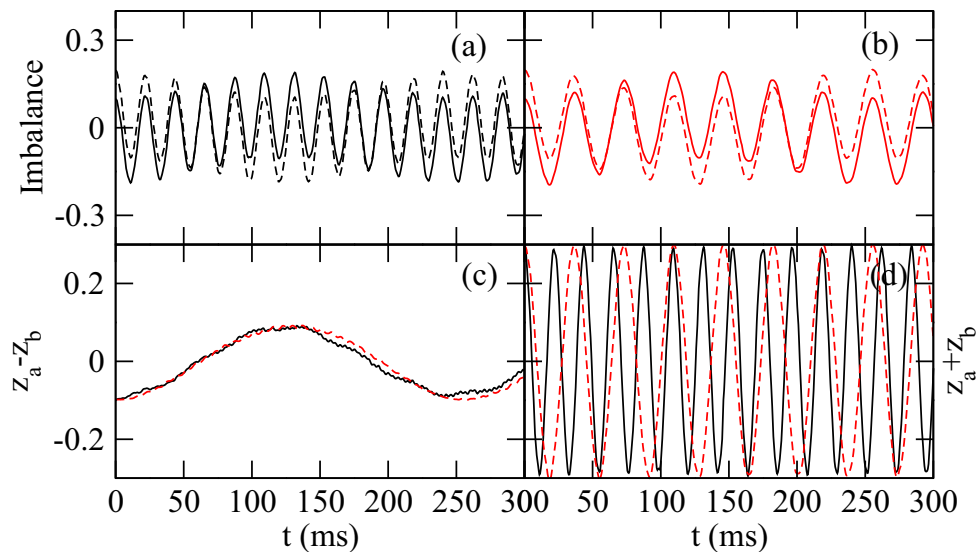


Figure 4.4: Behavior of the population imbalance in NPSE (red) and 1D-TDGPE (black) simulations in the zero magnetization case, $f_a = f_b$. The initial conditions are $z_a(0) = 0.1$, $z_b(0) = 0.2$ and $\delta\phi(0) = 0$. The upper panels correspond to (a) $z_a(t)$ (solid line) and $z_b(t)$ (dashed line) obtained with the 1D-TDGPE equations, (b) $z_a(t)$ and $z_b(t)$ obtained with the NPSE equations, (c) behavior of $z_a(t) - z_b(t)$ for 1D-TDGPE (solid) and NPSE (dashed), and (d) behavior of $z_a(t) + z_b(t)$.

component is strongly driven by the most populated one and shows an anti-Josephson behavior as described in Ref. [124].

Another prediction is related to the behavior of $z_a + z_b$ and $z_a - z_b$ in the non-polarized case, $f_a = f_b$. As explained in Sec. 4.2.3, in this case the difference, $z_a - z_b$, should enhance the long mode which oscillates with the Rabi frequency of the system, while the sum $z_a + z_b$ should mostly oscillate with the Josephson frequency. In the right part of Fig. 4.3 we present the extreme case when $z_a(0) = -z_b(0)$ computed with TDGPE, NPSE and I2M. In this case, both population imbalances and phase differences oscillate mostly with the Rabi frequency of the system, keeping during the time evolution $z_a + z_b \sim 0$.

As seen in Fig. 4.4 both 1D reductions produce qualitatively similar physics. The only important difference is that the frequency of the Josephson oscillations is higher in the 1D-TDGPE, as occurred already for the single component, see Sec. 3.3.

Interestingly, they predict different Josephson oscillations while the Rabi frequencies are similar. In panel (c) of Fig. 4.4 the long oscillation corresponding to the Rabi mode is seen to agree well with the corresponding long oscillation seen in the right panels of Fig. 4.3. The Josephson-like oscillations of binary mixtures of spinor $F = 1$ ^{87}Rb BECs around the $(z_a^0, \delta\phi_a^0, z_b^0, \delta\phi_b^0) = (0, 0, 0, 0)$ are therefore essentially controlled by two frequencies, ω_R and ω_J .

As a general statement, in the conditions of the Heidelberg experiment, as occurred for the scalar case, the I2M produces more reliable results than the S2M model, which are not shown in the figures. Notice that the parameters that we use for the I2M are extracted from the TDGPE calculation as given in Sec. 3.3. Other representative cases with $(\delta\phi_a(0), \delta\phi_b(0)) = (0, 0)$ but with larger initial imbalances, $z_i(0) \sim 0.5$ are shown

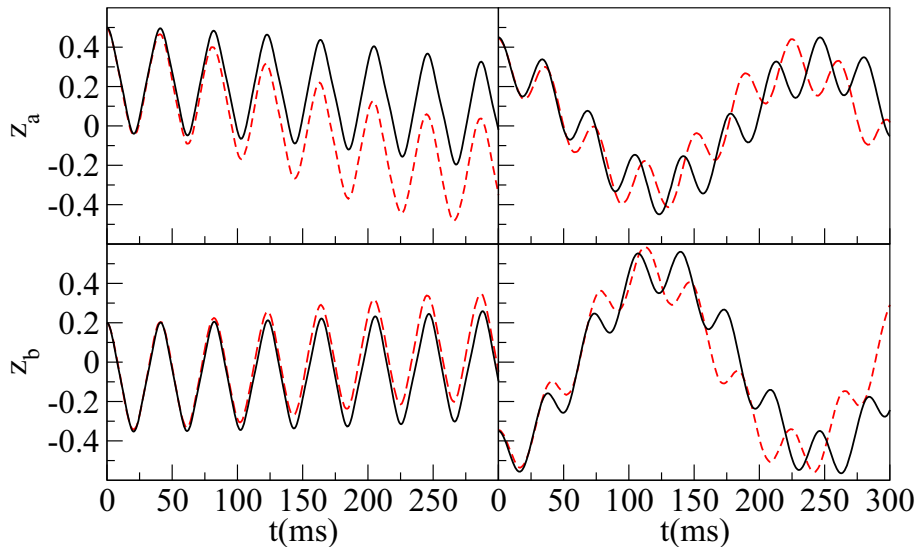


Figure 4.5: (left panels) Evolution of the population imbalance of each component for a binary mixture with $f_a = 0.25$. The upper panel shows $z_a(t)$, and the bottom panel $z_b(t)$. The solid (black) line corresponds to the I2M model and the dashed (red) line to the NPSE. The initial conditions are $z_a(0) = 0.5$, $z_b(0) = 0.2$, $\delta\phi_a(0) = \delta\phi_b(0) = 0$. (right panels) As in the left panel, but with $f_a = 0.6$ and initial conditions $z_a(0) = 0.45$, $z_b(0) = -0.35$, $\delta\phi_a(0) = \delta\phi_b(0) = 0$.

in Fig. 4.5. On the left side of the figure we show the population imbalance of each component for a simulation with $f_a = 0.25$. In this case the dynamics is controlled by ω_J . The panel on the right depicts a simulation with $f_a = 0.6$ and close to opposite initial population imbalances. In this case, both frequencies ω_J and ω_R show up in the evolution. The I2M provides a satisfactory description of the dynamics.

4.3.3 Small oscillations around $z_{a,b}^0$, $\delta\phi_a^0 = 0$ and $\delta\phi_b^0 = \pi$

As explained above, for these conditions there can exist up to three stationary points depending on the specific value of f_a considered. The trivial equilibrium point exists provided $f_a \lesssim 0.43$, see Fig. 4.1. This prediction of the two-mode models is observed both in the TDGPE and NPSE as it can be seen in Fig. 4.6. In the figure, we consider a simulation with $z_a(0) = 0.1$, $z_b(0) = -0.15$, and $f_b = 0.2 < 0.43$ (left panels). The population imbalance (upper panel) of both components oscillates in the usual Josephson regime. At the same time, the phase difference oscillates with its characteristic phase-shift of $\pi/2$ with respect to the imbalance (lower panel). The phase of the a component oscillates around $\delta\phi_a = 0$ while $\delta\phi_b$ does oscillate around $\delta\phi_b = \pi$.

A completely different picture emerges when the fraction of atoms in both components is exchanged, $f_a = 0.2 < 0.43$ (right panels), with most of the atoms populating the b component. In this case, the oscillation amplitude is large, both components remain trapped on their original sides and the phase difference becomes unbounded. This should be considered as a genuine effect of the binary mixture as each component follows a running phase mode at each side of the potential barrier.

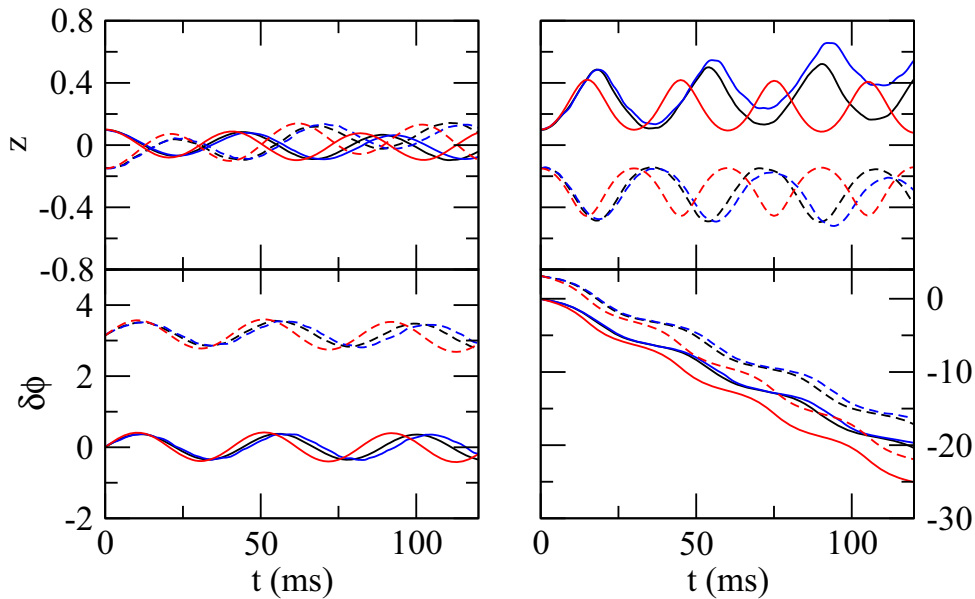


Figure 4.6: Two simulations with the same initial conditions, $z_a(0) = 0.1$, $z_b(0) = -0.15$, $\delta\phi_a(0) = 0$ and $\delta\phi_b(0) = \pi$ but with different compositions of the mixture. The case on the left has $f_b = 0.2$ while the case on the right $f_b = 0.8$. The blue lines are obtained by means of a full TDGPE, the black lines are the NPSE results, and the red lines are the I2M results. Solid and dashed lines correspond to the a and b components, respectively.

The comparison between the NPSE and TDGPE is very satisfactory. The NPSE captures almost completely the dynamics up to times of 100 ms. In all cases, the NPSE reproduces correctly both the phase difference and population imbalance. The only sizable discrepancies occur for times $\gtrsim 80$ ms in the run without equilibrium point (right panel).

The I2M gives a good qualitative picture of both cases but fails to provide predictions as accurate as the NPSE, as happened in the scalar case, see for instance Figs. 3.10 and 3.12. In particular the predicted periods of oscillation are much longer than the actual ones.

An example of simulations around non-trivial equilibrium points is presented in Fig. 4.7. As explained previously, these involve very large and opposite initial population imbalances for both components. In Fig. 4.7 we consider a case with initial conditions very close to the predicted equilibrium point using the standard two-mode, and described in Fig. 4.1, $z_a(0) = -0.78$, and $z_b(0) = 0.99$, with $f_a = 0.1$. Also in the same figure we consider a similar run but with $f_a = 0.9$. In both cases the NPSE and TDGPE predict a very similar dynamics. These simulations will be discussed again in Sec. 4.3.5 as they exhibit effects which clearly go beyond a two-mode approximation.

4.3.4 Small oscillations around $z_{a,b}^0$ and $\delta\phi_{a,b}^0 = \pi$

The trivial equilibrium point is not stable in the considered conditions as seen in Fig. 4.1. The non-trivial one, however, is only attainable if extremely imbalanced configurations for both components are considered. This case would correspond essentially to having both components in a π mode state, which in our conditions only exists for $z \sim 1$ as can

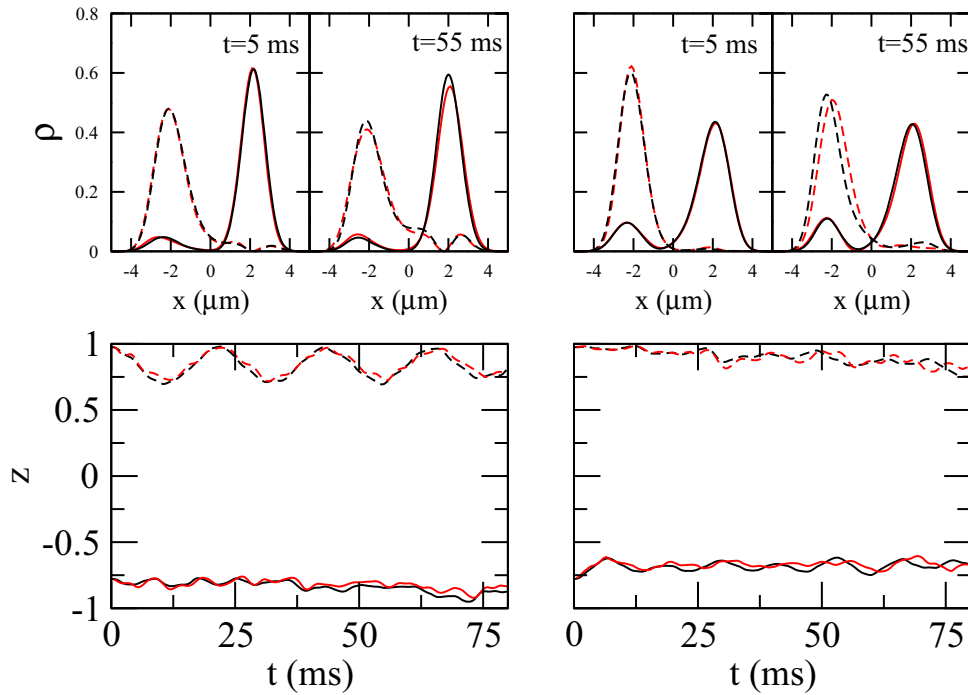


Figure 4.7: Two simulations with the same initial conditions, $z_a(0) = -0.78$, $z_b(0) = 0.99$, $\delta\phi_a = 0$ and $\delta\phi_b = \pi$, but with different composition. The case on the left has $f_a = 0.1$ while the case on the right $f_a = 0.9$. The red lines are obtained by means of a full TDGPE while the black lines are the NPSE results. Solid and dashed lines correspond to the a and b components, respectively.

be seen in the blue spots in panel (c) of Fig. 3.7. In Fig. 4.8 we present two simulations with different initial conditions. First, we consider a simulation with $z_a(0) = 0.4$ and $z_b(0) = -0.2$, with $f_a = 0.9$. The behavior is understood in simple terms, the most populated component remains self-trapped while the other component is forced by the other one. The phase evolves unboundedly. The figure again contains TDGPE and NPSE simulations.

The second simulation (right panels) is closer to a non-trivial equilibrium point, we consider $z_a(0) = 0.9$ and $z_b(0) = 0.85$ with $f_a = 0.9$. In this case, both components remain self-trapped, the phase difference is unbounded, but we do not get the expected behavior of two π modes because the initial imbalances are not close enough to $z^0 \sim 1$.

4.3.5 Effects beyond two-mode

Most of the dynamics described in the previous sections can to a large extent be understood within the two-mode models developed in Sec. 4.2. There are, however, a number of situations where the two-mode fails. Some are a direct consequence of having two components evolving in the same double-well potential, others are due to having initial configurations, mostly with large initial imbalances, producing situations where the atom-atom interaction energy per atom is comparable to the gap between the first excited state and the second/third excited states.

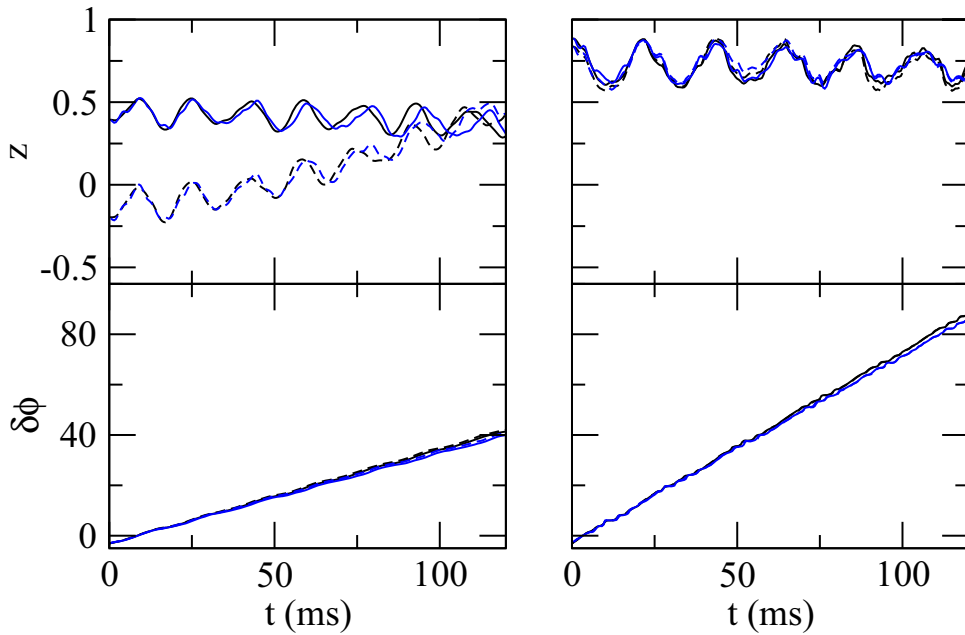


Figure 4.8: Two simulations corresponding to (left) $z_a(0) = 0.4$, $z_b(0) = -0.2$, $\delta\phi_a(0) = \pi$, $\delta\phi_b(0) = \pi$ and $f_a = 0.9$, and (right) $z_a(0) = 0.9$, $z_b(0) = 0.85$, $\delta\phi_a(0) = \pi$, $\delta\phi_b(0) = \pi$ and $f_a = 0.9$. The blue lines are obtained by means of a full TDGPE while the black lines are the NPSE results. Solid and dashed lines correspond to the a and b components, respectively.

We can distinguish two different cases: (a) involving excitations along the coordinate which contains the barrier, (b) involving excitations of the transverse coordinates.

An example of (a) is seen in Fig. 4.7. There, as clearly seen in the density profiles along the x direction, the two-mode approximation is clearly not valid. The simplest way of seeing this is by noting the zero in the density of one of the components at $x \sim 2\mu$ m. This effect beyond two-mode is well taken care of by the NPSE which reproduces the density profile quite well during most of the time evolution considered in the simulation. Thus, the excitations of higher modes along the direction which has not been integrated out in the 1D reduction do not pose a great difficulty to the 1D reductions.

The second type, (b), of effects beyond two-mode involve excitations of the transverse components. These effects are present in any binary mixture calculation whenever the intra- and inter-species interactions are not equal. To enhance this effect, and also to explore the interesting symmetry breaking phenomena described in Ref. [122], we consider a case with $g_{aa} = g_{bb}$, but with $g_{ab} = g_{ba} = 2.3g_{aa}$. Therefore, now the inter-species interaction strength is larger than the intra-species one. The two-mode prediction for this case, S2M, which was analyzed in Ref. [122] shows a large symmetry breaking pattern during the time evolution of the system. In Fig. 4.9 we consider a full TDGPE simulation of a representative example with $z_a(0) = -0.2$, $z_b(0) = 0.1$, $\delta\phi_a(0) = \delta\phi_b(0) = 0$, and $f_a = 0.7$.

The qualitative prediction of the I2M also shows the symmetry breaking, and the two components do separate from each other and mostly concentrate on one of the wells as time evolves. But, as it can be seen in the 3D depictions of $\rho(x, y; t)$ at three different

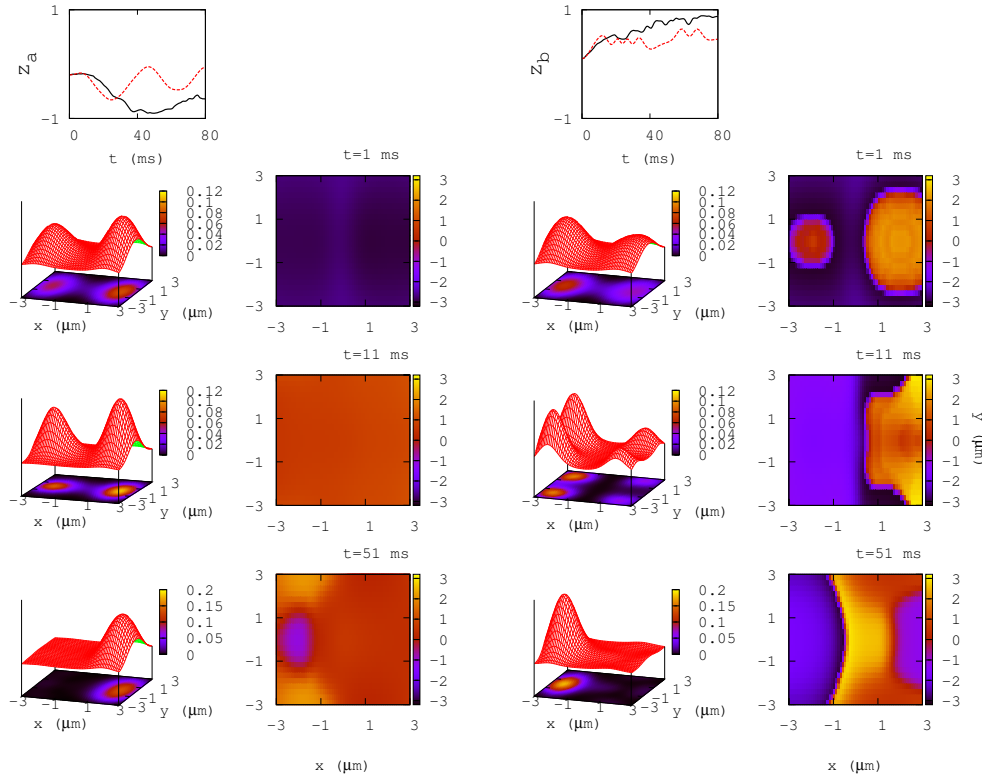


Figure 4.9: Full TDGPE calculations of the dynamics of a binary mixture with $z_a(0) = -0.2$, $z_b(0) = 0.1$, $\delta\phi_a(0) = 0$, $\delta\phi_b(0) = 0$, $f_a = 0.7$ and $f_b = 0.3$. As explained in the text in this case, $g_{aa} = g_{bb}$ and $g_{ab} = 2.3g_{aa}$. The upper two plots depict $z_a(t)$ (left) and $z_b(t)$ (right). Then each row contains from left to right: 3D depictions complemented by contour plots of $\rho_a(x, y; t)$, a contour plot of the averaged phase $\phi_a(x, y; t)$, 3D depictions complemented by contour plots of $\rho_b(x, y; t)$, and a contour plot of the averaged phase $\phi_b(x, y; t)$. Each row corresponds to a different time, 1 ms (upper), 11 ms (middle) and 51 ms (lower), respectively. In all cases, solid black lines are computed with TDGPE and dashed red ones with I2M.

times, the evolution of the system departs almost from the beginning from the two-mode. At $t = 1$ ms we have the density distributions of each component corresponding to a small initial imbalance. Then at $t = 11$ ms, we can already see that the most populated component is expelling the other one from the minima of the potential. This fact can be appreciated as a four peaked distribution, $\rho_b(x, y; t)$. After that, each of the components start to accumulate on their original sides following qualitatively the prediction of the I2M and thus presenting the symmetry breaking pattern discussed in Ref. [122]. The two-mode approximation is in this case broken for a short period of time, when the first modes along the transverse directions are excited due to the large inter-species interaction.

Chapter 5

Josephson effect beyond mean field

In the previous chapters, we have studied the Josephson effect within a mean-field approach, using the Gross-Pitaevskii equation. The main assumption in the derivation of this equation, see chapter 2, was to construct the total N -body state as a direct product of single-particle states. This restricts the kind of many-body correlations that can be described, and quantum effects such as squeezing or entanglement cannot be studied. Therefore, in order to investigate more involved and interesting many-body correlations one needs to consider a different framework.

In a BJJ, some features of quantum fluctuations are well described by the two-site Bose-Hubbard model (BH) [74], which is the quantization of a two-mode approximation. First studies of BJJ using this model were done by G. J. Milburn et al. [83] and J. Javanainen et al. [84]. Later works, paid special attention to the transition between the Josephson and self-trapped regimes [128], and to the ground state properties when atom-atom interactions are attractive [129, 85, 130]. In the latter case, the ground state presents an interesting structure, as it can be described as the superposition of two different states, each one localized in a different mode [131]. For an external BJJ, this corresponds to having most of the particles in the left well and having most of the particles in the right well at the same time. These states are called cat-like states, in analogy with the Schrödinger's cat¹. As we will see, this cat-like structure is a signature of a highly correlated quantum state, in the sense that it is very far away from the mean-field description.

The chapter is organized as follows. In section 5.1 we recall the Hamiltonian describing N weakly interacting atoms in second quantization. In section 5.2 we write the Bose-Hubbard Hamiltonian and discuss the main parameters that are used to describe a single-component BJJ. In section 5.3 we study the static properties of such system focusing on its ground state, which shows a very rich phenomenology when the interaction or the number of particles change. In order to obtain useful insight into the physical nature of the ground state, in section 5.3.1 we propose a variational wave function [94].

The dynamics of a scalar BJJ are briefly reviewed in section 5.4, where we also compare the results with the predictions of the mean-field S2M model described in chapter 3.

¹The Schrödinger's cat is a thought experiment in which the cat may be both alive and dead, depending on an earlier random event. The state of the cat is expressed as the superposition of a state in which the cat is alive, and one in which the cat is dead: $|\text{cat}\rangle = \frac{1}{\sqrt{2}}(|\text{alive}\rangle + |\text{dead}\rangle)$. In our case, a perfect cat state corresponds to a quantum state which is a superposition of having all the particles in the left well, at the same time as having all the particles in the right one.

Finally, an approximation to the BH model is also reviewed in section 5.5 [132, 130]. We show that this approximation, although its semi-classical nature, is able to capture the cat-like structure of the ground state.

5.1 Second quantization

In second quantization, the field operators $\hat{\Psi}^\dagger(\mathbf{r})$ and $\hat{\Psi}(\mathbf{r})$ create and destroy a particle at position \mathbf{r} , respectively, and obey bosonic commutation rules [6]

$$[\hat{\Psi}(\mathbf{r}), \hat{\Psi}^\dagger(\mathbf{r}')] = \delta(\mathbf{r} - \mathbf{r}'); \quad [\hat{\Psi}(\mathbf{r}), \hat{\Psi}(\mathbf{r}')] = [\hat{\Psi}^\dagger(\mathbf{r}), \hat{\Psi}^\dagger(\mathbf{r}')] = 0. \quad (5.1)$$

They can be expressed as linear combinations of creation and annihilation operators which \mathbf{r} -representation is given by the single-particle wave function $\varphi_\alpha(\mathbf{r}) = \langle \mathbf{r} | \alpha \rangle$:

$$\hat{\Psi}(\mathbf{r}) = \sum_\alpha \varphi_\alpha(\mathbf{r}) \hat{a}_\alpha; \quad \hat{\Psi}^\dagger(\mathbf{r}) = \sum_\alpha \varphi_\alpha^*(\mathbf{r}) \hat{a}_\alpha^\dagger, \quad (5.2)$$

where $\{|\alpha\rangle\}$ is an orthonormal basis of single-particle states. The operators \hat{a}, \hat{a}^\dagger obey the following commutation rules $[\hat{a}_\alpha, \hat{a}_\beta^\dagger] = \delta_{\alpha\beta}$ and $[\hat{a}_\alpha, \hat{a}_\beta] = [\hat{a}_\alpha^\dagger, \hat{a}_\beta^\dagger] = 0$.

The time evolution of these field operators is given by the Heisenberg equation:

$$i\hbar \frac{\partial}{\partial t} \hat{\Psi}(\mathbf{r}, t) = [\hat{\Psi}(\mathbf{r}, t), \hat{H}], \quad (5.3)$$

where \hat{H} is the N -particle Hamiltonian. We consider a dilute system of N bosons with short-range atom-atom interactions, in such a way that interactions can be assumed to be in s-wave and can be represented by a contact interaction. Under these assumptions, the Hamiltonian reads [6]:

$$\hat{H} = \int d\mathbf{r} \left[-\frac{\hbar^2}{2M} \hat{\Psi}^\dagger(\mathbf{r}) \nabla^2 \hat{\Psi}(\mathbf{r}) + \hat{\Psi}^\dagger(\mathbf{r}) V_{\text{ext}}(\mathbf{r}) \hat{\Psi}(\mathbf{r}) + \frac{g_{3D}}{2} \hat{\Psi}^\dagger(\mathbf{r}) \hat{\Psi}^\dagger(\mathbf{r}) \hat{\Psi}(\mathbf{r}) \hat{\Psi}(\mathbf{r}) \right]. \quad (5.4)$$

Using the bosonic commutation rules (5.1), the Heisenberg equation (5.3) becomes

$$i\hbar \frac{\partial \hat{\Psi}(\mathbf{r}, t)}{\partial t} = \left[-\frac{\hbar^2}{2M} + V_{\text{ext}}(\mathbf{r}) + g_{3D} \hat{\Psi}^\dagger(\mathbf{r}, t) \hat{\Psi}(\mathbf{r}, t) \right] \hat{\Psi}(\mathbf{r}, t). \quad (5.5)$$

This equation coincides with the TDGPE (2.15) when the field operator $\hat{\Psi}(\mathbf{r}, t)$ is replaced by the wave function $\Psi(\mathbf{r}, t)$, that describes the condensate in the mean-field approach.

Moreover, when the number of particles in the condensate is of the order of the total number of particles, $N_0 \sim N$, one can decompose the field operator as

$$\hat{\Psi}(\mathbf{r}, t) = \Psi(\mathbf{r}, t) + \hat{\Psi}'(\mathbf{r}, t), \quad (5.6)$$

where $\Psi(\mathbf{r}, t) = \langle \hat{\Psi}(\mathbf{r}, t) \rangle$ is identified with the condensate wave function, and $\hat{\Psi}'(\mathbf{r}, t)$ describes the fluctuations around the condensate. This decomposition is known as Bogoliubov prescription [133]. At zeroth order, i.e. assuming that the non-condensed fraction is negligible, the field operator is described by the complex wave function $\Psi(\mathbf{r}, t)$, and we recover the TDGPE, Eq. (2.15).

5.2 Two-site Bose-Hubbard Hamiltonian

In this section, we present the tools to describe a system of N bosons populating only two single-particle states. For simplicity we focus in an external BJJ, consisting on N particles confined in a double-well potential². Like in the previous chapters, we assume that the condensates in each well are weakly linked, and that a two-mode approximation is justified. Therefore, the field operator can be written as

$$\hat{\Psi}(\mathbf{r}) = \hat{\Psi}_L(\mathbf{r}) + \hat{\Psi}_R(\mathbf{r}) = \hat{a}_L\varphi_L(\mathbf{r}) + \hat{a}_R\varphi_R(\mathbf{r}), \quad (5.7)$$

where $\hat{a}_{L(R)}$ are bosonic operators that annihilate a particle in the mode $\varphi_{L(R)}$, which is a mode localized in $L(R)$ well. They follow the commutation rules $[\hat{a}_i, \hat{a}_j^\dagger] = \delta_{i,j}$ and $[\hat{a}_i, \hat{a}_j] = [\hat{a}_i^\dagger, \hat{a}_j^\dagger] = 0$.

With this approximation, and neglecting crossed terms of $\varphi_{L,R}(\mathbf{r})$ of order larger than 2, the Hamiltonian (5.4) becomes the two-site Bose-Hubbard (BH) Hamiltonian:

$$\hat{H} = E_L^0 \hat{N}_L + E_R^0 \hat{N}_R - J(\hat{a}_L^\dagger \hat{a}_R + \hat{a}_L \hat{a}_R^\dagger) + \sum_{i=L,R} \frac{U_i}{2} \hat{N}_i(\hat{N}_i - 1), \quad (5.8)$$

where $\hat{N}_i = \hat{a}_i^\dagger \hat{a}_i$ is the number of particles operator in site i , and

$$\begin{aligned} E_i^0 &= \int d\mathbf{r} \left[\frac{\hbar}{2M} |\nabla \varphi_i(\mathbf{r})|^2 + \varphi_i^2(\mathbf{r}) V_{\text{ext}}(\mathbf{r}) \right], \\ J &= - \int d\mathbf{r} \left[\frac{\hbar}{2M} \nabla \varphi_L(\mathbf{r}) \cdot \nabla \varphi_R(\mathbf{r}) + \varphi_L(\mathbf{r}) V_{\text{ext}}(\mathbf{r}) \varphi_R(\mathbf{r}) \right], \\ U_i &= g_{3D} \int d\mathbf{r} \varphi_i^4(\mathbf{r}). \end{aligned} \quad (5.9)$$

Notice that these parameters are analogous to the ones obtained with the mean-field description, Eqs. (3.6), (3.8) and (3.7).

We focus in quasi-symmetric double-well potentials, $U_L = U_R = U$ and $E_L^0 = E_R^0 = E^0$. Measuring the energy with respect to $E^0 N$, where N is the total number of particles, we get

$$\hat{H} = -J(\hat{a}_L^\dagger \hat{a}_R + \hat{a}_L \hat{a}_R^\dagger) + \frac{U}{2} [\hat{N}_L(\hat{N}_L - 1) + \hat{N}_R(\hat{N}_R - 1)] - \varepsilon(\hat{a}_L^\dagger \hat{a}_L - \hat{a}_R^\dagger \hat{a}_R), \quad (5.10)$$

where we have included a small bias $\varepsilon \ll J$, in order to break the degeneracy between the left and right modes (positive values of ε promote the left site). $U > 0$ ($U < 0$) describe repulsive (attractive) interactions.

A natural basis to study this system is the Fock basis, which is characterized by the number of atoms in each site $|N_L, N_R\rangle$ and which spans an $N + 1$ dimensional space

$$\{ |N, 0\rangle, |N - 1, 1\rangle, \dots, |0, N\rangle \}. \quad (5.11)$$

²The case of an internal BJJ is analogous

The action of the creation and annihilation operators on these states is defined as

$$\begin{aligned}\hat{a}_L^\dagger|N_L, N_R\rangle &= \sqrt{N_L+1}|N_L+1, N_R\rangle \\ \hat{a}_L|N_L, N_R\rangle &= \sqrt{N_L}|N_L-1, N_R\rangle,\end{aligned}\quad (5.12)$$

and the corresponding definitions for \hat{a}_R^\dagger and \hat{a}_R . Therefore, the Fock states can be written as

$$|N_L, N_R\rangle = \frac{1}{\sqrt{N_L!N_R!}}(a_L^\dagger)^{N_L}(a_R^\dagger)^{N_R}|0, 0\rangle. \quad (5.13)$$

On the other hand, a general N-body state can be expressed in terms of the basis $\{|N_L, N_R\rangle\}$ as

$$|\Psi\rangle = \sum_{k=0}^N c_k |k, N-k\rangle, \quad (5.14)$$

which has an average number of atoms in each mode of $N_i = \langle\Psi|a_i^\dagger a_i|\Psi\rangle$, with $i = L, R$. A good characterization of the state $|\Psi\rangle$ is given by the expectation value of the population imbalance operator, $\hat{Z} = (\hat{N}_L - \hat{N}_R)/N$, and its dispersion:

$$z = \langle\Psi|\hat{Z}|\Psi\rangle \quad ; \quad \sigma_z = \sqrt{\langle\Psi|\hat{Z}^2|\Psi\rangle - \langle\Psi|\hat{Z}|\Psi\rangle^2}. \quad (5.15)$$

Moreover, the one-body density matrix $\rho_{ij} = \langle\Psi|\hat{\rho}_{ij}|\Psi\rangle$, with $\hat{\rho}_{ij} = a_i^\dagger a_j$ and $i, j = L, R$, characterizes the degree of condensation of the system through its eigenvalues: the two normalized eigenvalues n_1 and n_2 fulfill $n_1 + n_2 = 1$, and each of them represents the occupation of the single-particle state $|n_i\rangle$, eigenstate of ρ . When the eigenvalues of the density matrix are strictly $n_1 = 1$ and $n_2 = 0$, the system is fully condensed in $|n_1\rangle$, and it is possible to express $|\Psi\rangle$ by means of a mean-field state constructed as $|\Psi\rangle_N = |n_1\rangle \otimes \cdots \otimes |n_1\rangle \equiv |n_1\rangle^{\otimes N}$. On the other hand, when neither n_1 nor n_2 are zero, the system is not condensed and it's said to be fragmented.

5.3 Static properties

In this section we study the static properties of the system, focusing on the physical nature of the ground state. As we will see, for some parameter values, the ground state is quasi-degenerate with the first excited state. We start by considering the lowest energy levels of the system as a function of $\Lambda \equiv NU/(2J)$. The usual way to proceed [131, 134, 85, 129, 132] is to calculate the matrix elements of the BH Hamiltonian in the Fock basis, and diagonalize it to find the eigenvalues and eigenstates. It is then straightforward to calculate also the population imbalance and the degree of condensation of each state. We fix $J = 1$, which is equivalent to measure the energy in units of J . We also introduce a small bias $\varepsilon/J = 10^{-8}$, and consider attractive interactions $U < 0$.

In Fig. 5.1, we report the energies of the first three excited states with respect to the ground state of the system as a function of Λ for two different numbers of particles, $N = 50$ and $N = 500$, obtained by direct diagonalization of the two-site BH Hamiltonian [131]. For vanishing atom-atom interactions, $\Lambda = 0$, the energy gap for consecutive states is constant (except for the bias) along the spectrum, and the gap is independent of the

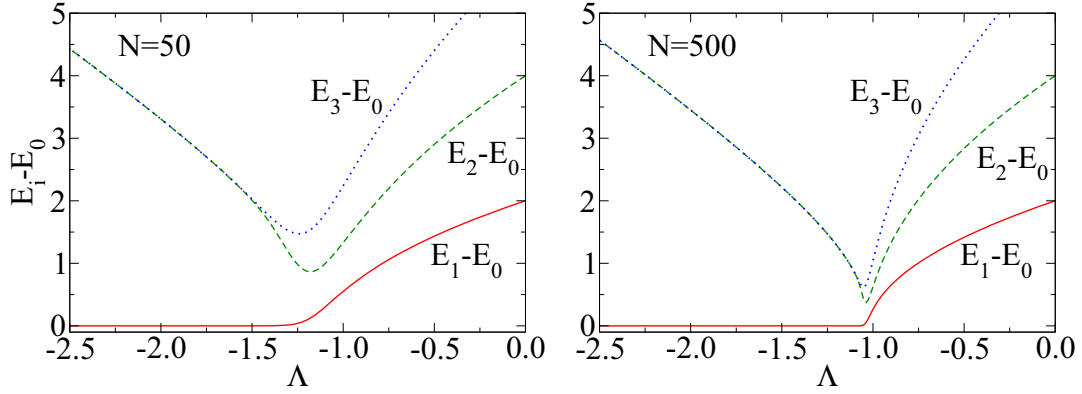


Figure 5.1: Energies of the lowest energy levels with respect to the ground state energy E_0 , as a function of Λ , for $N = 50$ (left panel) and $N = 500$ (right panel). All energies are measured in units of J .

number of particles. As $|\Lambda|$ increases the eigenvalues start to merge in pairs (the ground with the first excited, the second with the third, etc.) but due to both ε and J , they do not reach complete degeneracy. Moreover, the convergence of the merging process depends on the number of particles: for higher N it occurs at smaller values of $|\Lambda|$ reaching the value $|\Lambda| = 1$, when the number of particles tends to infinity. Recall that with the S2M, see Sec. 3.2.1 the relevant parameter was $\Lambda^{\text{S2M}} = NU/2K$, and the critical value for which self-trapped orbits appeared was $|\Lambda_c^{\text{S2M}}| = 1$, in agreement with the value found here.

In Fig. 5.2 we plot the spectral decomposition of the ground and first excited states in the Fock space for different values of Λ , and $N = 50$. The plotted values $|c_k|^2$ give the probability that the state has k particles in the left well and $N - k$ particles in the right one. Notice that if the spectral decomposition of the state is peaked at high values of k , it means that for this state most of the atoms are located on the left side of the double well. For weak interactions, $|\Lambda| < 1.3$, the spectral decomposition of the ground and the first excited states are clearly different, (as were also the energies in Fig. 5.1). For stronger interactions, $-1.6 \leq \Lambda \leq -1.3$, the two states become very close in energy and their spectral decompositions $|c_k|^2$ are very similar. However, one should notice that the ground state is symmetric, $c_{N/2+k} = c_{N/2-k}$, and the first excited one is antisymmetric, $c_{N/2+k} = -c_{N/2-k}$. This configuration, in which particles are in a superposition of two states, each of which localized in a different well, is known as cat-like state³. This is a strongly correlated state in the sense that can not be described by a mean-field description, i.e. the state is not Bose condensed.

Finally, for $|\Lambda| > 1.6$, the two states become again clearly different: the ground state is peaked at a high value of k , i.e. with a large amount of atoms in the left well, while the first excited has its peak at a low value of k , with many atoms in the right well. Note that the energies of these states are very close to each other, and that as we have said before, ε is set to make the ground state to localize in the left well.

A useful characterization of the ground state is provided by the population imbalance

³Strictly speaking, the purest cat-state would correspond to the state $1/\sqrt{2}(|N, 0\rangle + |0, N\rangle)$. The states we refer to as cat-like states are sometimes called kitten states with a certain degree of 'catness' [135].

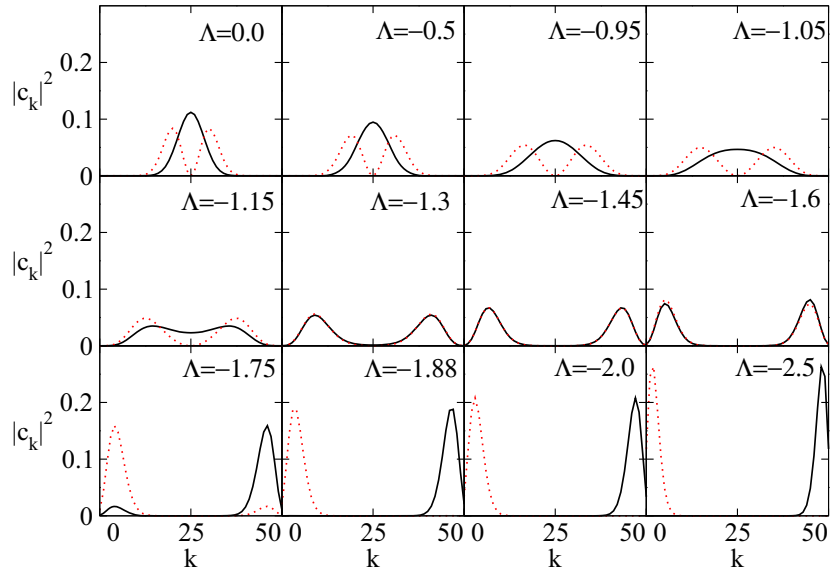


Figure 5.2: Spectral decomposition ($|c_k|^2$) in the Fock space of the ground (black solid line) and first excited (red dotted line) states for different values of Λ , with $N = 50$. To help in the reading of the figure, instead of plotting the discretized values $|c_k|^2$ we have generated a smooth curve by joining the different points.

z . As shown in Fig. 5.3 (a), it remains zero up to a certain value of $|\Lambda|$ (~ 1.65 for $N = 50$), and approaches 1 as $|\Lambda|$ increases further. The figure also shows σ_z , which starts from small values associated to a relatively narrow binomial distribution and increases in the range where the strongly cat-like state is present. Finally decreases abruptly when $|\Lambda|$ increases further and the ground state populates massively the L state. Thus $z \rightarrow 1$ and $\sigma_z \rightarrow 0$ for $|\Lambda| \rightarrow \infty$.

The degree of condensation of the ground state $|\Psi_{\text{gs}}\rangle$ is determined by the eigenvalues n_1 and n_2 of the one-body density matrix, which are plotted in Fig. 5.2 (b). These condensate fractions measure the macroscopic occupations of the single-particle states $|n_1\rangle$ and $|n_2\rangle$, eigenfunctions of the one-body density matrix, $\langle\Psi_{\text{gs}}|\hat{\rho}|\Psi_{\text{gs}}\rangle$. The regions where these values are not close to 1 and 0, signal the occurrence of fragmentation of the ground state and the impossibility to describe the system by means of a mean-field state. In the region, $-1 < \Lambda < 0$, n_1 is rather close to 1 ($n_1 \sim 0.99$), and the macroscopically occupied state is given by $|n_1\rangle = (|L\rangle + |R\rangle)/\sqrt{2}$, with $|L(R)\rangle \equiv a_{L(R)}^\dagger|0\rangle$. However, this slight fragmentation produces noticeable differences in the spectral decomposition of the mean-field state build with the state $|n_1\rangle$ and the exact ground state [94]. The fragmentation is particularly important for $-1.25 > \Lambda > -1.75$, which is roughly the same interval where the cat-like structure takes place. However, the macro-occupied state $|n_1\rangle$ remains equal to the one previously discussed. The correlations beyond mean-field affect the degree of condensation, but not the single state that is mainly occupied. This is because the ground state remains almost symmetric (except for the bias) in the Fock space (see Fig. 5.2), i.e. with z almost zero. This is reflected in the symmetric character of the one-body density matrix, which in turn implies that $|n_1\rangle$ is the normalized symmetric combination of $|L\rangle$ and $|R\rangle$. For further increasing $|\Lambda|$, the system becomes again condensed: $n_1 \rightarrow 1$ and

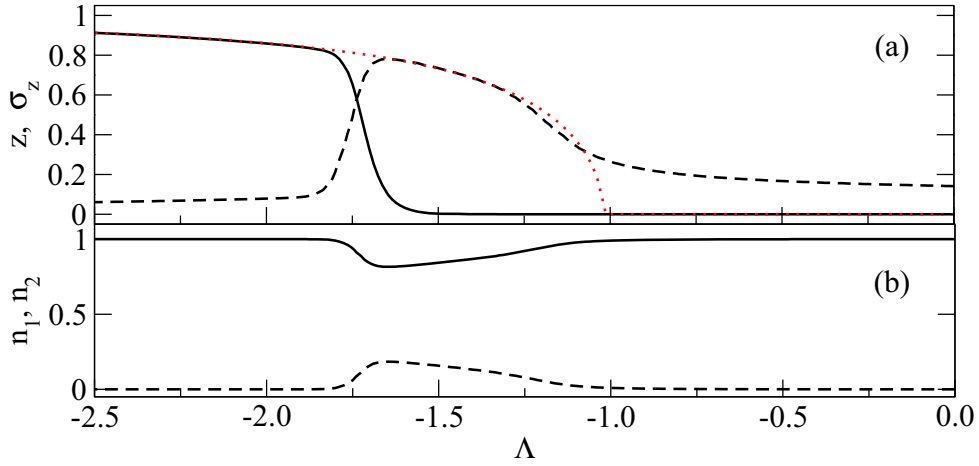


Figure 5.3: (a) Population imbalance z (black solid line) and its dispersion σ_z (black dashed line), see Eqs. (5.15), of the exact ground state as a function of Λ . The semi-classical prediction of the imbalance (red dot-dashed), see Eq. (5.25), is also plotted [85, 130]. (b) Solid and dotted lines depict the condensed fractions n_1 and n_2 of the one-body density matrix of the exact ground state as a function of Λ . In all cases $N = 50$.

due to the bias $|n_1\rangle \rightarrow |L\rangle$.

On the other hand, in chapter 3 we also discussed the stable solutions of the system of equations (5.25), see Table 3.1. For attractive interactions $U < 0$, the ground state had $z = 0$ when $\Lambda > -1$ and $z = \pm\sqrt{1 - 1/\Lambda^2}$ when $\Lambda < -1$. Therefore, in the semiclassical approximation, the population imbalance of the ground state has a bifurcation at $\Lambda = 1$, see 3.2.3.

In Fig. 5.3 we also plot the semi-classical predictions of the population imbalance, with only the upper branch $z > 0$. We can see how the bifurcation predicted with the semi-classical two-mode equations is related to highly correlated states in the BH picture. Note that in the region $\Lambda \simeq -1$ the dispersion of the population imbalance increases, and the state has a cat-like structure.

5.3.1 Variational ansatz for the ground state

Following a similar procedure as in Ref. [131] we propose a new variational ansatz to describe the ground state [94], which will be valid for all values of Λ . This state is a combination of two different mean-field states, that include at the same time the possibility of a mean-field state and the existence of a cat-state:

$$|\Psi_{\text{var}}\rangle = \frac{A}{\sqrt{N!}} [\alpha a_L^\dagger + \beta a_R^\dagger]^N |0\rangle + \frac{B}{\sqrt{N!}} [\beta a_L^\dagger + \alpha a_R^\dagger]^N |0\rangle. \quad (5.16)$$

The variational parameters α , β , A and B are taken real. Note that the two mean-field states are not necessarily orthogonal and therefore the normalization conditions are imposed in the following way:

$$\alpha^2 + \beta^2 = 1, \quad A^2 + B^2 + 2(2\alpha\beta)^N AB = 1. \quad (5.17)$$

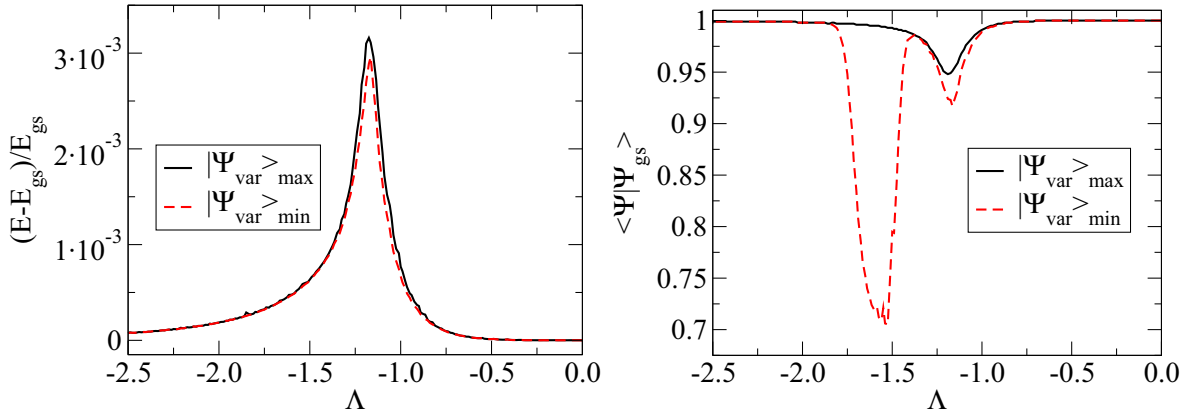


Figure 5.4: (left) Relative difference with respect to the exact ground state energy of the expectation value of the Hamiltonian with $|\Psi_{\text{var}}\rangle_{\text{min}}$ (red dashed line) and $|\Psi_{\text{var}}\rangle_{\text{max}}$, (black solid line). (right) Overlap with the exact ground state of the system as a function of Λ for $|\Psi_{\text{var}}\rangle_{\text{min}}$ (red dashed line) and $|\Psi_{\text{var}}\rangle_{\text{max}}$ (black solid line).

The expectation value of the Hamiltonian (5.10) with this ansatz, and $\varepsilon = 0$, is given by

$$\begin{aligned} \frac{E}{JN} &= \left[-2\alpha\beta + \frac{N-1}{N} \frac{\Lambda}{4} (1 - 4\alpha^2\beta^2) + \frac{1}{2\alpha\beta} \right] (A^2 + B^2) \\ &+ \frac{\varepsilon}{J} (\beta^2 - \alpha^2) (A^2 - B^2) + \frac{N-1}{N} \frac{\Lambda}{4} - \frac{1}{2\alpha\beta}. \end{aligned} \quad (5.18)$$

To determine the parameters of the variational state we follow two different criteria. The first consists in performing a numerical minimization of the expectation value of the energy, Eq. (5.18). The many-body state thus computed is named $|\Psi_{\text{var}}\rangle_{\text{min}}$. In the second procedure, which can be pursued only when we already have a numerical solution of the exact ground state, we determine the coefficients by maximizing the overlap of the variational state with the exact ground state, giving the state $|\Psi_{\text{var}}\rangle_{\text{max}}$.

The first procedure, which does not require the previous numerical solution of the ground state, produces by construction the closest energy to the exact ground state energy within the form of Eq. (5.16). As will be discussed in the following, the second criteria although requiring the previous numerical solution of the ground state, produces in all cases an energy almost as good as the variational one, while also improving the overlap with the numerically computed ground state. Thus, for certain applications where an analytical rendition of the state is preferable, our variational proposal⁴ should be very useful to clarify the physical structure of the ground state.

For $\Lambda = 0$, we obtain $\alpha = \beta = 1/\sqrt{2}$ and $A = B = 1/2$ for both conditions: minimum energy and maximum overlap. The state is the exact solution and coincides with the ground state. Thus, it has the exact energy and an overlap of 1 with the ground state, see Fig. 5.4. In the region ($|\Lambda| < 1$) the differences between the observables corresponding to these two variational states associated with the maximum overlap or with the minimum energy criteria are rather small. The state that minimizes the energy provides slightly better energies, however this difference is not significant in Fig. 5.4 (left), while

⁴In the sense that $\langle \Psi_{\text{var}} | H | \Psi_{\text{var}} \rangle_{\text{max}}$ provides also an upper bound to the ground state energy

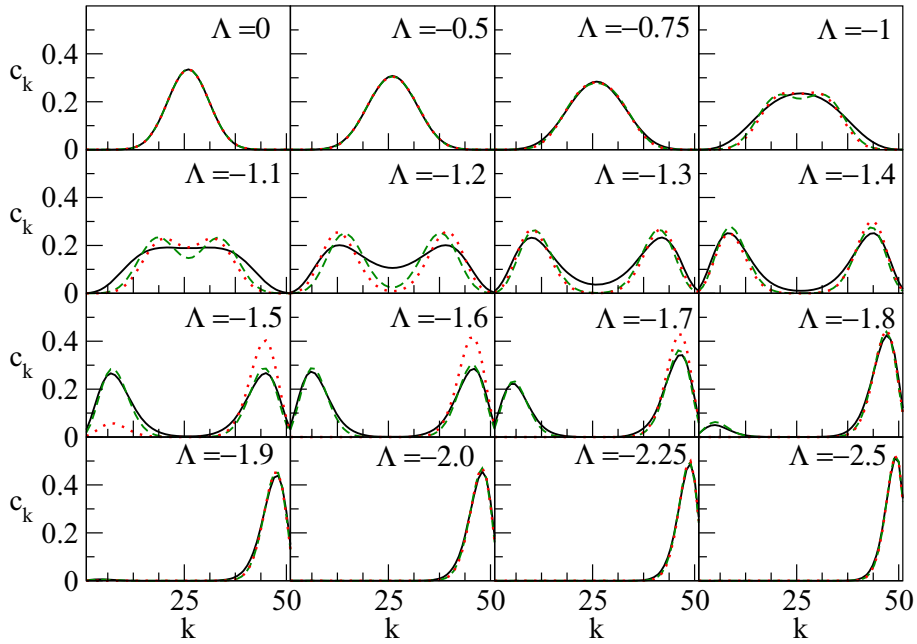


Figure 5.5: Spectral decomposition of the exact ground state (black solid line), and the states obtained using the ansatz defined in Eq. (5.16) when its overlap with the exact ground state is maximized (green dashed line) or when its energy is minimized (red dotted line).

the state that maximizes the overlap provides overlaps with the ground state closer to unity. However these differences are also not appreciable in Fig. 5.4 (right). The Fock decomposition of these two variational states $|\Psi_{\text{var}}\rangle_{\text{min}}$ and $|\Psi_{\text{var}}\rangle_{\text{max}}$ compared with the one of the ground state are shown in Fig. 5.5 for different values of Λ and $N = 50$.

Interestingly, the proposed state captures well the correlations beyond mean-field existing in the ground state of the problem before the classical bifurcation. These correlations, see Fig. 5.2 (a), produce small effects on the condensate fractions but become clearly visible when looking at the spectral decomposition of the ground state.

Once we cross the classical bifurcation, $\Lambda < -1$, the spectral decomposition of the ground state broadens and at $\Lambda \sim -1.1$ becomes quickly two-peaked. This region where the ground state has two maxima is what we refer to as the cat-state region. Unlike in the region before the bifurcation, here the two criteria used to compute the variational parameters provide fairly different results in some cases. The computed energy of the state is very close with both criteria, but its overlap with the ground state is different depending on the criteria used, see Fig. 5.4. This is a consequence of the clear differences seen in the spectral decomposition, Fig. 5.5. The variational solution obtained by minimizing the energy is seen to depart from the exact solution in the region $-1.75 < \Lambda < -1.5$, predicting an earlier transition to the 'self-trapped' domain.

To complete the characterization of the proposed states we also study the fragmentation of the ground state of the system. To this end, we calculate the one-body density matrix and look at its larger eigenvalue. If the largest eigenvalue (n_1) is significantly

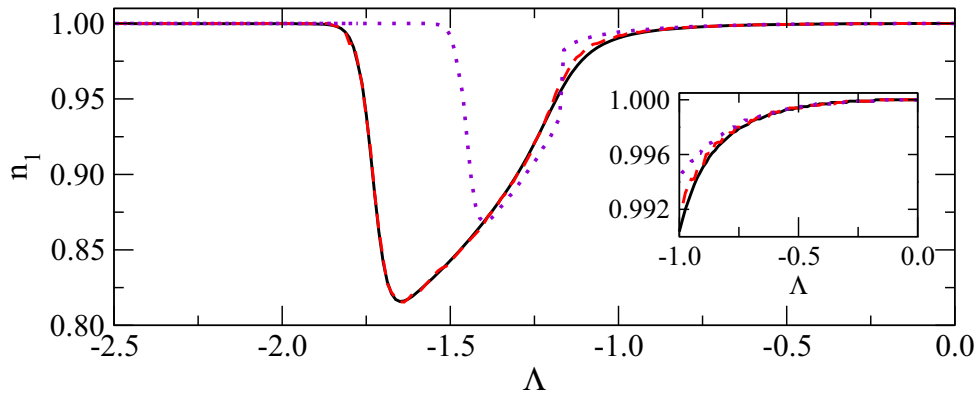


Figure 5.6: Largest eigenvalue of the one body density matrix, n_1 , as a function of Λ for the different many-body states discussed in the text: exact calculation (black solid line), $|\Psi_{\text{var}}\rangle_{\text{max}}$ (red dashed line), $|\Psi_{\text{var}}\rangle_{\text{min}}$ (violet dotted line). The inset shows the region before the bifurcation.

smaller than unity, we have fragmentation and the system is not condensed in one single state. It also indicates the impossibility to describe the system by a mean-field state and therefore reveals the existence of correlations beyond mean-field. The largest eigenvalue of the one-body density matrix associated to the exact ground state and the two variational states is reported in Fig. 5.6 for different values of $|\Lambda|$. The exact ground state gives rise to an n_1 very close to unity, in the region $|\Lambda| < 1$. However, the eigenvalue is strictly one only for $\Lambda = 0$, and is actually a smooth decreasing function of $|\Lambda|$. It decreases faster in the cat-like region reaching a minimum ($n_1 \sim 0.8$) (maximal fragmentation) around $\Lambda = -1.6$. For larger values of $|\Lambda|$ it grows again reaching the value 1 as the system condenses in the left well due to the bias.

The variational many-body states proposed $|\Psi_{\text{var}}\rangle_{\text{min}}$ and $|\Psi_{\text{var}}\rangle_{\text{max}}$ reproduce very well the exact n_1 in the region before the bifurcation, where the system is slightly fragmented, see the inset in Fig. 5.6. This small fragmentation, as discussed above, indicates the presence of some correlations beyond the mean-field already in this region. In the cat-state region, the $|\Psi_{\text{var}}\rangle_{\text{max}}$ also reproduces the exact n_1 .

5.4 Dynamical properties

An interesting feature of the Bose-Hubbard model is the possibility to easily study the dynamics of different observables. Here, we will describe the time-evolution of the population imbalance for an initial state that is fully condensed. We will take a state that consists in all the atoms in the left well, and study the degree of condensation as a function of time.

The time evolution of a state is defined by $|\Psi(t)\rangle = \hat{U} |\Psi(0)\rangle$, where \hat{U} is the time-evolution operator,

$$\hat{U} = e^{-\frac{i}{\hbar}\hat{H}t} = e^{-\frac{i}{\hbar}\hat{H}t} \sum_{k=0}^N |\varepsilon_k\rangle \langle \varepsilon_k| = \sum_{k=0}^N e^{-\frac{i}{\hbar}\varepsilon_k t} |\varepsilon_k\rangle \langle \varepsilon_k|, \quad (5.19)$$

where $|\varepsilon_k\rangle$ are the eigenstates of the BH Hamiltonian (5.8) with eigenenergy ε_k , and N is the total number of particles. The expectation value of an operator \hat{O} in the state $|\Psi(t)\rangle$ can be written as,

$$\begin{aligned} \langle \hat{O} \rangle_t &= \langle \Psi(t) | \hat{O} | \Psi(t) \rangle = \langle \Psi(0) | \hat{U}^\dagger \hat{O} \hat{U} | \Psi(0) \rangle \\ &= \sum_{k,m=0}^N e^{\frac{i}{\hbar}(\varepsilon_k - \varepsilon_m)t} \langle \Psi(0) | \varepsilon_k \rangle \langle \varepsilon_k | \hat{O} | \varepsilon_m \rangle \langle \varepsilon_m | \Psi(0) \rangle. \end{aligned} \quad (5.20)$$

On the other hand, we can write the eigenvectors of the Hamiltonian in terms of the Fock basis $\{|j\rangle\}$, as

$$|\varepsilon_k\rangle = \sum_{j=0}^N a_{kj} |j\rangle. \quad (5.21)$$

For an initial state that is taken to be a Fock state $|\Psi(0)\rangle = |I\rangle$, Eq. (5.20) becomes

$$\langle \hat{O} \rangle_t = \sum_{k,m=0}^N e^{\frac{i}{\hbar}(\varepsilon_k - \varepsilon_m)t} T(k, m), \quad (5.22)$$

where we have defined the time-independent matrix

$$T(k, m) = a_{Ik} \left(\sum_{j,n=0}^N a_{ik} a_{nm} \langle i | \hat{O} | n \rangle \right) a_{Im}. \quad (5.23)$$

We have focused in the time evolution of the population imbalance operator $\hat{Z} = (\hat{a}_L^\dagger \hat{a}_L - \hat{a}_R^\dagger \hat{a}_R)/N$, and we have calculated the evolution of the condensed fractions n_1 and n_2 by diagonalizing the one-body density matrix of the evolving state at each time step. In Fig. 5.7 we plot $z(t)$, $n_1(t)$ and $n_2(t)$ for an initial state with maximal imbalance $|N, 0\rangle$, in units of $t_R = 2\pi/\omega_R = \pi\hbar/J$, for different values of Λ and N . Note that as $\Lambda = NU/(2J)$, the runs with the same Λ correspond to weaker interactions when N increases. The time evolution of $|N, 0\rangle$ starts with $z = 1$, $n_1 = 1$ and $n_2 = 0$, as it can be expressed with a mean-field wave function: $|N, 0\rangle = |L\rangle^{\otimes N}$.

In the left panels, the interaction is weak, $\Lambda = -0.5$, and the evolution of the state is characterized by oscillations with a frequency close to ω_R . These oscillations, are more quickly damped for smaller number of particles. The condensed fractions, on the other hand, seem to evolve asymptotically to a fixed value close to 1/2, almost independent of the number of particles, indicating a fragmentation of the condensate.

For $\Lambda = -1.5$ the dynamics is more complicated than in the previous cases, specially for lower number of particles. The condensed fractions also evolve around a constant value of ~ 0.8 and ~ 0.2 , but not in a smooth way as for $\Lambda = -0.5$.

Finally, in the right panels, $\Lambda = -2.5$, we are in a self-trapped situation. The initial state is close to the ground state, which has become very asymmetric and therefore provides a $\langle z \rangle_t \neq 0$. Besides, as the initial state is of mean-field type and almost stationary, the condensed fractions stay rather constant and very close to 1 and 0.

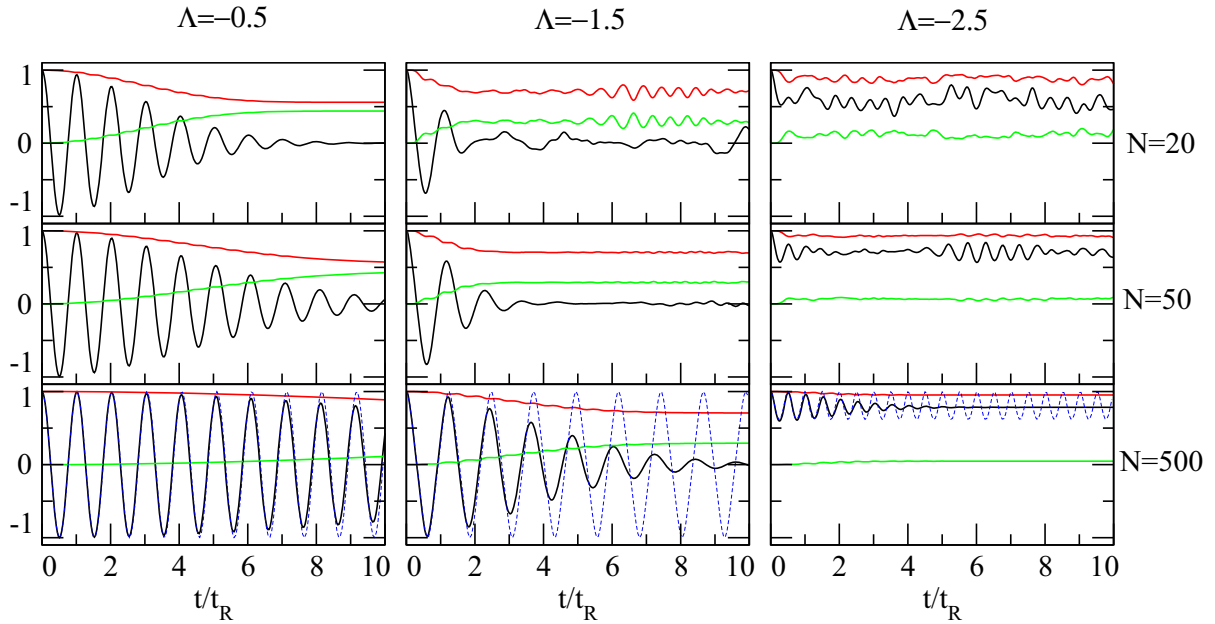


Figure 5.7: Evolution of the initial state $|N, 0\rangle$ as a function of time (in units of $t_{rabi} = 2\pi/\omega_R$) for different values of Λ and N . In all panels we plot the imbalance (solid black), and the condensed fractions n_1 (solid red) and n_2 (solid green). In the lower panels we also plot the semi-classical evolution of z , Eq. (5.25) (dashed blue).

It is also useful to explore the semi-classical limit of the Bose-Hubbard model, when $N \rightarrow \infty$. The standard procedure is to replace the operators \hat{a}_j and \hat{a}_j^\dagger by c-numbers $\sqrt{N_j}e^{i\phi_j}$ and $\sqrt{N_j}e^{-i\phi_j}$. The Hamiltonian (5.8), neglecting the bias term becomes:

$$\frac{H}{NJ} = -\frac{U}{2J} + \frac{\Lambda}{2} [1 + z^2] - \sqrt{1 - z^2} \cos(\phi_R - \phi_L). \quad (5.24)$$

The equations of motion for the imbalance z and phase difference $\delta\phi = \phi_R - \phi_L$ are:

$$\begin{cases} \dot{z} = -\sqrt{1 - z^2} \sin \delta\phi \\ \dot{\delta\phi} = \Lambda z + \frac{z}{\sqrt{1 - z^2}} \cos \delta\phi. \end{cases} \quad (5.25)$$

These equations are the S2M equations for a symmetric double well that we discussed in chapter 3 [68], see Eqs. (3.13)⁵. The evolution of the imbalance in this semi-classical limit is plotted in the lower panels of Fig. 5.7 (dashed-blue), and it is independent of the number of particles. One can see that the agreement with the Bose-Hubbard description improves as N increases.

5.5 $1/N$ approximation to the BH model

Another approximation that helps to get analytical insight into the physical nature of correlations in the states of the BH model is provided by the so-called $1/N$ approximation,

⁵Notice that in the equations derived in this section, the Rabi frequency is hidden in the time, which is measured in units of t_R .

which was discussed in Refs. [130, 132].

The time-evolution of a system of N atoms in a state $|\Psi(t)\rangle$,

$$i\frac{\partial}{\partial t} |\Psi(t)\rangle = \hat{H} |\Psi(t)\rangle, \quad (5.26)$$

where \hat{H} is the Bose-Hubbard Hamiltonian given by Eq. (5.10)⁶, can be written in terms of the Fock basis

$$|\Psi(t)\rangle = \sum_{k=0}^N c_k(t) |k, N-k\rangle, \quad (5.27)$$

and obtain a system of differential equations, relating the coefficients $c_k(t)$:

$$\frac{i}{N} \frac{dc_k(t)}{dt} = a_k c_k(t) - J(c_{k-1} b_{k-1} + c_{k+1} b_k), \quad (5.28)$$

where

$$\begin{aligned} a_k &= \frac{\varepsilon}{N}(N-2k) + \frac{U}{2N} \left[k^2 + (N-k)^2 - N \right] \\ b_k &= \frac{1}{N} \sqrt{(k+1)(N-k)}. \end{aligned} \quad (5.29)$$

Introducing $x = k/N$, and assuming that $h \equiv 1/N$ is small, one can define a continuous wave function $\Psi(x, t) = c_k(t)/\sqrt{N}$. Then, the coefficients a_k and b_k can be considered functions of x

$$\begin{aligned} a(x) &= \varepsilon(1-2x) + \frac{UN}{2} \left[x^2 + (1-x)^2 - h \right] \\ b(x) &= \sqrt{(x+h)(1-x)}. \end{aligned} \quad (5.30)$$

Notice that $c_{k+1}(t) = \sqrt{N}\Psi(x+h, t)$ results in $c_{k+1}(t) = \sqrt{N}e^{h\partial_x}\Psi(x, t)$ by expanding $\Psi(x+h, t)$ around $h=0$. In a similar way, $c_{k-1}(t) = \sqrt{N}e^{-h\partial_x}\Psi(x, t)$, $b_{k-1} = e^{-h\partial_x}b(x)$, and $b_{k-1}c_{k-1} = \sqrt{N}e^{-h\partial_x}[b(x)\Psi(x, t)]$. Then, Eq. (5.28) becomes,

$$ih\frac{\partial\Psi(x, t)}{\partial t} = a(x)\Psi(x, t) - J \left[e^{-h\partial_x}(b(x)\Psi(x, t)) + b(x)e^{h\partial_x}\Psi(x, t) \right] \quad (5.31)$$

As h is considered to be small, one retains only terms up to second order in h . Therefore,

$$\begin{aligned} e^{\pm h\partial_x} &\simeq 1 \pm h\partial_x + \frac{1}{2}(h\partial_x)^2, \\ b(x) &\simeq b_0(x) + h\partial_h b(x)|_{h=0} + \frac{1}{2}h^2\partial_h^2 b(x)|_{h=0}, \end{aligned} \quad (5.32)$$

⁶In Ref. [130] the Hamiltonian is written per particle and in units of J : $\hat{H}' = [\hat{H} - \hat{N}\varepsilon + U\hat{N}/2]/(JN)$. Moreover, they use $\varepsilon' = -2\varepsilon/J$ and $\gamma' = UN/(2J)$.

where $b_0(x) = b(x)|_{h=0}$, and

$$\begin{aligned}
ih \frac{\partial \Psi(x, t)}{\partial t} = & a(x) \Psi(x, t) - J \left\{ \left[2b_0(x) + h \left(2\partial_h b(x)|_{h=0} - \partial_x b_0(x) \right) \right. \right. \\
& \left. \left. + h^2 \left(\partial_h^2 b(x)|_{h=0} - \partial_x (\partial_h b(x)|_{h=0}) + \frac{1}{2} \partial_x^2 b_0(x) \right) \right] \Psi(x, t) \right. \\
& \left. + h^2 (\partial_x b_0(x)) \partial_x \Psi(x, t) + h^2 b_0(x) \partial_x^2 \Psi(x, t) \right\}. \quad (5.33)
\end{aligned}$$

Finally, defining $z = 1 - 2x$, with $z \in [-1, 1]$, and considering $h \ll 1$ one gets [130]

$$ih \frac{\partial \Psi(z, t)}{\partial t} = V_{\text{eff}}(z) \Psi(z, t) - 2Jh^2 \partial_z \left(\sqrt{1 - z^2} \partial_z \Psi(z, t) \right), \quad (5.34)$$

where the effective potential, in units of J , is:

$$\frac{V_{\text{eff}}(z)}{J} = \frac{\varepsilon}{J} z + \frac{\Lambda}{2} (1 + z^2) - \sqrt{1 - z^2}, \quad (5.35)$$

with $\Lambda = NU/(2J)$. The Eq. (5.34), provides a simple equation for the function $\Psi(z, t)$, which represents the many-body state in terms of the coefficients of the Fock states. Moreover, it can be interpreted as the equation of motion of a particle with variable mass, $-h^2/(2M) \equiv -2h^2\sqrt{1 - z^2}$, confined in a potential $V_{\text{eff}}(z)$.

Therefore, one can analyze the effective potential in order to find the stationary points of the system. Taking $\varepsilon = 0$, these points are $z = 0$ and $z_{\pm} = \pm \sqrt{1 - \frac{1}{\Lambda^2}}$, which only exist for $|\Lambda| > 1$. For attractive interactions, where $\Lambda < 0$, $z = 0$ is a minimum when $|\Lambda| < 1$, and a maximum when $|\Lambda| > 1$. The other two points, z_{\pm} , are minima when they exist, this is when $z = 0$ becomes a maximum. Notice that this results are in perfect agreement with the S2M predictions, see Sec. 3.2.1, and with the BH observations of the ground state, see Sec. 5.3.

In Fig. 5.8, we plot the energy per particle of the ground state of a system of N bosons, and as a function of Λ . We compare the results obtained using exact diagonalization of the BH Hamiltonian, and with the $1/N$ approximation. As we can see, both models predict similar energies for weak interactions, and when the number of particles increases.

Moreover, by approximating the effective potential around each minima z_{\pm} by a parabola, one can obtain an approximation for the ground state energy⁷ [130], which in units of J reads

$$E_{\text{g.s.}} = \frac{1}{2\Lambda} + \Lambda + h\sqrt{\Lambda^2 - 1} \quad \text{for } \Lambda < -1. \quad (5.36)$$

Notice that this equation is only valid when z_{\pm} exists, i.e. when $\Lambda < -1$, and as we can see in Fig. 5.8, it reproduces rather well the energy of the exact ground state.

⁷The equation in Ref. [130] and the one written here differ a factor of $\Lambda/2$, related to a constant factor in the initial definition of the Hamiltonian.

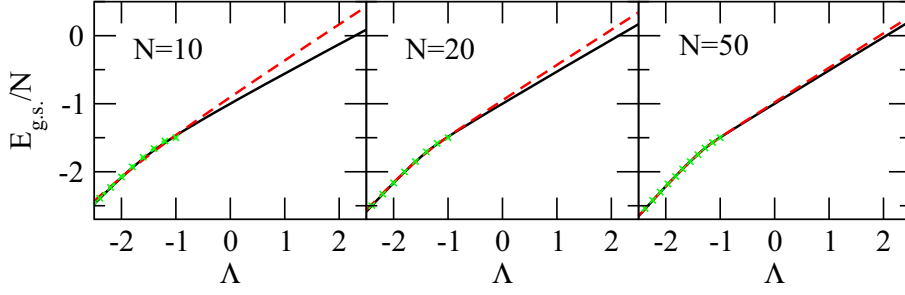


Figure 5.8: Comparison of the ground state energy for three different number of particles, using the $1/N$ approximation Eq. (5.34) (solid-black), the Bose-Hubbard model Eq. (5.26) (dashed red), and the parabolic model Eq. (5.36) (dotted green).

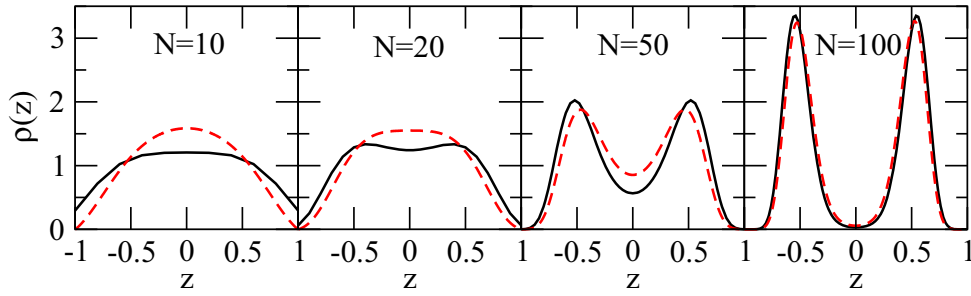


Figure 5.9: Comparison of the ground state density predicted by the BH model (solid-black) and with the $1/N$ approximation (dashed-red), for different number of particles. In all cases $\Lambda = -1.2$.

It is also interesting to compare the density profiles predicted by the $1/N$ approximation and by the exact diagonalization of the BH model. For the $1/N$ approximation, one can define the density profile $|\Psi(z)|^2$, associated to the modulus square of the coefficients that express the ground state in terms of the Fock state. In Fig. 5.9 we fix the interactions to $\Lambda = -1.2$ and plot the density profile of the ground state obtained with exact diagonalization of the BH Hamiltonian, defined by the coefficients $|c_k|^2$ of the ground state $|\Psi\rangle_{\text{gs}} = \sum_k c_k |k, N-k\rangle$, and with the $1/N$ approximation, $|\Psi(z)|^2$, with the analogy $z \rightarrow 1 - 2k$. As we can see, the density profiles provided by the $1/N$ approximation converge to the $|c_k|^2$ provided by the exact diagonalization. Moreover, it is clear from the figure that the $1/N$ approximation captures the cat-like structure of the ground state, in contrast to a mean-field description.

Chapter 6

Josephson effect in spinor condensates

Spinor condensates are a special kind of BEC, in which atoms have a spin degree of freedom [53, 54]. When these atoms collide in pairs, the third component of the spin of these atoms may change. However, the total third component of the spin has to be preserved. The first experimental realization of a spinor condensate was done in the group of W. Ketterle [136, 55]. They condensed sodium atoms in the three magnetic sublevels $m_F = 0, \pm 1$ of the hyperfine multiplet with total spin $F = 1$. Due to spin-changing collisions, an atom in the $m_F = 1$ state may scatter with another in the $m_F = -1$ state to give two atoms in the $m_F = 0$ state. Notice the total number of particles of each species is not conserved.

As we will see in more detail in Sec. 6.1, spin-changing collisions determine the character of the condensate, which can be polar or ferromagnetic. In the polar case, the ground state has rotational symmetry and zero magnetization, with all the atoms in the $m_F = 0$ hyperfine state. On the other hand, the ground state of a ferromagnetic BEC has all the spins aligned and therefore, it is a state with broken rotational symmetry and maximum magnetization.

H. Saito and M. Ueda studied a ferromagnetic spin-1 BEC with all the atoms initially condensed in the $m_F = 0$ hyperfine state [137]. This configuration is not stable with respect to the spin-changing-collision term in the Hamiltonian, as we will discuss in chapter 7. Therefore, quantum fluctuations in the other two components $m_F = \pm 1$ are enough to trigger a fast population transfer from $m_F = 0$ to $m_F = \pm 1$, giving rise to spontaneous magnetization and structure domain formation. The experimental work of L. E. Sadler and collaborators studied a similar setup, in which the instability was created by changing the external magnetic field [138]. The spin-dynamics of a spinor $F = 1$ BEC within a mean-field framework, has been addressed by J. Mur-Petit et al. [139] and by M. Moreno-Cardoner et al. [140], both at zero and at finite temperature. Moreover, spin structure and domain formation have been studied with both ferromagnetic [141, 142] and polar [143] condensates.

In this chapter, we study the Josephson effect that takes place when the condensate is made of spin-1 atoms. The spin-changing collisions between atoms open new possibilities, and therefore, spinor condensates show an even richer phenomenology than a binary

mixture. Previous works were done by Ö. E. Müstecaplıođlu et al., who studied the dynamical properties of a spin-1 in a double-well potential [120]. They paid special attention to the dynamics of the magnetization at each side of the double well. In a more recent work of the same group, they analyzed the quantum correlations of the condensate focusing on the squeezing of the states [95].

Here, we consider two fronts: first, we study the interplay between Josephson phenomena and population transfer dynamics. This is studied in a mean-field picture, accurate enough for experiments with large number of atoms. We extend the two-mode approximation to the Gross-Pitaevskii equation for a spin-1 condensate, in a similar way as it was done with a single-component BEC (see Sec. 3.2.1) and with a binary mixture (see Sec. 4.2.1). Second, we study the new phases appearing in the ground state by using a generalization of the Bose-Hubbard model. We describe a novel phenomenon: the delocalization of the ultracold atomic cloud by means of the formation of spin singlets, which are correlated states between two atoms.

The chapter is organized as follows: in section 6.1 we review the formalism to describe a spin $F = 1$ condensate in second quantization, and also recall the corresponding mean-field Gross-Pitaevskii equations. In section 6.2 we apply the two-mode approximation in the TDGPE in order to find the S2M equations for a spinor condensate. We also discuss the dynamical equations when the population imbalances and phase differences of each component are small. We show that in such conditions, the evolution of the number of particles in each component decouples from the Josephson dynamics.

The generalization of the two-site Bose-Hubbard for a spinor condensate is reviewed in section 6.3. In section 6.4 we discuss the ground state properties starting with a single well. Then, we discuss the ground state for a double well and for the particular case of zero magnetization ($\mathcal{M} = 0$). We compare both the mean-field and Bose-Hubbard predictions. At the end of this section, we discuss the discrepancies that we have found between these two models when describing the ground state. We show that the creation of spin singlets, which is not captured by the mean-field description, plays an important role in the spatial symmetry breaking of the ground state.

6.1 Spinor condensates

In this section, we recall the formalism that describes a spinor BEC. For simplicity, we restrict the discussion to isotopes with total spin $F = 1$, although similar arguments can apply to higher spins [4]. Experimentally, one can achieve $F = 1$ spinor condensates with alkali atoms. For example, ^{87}Rb and ^{23}Na have a nuclear spin $I = 3/2$ and only one electron in the last shell $S = 1/2$. The coupling of these two angular momenta gives $\mathbf{F} = \mathbf{I} + \mathbf{S}$, with possible values $F = 1, 2$. In our study, we consider only the lowest hyperfine spin manifold $F = 1$ [53]¹.

Two identical bosons of $F = 1$ in an s state of relative motion can couple to build states with total angular momentum $\mathcal{F} = 0$ or 2 . Thus, one can write the effective interaction for low-energy collisions as $g_{\mathcal{F}} = 4\pi\hbar^2 a_{\mathcal{F}}/M$, where $a_{\mathcal{F}}$ is the s -wave scattering length in

¹In an optical trap all atomic hyperfine spin components are equally trapped, but the low collision energies available in the condensate populate only the lowest hyperfine spin manifold of $F = 1$.

the total spin channel \mathcal{F} . Therefore, the contact potential distinguishes between different total spins [144]:

$$\mathcal{V}(\mathbf{r}_1, \mathbf{r}_2) = \delta(\mathbf{r}_1 - \mathbf{r}_2)(g_0\mathcal{P}_0 + g_2\mathcal{P}_2). \quad (6.1)$$

The operators $\mathcal{P}_{\mathcal{F}}$ project the wave function of a pair of atoms on a state of total angular momentum \mathcal{F} . In terms of the total angular momentum of each atom, $\mathbf{F}_1, \mathbf{F}_2$, one gets [4]:

$$\mathcal{V}(\mathbf{r}_1, \mathbf{r}_2) = \delta(\mathbf{r}_1 - \mathbf{r}_2)(c_0 + c_2\mathbf{F}_1 \cdot \mathbf{F}_2), \quad (6.2)$$

with $c_0 = (g_0 + 2g_2)/3$ and $c_2 = (g_2 - g_0)/3$. The first one, c_0 , is always positive, whereas c_2 is positive for anti-ferromagnetic interactions (^{23}Na) and negative for ferromagnetic interactions (^{87}Rb).

In second quantization, the many-body Hamiltonian of a system of N atoms with the atom-atom interaction given in (6.2) can be written as [95]:

$$\hat{H} = \int d\mathbf{r} \left[\frac{\hbar^2}{2M} \nabla \hat{\Psi}_m^\dagger \nabla \hat{\Psi}_m + V_{\text{ext}} \hat{\Psi}_m^\dagger \hat{\Psi}_m + \frac{c_0}{2} \hat{\Psi}_m^\dagger \hat{\Psi}_n^\dagger \hat{\Psi}_n \hat{\Psi}_m + \frac{c_2}{2} \hat{\Psi}_m^\dagger \hat{\Psi}_{m'}^\dagger \mathbf{F}_{mn} \cdot \mathbf{F}_{m'n'} \hat{\Psi}_{n'} \hat{\Psi}_n \right] \quad (6.3)$$

where, following Einstein convention, repeated indices are summed over. $\mathbf{F} = (F_x, F_y, F_z)$ is the spin vector operator, where $F_{x,y,z}$ are the spin-1 matrices, and $\hat{\Psi}_m(\mathbf{r})(\hat{\Psi}_m^\dagger(\mathbf{r}))$ is the annihilation (creation) operator of a spin-1 particle in the Zeeman state $m \equiv m_F = 0, \pm 1$ at position \mathbf{r} . These operators obey bosonic commutation rules: $[\hat{\Psi}_m(\mathbf{r}), \hat{\Psi}_n(\mathbf{r}')] = [\hat{\Psi}_m^\dagger(\mathbf{r}), \hat{\Psi}_n^\dagger(\mathbf{r}')] = 0$ and $[\hat{\Psi}_m(\mathbf{r}), \hat{\Psi}_n^\dagger(\mathbf{r}')] = \delta_{mn}\delta(\mathbf{r} - \mathbf{r}')$. Moreover, the Hamiltonian (6.3) can be written as $\hat{H} = \hat{H}_S + \hat{H}_A$,

$$\hat{H}_S = \sum_m \int d\mathbf{r} \hat{\Psi}_m^\dagger \left(-\frac{\hbar^2 \nabla^2}{2M} + V_{\text{ext}}(\mathbf{r}) \right) \hat{\Psi}_m + \frac{c_0}{2} \sum_{m,n} \int d\mathbf{r} \hat{\Psi}_m^\dagger \hat{\Psi}_n^\dagger \hat{\Psi}_m \hat{\Psi}_n \quad (6.4)$$

$$\begin{aligned} \hat{H}_A = \frac{c_2}{2} \int d\mathbf{r} & \left[\hat{\Psi}_1^\dagger \hat{\Psi}_1^\dagger \hat{\Psi}_1 \hat{\Psi}_1 + \hat{\Psi}_{-1}^\dagger \hat{\Psi}_{-1}^\dagger \hat{\Psi}_{-1} \hat{\Psi}_{-1} + 2\hat{\Psi}_1^\dagger \hat{\Psi}_0^\dagger \hat{\Psi}_1 \hat{\Psi}_0 + 2\hat{\Psi}_{-1}^\dagger \hat{\Psi}_0^\dagger \hat{\Psi}_{-1} \hat{\Psi}_0 \right. \\ & \left. - 2\hat{\Psi}_1^\dagger \hat{\Psi}_{-1}^\dagger \hat{\Psi}_1 \hat{\Psi}_{-1} + 2\hat{\Psi}_0^\dagger \hat{\Psi}_0^\dagger \hat{\Psi}_1 \hat{\Psi}_{-1} + 2\hat{\Psi}_1^\dagger \hat{\Psi}_{-1}^\dagger \hat{\Psi}_0 \hat{\Psi}_0 \right]. \end{aligned} \quad (6.5)$$

Notice that apart from contact interactions we also have spin-changing contact collisions, due to the terms $\hat{\Psi}_1^\dagger \hat{\Psi}_{-1}^\dagger \hat{\Psi}_0 \hat{\Psi}_0$ and $\hat{\Psi}_0^\dagger \hat{\Psi}_0^\dagger \hat{\Psi}_1 \hat{\Psi}_{-1}$ in Eq. (6.5). In these collisions, two particles with $m = 0$ collide and become two particles with $m = +1$ and $m = -1$, and the reversed process. Therefore, the number of particles of each species is not conserved as it was the case with binary mixtures (see Chap. 4).

Mean-field description

For a spin-1 BEC in the mean-field approximation, the single-particle state in which all particles are condensed $\varphi(\mathbf{r})$ is a superposition of the three hyperfine states [4],

$$\varphi(\mathbf{r}) = \varphi_1(\mathbf{r}) |1, 1\rangle + \varphi_0(\mathbf{r}) |1, 0\rangle + \varphi_{-1}(\mathbf{r}) |1, -1\rangle \quad (6.6)$$

where we have used the notation $|F, m\rangle$ for the spin degrees of freedom. The N -body wave function is then

$$\Psi(\mathbf{r}_1; \dots; \mathbf{r}_N) = \prod_{i=1}^N \varphi(\mathbf{r}_i) \quad (6.7)$$

Working with the wave function (6.7) is equivalent to replacing the field operators $\hat{\Psi}_m$ in (6.3) by their expectation values Ψ_m [4].

In the mean-field approximation, the N -body state can also be written as a spinor,

$$\mathbf{\Psi}(\mathbf{r}) = \begin{pmatrix} \Psi_1(\mathbf{r}) \\ \Psi_0(\mathbf{r}) \\ \Psi_{-1}(\mathbf{r}) \end{pmatrix} = \sqrt{n(\mathbf{r})} \begin{pmatrix} \xi_1(\mathbf{r}) \\ \xi_0(\mathbf{r}) \\ \xi_{-1}(\mathbf{r}) \end{pmatrix} \quad (6.8)$$

where $\boldsymbol{\xi}(\mathbf{r})$ is a three-component spinor, normalized according to the condition $\sum_m \xi_m^* \xi_m = 1$, and $n(\mathbf{r}) = \sum_m |\Psi_m(\mathbf{r})|^2$ is the total density [145].

The mean-field energy functional results

$$E[\mathbf{\Psi}] = \int d\mathbf{r} \left\{ \Psi_m^* H_{\text{sp}} \Psi_m + \frac{c_0}{2} \Psi_m^* \Psi_n^* \Psi_n \Psi_m + \frac{c_2}{2} \Psi_m^* \Psi_{m'}^* \mathbf{F}_{mn} \cdot \mathbf{F}_{m'n'} \Psi_{n'} \Psi_n \right\}, \quad (6.9)$$

where we have defined the single-particle Hamiltonian

$$H_{\text{sp}} = -\frac{\hbar^2}{2M} \nabla^2 + V_{\text{ext}}(\mathbf{r}). \quad (6.10)$$

Finally, the spinor TDGPE [53, 54] can be obtained using a least-action principle approach:

$$\begin{cases} i\hbar \frac{\partial \Psi_{\pm 1}}{\partial t} = \left[H_{\text{sp}} + c_0 n + c_2 (n_{\pm 1} + n_0 - n_{\mp}) \right] \Psi_{\pm 1} + c_2 \Psi_0^2 \Psi_{\mp}^* \\ i\hbar \frac{\partial \Psi_0}{\partial t} = \left[H_{\text{sp}} + c_0 n + c_2 (n_1 + n_-) \right] \Psi_0 + 2c_2 \Psi_1 \Psi_0^* \Psi_{-1}, \end{cases} \quad (6.11)$$

where for each component $m = 0, \pm 1$, $n_m(\mathbf{r}, t) = |\Psi_m(\mathbf{r}, t)|^2$ is the density of the atoms at time t , and $n(\mathbf{r}, t) = \sum_m n_m(\mathbf{r}, t)$ is the total density. These coupled equations describe the time-evolution of the spinor condensate taking into account the exchange of atoms between the different components, and conserving the total magnetization $\mathcal{M} = \sum_m m \times N_m$.

6.2 Josephson effect: mean-field description

In the previous chapters, we have studied the Josephson effect within a mean-field framework in scalar condensates (Chap. 3) and binary mixtures (Chap. 4). In both systems we have solved the 3-dimensional Gross-Pitaevskii equation and have analyzed the two-mode approaches, which give simple equations relating the population imbalance and phase difference of each component. In the current problem with atoms with internal spin, one

can assume that the two-mode approximation also provides good insight of the physics. This is partly because the population transfer dynamics is local, and therefore, one can expect the decoupling of the particle dynamics and the spatial dynamics.

We consider a spinor BEC trapped in a symmetric double-well potential, described by the coupled TDGPE (6.11). Following a similar procedure as in Sec. 3.2, we apply a two-mode approximation. The weakly linked condition, $E_{\text{sp}}^1 - E_{\text{sp}}^0 \ll E_{\text{sp}}^2 - E_{\text{sp}}^0$, where E_{sp}^i is the energy of the i -th single-particle state, allows to describe the system using only the ground φ_{m+} and first excited φ_{m-} states of each component $m = 0, \pm 1$. In addition, as the three components have the same mass, for $|c_2| \ll |c_0|$ the ground and first excited states can be taken independent of m , namely φ_+ and φ_- , and stationary solutions of:

$$\mathcal{H}_0 = -\frac{\hbar^2}{2M}\nabla^2 + V_{\text{ext}}(\mathbf{r}) + c_0 n(\mathbf{r}) , \quad (6.12)$$

where $n(\mathbf{r}) = \sum_m n_m(\mathbf{r})$ is the total density of the condensate. This is what is known as the single mode approximation (SMA) [144]. However, for $|c_2| \sim |c_0|$ it has been shown [146] that either when $c_2 < 0$ or in the particular case of $c_2 > 0$ and zero magnetization, the three components $m = 0, \pm 1$ have also the same wave function, recovering the SMA. In general, the wave functions are not eigenstates of \mathcal{H}_0 and are found by solving the full TDGPEs, Eqs. (6.11).

Defining the left and right modes as, $\varphi_L = (\varphi_+ + \varphi_-)/\sqrt{2}$ and $\varphi_R = (\varphi_+ - \varphi_-)/\sqrt{2}$, the wave function of each component under the SMA and the two-mode ansatz is:

$$\Psi_m(\mathbf{r}, t) = \psi_{mL}(t)\varphi_L(\mathbf{r}) + \psi_{mR}(t)\varphi_R(\mathbf{r}) , \quad (6.13)$$

where the time dependent coefficients are $\psi_{mj}(t) = \sqrt{N_{mj}(t)}e^{i\phi_{mj}(t)}$. The number of particles at each side of the barrier, neglecting the small overlap between the left and right modes, are

$$\begin{aligned} N_{mL} &= \int_{-\infty}^0 dx \int_{-\infty}^{+\infty} dy \int_{-\infty}^{+\infty} dz |\Psi_m(\mathbf{r}, t)|^2 , \\ N_{mR} &= \int_0^{+\infty} dx \int_{-\infty}^{+\infty} dy \int_{-\infty}^{+\infty} dz |\Psi_m(\mathbf{r}, t)|^2 . \end{aligned} \quad (6.14)$$

Inserting this ansatz into the TDGPEs, Eqs. (6.11), we get a system of eight coupled non-linear differential equations relating the population imbalance and the phase difference of each component $m = 0, \pm 1$, defined by

$$\begin{aligned} z_m(t) &= \frac{N_{mL}(t) - N_{mR}(t)}{N_m(t)} \\ \delta\phi_m(t) &= \phi_{mR}(t) - \phi_{mL}(t) , \end{aligned} \quad (6.15)$$

the population of the $m = 0$ component, $N_0(t)$, and the phase $\Delta\phi_L(t) = 2\phi_{0L}(t) - \phi_{-1L}(t) - \phi_{+1L}(t)$. Following a similar procedure as in the scalar condensate and the binary mixture, the equations are obtained by neglecting crossed terms of the left and right modes of the order larger than 1 [98]:

$$\begin{aligned}
\hbar\dot{z}_{-1} &= \frac{\xi_2 N_0 \sqrt{N_{-1} N_{+1}}}{N_{-1}} \left[(1 - z_{-1}) \sqrt{(1 + z_{-1})(1 + z_{+1})} (1 + z_0) \sin \Delta\phi_L \right. \\
&\quad \left. - (1 + z_{-1}) \sqrt{(1 - z_{-1})(1 - z_{+1})} (1 - z_0) \sin \Delta\phi_R \right] - 2K \sqrt{1 - z_{-1}^2} \sin \delta\phi_{-1}, \\
\hbar\dot{z}_{+1} &= \frac{\xi_2 N_0 \sqrt{N_{-1} N_{+1}}}{N_{-1}} \left[(1 - z_{+1}) \sqrt{(1 + z_{-1})(1 + z_{+1})} (1 + z_0) \sin \Delta\phi_L \right. \\
&\quad \left. - (1 + z_{+1}) \sqrt{(1 - z_{-1})(1 - z_{+1})} (1 - z_0) \sin \Delta\phi_R \right] - 2K \sqrt{1 - z_{+1}^2} \sin \delta\phi_{+1}, \\
\hbar\dot{z}_0 &= -2\xi_2 \sqrt{N_{-1} N_{+1}} (1 - z_0^2) \left[\sqrt{(1 + z_{-1})(1 + z_{+1})} \sin \Delta\phi_L \right. \\
&\quad \left. - \sqrt{(1 - z_{-1})(1 - z_{+1})} \sin \Delta\phi_R \right] - 2K \sqrt{1 - z_0^2} \sin \delta\phi_0, \tag{6.16}
\end{aligned}$$

$$\begin{aligned}
\hbar\delta\dot{\phi}_{-1} &= 2\xi_0 \sum_{\alpha} N_{\alpha} z_{\alpha} + 2K \frac{z_{-1}}{\sqrt{1 - z_{-1}^2}} \cos \delta\phi_{-1} + 2\xi_2 (N_{-1} z_{-1} + N_0 z_0 - N_{+1} z_{+1}) \\
&\quad - \frac{\xi_2 N_0 \sqrt{N_{-1} N_{+1}}}{N_{-1} \sqrt{1 - z_{-1}^2}} \left[\sqrt{(1 + z_{-1})(1 - z_{+1})} (1 - z_0) \cos \Delta\phi_R \right. \\
&\quad \left. - \sqrt{(1 - z_{-1})(1 + z_{+1})} (1 + z_0) \cos \Delta\phi_L \right], \\
\hbar\delta\dot{\phi}_{+1} &= 2\xi_0 \sum_{\alpha} N_{\alpha} z_{\alpha} + 2K \frac{z_{+1}}{\sqrt{1 - z_{+1}^2}} \cos \delta\phi_{+1} + 2\xi_2 (-N_{-1} z_{-1} + N_0 z_0 + N_{+1} z_{+1}) \\
&\quad - \frac{\xi_2 N_0 \sqrt{N_{-1} N_{+1}}}{N_{+1} \sqrt{1 - z_{+1}^2}} \left[\sqrt{(1 - z_{-1})(1 + z_{+1})} (1 - z_0) \cos \Delta\phi_R \right. \\
&\quad \left. - \sqrt{(1 + z_{-1})(1 - z_{+1})} (1 + z_0) \cos \Delta\phi_L \right], \\
\hbar\delta\dot{\phi}_0 &= 2\xi_0 \sum_{\alpha} N_{\alpha} z_{\alpha} + 2K \frac{z_0}{\sqrt{1 - z_0^2}} \cos \delta\phi_{+1} + 2\xi_2 (N_{-1} z_{-1} + N_{+1} z_{+1}) \\
&\quad - 2\xi_2 \sqrt{N_{-1} N_{+1}} \left[\sqrt{(1 - z_{-1})(1 - z_{+1})} \cos \Delta\phi_R \right. \\
&\quad \left. - \sqrt{(1 + z_{-1})(1 + z_{+1})} \cos \Delta\phi_L \right], \tag{6.17}
\end{aligned}$$

$$\begin{aligned}
\hbar\dot{N}_0 &= -2\xi_2 N_0 \sqrt{N_{-1}N_{+1}} \left[\sqrt{(1+z_{-1})(1+z_{+1})}(1+z_0) \sin \Delta\phi_L \right. \\
&\quad \left. + \sqrt{(1-z_{-1})(1-z_{+1})}(1-z_0) \sin \Delta\phi_R \right], \\
\hbar\Delta\dot{\phi}_L &= 2\xi_2 \left[N_0 - N_{-1} - N_{+1} + N_0 z_0 - N_{-1} z_{-1} - N_{+1} z_{+1} \right] \\
&\quad + 2K \sqrt{\frac{1-z_0}{1+z_0}} \cos \delta\phi_0 - K \sqrt{\frac{1-z_{-1}}{1+z_{-1}}} \cos \delta\phi_{-1} - K \sqrt{\frac{1-z_{+1}}{1+z_{+1}}} \cos \delta\phi_{+1} \\
&\quad - \xi_2 \sqrt{N_{-1}N_{+1}} \sqrt{(1+z_{-1})(1+z_{+1})} \cos \Delta\phi_L \\
&\quad \times \left[4 - \frac{N_0(1+z_0)}{N_{-1}(1+z_{-1})} - \frac{N_0(1+z_0)}{N_{+1}(1+z_{+1})} \right], \tag{6.18}
\end{aligned}$$

where the parameter

$$K = - \int d^3r \left[\frac{\hbar^2}{2M} \nabla\varphi_L \cdot \nabla\varphi_R + \varphi_L V_{\text{ext}} \varphi_R \right] \tag{6.19}$$

takes into account the tunneling between wells, and

$$\xi_{0(2)} = \frac{c_{0(2)}}{2} \int d^3r \varphi_L^4(\mathbf{r}) = \frac{c_{0(2)}}{2} \int d^3r \varphi_R^4(\mathbf{r}) \tag{6.20}$$

is proportional to the strength of the atom-atom interaction in each well.

Note that this system of equations contains only 8 independent variables, as the phase $\Delta\phi_R(t) = 2\phi_{0R}(t) - \phi_{-1R}(t) - \phi_{+1R}(t)$ can be written as a function of $\Delta\phi_L$ and $\delta\phi_\alpha$, and the knowledge of the total number of particles N and magnetization $\mathcal{M} = N_{+1}(t) - N_{-1}(t)$, allows to determine the population of the other components $N_{\pm 1}(t) = (N - N_0(t) \mp \mathcal{M})/2$.

These equations reduce to the S2M equations for a scalar condensate, Eqs. (3.13), when $N_0 = N_{-1} = 0$, $z_0 = z_{-1} = 0$ and $\delta\phi_0 = \delta\phi_{-1} = 0$, and to the binary mixture without population exchange, Eqs. (4.10), when $N_0 = 0$, $z_0 = 0$, $\delta\phi_0 = 0$ and $c_2 = 0$.

6.2.1 Population transfer in the Josephson regime

In this section, we consider the simplest scenario, which already contains relevant physics. We restrict our analysis to zero total magnetization, $\mathcal{M} = 0$, small imbalances, $z_m \sim 0$, small phase differences, $\delta\phi_m \sim 0$, and small $\Delta\phi_{L(R)} \sim 0$. In absence of spin-changing collisions, this condition would correspond to a gentle Josephson oscillation triggered by a small imbalance of population.

In such conditions one can prove that the total population of the different components, $N_m(t)$, fully decouples from the Josephson tunneling dynamics. The time evolution of N_0 is given by,

$$\ddot{N}_0(t) = -4U_2^2 N_0(t)(N - N_0(t))(N_0(t) - N/2), \tag{6.21}$$

with $\hbar U_2 = 2\xi_2$. The population of the other two components is given by: $N_{\pm 1}(t) = (N - N_0(t))/2$. It is interesting to notice that in the particular case that $N_0(t) \sim N/2$,

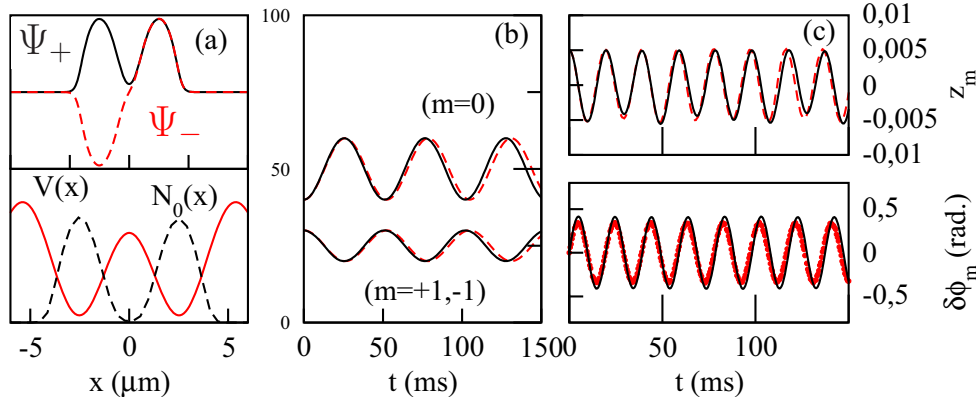


Figure 6.1: (a) (above) Ψ_+ and Ψ_- . (below) Potential in the x direction together with one of the initial population profiles used in the simulations (arbitrary units). The solid (black) curves show the evolution of the total population (b) and of the population imbalances and phase differences (c) corresponding to simulation I of Tab. 6.1. The dashed (red) lines depict the two-mode calculation.

the behavior of N_0 becomes sinusoidal, $N_0(t) = N/2 + (N_0(0) - N/2) \cos(\omega_T t)$, where we have defined the “population transfer frequency”, $\omega_T = NU_2$.

The system of equations governing the dynamics of the population imbalances, z_m , and phase differences, $\delta\phi_m$, becomes:

$$\begin{aligned}
\dot{z}_{\pm 1} &= -\omega_R \delta\phi_{\pm 1} - (N_0/2) U_2 (\delta\phi + z_{\pm 1} \Delta\phi), \\
\dot{z}_0 &= -\omega_R \delta\phi_0 + \bar{N} U_2 (\delta\phi + z_0 \Delta\phi), \\
\delta\dot{\phi}_{\pm 1} &= U (\bar{N} z_{\pm 1} + N_0 z_0) + U' \bar{N} z_{\mp 1} \\
&\quad + \omega_R z_{\pm 1} + U_2 \frac{N_0}{2} (2z_0 - z_{\pm 1} + z_{\mp 1}), \\
\delta\dot{\phi}_0 &= (U + U_2) \bar{N} (z_{-1} + z_{+1}) + U_0 N_0 z_0 + \omega_R z_0 \\
\Delta\dot{\phi} &= 8(N_0 - N/2) U_2,
\end{aligned} \tag{6.22}$$

where $\delta\phi = \Delta\phi_L - \Delta\phi_R$, $\Delta\phi = \Delta\phi_L + \Delta\phi_R$, $\bar{N} \equiv N_{+1} = N_{-1} = (N - N_0)/2$, $\hbar U_0 = 2\xi_0$, $U = U_0 + U_2$, $U' = U_0 - U_2$, and $\omega_R = 2K/\hbar$ is the Rabi frequency.

6.2.2 Numerical simulations

We consider a gas of ^{87}Rb atoms in a setup similar to that described in the experiments with scalar condensates [70] but with two important differences: the total number of atoms and the barrier height. In our case, in order to enhance population transfer effects, we consider a larger number of atoms, $N = 15000$. We use the same kind of double-well potential but with a higher barrier and a tighter confinement in the x direction to ensure a clear Josephson tunneling situation. The potential then reads,

$$V(\vec{r}) = \frac{M}{2} (\omega_x^2 x^2 + \omega_y^2 y^2 + \omega_z^2 z^2) + V_0 \cos^2(\pi x/q_0)$$

with $\omega_x = 2\pi \times 100$ Hz, $\omega_y = 2\pi \times 66$ Hz, $\omega_z = 2\pi \times 90$ Hz, $q_0 = 5.2\mu\text{m}$, $V_0 = 3500 h$ Hz and M is the mass of the atoms. As in the experimental setup [70] we assume that the dynamics takes place essentially on the x axis.

The numerical simulations of Eqs. (6.11) are performed in the following way. First, using an imaginary time evolution method we compute the ground, Ψ_+ , and first excited state, Ψ_- of a scalar BEC, $c_2 = 0$, under the same conditions. Then, for a given initial population imbalances for all the components, we build the wave functions at $t = 0$ by the appropriate linear combinations of Ψ_+ and Ψ_- . After that, we study the time evolution of the system by means of the split operator method. The number of particles in each component is $N_{m,L}(t) = \int_{-\infty}^0 dx \int_{-\infty}^{\infty} \int_{-\infty}^{\infty} dy dz n_m(\mathbf{r}, t)$, $N_{m,R}(t) = N_m(t) - N_{m,L}(t)$ and $\phi_{m,R(L)}$ are the space average of the phase of $\Psi_m(\mathbf{r}, t)$ at each side of the barrier. Lets us emphasize that the phase of $\Psi_m(\mathbf{r}, t)$ is almost spatially constant at each side of the trap during the GP simulations. The population imbalance and phase difference are defined as usual, see Eq. (6.15)

From the ground and first excited states of the system computed numerically, see Fig. 6.1, we build the left and right modes as explained above and compute the microscopic parameters entering in the two-mode description. The resulting values are: $\omega_R = 0.00386$ KHz, $NU_0 = 26.604$ KHz and $NU_2 = 0.12366$ KHz. This completely fixes from a microscopic level the parameters used in the two-mode description.

First let us consider the simplest full GP simulation, listed as I in Table 6.1. In this case, the three components start from the same initial population imbalances and basically give a similar Josephson tunneling behavior for the three components. As can be seen in Fig. 6.1 the Josephson regime is identified by the coupled behavior of z_m and $\delta\phi_m$. Together with the Josephson oscillation there is a transfer of population between the three different states, see panel (b) of Fig. 6.1. In this regime, the population transfer dynamics decouples from the Josephson tunneling and thus allows to clearly identify the value of NU_2 , which is of course directly linked to c_2 . The agreement between the two-mode and the full GP simulation is remarkable as can be seen in Fig. 6.1. Taking into account that for ^{87}Rb $|c_2| \ll c_0$ and therefore $U_2N \ll U_0N$, it is easy to prove from the above two-mode equations that, for this case, the behavior of the imbalance of all the components follows: $\ddot{z}_m = -\omega_J^2 z_m$ with $\omega_J = \omega_R \sqrt{1 + NU_0/\omega_R}$. Which corresponds to the Josephson frequency of a scalar condensate completely decoupled from the population transfer [68]. Therefore, the Josephson tunneling is directly related to the spin independent coupling, proportional to U_0 .

Now we consider three distinct cases: IIa, IIIa, IVa, listed in Table 6.1. They correspond to different initial population imbalances for the three components and to a different

Table 6.1: Conditions of the different full spinor GP simulations, Eqs.(6.11). $\delta\phi_m(0) = 0$ in all cases.

Sim	$N_0(0)/N$	$z_{-1}(0)$	$z_0(0)$	$z_{+1}(0)$	Transfer
I	0.4	0.005	0.005	0.005	YES
IIa(b)	0.6	0.010	0.000	0.020	YES(NO)
IIIa(b)	0.6	0.000	0.010	0.000	YES(NO)
IVa(b)	0.6	0.010	0.000	-0.010	YES(NO)

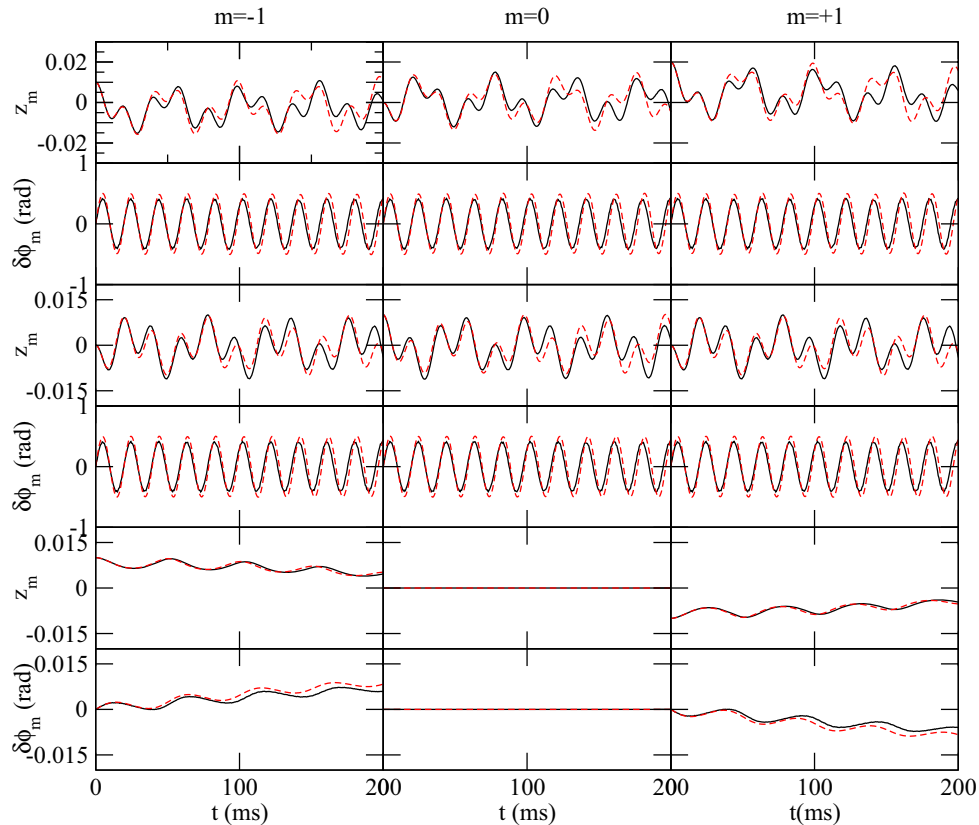


Figure 6.2: Full simulation of Eqs. (7.3) and two-mode analysis of some cases listed in Table 6.1. The first/second, third/fourth and fifth/sixth rows correspond to simulations IIa, IIIa, IVa, respectively. Solid lines correspond to the GP simulations. Dashed lines depict two-mode results with the parameters computed microscopically as described in the text. In most cases the two lines in each panel are almost indistinguishable.

initial number of atoms populating each sublevel from the one used in I. In figure 6.2 we show the results of the full GP simulations (solid lines). Runs IIa and IIIa produce essentially Josephson tunneling dynamics modulated by a longer oscillation. Simulation IVa, describes a much longer tunneling, i.e., the ± 1 components remain mostly on their original side of the trap while the 0 one remains mostly balanced. In the first two cases the oscillations of the phase differences are fully characterized by ω_J . In the same figure, and almost indistinguishable from the full GP results, we present the predictions of the two-mode model.

As mentioned above the population transfer dynamics fully decouples from the Josephson tunneling of the three components in the considered conditions. Its counterpart is however not true, the Josephson dynamics gets affected by the population transfer as we will discuss in the following.

To clearly see the effect of the population transfer terms on top of the Josephson tunneling dynamics we consider the same configurations, labeled as “a”, but without the population transfer terms, “b”. The two-mode model, without the corresponding transfer terms, also reproduces the dynamics of the “b” runs. In Fig. 6.3 we depict in all cases a comparison between the full GP solution and the same case but neglecting the population

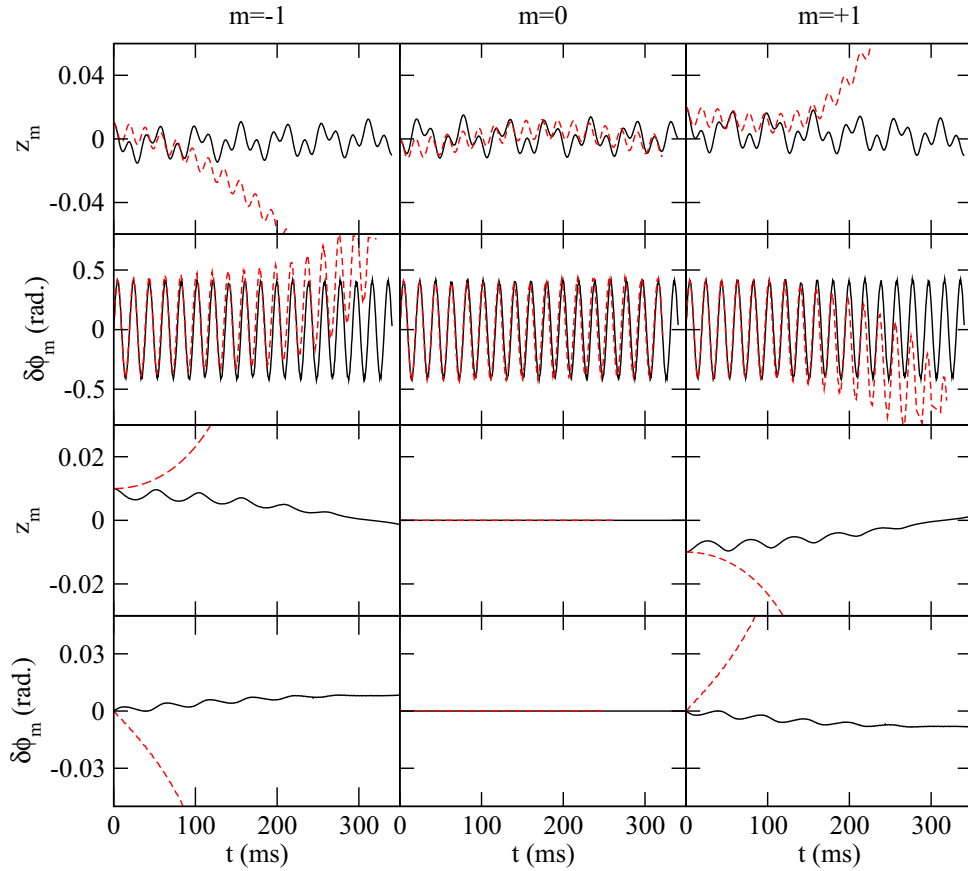


Figure 6.3: The first/second, and third/fourth rows correspond to simulations IIa(b) and IVa(b) described in Table 6.1. Solid (black) lines correspond to IIa and IVa while dashed (red) lines stand for IIb and IVb, which do not include the population transfer terms.

transfer term.

The effects of population transfer are clearly seen on the evolution of z_m . In simulation II, which has $z_0(0) = 0$ it is observed that the long oscillation which modulates the full runs, ω_T , is not present when we switch off the transfer term. Instead the population imbalance shows a Josephson-like tunneling oscillation which for $t \sim 100$ ms loses the small z_m regime. Therefore, the transfer term tends to stabilize the Josephson-like behavior over longer periods of time. The absence of the transfer of populations term does not show up on the behavior of the phase difference, as can be seen in Fig. 6.3, which mostly follows the same evolution as for the GP equations including the transfer term.

As in the case of binary mixtures [124], taking opposite initial imbalances for the $m = \pm 1$ components enhances the Rabi like oscillation and cancels the Josephson one. Simulation IV corresponds to such a case, with $z_{-1}(0) = -z_{+1}(0)$ and $z_0(0) = 0$. The Rabi oscillation gives rise to a long tunneling behavior but in this case modulated by the ω_T oscillation, as can be seen in Fig. 6.3 and in the lowest panel of Fig. 6.4. If we switch off the transfer term the ω_T oscillation disappears and the limit of small z and $\delta\phi$ becomes unstable.

Finally, Fig. 6.4 summarizes the relevant frequencies which enter in the interplay

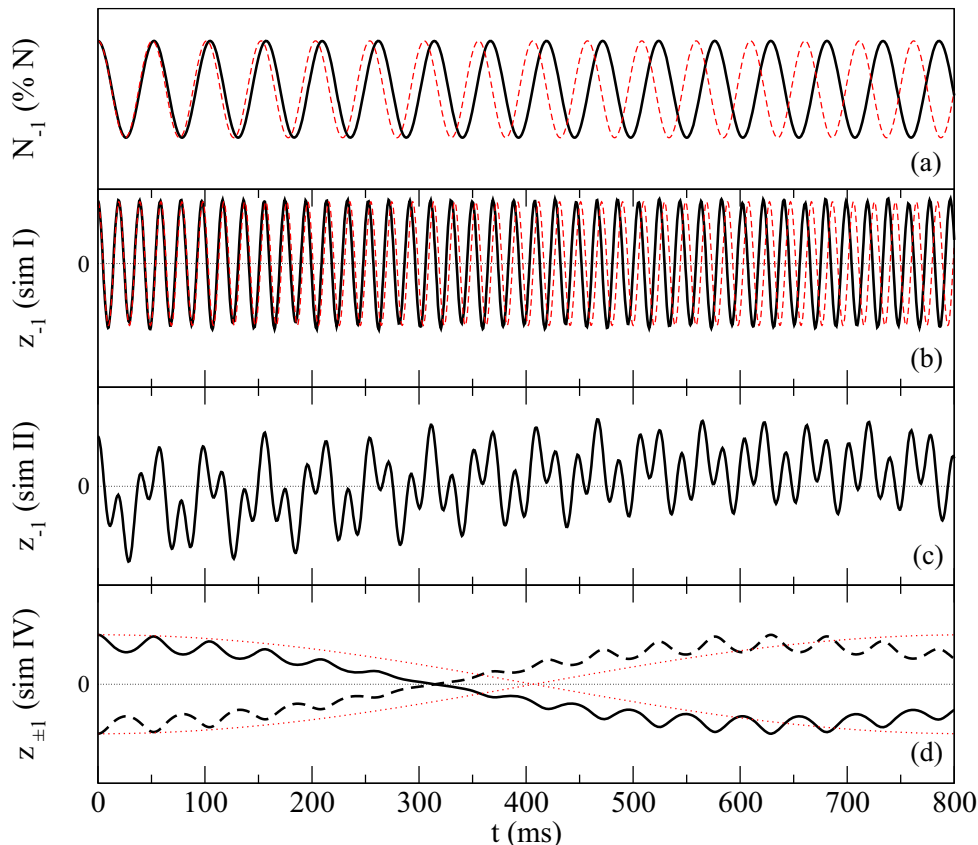


Figure 6.4: Frequencies playing a roll in the problem. (a) Time evolution of the number of atoms populating the $m = -1$ sublevel in simulation I, solid line. The dashed line depicts a $\cos(\omega_T t)$ which is the two-mode prediction for $N_0 \sim N/2$. (b) Full GP evolution for z_{-1} of simulation I, solid line. The dashed line shows a $\cos(\omega_J t)$ behavior, clearly identifying the Josephson time scale. (c) Full GP evolution of z_{-1} for simulation II. The dynamics is governed by (ω_T, ω_J) . (d) The solid black (red-dashed) line corresponds to the GP evolution of z_{-1} (z_{+1}) of simulation IV. The dotted lines follow a $\cos(\omega_R t)$, which drives the long-time scale of the problem. The scales in the vertical axes are not shown for clarity.

between Josephson tunneling and population transfer dynamics in the considered regime. The first panel isolates $\omega_T = NU_2$, governing the transfer of populations, whereas the second one shows ω_J , which sets the fast behavior of the imbalances. The third panel shows z_{-1} from simulation II, which is dominated by (ω_T, ω_J) and the fourth one shows both $z_{\pm 1}$ from simulation IV, that are dominated by two frequencies (ω_T, ω_R) .

6.3 Bose-Hubbard model for $F = 1$ spinors in a double well

In this section, we want to go beyond the mean-field description and study quantum fluctuations and many-body effects. Following a similar procedure as in chapter 5, we

introduce the generalization of the two-site BH Hamiltonian for a $F = 1$ BEC [96]:

$$\begin{aligned}
H = & -J \sum_{\alpha=0,\pm 1} \left(\hat{a}_{\alpha L}^\dagger \hat{a}_{\alpha R} + \hat{a}_{\alpha R}^\dagger \hat{a}_{\alpha L} \right) + \frac{U_0}{2} \left(\hat{N}_L(\hat{N}_L - 1) + \hat{N}_R(\hat{N}_R - 1) \right) \quad (6.23) \\
& + \frac{U_2}{2} \left(\hat{\mathbf{S}}_L^2 - 2\hat{N}_L + \hat{\mathbf{S}}_R^2 - 2\hat{N}_R \right) + \sum_{j=L,R} \varepsilon_j \hat{N}_j,
\end{aligned}$$

where J is the tunneling coupling between sites, U_0 is equivalent to scalar interactions, and therefore spin-independent, while U_2 derives from the spin interactions. The operator $\hat{a}_{\alpha j}$ ($\hat{a}_{\alpha j}^\dagger$) is the annihilation (creation) operator of a particle of component m_α in the j -th site, and obeys the usual bosonic commutation rules, $[\hat{a}_{\alpha j}, \hat{a}_{\beta k}] = [\hat{a}_{\alpha j}^\dagger, \hat{a}_{\beta k}^\dagger] = 0$ and $[\hat{a}_{\alpha j}, \hat{a}_{\beta k}^\dagger] = \delta_{\alpha\beta} \delta_{jk}$. The number of particles populating the α component is defined as $\hat{N}_{\alpha j} = \hat{a}_{\alpha j}^\dagger \hat{a}_{\alpha j}$, and the total number of particles in the j -th site is $\hat{N}_j = \sum_\alpha \hat{N}_{\alpha j}$. The operator $\hat{\mathbf{S}}_j$ is a pseudo-angular momentum operator in the j -site defined as:

$$\begin{aligned}
\hat{S}_j^{(z)} &= \hat{N}_{+1j} - \hat{N}_{-1j} = \hat{a}_{+1j}^\dagger \hat{a}_{+1j} - \hat{a}_{-1j}^\dagger \hat{a}_{-1j} \\
\hat{S}_j^{(+)} &= \sqrt{2} \left(\hat{a}_{+1j}^\dagger \hat{a}_{0j} + \hat{a}_{0j}^\dagger \hat{a}_{-1j} \right) \\
\hat{S}_j^{(-)} &= \hat{S}_j^{(+)\dagger}, \quad (6.24)
\end{aligned}$$

with $[\hat{S}_j^{(+)}, \hat{S}_k^{(-)}] = 2\delta_{jk} \hat{S}_j^{(z)}$ and $[\hat{S}_j^{(z)}, \hat{S}_k^{(\pm)}] = \pm \delta_{jk} \hat{S}_j^{(\pm)}$. Finally, ε_j acts as a bias that breaks the degeneracy between wells and controls the spatial symmetry breaking.

To describe this system, we introduce the Fock basis, that is labeled by the number of particles of each component in each well: $\{ |N_{-1L}, N_{-1R}, N_{0L}, N_{0R}, N_{+1L}, N_{+1R}\rangle \}$, which are constrained by a fixed total number of particles, $N = \sum_{\alpha j} N_{\alpha j}$, and magnetization, $\mathcal{M} = \sum_j (N_{+1j} - N_{-1j})$. The minimum dimension of the Hilbert space spanned by this basis is $N+1$ and corresponds to maximum magnetization ($\mathcal{M} = N$ or $\mathcal{M} = -N$). In this case all the particles are in the same state $m = +1$ or $m = -1$, and the system reduces to the single-component case with an effective interaction $U_0 + U_2$. When the magnetization decreases, the dimension grows and reaches its maximum $(N+2)(N+4)(12+6N+N^2)/96$ for $\mathcal{M} = 0$, growing with N as N^4 .

For our subsequent discussion, it is useful to introduce another basis, which is defined as the simultaneous eigenstates of the number of particles \hat{N}_j , the angular momentum $\hat{\mathbf{S}}_j^2$, and the magnetization $\hat{S}_j^{(z)}$ in each $j = L, R$:

$$\begin{aligned}
\hat{N}_j |s_j, m_j, n_j\rangle &= n_j |s_j, m_j, n_j\rangle, \\
\hat{\mathbf{S}}_j^2 |s_j, m_j, n_j\rangle &= s_j(s_j + 1) |s_j, m_j, n_j\rangle, \\
\hat{S}_j^{(z)} |s_j, m_j, n_j\rangle &= m_j |s_j, m_j, n_j\rangle, \quad (6.25)
\end{aligned}$$

and where the sum $s_j + n_j$ has to be even [147].

It is interesting to compare the results derived from the mean-field approach (see Sec. 6.2) with the ones resulting from the Bose-Hubbard model in the spinorial case. The standard procedure to match these two approaches consists in replacing the field operators

$\hat{a}_{\alpha j}(\hat{a}_{\alpha j}^\dagger)$ by c-numbers $\sqrt{N_{\alpha j}}e^{i\phi_{\alpha j}}(\sqrt{N_{\alpha j}}e^{-i\phi_{\alpha j}})$. The obtained semiclassical Hamiltonian is

$$\begin{aligned} H_s = & -2J \sum_{m=0,\pm 1} \sqrt{N_{mL}N_{mR}} \cos \delta\phi_m + \frac{U_0}{2}(N_L^2 + N_R^2) + \frac{U_2}{2} \left[(N_{+1L} - N_{-1L})^2 + 2N_{0L} \right. \\ & + (N_{+1L} + N_{-1L})(2N_{0L} + 1) + 4N_{0L}\sqrt{N_{+1L}N_{-1L}} \cos \Delta\phi_L + (N_{+1R} - N_{-1R})^2 \\ & \left. + (N_{+1R} + N_{-1R})(2N_{0R} + 1) + 2N_{0R} + 4N_{0R}\sqrt{N_{+1R}N_{-1R}} \cos \Delta\phi_R \right]. \end{aligned} \quad (6.26)$$

Assuming that the variables (N_{mj}, ϕ_{mj}) are canonical conjugate, we obtain the equations of motion using Hamilton's equations $\dot{N}_{mj} = \partial H_s / \partial \phi_{mj}$ and $\dot{\phi}_{mj} = -\partial H_s / \partial N_{mj}$.

Remarkably, we find that the dynamics predicted by the usual semiclassical version of the Bose-Hubbard Hamiltonian and the mean-field two-mode equations derived in Sec. 6.2 is exactly the same, when $J = K$, $U_0 = 2\xi_0$ and $U_2 = 2\xi_2$.

6.4 Ground state properties

In this section, first we review the results for the ground state of a spinor $F = 1$ condensate confined in a single well, and then discuss the results found with the double well.

6.4.1 Single well

Mean-field description

The Gross-Pitaevskii equations, Eqs. (6.11), are invariant under the gauge transformation $\Psi \rightarrow e^{i\theta}\Psi$, where $\Psi = (\Psi_{-1}, \Psi_0, \Psi_{+1})$, and any spin rotation $\Psi \rightarrow \mathcal{U}(\alpha, \beta, \tau)\Psi$, where $\mathcal{U}(\alpha, \beta, \tau) = e^{-iF_z\alpha}e^{-iF_y\beta}e^{-iF_z\tau}$. F_i are the corresponding spin-1 matrices, and (α, β, τ) the Euler angles [53], that define the spin rotation, with ranges $\theta, \alpha, \tau \in (-\pi, \pi)$ and $\beta \in (-\pi/2, \pi/2)$. This invariance leads to a degeneracy in the eigenstates of the Hamiltonian [53].

For the polar case, $c_2 > 0$, the degenerate ground state is:

$$|\Psi_{\text{g.s.}}\rangle_{c_2>0} = e^{i\theta} \begin{pmatrix} -\frac{1}{\sqrt{2}}e^{-i\alpha} \sin \beta \\ \cos \beta \\ \frac{1}{\sqrt{2}}e^{i\alpha} \sin \beta \end{pmatrix}, \quad (6.27)$$

that has an average number of atoms in the different components of $(N_{-1}, N_0, N_{+1}) = (\sin^2 \beta, 2 \cos^2 \beta, \sin^2 \beta)/2$, depending only on β .

For the ferromagnetic case, $c_2 < 0$, the ground state set is:

$$|\Psi_{\text{g.s.}}\rangle_{c_2<0} = e^{i\theta-\tau} \begin{pmatrix} e^{-i\alpha} \cos^2 \frac{\beta}{2} \\ \sqrt{2} \cos \frac{\beta}{2} \sin \frac{\beta}{2} \\ e^{i\alpha} \sin^2 \frac{\beta}{2} \end{pmatrix}, \quad (6.28)$$

with $(N_{-1}, N_0, N_{+1}) = (\cos^4(\beta/2), (\sin^2 \beta)/2, \sin^4(\beta/2))$.

Note that, for the particular case of $\mathcal{M} = 0$, the angle β can take any value for $c_2 > 0$ whereas only one value is allowed for $c_2 < 0$, i.e. $\beta = \pi/2$.

Quantized description

As the number of particles is fixed, in the quantized Hamiltonian:

$$H = \frac{U_0}{2} \hat{N}(\hat{N} - 1) + \frac{U_2}{2} (\hat{\mathbf{S}}^2 - 2\hat{N}) , \quad (6.29)$$

the only relevant term to find the ground state is the one proportional to U_2 [144]. In the following, we consider an even number of particles, although similar arguments apply for an odd N .

For $U_2 > 0$, the ground state has the minimal value of \hat{S}^2 , i.e. $s = 0$, and there is only one possible magnetization $\mathcal{M} = 0$. In the basis labeled by $|N_{-1}, N_0, N_{+1}\rangle$, the ground state can be written as [144]:

$$|\Psi_{\text{g.s.}}\rangle = \sum_{k=0}^{N/2} A_k |k, N - 2k, k\rangle , \quad (6.30)$$

$$A_k = -\sqrt{\frac{N - 2k + 2}{N - 2k + 1}} A_{k-1} , \quad (6.31)$$

which gives an average number of atoms of $\langle \hat{N}_{+1} \rangle = \langle \hat{N}_0 \rangle = \langle \hat{N}_{-1} \rangle = N/3$ and large fluctuations in each component, e.g. $\langle \Delta \hat{N}_0 \rangle \approx 2N/\sqrt{5}$ for $N \gg 1$.

On the other hand, when $U_2 < 0$ the ground state maximizes the pseudo-spin, so that $s = N$, and the magnetization can take any even value from $\mathcal{M} = 0$ to $\mathcal{M} = \pm N$. These states have the general form:

$$|\Psi_{\text{g.s.}}\rangle = \sum_k B_k^{(\mathcal{M})} |k, N - 2k - \mathcal{M}, k + \mathcal{M}\rangle , \quad (6.32)$$

where the amplitudes $B_k^{(\mathcal{M})}$ are obtained by applying repeatedly the rising operator $S^{(+)}$ on the initial state $|N, 0, 0\rangle$, which has $\mathcal{M} = -N$ and only $B_N^{(-N)} = 1$. In this case, the amplitudes $B_k^{(\mathcal{M})}$ have a narrow distribution around a certain k value, which indicates that the number of particles in each component is reasonably well defined [144].

Finally, note that in both cases the BH description is compatible with the mean-field results presented in Sec. 6.2 when $N \gg 1$.

6.4.2 Double well

Mean-field description

For a spinor $F = 1$ condensate with zero magnetization, we obtain the ground state by minimizing the semiclassical two-mode Hamiltonian. We assume that the ground state has the same population imbalance for each component $\alpha = 0, \pm 1$, $z_\alpha \equiv z$, and the same phase difference $\delta\phi_\alpha \equiv \delta\phi$.

The solution for z , $\delta\phi$, is the same as in the scalar case but with an interaction parameter $\Lambda = NU_0/(2J)$ for $U_2 > 0$, and $\Lambda = N(U_0 + U_2)/(2J)$ for $U_2 < 0$. In Fig. 6.5 we plot the bifurcation point, defined by $\Lambda = \Lambda_c = -1$, as a function of both U_0/J and

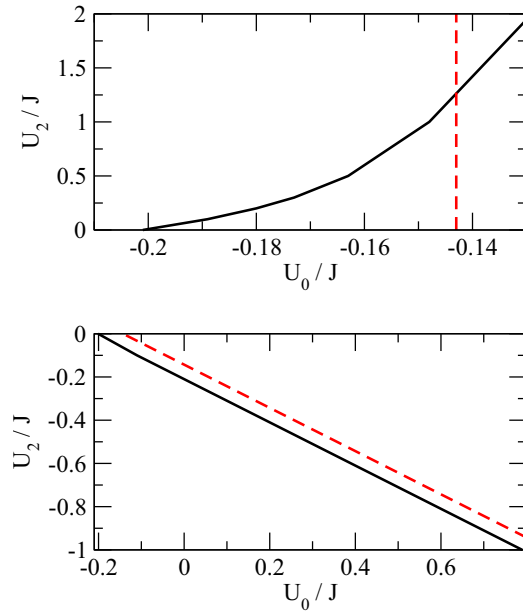


Figure 6.5: Characterization of the bifurcation for $U_2/J > 0$ (top) and $U_2/J < 0$ (bottom) for $N = 14$ and $\mathcal{M} = 0$. In dashed-red we plot the bifurcation point predicted by the mean-field two-mode description, that corresponds to $\Lambda_c = -1$. And in solid-black the bifurcation obtained with the two-site Bose-Hubbard model, which corresponds to the value of U_0/J , for each U_2/J , where the dispersion σ_z has an inflexion point.

U_2/J . Recall that the bifurcation point, see Sec. 5.3, was defined by the parameter Λ_c in which the population imbalance in the ground state goes from $z = 0$ to $z = \pm\sqrt{1 - 1/\Lambda^2}$.

The distribution in the number of particles and the phase $\Delta\phi_L$ for the ground state are found to be $(N/2, 0, N/2)$ and $\Delta\phi_L = \pi$ for $U_2 > 0$, and $(N/4, N/2, N/4)$ and $\Delta\phi_L = 0$ for $U_2 < 0$. These solutions are compatible with the semiclassical results for the single well.

Two-site Bose-Hubbard

We study the spin $F = 1$ condensate, where the ground state is found by diagonalizing the BH Hamiltonian Eq. (6.23) for a fixed number of particles and magnetization. The distribution of the number of particles of this state turns out to be only dependent of the sign of U_2 and equal to the distribution found for the single well, described by Eqs. (6.30) and (6.32). This is because neither J nor U_0 depend on the spin component m , and only the U_2 term determines the population of the components. Therefore, there are only two relevant parameters to characterize the GS: the total population imbalance $\hat{z} = \frac{1}{N} \sum_{\alpha} (\hat{N}_{\alpha L} - \hat{N}_{\alpha R})$ and its dispersion $\sigma_z = \sqrt{\langle \hat{z}^2 \rangle - \langle \hat{z} \rangle^2}$. In the following, we focus in the case of $\mathcal{M} = 0$.

Applying the same arguments used for the single well, for $U_2 > 0$ the ground state minimizes the pseudo-spin in each side, $s_L = s_R = 0$, so that effectively the U_2 term in the Hamiltonian for the ground state reduces to the constant term $-U_2 N$. The Hamiltonian is equivalent to a scalar Hamiltonian Eq. (5.10) with interaction U_0 , and thus, the bifurcation is independent of U_2 .

When $U_2 < 0$ the ground state maximizes the pseudo-spin in both sides, so $s_L = N_L$ and $s_R = N_R$, and the spin-changing term of the Hamiltonian reduces to:

$$\frac{U_2}{2} \left[\hat{N}_L(\hat{N}_L - 1) + \hat{N}_R(\hat{N}_R - 1) \right]. \quad (6.33)$$

This allows us to consider the Hamiltonian as a scalar one, Eq. (5.10), with an effective interaction $U_0 + U_2$.

The quantum analog of the semiclassical bifurcation is defined in a similar way as in the scalar case, and is taken, for every U_2/J , as the value of U_0/J for which σ_z has an inflexion point. In Fig. 6.5 we plot this point for different values of U_2 , where we can see that for $U_2 > 0$ (top) this point depends on the strength of the interaction in contrast to the mean-field two-mode predictions, also plotted. This means that the many-body state delocalizes when the value of U_2 is increased, and at some point, and due to the bias, localizes in the left region of the Fock space. This discrepancy between the full quantum and the semiclassical two-mode descriptions will be explained in the next section. On the other hand, when $U_2 < 0$, the bifurcation point has exactly the same dependence with the strength of U_2 as the mean-field two-mode prediction.

6.4.3 Spin driven symmetry breaking

In this section we derive analytically a Hamiltonian that allows us to explain why the system delocalizes as we increase the value of U_2 . To this aim, we study the ground state of the system when the spin interaction prevails on the hopping. In such cases, the system can be described in a reduced Hilbert space by means of an effective Hamiltonian. We characterize the *seniority* of the ground state [148], as the number of pairs of atoms that are coupled to total spin 0 in the many-body state. As we will see in the following, the symmetry breaking described in the previous section is directly linked to the presence of a large amount of spin-zero pairs in the many-body ground state.

It is useful to define the creation operator of a spin singlet:

$$\hat{\Theta}^\dagger = \hat{a}_0^{\dagger 2} - 2\hat{a}_1^\dagger \hat{a}_{-1}^\dagger, \quad (6.34)$$

which creates a two-particle spin-zero state. It can be applied to the vacuum k times to produce k singlets. This state, in the basis defined by (6.25) is:

$$|0, 0, 2k\rangle_j = \frac{(\hat{\Theta}^\dagger)^k}{\sqrt{(2k+1)!}} |0, 0, 0\rangle_j, \quad (6.35)$$

with $j = L, R$.

Fixing the total number of particles N and the total magnetization \mathcal{M} , the basis can be labeled only by four quantum numbers:

$$|s_L, m_L, n_L\rangle |s_R, \mathcal{M} - m_L, N - n_L\rangle = |s_L, s_R, m_L, n_L\rangle. \quad (6.36)$$

In Fig. 6.5 one can see that the spin interaction influences the occurrence of the bifurcation and its behavior changes depending on the sign of U_2 . The case of $U_2 < 0$

is easily understood, since in this regime the spin on each site tends to be as large as possible. When the system starts to localize one can assume that $\mathbf{S}_j^2 \simeq n_j(n_j + 1)$, so that Eq. (6.23) reduces to a scalar Bose-Hubbard Hamiltonian with an effective U_0 given by $U_0 + U_2$.

Also for $U_2 > 0$, Fig. 6.5 shows that the spin interaction leads to a bifurcation, but the explanation is not as straightforward as in the $U_2 < 0$ case. The mechanism at the basis of the localization is the creation of local singlets, promoted by the U_2 term, which competes with the hopping.

To understand this mechanism, let us consider the case of an even number of particles $N = 2N_S$ with $U_0 < 0$, in the limit where U_2 is the dominant energy scale ($U_2 \gg |U_0|, J$). We also impose that $|U_0| < \frac{4J}{N-1}$ i.e. smaller than the critical point for the bifurcation in the equivalent scalar case (see Appendix B). So the following constraints are satisfied $U_2 \gg J > (N-1)|U_0|/4$.

In this regime, the hopping can be considered as a perturbation and U_0 represents the smallest energy scale. The unperturbed Hamiltonian is:

$$\hat{H}_2 = \frac{U_2}{2} (\hat{\mathbf{S}}_L^2 + \hat{\mathbf{S}}_R^2) - U_2 \hat{N}, \quad (6.37)$$

whose ground state is degenerate:

$$|k\rangle \equiv |s_L = 0, s_R = 0, m_L = 0, n_L = 2k\rangle, \quad (6.38)$$

with $k = 0, 1, \dots, N_S$. This state represents k singlets in L and $N_S - k$ singlets in R . We note that the term $\hat{H}_0 = U_0 \hat{N}_L (\hat{N}_L - \hat{N}_R) + \frac{U_0 \hat{N}}{2} (\hat{N} - 1)$ commutes with \hat{H}_2 so, even if it is the smallest contribution, it can be included in the unperturbed Hamiltonian. Moreover, this term breaks the degeneracy:

$$\left(\hat{H}_0 + \hat{H}_2 \right) |k\rangle = \epsilon_0(k) |k\rangle, \quad (6.39)$$

with

$$\epsilon_0(k) = 4U_0 k (k - N_S) + U_0 N_S (2N_S - 1) - 2U_2 N_S. \quad (6.40)$$

The aim is to construct an effective perturbative Hamiltonian in this subspace:

$$H_{\text{eff}} = \sum_{k, k'} \epsilon_{k, k'} |k\rangle \langle k'|. \quad (6.41)$$

Since the hopping term destroys a singlet, allowing one particle to move from one site to the other, in order to remain in the singlet subspace the first contribution to the effective Hamiltonian will be of second order in J . Following [149], the form of the effective Hamiltonian is:

$$H_{\text{eff}} = \sum_k \epsilon_0(k) |k\rangle \langle k| - \frac{J^2}{2} \sum_{k, k'} \langle k| \hat{H}_J \left[\sum_{\alpha} \left(\frac{1}{\bar{\epsilon}_0(\alpha) - \epsilon_0(k)} + \frac{1}{\bar{\epsilon}_0(\alpha) - \epsilon_0(k')} \right) |\psi_{\alpha}\rangle \langle \psi_{\alpha}| \right] \hat{H}_J |k'\rangle |k\rangle \langle k'|, \quad (6.42)$$

where

$$\hat{H}_J = \sum_{\sigma=0,\pm 1} \left(\hat{a}_{L,\sigma}^\dagger \hat{a}_{R,\sigma} + \hat{a}_{R,\sigma}^\dagger \hat{a}_{L,\sigma} \right), \quad (6.43)$$

and $|\psi_\alpha\rangle$ are intermediate states with one singlet broken but still eigenstates of $(\hat{H}_0 + \hat{H}_2)$ with

$$(\hat{H}_0 + \hat{H}_2) |\psi_\alpha\rangle = \bar{\epsilon}_0(\alpha) |\psi_\alpha\rangle. \quad (6.44)$$

In our case, α corresponds to a set of indexes $\{\sigma, \gamma, k\}$ characterizing the intermediate states:

$$|\psi_{\sigma,\gamma,k}\rangle = |s_L = 1, s_R = 1, m_L = \sigma, n_L = 2k + \gamma\rangle, \quad (6.45)$$

with $\sigma = 0, \pm 1$ and $\gamma = \pm 1$. Note that $|\sigma, 1, k\rangle = |\sigma, -1, k+1\rangle$ and $|\sigma, -1, k\rangle = |\sigma, 1, k-1\rangle$. So the form of the effective Hamiltonian is:

$$H_{\text{eff}} = \sum_k \left[D(k) |k\rangle \langle k| + T(k) (|k-1\rangle \langle k| + |k\rangle \langle k-1|) \right] \quad (6.46)$$

with

$$D(k) = \epsilon_0(k) - 3J^2 \left(\frac{f^2(k)}{\Delta_{k,1}} + \frac{g^2(k)}{\Delta_{k,-1}} \right), \quad (6.47)$$

$$T(k) = -\frac{J^2 3f(k-1)g(k)}{2} \left(\frac{1}{\Delta_{k,1}} + \frac{1}{\Delta_{k-1,1}} \right), \quad (6.48)$$

$$f(k) = \frac{1}{3} \sqrt{2(3N_S + k(2N_S - 3 - 2k))}, \quad (6.49)$$

$$g(k) = \frac{1}{3} \sqrt{2k(2N_S + 3 - 2k)} \quad (6.50)$$

$$\begin{aligned} \Delta_{k,\gamma} &= \bar{\epsilon}_0(\gamma, k) - \epsilon_0(k) = \\ &= 2U_2 + \gamma U_0 [4k + \gamma - 2N_S]. \end{aligned} \quad (6.51)$$

This Hamiltonian resembles the scalar one but with the singlets playing the role of the particle (see Appendix B). The hopping term is of the order of $\frac{T^2}{U_2}$. It is possible to see numerically that, for $U_0 = 0$, the ground state energy of H_{eff} scales as:

$$E_0^{\text{eff}}(U_0 = 0) = -c \frac{J^2}{U_2} N_s^2, \quad (6.52)$$

where c is a constant of the order of $c \simeq 0.7$. The presence of U_0 will give a correction

$$E_1^{\text{eff}} = U_0 N_s (N_s - 1). \quad (6.53)$$

As in the scalar case, $E_0^{\text{eff}} + E_1^{\text{eff}}$ has to be compared with the atomic limit $\frac{J^2}{U_2} = 0$, giving $\epsilon_0(0) = U_0 N_s (2N_s - 1)$. So the condition for the bifurcation is:

$$E_0^{\text{eff}} + E_1^{\text{eff}} \simeq U_0 N_s (2N_s - 1), \quad (6.54)$$

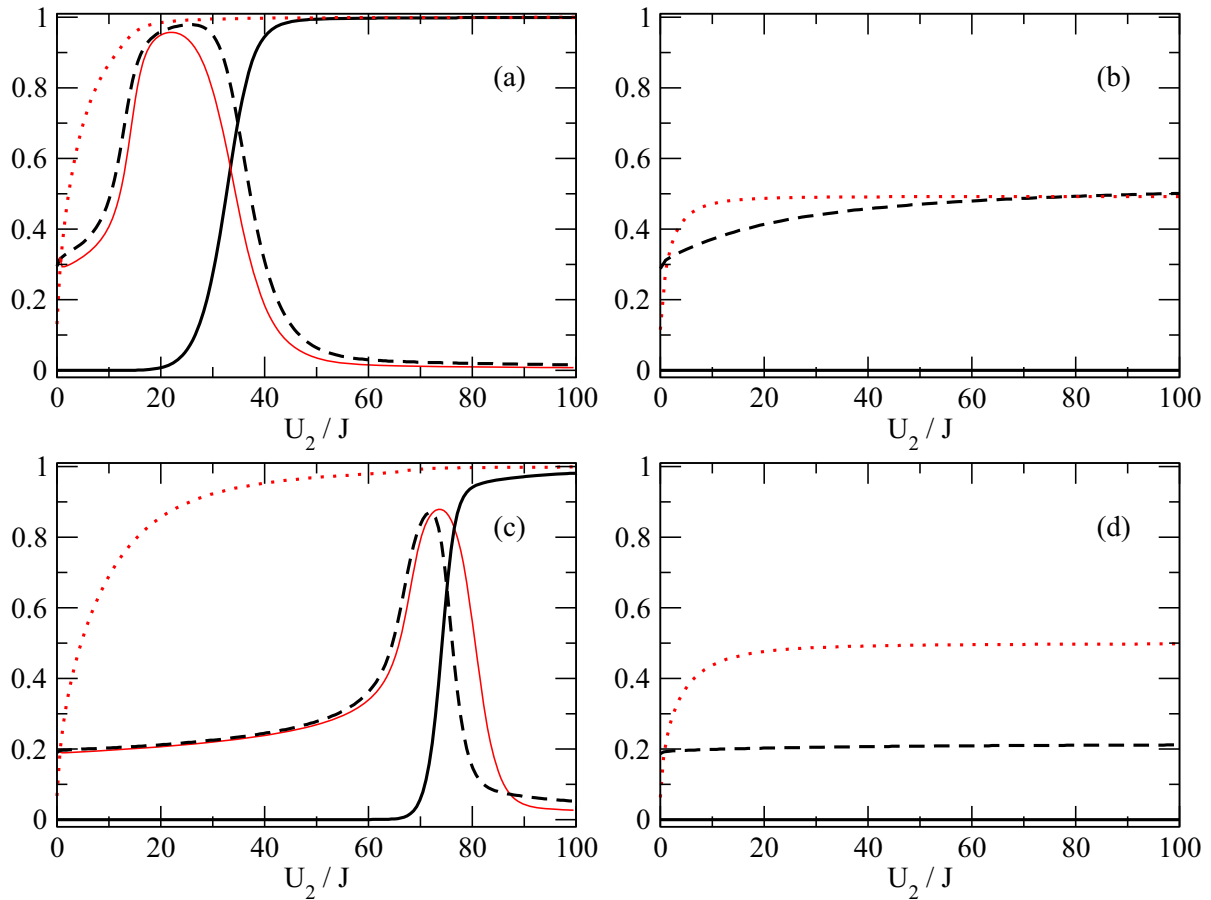


Figure 6.6: Expected value of the population imbalance $\langle \hat{z} \rangle$ (thick-solid) and its dispersion σ_z (thick-dashed) as a function of U_2/J and with $U_0/J = -0.05$ for two different number of particles $N = 14$ (a), $N = 15$ (b), $N = 30$ (c) and $N = 31$ (d); The analytical dispersion of the population imbalance (thin-solid-red) is also plotted in (a-c), as well as n_{ps}^L (a-c) and n_{ts}^L (b-d) (dotted-red). In all figures we take $\varepsilon_L/J = 10^{-6}$ and $\varepsilon_R/J = 0$.

which reads:

$$\frac{J^2}{U_2|U_0|} \simeq c. \quad (6.55)$$

It is worth stressing that these expansion is only valid for an even number of particles. Here, in contrast to what happens in the scalar case, the bifurcation condition seems independent on the number of particles. This is not completely true, because the condition (6.55) makes sense only if the bifurcation is not reached in the corresponding scalar case. This means (see Appendix B.11 for details) that $|U_0| < 4J/(N-1)$ and for large N the bifurcation needs higher values of U_2 to occur. In the limit of $N \rightarrow \infty$, there is no distinction between even and odd filling.

The BH model has been studied numerically by Davidson diagonalization method which allows to find the lowest eigenstates of sparse matrices. The diagonalization is carried out in the subspaces with fixed N and \mathcal{M} . In all the simulations we take a bias $\varepsilon_L = 10^{-6}$ and $\varepsilon_R = 0$.

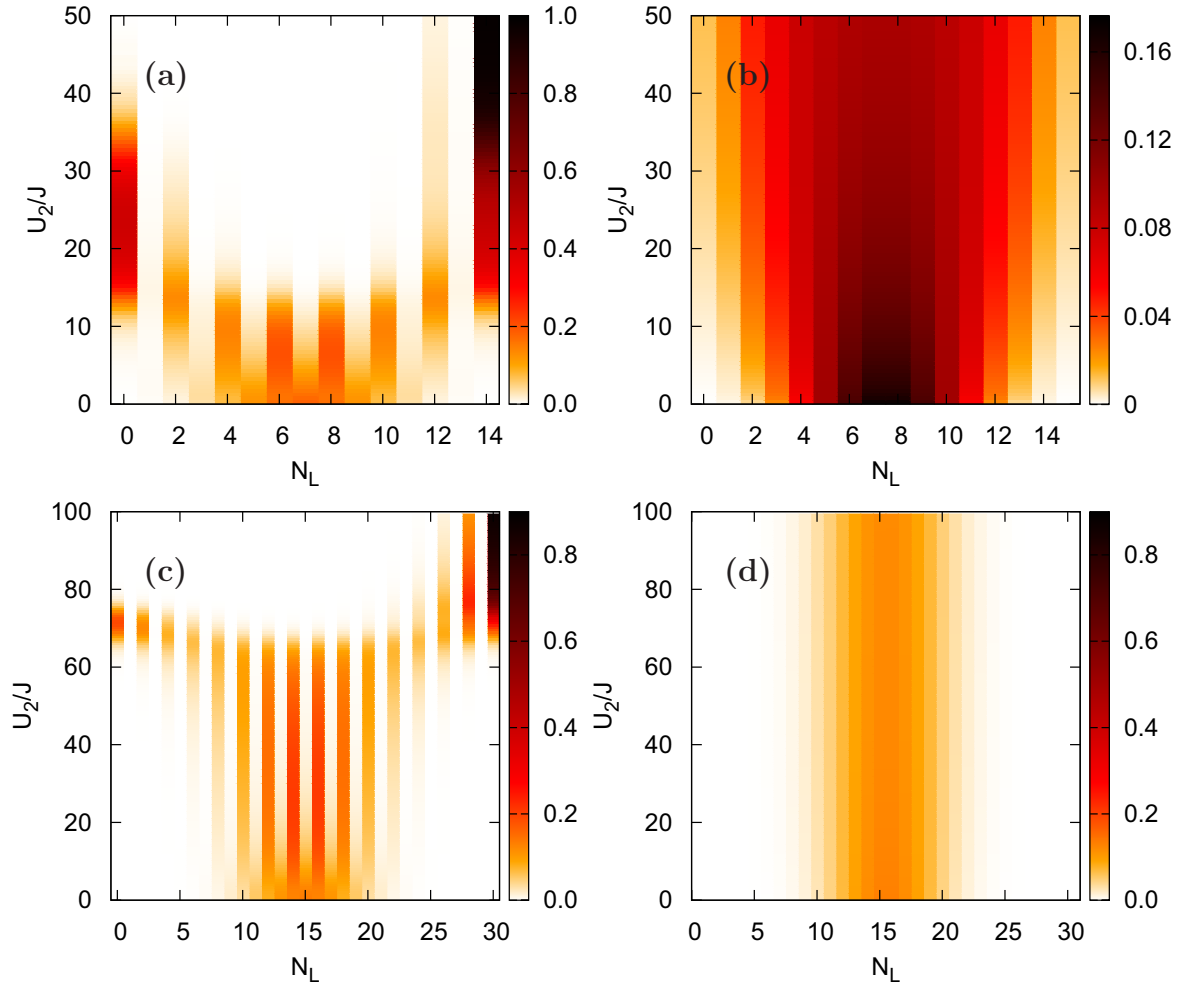


Figure 6.7: Representation of the ground state of a spinor condensate. The color corresponds to the value of the coefficients $|c_{N_L}|^2$, which are plotted as a function of the number of particles in the left well N_L and the interaction U_2/J , for $N = 14$ (a), $N = 15$ (b), $N = 30$ (c) and $N = 31$ (d). In all figures we take $U_0 = -0.05$, $\varepsilon_L/J = 10^{-6}$ and $\varepsilon_R/J = 0$.

One can write the ground state isolating the terms including singlets in L , R or both

$$\begin{aligned}
 |GS\rangle &= \sum_k c_k |0, 0, 2k\rangle_L |0, 0, N - k\rangle_R + \sum_k d_k^L |0, 0, 2k\rangle_L |\nu_k\rangle_R \\
 &+ \sum_k d_k^R |\nu_k\rangle_L |0, 0, 2k\rangle_R + |\phi_0\rangle,
 \end{aligned} \tag{6.56}$$

where $|\nu_k\rangle$ and $|\phi_0\rangle$ are not singlet states, i.e. they do not have the form (6.35). The component in which both sites are populated only by singlets is referred as *pure singlet* component, meaning that it lies in the subspace of singlets defined in the perturbative expansion. So, we can define the average density of pure singlets on site L as

$$n_{ps}^L = \frac{2}{N} \sum_k k |c_k|^2, \tag{6.57}$$

and the average density of total singlets on site L as

$$n_{ts}^L = \frac{2}{N} \sum_k k (|c_k|^2 + |d_k|^2). \quad (6.58)$$

Clearly, if the number of bosons is odd, $n_{ps}^L = 0$ and singlets can be created only in one site.

Here, we fix a value of U_0 corresponding to a state out of the bifurcation in the scalar case, and increase the value of U_2 . In Fig. 6.6 (a) and (c) we plot the value of n_{ps}^L for an even number of particle as a function of U_2 . As expected, increasing U_2 the density of pure singlets grows and saturates to one, confirming the validity of the Hilbert space truncation we did in the perturbative expansion. In the same plots, the population imbalance and its dispersion are also reported, showing the occurrence of a quantum analogous to the bifurcation. As discussed In Sec. 6.4.2, the bifurcation can be characterized by the inflection point of the dispersion, which appears when almost all the population is constituted by singlets. The exact dispersion is compared with the one obtained from the effective Hamiltonian, showing a good agreement.

As previously commented, for any finite number of particles, no localization should occur since the spatial symmetry is not broken. Nevertheless, after the bifurcation point, the small symmetry breaking induced by the bias is sufficient to localize the condensate. When this occurs, the dispersion of the imbalance drops abruptly. This phenomenon appears evident looking at the density distribution of the L -site (Figs. 6.7 (a) and (c)). Here, we observe that the density, symmetric and unimodal for small U_2 , spreads when increasing U_2 . At the same time the odd occupation probabilities are suppressed because of the population of singlets. At the inflection point, the density becomes flat and starts to be bimodal. Then, the bias causes the localization on the left well.

On the other hand, the same analysis can be done for an odd number of particles (Figs. 6.6 and 6.7 (b) and (d)). Here, as stressed before, there are no pure singlets components and the density of total singlet is plotted, showing a saturation to $1/2$. No bifurcation appears and the imbalance dispersion does not have inflection points. This difference between the even and odd cases disappears for a large number of particles when no bifurcation should occur, recovering the semiclassical picture where the bifurcation is independent on U_2 .

Chapter 7

Temperature effects in spinor BEC

Spin-changing collisions usually involve quite small energies. For example, in the previous chapter, we had to increase the number of particles in the mean-field simulations in order to enhance population transfer effects, see Sec. 6.2. In this chapter, we take profit of this low-energy process to get information about the system. For instance, if we consider a $F = 1$ condensate with atoms in the $m = 0$ manifold, even at very low energies, we should get a certain population of the other two components $m = \pm 1$. Furthermore, by measuring these populations we should be able to infer the temperature of the system.

BEC thermometry is typically performed using time-of-flight measurements, either from the expansion velocity of the thermal cloud or from a bimodal fitting which allows to establish the ratio between the shapes of the condensate and the thermal cloud. These techniques fail however for very low temperatures for which the thermal population is small compared to the number of particles in the condensate, see Fig. 7.1. Another recent proposal is the use of low-energy phase fluctuations for thermometry, by observing the temperature dependent phase difference between condensates in a double-well potential [150].

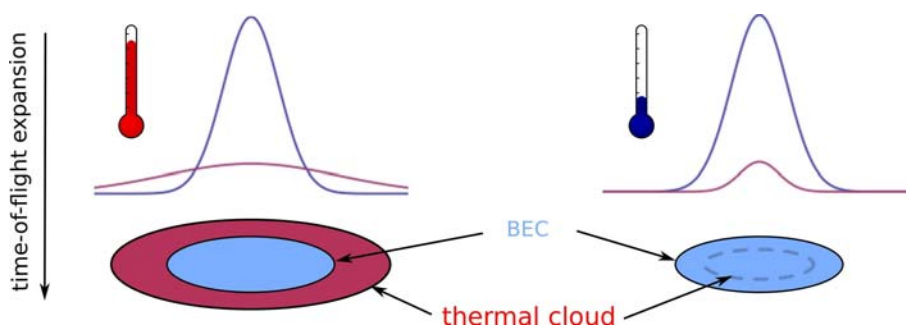


Figure 7.1: At high temperatures (left) both the thermal cloud and the condensate are visible when a time-of-flight measurement is done. At low temperatures (right) if the number of particles in the condensate is much larger than the number of particles in the thermal cloud, the latter one is not visible.

In recent years, an important effort has been devoted to produce systems of ultracold atoms with an atom-atom interaction more complicated than the contact interaction. An important step on this direction has been the condensation of ultracold gases with

dipole-dipole interactions. Dipolar interactions are completely different from contact interactions: 1) they are long-ranged, in contrast to the short-ranged Van-der-Waals forces, usually parametrized in BEC physics as contact interactions, and 2) they are anisotropic, coupling in some cases the spin and angular momentum degrees of freedom. The current status on dipolar BEC has been reviewed in Ref. [52].

In this chapter, we study spin fluctuations in spinor BECs and dipolar spinor BECs, and in particular the dependence of these fluctuations on temperature [99]. We will see that the very low energy associated to both spin-changing collisions and spin-relaxation due to dipole-dipole interactions, opens interesting possibilities for thermometry purposes down to extremely low temperatures (first very promising results on spin thermometry in chromium have been reported in Ref. [151]). Moreover, we show that the dependence of the entropy of the gas on the Zeeman energy allows for a possible mechanism for adiabatic cooling.

In Sec. 7.1 we analyze the case of a stable spin-1 BEC prepared in the $m = 0$ Zeeman sublevel. We study by means of the corresponding Bogoliubov analysis the thermally activated spin fluctuations resulting from spin-changing collisions. Sec. 7.2 is devoted to the case of a chromium condensate prepared in the maximally stretched Zeeman state, $m = -3$. This case differs significantly from the spin-1 case, since the thermally activated spin fluctuations result from the spin-relaxation induced by the dipole-dipole interactions. In both scenarios spin fluctuations may be employed for deep temperature thermometry and adiabatic cooling.

7.1 $F = 1$ spinor BEC

The many-body Hamiltonian of a $F = 1$ spinor BEC was discussed in Chap. 6, Eq. (6.3):

$$\hat{H} = \int d\mathbf{r} \left[\hat{\Psi}_m^\dagger \left(H_{\text{sp}} + H_m \right) \hat{\Psi}_m + \frac{c_0}{2} \hat{\Psi}_m^\dagger \hat{\Psi}_n^\dagger \hat{\Psi}_n \hat{\Psi}_m + \frac{c_2}{2} \hat{\Psi}_m^\dagger \hat{\Psi}_{m'}^\dagger \mathbf{F}_{mn} \cdot \mathbf{F}_{m'n'} \hat{\Psi}_{n'} \hat{\Psi}_n \right], \quad (7.1)$$

where we have included a term that describes the effect of an external magnetic field [95, 144],

$$H_m = pm + qm^2. \quad (7.2)$$

The term $p = g_L \mu_B B_0$ characterizes the linear Zeeman effect in a homogeneous magnetic field B_0 , with g_L the Landé factor and μ_B the Bohr magneton. The quadratic Zeeman effect is described by the factor $q = \mu_B^2 B_0^2 / 8C_{\text{hfs}}$, where C_{hfs} is the hyperfine coupling strength. Note that collisions conserve the total spin projection and hence the linear Zeeman energy is a conserved quantity which may be gauged out.

In the following, we assume a condensate stable in the $m = 0$ component (we will discuss the conditions for stability below). We will be particularly interested in the creation of spin excitations in $m = \pm 1$ due to spin-changing collisions. In the presence of fluctuations the spinor BEC is described by the field operator $\hat{\Psi} = (0, \Psi_0, 0) + (\delta\hat{\Psi}_{-1}, \delta\hat{\Psi}_0, \delta\hat{\Psi}_{+1})$, where the BEC wavefunction Ψ_0 fulfills the Gross-Pitaevskii equation

$$\left[-\frac{\hbar^2 \nabla^2}{2M} + V_{\text{ext}}(\mathbf{r}) + c_0 n_0(\mathbf{r}) \right] \Psi_0(\mathbf{r}) = \mu \Psi_0(\mathbf{r}). \quad (7.3)$$

This component is considered as a particle reservoir with a constant chemical potential μ , and a density profile $n_0(\mathbf{r}) = |\Psi_0(\mathbf{r})|^2$.

To describe the fluctuations of the system in the $m = \pm 1$ components, it is convenient to work in the grand canonical ensemble (gc) $\hat{H}^{\text{gc}} = \hat{H} - \mu\hat{N}$. This statistical ensemble considers the system in equilibrium with an external reservoir with respect to both particle and energy exchange.

Retaining up to second order in the fluctuations $\delta\hat{\Psi}_{\pm 1}$ we obtain an effective Hamiltonian for $\delta\hat{\Psi}_{\pm 1}$

$$\begin{aligned} \hat{H}_{\text{gc}}^{(2)} &= \sum_{m=\pm 1} \int d\mathbf{r} \delta\hat{\Psi}_m^\dagger(\mathbf{r}) \left[-\frac{\hbar^2 \nabla^2}{2M} + \mathcal{V}(\mathbf{r}) + q \right] \delta\hat{\Psi}_m(\mathbf{r}) \\ &+ c_2 \int d\mathbf{r} n_0(\mathbf{r}) \left[\delta\hat{\Psi}_{+1}(\mathbf{r}) \delta\hat{\Psi}_{-1}(\mathbf{r}) + \delta\hat{\Psi}_{+1}^\dagger(\mathbf{r}) \delta\hat{\Psi}_{-1}^\dagger(\mathbf{r}) \right], \end{aligned}$$

where $\mathcal{V}(\mathbf{r}) = V_{\text{ext}}(\mathbf{r}) + (c_0 + c_2)n_0(\mathbf{r}) - \mu$ is a time-independent density-dependent effective potential. To describe the system, it is useful to define the basis $\psi(k, \mathbf{r})$, where k labels the necessary quantum numbers to characterize the single particle states which are defined by the eigenfunctions of the effective Hamiltonian $H_{\text{eff}} = -\hbar^2 \nabla^2 / (2M) + \mathcal{V}(\mathbf{r}) + q$, with eigenvalues $H_{\text{eff}}\psi(k, \mathbf{r}) = \varepsilon_k \psi(k, \mathbf{r})$.

In the next sections, we discuss: A) The particular case of an homogeneous external potential, where the diagonalization of $H_{\text{gc}}^{(2)}$ can be performed analytically, B) The case of a trapped condensate using a local density approximation.

7.1.1 Homogeneous condensate

When the trapping potential $V_{\text{ext}}(\mathbf{r}) = V_0$ is constant in space, and set to zero for simplicity, the order parameter of the $m = 0$ condensate Ψ_0 , is a constant function, and Eq. (7.3) reduces to $\mu = c_0 n_0$. The effective potential is also a constant $\mathcal{V} = c_2 n_0$ and the eigenfunctions of the effective Hamiltonian (H_{eff}) are plane waves $\hat{\psi}(\mathbf{k}, \mathbf{r}) = 1/(2\pi)^{3/2} e^{i\mathbf{k}\cdot\mathbf{r}}$, where \mathbf{k} is the momentum of the atom. The fluctuations $\delta\hat{\Psi}_{\pm 1}$ in this basis are:

$$\delta\hat{\Psi}_m(\mathbf{r}) = \int d\mathbf{k} \delta\hat{\Psi}_m(\mathbf{k}) \frac{e^{i\mathbf{k}\cdot\mathbf{r}}}{(2\pi)^{3/2}}, \quad (7.4)$$

and the eigenvalues of H_{eff} are $\varepsilon_k = \frac{\hbar^2 k^2}{2M} + c_2 n_0 + q$. The Hamiltonian Eq. (7.4) in momentum space becomes:

$$\begin{aligned} \hat{H}_{\text{gc}}^{(2)} &= \int d\mathbf{k} \varepsilon_k \sum_{m=\pm 1} \delta\hat{\Psi}_m^\dagger(\mathbf{k}) \delta\hat{\Psi}_m(\mathbf{k}) \\ &+ c_2 n_0 \int d\mathbf{k} \left[\delta\hat{\Psi}_{+1}(\mathbf{k}) \delta\hat{\Psi}_{-1}(-\mathbf{k}) + \delta\hat{\Psi}_{+1}^\dagger(\mathbf{k}) \delta\hat{\Psi}_{-1}^\dagger(-\mathbf{k}) \right]. \end{aligned} \quad (7.5)$$

To diagonalize this Hamiltonian, it is convenient to introduce the symmetric and anti-symmetric operators

$$\hat{S}_{\mathbf{k}} = \frac{1}{\sqrt{2}} \left(\delta\hat{\Psi}_{+1}(\mathbf{k}) + \delta\hat{\Psi}_{-1}(\mathbf{k}) \right); \quad \hat{A}_{\mathbf{k}} = \frac{1}{\sqrt{2}} \left(\delta\hat{\Psi}_{+1}(\mathbf{k}) - \delta\hat{\Psi}_{-1}(\mathbf{k}) \right), \quad (7.6)$$

that also fulfill bosonic commutation relations i.e., $[\hat{S}_{\mathbf{k}}, \hat{S}_{\mathbf{k}'}^\dagger] = [\hat{A}_{\mathbf{k}}, \hat{A}_{\mathbf{k}'}^\dagger] = \delta(\mathbf{k} - \mathbf{k}')$ and all the other commutators relating these two operators equal to zero. Using these operators, the Hamiltonian Eq. (7.5) splits into two different parts, $\hat{H}_{(2)}^{\text{gc}} = \hat{H}_S + \hat{H}_A$, with:

$$\begin{aligned}\hat{H}_S &= \int d\mathbf{k} \left(\frac{\hbar^2 k^2}{2M} + c_2 n_0 + q \right) \hat{S}_{\mathbf{k}}^\dagger \hat{S}_{\mathbf{k}} + \frac{c_2 n_0}{2} \int d\mathbf{k} \left[\hat{S}_{\mathbf{k}}^\dagger \hat{S}_{-\mathbf{k}}^\dagger + \hat{S}_{\mathbf{k}} \hat{S}_{-\mathbf{k}} \right] \\ \hat{H}_A &= \int d\mathbf{k} \left(\frac{\hbar^2 k^2}{2M} + c_2 n_0 + q \right) \hat{A}_{\mathbf{k}}^\dagger \hat{A}_{\mathbf{k}} - \frac{c_2 n_0}{2} \int d\mathbf{k} \left[\hat{A}_{\mathbf{k}}^\dagger \hat{A}_{-\mathbf{k}}^\dagger + \hat{A}_{\mathbf{k}} \hat{A}_{-\mathbf{k}} \right].\end{aligned}$$

As the modes associated to $\hat{S}_{\mathbf{k}}$ and $\hat{A}_{\mathbf{k}}$ are decoupled, we can solve separately the two pieces (\hat{H}_S, \hat{H}_A) of the Hamiltonian. First we apply a Bogoliubov transformation to the symmetric mode \hat{S} :

$$\hat{S}_{\mathbf{k}} = r_{\mathbf{k}} \hat{B}_{\mathbf{k}}^{(S)} + t_{\mathbf{k}} \hat{B}_{-\mathbf{k}}^{(S)\dagger}; \quad \hat{S}_{\mathbf{k}}^\dagger = r_{\mathbf{k}}^* \hat{B}_{\mathbf{k}}^{(S)\dagger} + t_{\mathbf{k}}^* \hat{B}_{-\mathbf{k}}^{(S)}. \quad (7.7)$$

In the homogeneous case, the coefficients r_k and t_k are real and depend only on the modulus of \mathbf{k} . Moreover, as the operators $\hat{B}_{\mathbf{k}}^{(S)}$ and $\hat{B}_{\mathbf{k}}^{(S)\dagger}$ should also fulfill bosonic commutation rules, $[\hat{B}_{\mathbf{k}}^{(S)}, \hat{B}_{\mathbf{k}'}^{(S)}] = [\hat{B}_{\mathbf{k}}^{(S)\dagger}, \hat{B}_{\mathbf{k}'}^{(S)\dagger}] = 0$ and $[\hat{B}_{\mathbf{k}}^{(S)}, \hat{B}_{\mathbf{k}'}^{(S)\dagger}] = \delta(\mathbf{k} - \mathbf{k}')$, it turns out that the coefficients, r_k and t_k , have to be related by $r_k^2 - t_k^2 = 1$.

In terms of these new operators the hamiltonian \hat{H}_S becomes:

$$\begin{aligned}\hat{H}_S &= \int d\mathbf{k} \left\{ \varepsilon_k \left[r_k^2 \hat{B}_{\mathbf{k}}^{(S)\dagger} \hat{B}_{\mathbf{k}}^{(S)} + t_k^2 \hat{B}_{-\mathbf{k}}^{(S)} \hat{B}_{-\mathbf{k}}^{(S)\dagger} \right] + c_2 n_0 r_k t_k \left[\hat{B}_{\mathbf{k}}^{(S)\dagger} \hat{B}_{\mathbf{k}}^{(S)} + \hat{B}_{-\mathbf{k}}^{(S)\dagger} \hat{B}_{-\mathbf{k}}^{(S)} + 1 \right] \right. \\ &\quad \left. + \left[\varepsilon_k r_k t_k + \frac{c_2 n_0}{2} (r_k^2 + t_k^2) \right] \left(\hat{B}_{\mathbf{k}}^{(S)\dagger} \hat{B}_{-\mathbf{k}}^{(S)\dagger} + \hat{B}_{-\mathbf{k}}^{(S)} \hat{B}_{\mathbf{k}}^{(S)} \right) \right\}. \quad (7.8)\end{aligned}$$

The relation $r_k^2 - t_k^2 = 1$ suggests the introduction of a new variable γ_k , through the change of variable: $r_k = \cosh \gamma_k$ and $t_k = \sinh \gamma_k$. The non-diagonal term in Eq. (7.8) can be eliminated by imposing the condition

$$\varepsilon_k r_k t_k + \frac{c_2 n_0}{2} (r_k^2 + t_k^2) = 0, \quad (7.9)$$

which expressed in terms of γ_k reads $\tanh(2\gamma_k) = -(c_2 n_0)/\varepsilon_k$. Rearranging terms in the Hamiltonian \hat{H}_S and dropping a constant factor $\frac{c_2 n_0}{2} \sinh 2\gamma_k$, we obtain:

$$\hat{H}_S = \int d\mathbf{k} \sqrt{\varepsilon_k^2 - c_2^2 n_0^2} \hat{B}_{\mathbf{k}}^\dagger \hat{B}_{\mathbf{k}}, \quad (7.10)$$

which is already in diagonal form, with an energy spectrum that only depends on the modulus of \mathbf{k} :

$$E_k = \sqrt{\varepsilon_k^2 - c_2^2 n_0^2}. \quad (7.11)$$

Considering now the part of the Hamiltonian containing the asymmetric operator $\hat{A}_{\mathbf{k}}$, we find a similar result with $\tanh(2\gamma_k^A) = c_2 n_0/\varepsilon_k$, and the same energies E_k . Therefore, the total Hamiltonian, Eq. (7.5), except for a constant term, becomes:

$$\hat{H}_{\text{gc}}^{(2)} = \int d\mathbf{k} E_k \left[\hat{B}_{\mathbf{k}}^{(S)\dagger} \hat{B}_{\mathbf{k}}^{(S)} + \hat{B}_{\mathbf{k}}^{(A)\dagger} \hat{B}_{\mathbf{k}}^{(A)} \right], \quad (7.12)$$

where $B_{\mathbf{k}}^{(S)}$ and $B_{\mathbf{k}}^{(A)}$ are independent modes. Note that these excitations are stable as long as E_k is real, which reduces to the stability condition: $q > q_{cr}$, with $q_{cr} = (|c_2| - c_2)n_0$. As we can see, only the spin-dependent interactions change the critical value of the magnetic field for which the $m = 0$ component is stable. This is because these interactions are responsible for the transferring of atoms to the other two components $m = \pm 1$. Finally, the number of particles populating component m with momentum \mathbf{k} ,

$$n_{\pm 1}(\mathbf{k}) = \delta\hat{\Psi}_{\pm 1}^\dagger(\mathbf{k})\delta\hat{\Psi}_{\pm 1}(\mathbf{k}), \quad (7.13)$$

can be written in terms of the Bogoliubov operators $\hat{B}_{\mathbf{k}}^{(S)}$ and $\hat{B}_{\mathbf{k}}^{(A)}$, and their conjugates.

Once the Hamiltonian has been diagonalized, Eq. (7.12), and the stability condition is satisfied, one can easily obtain the thermal average of an observable, by taking into account the thermal occupation of the different eigenmodes:

$$\langle \hat{B}_{\mathbf{k}}^{(i)\dagger} \hat{B}_{\mathbf{k}}^{(i)} \rangle = \frac{1}{e^{-\beta E_{\mathbf{k}}^{(i)}} - 1}, \quad (7.14)$$

with $i = S, A$, $\beta = 1/(k_B T)$, and k_B the Boltzman constant. Moreover, one can realize that the crossed thermal averages $\langle \hat{B}_{\mathbf{k}}^{(S)\dagger} \hat{B}_{\mathbf{k}}^{(A)} \rangle = \langle \hat{B}_{\mathbf{k}}^{(A)\dagger} \hat{B}_{\mathbf{k}}^{(S)} \rangle = 0$.

Using the occupation of the eigenmodes, one can establish the appearance and occupation of atoms in the states with spin component $m = \pm 1$

$$\langle n_{\pm 1}(k) \rangle = \frac{\varepsilon_k}{E_k} \frac{1}{e^{\frac{E_k}{k_B T}} - 1} + \frac{\varepsilon_k}{2E_k} - \frac{1}{2}, \quad (7.15)$$

which results the same for both components. The occupation of the $m \pm 1$ states gives a measure of the thermal depletion of the $m = 0$ condensate.

Note, however, that in Eq. (7.15) there is a temperature-independent term, which survives when temperature goes to zero. This term represents the depletion of the condensate associated to quantum fluctuations.

Integrating the momentum distribution, one gets the total density:

$$\langle n_{\pm 1} \rangle = \frac{1}{(2\pi)^3} \int d\mathbf{k} \langle n_{\pm 1}(k) \rangle. \quad (7.16)$$

For a magnetic field equal to the critical value, $q_{cr} = -2c_2 n_0$, the density of atoms in the spin component $m = \pm 1$ reads

$$\langle n_{\pm 1} \rangle = 4\pi k_0^3 \mathcal{F}(T), \quad (7.17)$$

where $k_0^2 = 2M|c_2|n_0/\hbar^2$, and

$$\mathcal{F}[T] = \int_0^\infty x^2 dx \left[\frac{(x^2 + 1)}{\sqrt{x^2(x^2 + 2)}} \frac{1}{e^{\sqrt{x^2(x^2 + 2)} \frac{|c_2|n_0}{k_B T}} - 1} + \frac{(x^2 + 1)}{2\sqrt{x^2(x^2 + 2)}} - \frac{1}{2} \right]. \quad (7.18)$$

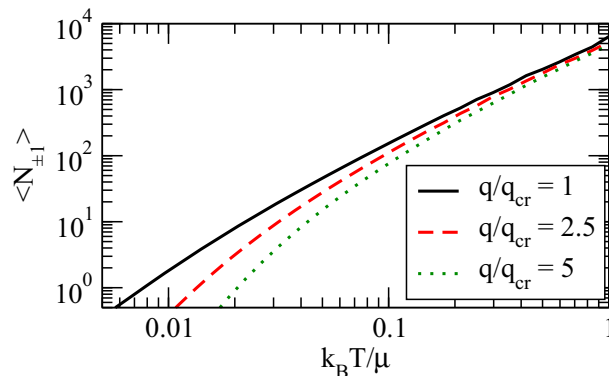


Figure 7.2: Total number of atoms $\langle N_{\pm 1} \rangle$ in the trap as a function of q/q_{cr} and $k_B T/\mu$ for the case discussed in the text.

7.1.2 Confined condensate: local density approximation

We consider at this point a trapped BEC in the Thomas-Fermi regime with density profile given by Eq. (2.17). For a sufficiently smooth density profile, we may employ the local density approximation (LDA): we associate to each value of the local density $n_0(\mathbf{r})$, a local chemical potential $\mu(\mathbf{r}) = \mu - V_{\text{ext}}(\mathbf{r}) = c_0 n_0(\mathbf{r})$, and the corresponding excitation spectrum for the homogeneous case with that density, $E_k(\mathbf{r})$. Then, we evaluate the local density for the $m = \pm 1$, $n_{\pm 1}(\mathbf{r})$, from the expressions obtained above. The total number of atoms is obtained by integrating their local occupation over the density profile of the trap:

$$\langle N_{\pm 1} \rangle = \int d^3r \langle n_{\pm 1}(\mathbf{r}) \rangle. \quad (7.19)$$

The critical value of the magnetic field, q_{cr} is calculated at the trap center.

We consider in the following the specific case of $F = 1$ ^{87}Rb , for which $a_0 = 101.8a_B$ and $a_2 = 100.4a_B$ (with a_B the Bohr radius). As a consequence, $c_2 = -4.6 \times 10^{-3}c_0$ is small and negative, which provides a critical $q_{cr}/\mu = 2|c_2|/c_0 = 9.25 \times 10^{-3}$. For simplicity we consider that the atoms are confined in a spherically symmetric trap, with a harmonic frequency $\omega = 2\pi \times 50\text{Hz}$. For a typical value of $N = 10^5$ atoms, the density at the trap center becomes 10^{14} cm^{-3} .

In Fig. 7.2 we plot the total number of atoms $\langle N_{\pm 1} \rangle$ in the trap as a function of $k_B T/\mu$ for different values of q/q_{cr} . As expected, when approaching the critical q_{cr} the spin population is enhanced at low temperatures, due to the very low energy associated to spin excitations. At $q = q_{cr}$ the population of $m = \pm 1$ (always for $N = 10^5$ atoms in the BEC) is larger than 10 atoms for temperatures larger than $0.02\mu/k_B$. Although these numbers may be very small to be observed experimentally, a simple procedure may significantly enhance the experimental resolution of such small populations. If the system is abruptly brought into instability by sweeping into $q < q_{cr}$, spin excitations grow in a process similar to parametric amplification in non-linear optics [152]. Within the so-called linear regime, spin fluctuations are hence exponentially amplified with a growth rate Γ . As a result the population in ± 1 , is enhanced in time in the form $N_{\pm 1}(t) \simeq N_{\pm 1}(0)e^{\Gamma t}$, where $N_{\pm 1}(0)$ is the population in $m = \pm 1$ prior to the destabilization, i.e. that depicted

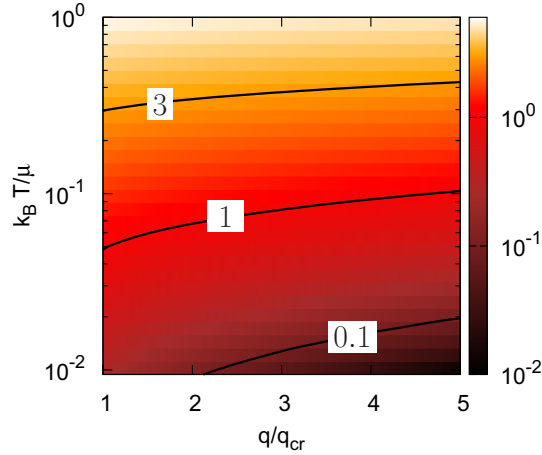


Figure 7.3: Entropy as a function of $k_B T/\mu$ and q/q_{cr} for the same case of Fig. 7.2. The black curves indicate various iso-entropic curves, the value of S/k_B is indicated.

in Fig. 7.2. A subsequent Stern-Gerlach arrangement in time-of-flight [152], allows for a separate imaging of the different Zeeman components. As a result even very small $N_{\pm 1}(0)$ may be experimentally resolved, opening the possibility of employing thermally activated spin fluctuations as a thermometer down to temperatures close to $0.01\mu/k_B$ where other thermometry methods typically fail.

Interestingly, the dependence of spin excitations on q may be employed as a possible mechanism for adiabatic cooling. For an homogeneous gas, the entropy density of the system is readily calculated from the spectrum of elementary excitations

$$\frac{s}{k_B} = -\frac{2}{(2\pi)^3} \int d\mathbf{k} \left[\ln(1 - e^{-E_k/k_B T}) + \frac{E_k}{k_B T} \frac{1}{1 - e^{-E_k/k_B T}} \right]. \quad (7.20)$$

Note that scalar excitations of the $m = 0$ condensate, $\frac{\hbar^2 k^2}{2M} \left(\frac{\hbar^2 k^2}{2M} + 2c_0 n_0 \right)$, corresponding to $\delta\hat{\Psi}_0$ fluctuations, also contribute in principle to the system entropy. However, if $c_2 \ll c_0$ (as it is typically the case), the entropy contribution of the scalar excitations may be neglected for $k_B T \ll \mu$. In particular, we have checked that for q in the vicinity of q_c the entropy contribution of the scalar modes is negligible for $k_B T/\mu < 0.25$. For a trapped gas, we employ again local density arguments, calculating the local entropy density associated to each position $s(\mathbf{r})$. Fig. 7.3 shows curves of equal entropy $S = \int d\mathbf{r} s(\mathbf{r})$ as a function of temperature and q/q_{cr} for the same case discussed in Fig. 7.2. Interestingly, the isotropic curves bend to lower temperatures when approaching q_{cr} . As a result, an adiabatic variation of the applied magnetic field may allow for adiabatic cooling. For example, in the figure, starting with $q = 5q_{cr}$ at $T = 0.1\mu/k_B$, the system may decrease its temperature down to $0.05\mu/k_B$ when approaching q_{cr} .

7.2 Dipolar $F = 3$ spinor BEC

In this section, we introduce the basic formalism of a dipolar scalar BEC together with the corresponding Thomas-Fermi approximation. Then, we consider the case of a chromium

BEC, which constitutes an example of spin-3 gas in which, crucially, strong magnetic dipole-dipole interactions induce spin relaxation. As a consequence the low temperature physics is considerably different compared to that of spin-1 BECs discussed in the previous section.

7.2.1 Dipolar scalar BEC

A dipolar scalar BEC is a single component BEC in which atoms have a high dipole magnetic moment, and therefore dipole-dipole interactions cannot be neglected. First, let us analyze in more detail the origin of this dipole-dipole interactions: The total angular momentum of the atoms $\mathbf{F} = \mathbf{I} + \mathbf{J}$ is the composition of the nuclear spin \mathbf{I} and the total angular momentum of its electrons $\mathbf{J} = \mathbf{S} + \mathbf{L}$, where \mathbf{S} and \mathbf{L} are the spin and orbital momenta, respectively. Because of this angular momentum, atoms have an intrinsic dipole magnetic moment μ_m ,

$$\mu_m = g_F \mu_B \sqrt{F(F+1)}, \quad (7.21)$$

with μ_B the Bohr magneton and g_J the Landé g-factor.

Due to the interaction between dipoles, these atoms have both contact and long-range interactions. For alkali gases the dipole-dipole interaction is usually neglected due to the small value of its magnetic dipole moment $\mu_m \simeq 1\mu_B$. In 2005, dipolar effects were observed for the first time with a BEC made of ^{52}Cr atoms [153], which can have a dipolar moment up to six times larger than alkali atoms ($\mu_m = 6\mu_B$), and thus, dipole-dipole interactions are 36 times stronger¹. Moreover, ^{164}Dy [47] and ^{168}Er [48] condensates have also been achieved very recently, and these atoms have an even larger dipolar moment (up to $\mu_m = 10\mu_B$ and $\mu_m = 7\mu_B$, respectively).

Let us consider a collection of atoms with their dipolar moments aligned in the z direction. The dipole-dipole interaction potential between two particles with dipole moment μ_m , and located at \mathbf{r} and \mathbf{r}' is:

$$V_{\text{dip}}(\mathbf{r} - \mathbf{r}') = 9\pi c_d \frac{1 - 3 \cos^2 \theta}{|\mathbf{r} - \mathbf{r}'|}, \quad (7.22)$$

where $c_d = \mu_0 \mu_m^2 / 36\pi^2$, μ_0 is the vacuum permeability, and θ is the angle between the vector $(\mathbf{r} - \mathbf{r}')$ and the magnetization axis z , see Fig. 7.4.

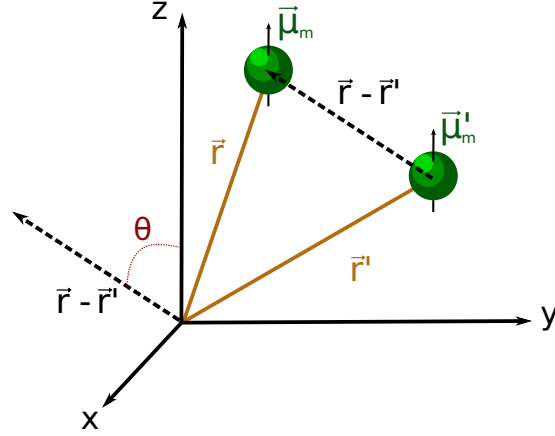
The TDGPE (2.15) with contact and dipole-dipole interaction becomes:

$$i\hbar \frac{\partial \Psi(\mathbf{r}, t)}{\partial t} = \left[H_{\text{sp}} + g_{3D} |\Psi(\mathbf{r}, t)|^2 + 9\pi c_d \int d\mathbf{r}' \frac{1 - 3 \cos^2 \theta}{|\mathbf{r} - \mathbf{r}'|} |\Psi(\mathbf{r}', t)|^2 \right] \Psi(\mathbf{r}), \quad (7.23)$$

and the GPE, with $\Psi(\mathbf{r}, t) = \Psi(\mathbf{r})e^{-i\mu t/\hbar}$, is:

$$\left[H_{\text{sp}} + g_{3D} |\Psi(\mathbf{r})|^2 + 9\pi c_d \int d\mathbf{r}' \frac{1 - 3 \cos^2 \theta}{|\mathbf{r} - \mathbf{r}'|} |\Psi(\mathbf{r}')|^2 \right] \Psi(\mathbf{r}) = \mu \Psi(\mathbf{r}). \quad (7.24)$$

¹Chromium has $6\mu_B$ because the valence shell in its ground state contains six electrons with parallel spin alignment. The maximum value of the dipolar moment is obtained for $m_F = \pm F$.

Figure 7.4: Interaction between two dipoles oriented in the z -direction.

Thomas-Fermi approximation

For dipolar condensates, the results of the Thomas-Fermi approximation obtained in Sec. 2.1.4 may not apply because of the dipole-dipole interactions. Neglecting the kinetic energy in Eq. (7.24), we obtain

$$V_{\text{ext}}(\mathbf{r}) + g_{3D}n(\mathbf{r}) + 9\pi c_d \int d\mathbf{r}' \frac{1 - 3\cos^3\theta}{|\mathbf{r} - \mathbf{r}'|} n(\mathbf{r}') = \mu, \quad (7.25)$$

which is a more complex equation for $n(\mathbf{r})$. However, Refs. [154, 155] showed that the density profile is also an inverted parabola, Eq. (2.17), but R_{\perp} and R_z are used as variational parameters in order to find the equilibrium configuration. For an axially symmetric external potential, $V_{\text{ext}}(\mathbf{r}) = M\omega_{\perp}^2(r^2 + \lambda^2 z^2)/2$, with $r^2 = x^2 + y^2$ and $\lambda = \omega_z/\omega_{\perp}$, Eq. (7.25) yields the transcendental equation:

$$\frac{\kappa^2}{\lambda^2} \left[3\varepsilon_{dd} \frac{f(\kappa)}{1 - \kappa^2} \left(\frac{\lambda}{2} + 1 \right) - 2\varepsilon_{dd} - 1 \right] = \varepsilon_{dd} - 1, \quad (7.26)$$

where $\kappa = R_{\perp}/R_z$ is the condensate anisotropy parameter, $\varepsilon_{dd} = 12\pi^2 c_d/g_{3D}$ and

$$f(\kappa) = \frac{1 + 2\kappa^2}{1 - \kappa^2} - \frac{3\kappa^2}{(1 - \kappa)^{3/2}} \operatorname{atanh} \sqrt{1 - \kappa^2}. \quad (7.27)$$

For $\varepsilon_{dd} > 1$ the dipolar Thomas-Fermi condensate is unstable, but there can exist metastable solutions. Once Eq. (7.27) is solved, we can use the obtained value of κ to find

$$R_{\perp} = \left[\frac{15g_{3D}N}{4\pi M\omega_{\perp}^2} \kappa \left\{ 1 - \varepsilon_{dd} \left(1 - \frac{3}{2} \frac{\kappa^2}{1 - \kappa^2} f(\kappa) \right) \right\} \right]^{1/5}, \quad (7.28)$$

and $R_z = R_{\perp}/\kappa$. The density profile, subject to a total number of particles N , is then

$$n(\mathbf{r}) = \begin{cases} \frac{15}{8\pi} \frac{N}{R_{\perp}^2 R_z} \left(1 - \frac{r_{\perp}^2}{R_{\perp}^2} - \frac{z^2}{R_z^2} \right) & \text{for } r_{\perp} \leq R_{\perp} \text{ and } z \leq R_z \\ 0 & \text{otherwise.} \end{cases} \quad (7.29)$$

The chemical potential is

$$\mu = g_{3D}n(0,0)\left(1 - \varepsilon_{ddf}(\kappa)\right). \quad (7.30)$$

7.2.2 Spin-3 dipolar condensate

Here, we study the effects of a dipolar condensate together with the phenomenology present in spinor condensates. In particular, let us consider a spinor dipolar condensate made of ^{52}Cr atoms. This isotope of chromium has a ground state of 7S_3 and thus $F = 3$. This means that there are seven different spin components: $m = 0, \pm 1, \pm 2, \pm 3$. Moreover, the magnetic moment can be up to $\mu = 6\mu_B$, and thus, dipole-dipole interactions cannot be neglected.

The Hamiltonian governing a ^{52}Cr condensate in a magnetic field in second quantization is [156]:

$$\hat{H} = \hat{H}_0 + \hat{V}_{\text{sr}} + \hat{V}_{\text{dd}}, \quad (7.31)$$

where \hat{H}_0 is a single-particle Hamiltonian that includes the interaction of the atoms with the magnetic field:

$$\hat{H}_0 = \sum_m \int d\mathbf{r} \hat{\Psi}_m^\dagger(\mathbf{r}) \left[H_{\text{sp}} + H_m \right] \hat{\Psi}_m(\mathbf{r}). \quad (7.32)$$

$\hat{\Psi}_m^\dagger(\mathbf{r})$ and $\hat{\Psi}_m(\mathbf{r})$ are the creation and annihilation boson operators of a particle in the m Zeeman state at \mathbf{r} , H_{sp} is the single-particle Hamiltonian (4.2) and H_m is the magnetic Hamiltonian (7.2).

The contact interactions between the atoms are described by:

$$\hat{V}_{\text{sr}} = \frac{1}{2} \int d\mathbf{r} : \left[c_0 \hat{n}^2(\mathbf{r}) + c_1 \hat{F}^2(\mathbf{r}) + c_2 \hat{\mathcal{P}}_0(\mathbf{r}) + c_3 \hat{O}^2(\mathbf{r}) \right] : \quad (7.33)$$

where the symbol $::$ denotes normal order, $\hat{n}(\mathbf{r}) = \sum_m \hat{\Psi}_m^\dagger(\mathbf{r}) \hat{\Psi}_m(\mathbf{r})$ is the total density, and

$$\begin{aligned} \hat{F}^i(\mathbf{r}) &= \sum_{m,n} \hat{\Psi}_m^\dagger(\mathbf{r}) S_{m,n}^i \hat{\Psi}_n(\mathbf{r}); & \hat{F}^2(\mathbf{r}) &= \sum_i (\hat{F}^i(\mathbf{r}))^2; \\ \hat{\mathcal{P}}_0(\mathbf{r}) &= \frac{1}{7} \sum_{m,n} (-1)^{m+n} \hat{\Psi}_m^\dagger(\mathbf{r}) \hat{\Psi}_{-m}^\dagger(\mathbf{r}) \hat{\Psi}_n(\mathbf{r}) \hat{\Psi}_{-n}(\mathbf{r}); \\ \hat{O}^{ij}(\mathbf{r}) &= \sum_{m,n} \hat{\Psi}_m^\dagger(\mathbf{r}) (S^i S^j)_{m,n} \hat{\Psi}_n(\mathbf{r}); & \hat{O}^2(\mathbf{r}) &= \sum_{i,j} (\hat{O}_{i,j}(\mathbf{r}))^2. \end{aligned}$$

The interaction constants are

$$\begin{aligned} c_0 &= \frac{1}{77} (-11g_2 + 81g_4 + 7g_6); & c_1 &= \frac{1}{18} (g_6 - g_2); \\ c_2 &= g_0 + \frac{1}{33} (-55g_2 + 27g_4 - 5g_6); & c_3 &= \frac{g_2}{126} - \frac{g_4}{77} + \frac{g_6}{198}, \end{aligned}$$

and the parameters g_S are related to the s-wave scattering length for total spin S , a_S , by $g_S = 4\pi\hbar^2 a_S/M$.

Finally, the dipole-dipole interaction is:

$$\begin{aligned} \hat{V}_{\text{dd}} = & -\sqrt{\frac{3\pi}{10}}c_d \iint \frac{d\mathbf{r} d\mathbf{r}'}{|\mathbf{r} - \mathbf{r}'|^3} : \left[\mathcal{F}_{z,z}(\mathbf{r}, \mathbf{r}')Y_{20}(\mathbf{r} - \mathbf{r}') + \mathcal{F}_{z,-}(\mathbf{r}, \mathbf{r}')Y_{21}(\mathbf{r} - \mathbf{r}') \right. \\ & \left. + \mathcal{F}_{z,+}(\mathbf{r}, \mathbf{r}')Y_{2-1}(\mathbf{r} - \mathbf{r}') + \mathcal{F}_{-,-}(\mathbf{r}, \mathbf{r}')Y_{22}(\mathbf{r} - \mathbf{r}') + \mathcal{F}_{+,+}(\mathbf{r}, \mathbf{r}')Y_{2-2}(\mathbf{r} - \mathbf{r}') \right] : , \end{aligned} \quad (7.34)$$

where $c_d = \mu_0\mu_B^2 g_L^2/4\pi$, $Y_{2m}(\mathbf{r} - \mathbf{r}')$ are the spherical harmonics,

$$\begin{aligned} \mathcal{F}_{z,z}(\mathbf{r}, \mathbf{r}') &= \sqrt{\frac{2}{3}} \left[3\hat{F}_z(\mathbf{r})\hat{F}_z(\mathbf{r}') - \hat{\mathbf{F}}(\mathbf{r}) \cdot \hat{\mathbf{F}}(\mathbf{r}') \right] \\ \mathcal{F}_{z,\pm}(\mathbf{r}, \mathbf{r}') &= \pm \left[\hat{F}_{\pm}(\mathbf{r})\hat{F}_z(\mathbf{r}') + \hat{F}_z(\mathbf{r}')\hat{F}_{\pm}(\mathbf{r}) \right] \\ \mathcal{F}_{\pm,\pm}(\mathbf{r}, \mathbf{r}') &= \hat{F}_{\pm}(\mathbf{r})\hat{F}_{\pm}(\mathbf{r}') , \end{aligned} \quad (7.35)$$

and $\hat{F}_{\pm}(\mathbf{r}) = \hat{F}_x(\mathbf{r}) \pm i\hat{F}_y(\mathbf{r})$.

The dipolar interaction results from the coupling to total angular momentum zero of two rank-two tensors in spin and coordinate space. Therefore, this interaction does not conserve spin and orbital angular momentum separately. An allowed process is, for example, two atoms in the state $m_F = -3$ are both transferred to $m_F = -2$. This leads the atoms to acquire orbital angular momentum and thus to the rotation of the different components, resembling the Einstein-de Haas effect [157].

7.2.3 Homogeneous condensate

In the following we consider that the linear and quadratic Zeeman effects are chosen in such a way that only the two lowest states of the Zeeman manifold, $m = -3$ and $m = -2$ contribute, whereas spin relaxation to other m states is energetically suppressed. In this simplified scenario, we assume a condensate of $m = -3$ atoms with small spin fluctuations populating the $m = -2$ component. This system can be described by the field $\hat{\Psi} \simeq \Psi_{-3} + \delta\hat{\Psi}_{-3} + \delta\hat{\Psi}_{-2}$, where the BEC wavefunction fulfills the GP equation

$$\begin{aligned} \mu\Psi_{-3}(\mathbf{r}) = & \left[-\frac{\hbar^2\nabla^2}{2M} + V_{\text{trap}}(\mathbf{r}) - 3p + 9q \right] \hat{\Psi}_{-3}(\mathbf{r}) + g_d n_{-3}(\mathbf{r})\Psi_{-3}(\mathbf{r}) \quad (7.36) \\ & -36\sqrt{\frac{\pi}{5}}c_d \int \frac{d\mathbf{r}'}{|\mathbf{r} - \mathbf{r}'|^3} Y_{20}(\widehat{\mathbf{r} - \mathbf{r}'})\Psi_{-3}^2(\mathbf{r}')\Psi_{-3}(\mathbf{r}) , \end{aligned}$$

with $g_d \equiv c_0 + 9c_1 + 81c_3$.

In homogeneous space, $V_{\text{trap}}(\mathbf{r}) = 0$, $\psi_{-3}(\mathbf{r}) = \psi_{-3}$ and $\mu = 9q - 3p + gn_{-3}$. Moving into momentum space, $\delta\hat{\psi}_m(\mathbf{k})$, we introduce the operators

$$\begin{aligned} \hat{O}_{-3,\pm}(\mathbf{k}) &\equiv \delta\hat{\psi}_{-3}(\mathbf{k}) \pm \delta\hat{\psi}_{-3}^\dagger(-\mathbf{k}) \\ \hat{O}_{-2,\pm}(\mathbf{k}) &\equiv e^{-i\phi_k}\delta\hat{\psi}_{-2}(\mathbf{k}) \pm \delta\hat{\psi}_{-2}^\dagger(-\mathbf{k})e^{i\phi_k} , \end{aligned} \quad (7.37)$$

where we have introduced spherical coordinates $\mathbf{k} = (k, \theta_k, \phi_k)$. These operators are governed by a set of coupled Heisenberg equations:

$$\begin{aligned} i\hbar \begin{pmatrix} \dot{\hat{O}}_{-3,+}(\mathbf{k}) \\ \dot{\hat{O}}_{-2,+}(\mathbf{k}) \end{pmatrix} &= \hat{R}(k) \begin{pmatrix} \hat{O}_{-3,-}(\mathbf{k}) \\ \hat{O}_{-2,-}(\mathbf{k}) \end{pmatrix} \\ i\hbar \begin{pmatrix} \dot{\hat{O}}_{-3,-}(\mathbf{k}) \\ \dot{\hat{O}}_{-2,-}(\mathbf{k}) \end{pmatrix} &= \hat{M}(\mathbf{k}) \begin{pmatrix} \hat{O}_{-3,+}(\mathbf{k}) \\ \hat{O}_{-2,+}(\mathbf{k}) \end{pmatrix}, \end{aligned} \quad (7.38)$$

where

$$\hat{R}(k) = \begin{pmatrix} \frac{\hbar^2 k^2}{2M} & 0 \\ 0 & \frac{\hbar^2 k^2}{2M} - U - 4\pi c_d n_{-3} \end{pmatrix}; \quad \hat{M}(\mathbf{k}) = \begin{pmatrix} M_{11} & M_{12} \\ M_{21} & M_{22} \end{pmatrix} \quad (7.39)$$

with $U \equiv 5q - p$, and

$$\begin{aligned} M_{11} &= \frac{\hbar^2 k^2}{2M} + 2gn_{-3} + 24\pi c_d n_{-3} (3 \cos^2 \theta_k - 1), \\ M_{12} &= M_{21} = 36\pi \sqrt{\frac{2}{3}} c_d n_{-3} \sin \theta_k \cos \theta_k, \\ M_{22} &= \frac{\hbar^2 k^2}{2M} - U - 4\pi c_d n_{-3} (1 - 3 \sin^2 \theta_k). \end{aligned} \quad (7.40)$$

Note that contrary to the spin-1 case, scalar fluctuations (given by $\delta\hat{\Psi}_{-3}$) couple with spin fluctuations (given by $\delta\hat{\Psi}_{-2}$) at first order. As a consequence, the elementary excitations have a hybrid scalar/spin character absent in the spin-1 case.

The corresponding Bogoliubov excitations may be written as a linear combination of the operators above:

$$\begin{pmatrix} \Lambda_+(\mathbf{k}) \\ \Lambda_-(\mathbf{k}) \\ \Lambda_+^\dagger(-\mathbf{k}) \\ \Lambda_-^\dagger(-\mathbf{k}) \end{pmatrix} = \begin{pmatrix} \alpha_+(\mathbf{k}) & \beta_+(\mathbf{k}) & \gamma_+(\mathbf{k}) & \delta_+(\mathbf{k}) \\ \alpha_-(\mathbf{k}) & \beta_-(\mathbf{k}) & \gamma_-(\mathbf{k}) & \delta_-(\mathbf{k}) \\ \alpha_+(\mathbf{k}) & \beta_+(\mathbf{k}) & -\gamma_+(\mathbf{k}) & -\delta_+(\mathbf{k}) \\ \alpha_-(\mathbf{k}) & \beta_-(\mathbf{k}) & -\gamma_-(\mathbf{k}) & -\delta_-(\mathbf{k}) \end{pmatrix} \begin{pmatrix} \hat{O}_{-3,-}(\mathbf{k}) \\ \hat{O}_{-2,-}(\mathbf{k}) \\ \hat{O}_{-3,+}(\mathbf{k}) \\ \hat{O}_{-2,+}(\mathbf{k}) \end{pmatrix}, \quad (7.41)$$

where

$$\begin{aligned} \alpha_\pm^2(\mathbf{k}) &= \frac{B^2(\mathbf{k})R_{11}(k)R_{22}(k)}{4E_\pm(\mathbf{k})} \left[B^2(\mathbf{k})R_{22}(k) + (E_\pm^2(\mathbf{k}) - A(\mathbf{k}))^2 R_{11}(k) \right]^{-1} \\ \beta_\pm(\mathbf{k}) &= \alpha_\pm(\mathbf{k}) \frac{E_\pm^2(\mathbf{k}) - A(\mathbf{k})}{B(\mathbf{k})}; \quad \gamma_\pm(\mathbf{k}) = \alpha_\pm(\mathbf{k}) \frac{E_\pm(\mathbf{k})}{R_{11}(k)}; \quad \delta_\pm(\mathbf{k}) = \beta_\pm(\mathbf{k}) \frac{E_\pm(\mathbf{k})}{R_{22}(k)}. \end{aligned} \quad (7.42)$$

The excitation Hamiltonian acquires the form

$$\hat{H} = \int d\mathbf{k} \sum_{\lambda=\pm} E_\lambda(\mathbf{k}) \hat{\Lambda}_\lambda^\dagger(\mathbf{k}) \hat{\Lambda}_\lambda(\mathbf{k}). \quad (7.43)$$

with eigenenergies:

$$E_\pm^2(\mathbf{k}) = \frac{1}{2}(A(\mathbf{k}) + D(\mathbf{k})) \pm \frac{1}{2}\sqrt{(A(\mathbf{k}) - D(\mathbf{k}))^2 + 4C(\mathbf{k})B(\mathbf{k})}, \quad (7.44)$$

where $A(\mathbf{k}) \equiv R_{11}(k)M_{11}(\mathbf{k})$, $B(\mathbf{k}) \equiv R_{11}(k)M_{21}(\mathbf{k})$, $C(\mathbf{k}) \equiv R_{22}(k)M_{12}(\mathbf{k})$, and $D(\mathbf{k}) \equiv R_{22}(k)M_{22}(\mathbf{k})$. The modes are stable, i.e. possess real eigen-energies, if $U < U_{cr} = -4\pi n_3 c_d$. Note that stability is just governed by the interplay between Zeeman energies and the spin relaxation due to the dipole-dipole interactions.

Defining the matrices:

$$\hat{\Delta} = \frac{1}{\alpha_+\beta_- - \alpha_-\beta_+} \begin{pmatrix} \beta_- & -\beta_+ \\ -\alpha_- & \alpha_+ \end{pmatrix}; \quad \hat{\Gamma} = \frac{1}{\gamma_+\delta_- - \gamma_-\delta_+} \begin{pmatrix} \delta_- & -\delta_+ \\ -\gamma_- & \gamma_+ \end{pmatrix}, \quad (7.45)$$

we may express the population in $m = -2$ in the form

$$\langle \hat{n}_{-2}(k, \theta_k) \rangle = \frac{\mathcal{A}_{2+}}{e^{\frac{E_+}{k_B T}} - 1} + \frac{\mathcal{A}_{2-}}{e^{\frac{E_-}{k_B T}} - 1} + Q_{-2}, \quad (7.46)$$

where we introduce the amplitudes

$$\mathcal{A}_{2+}(\mathbf{k}) = \frac{1}{8} \left[\Gamma_{21}^2(\mathbf{k}) + \Delta_{21}^2(\mathbf{k}) \right]; \quad \mathcal{A}_{2-}(\mathbf{k}) = \frac{1}{8} \left[\Gamma_{22}^2(\mathbf{k}) + \Delta_{22}^2(\mathbf{k}) \right], \quad (7.47)$$

and the zero temperature quantum fluctuations

$$Q_{-2}(\mathbf{k}) = \frac{1}{16} \left\{ \left[\Gamma_{21}(\mathbf{k}) + \Delta_{21}(\mathbf{k}) \right]^2 + \left[\Gamma_{22}(\mathbf{k}) + \Delta_{22}(\mathbf{k}) \right]^2 \right\}. \quad (7.48)$$

Contrary to the spin-1 case discussed in the previous section, $\langle \hat{n}_{-2} \rangle$ has in general an angular dependence, which results from the anisotropy of the dipole-dipole interactions. We may quantify the anisotropy of the spin population by means of $\chi = \int (3 \cos^2 \theta_k - 1) \langle \hat{n}_{-2}(k, \theta_k) \rangle d^3 k$. An isotropic distribution is characterized by $\chi = 0$, whereas positive values indicate a distribution preferentially oriented along $\theta_k = \pi/2$. The anisotropy χ presents an interesting dependence as a function of temperature and U/U_{cr} , depicted in Fig. 7.5 for the case of $n_{-3} = 10^{14} \text{ cm}^{-3}$ and $U_{cr}/\mu_0 = -0.05$, where $\mu_0 = gn_{-3}$. At low T , χ has small positive values, increasing when U/U_{cr} increases (for very low $T \lesssim 0.01\mu_0/k_B$, χ acquires a maximum for intermediate U values). For larger T , $\chi < 0$ for low U/U_{cr} indicating a momentum distribution oriented along $\theta_k = 0$, whereas at larger U/U_{cr} the distribution becomes basically isotropic.

7.2.4 Confined condensate: local density approximation

We consider at this point the case of a trapped chromium condensate. In general, LDA must be carefully considered, due to the long range character of the dipole-dipole interactions. However, when the characteristic length of this interaction, $a_{dd} = 3Mc_d/\hbar$, is much smaller than the typical length of the condensate harmonic trap, $a_{h.o} = \sqrt{\hbar/M\omega}$, the LDA can still be used to calculate the number of particles in the $m = -2$ state, as long as the density profile of the $m = -3$ BEC varies smoothly with r . This approximation allows to estimate the total number of atoms in $m = -2$, but is of course not appropriate to study its angular distribution.

In order to find the density profile $n_{-3}(\mathbf{r})$ we may use the Thomas-Fermi approximation for a dipolar gas, presented in Sec. 7.2.1, Eq. (7.29), for an axially symmetric harmonic

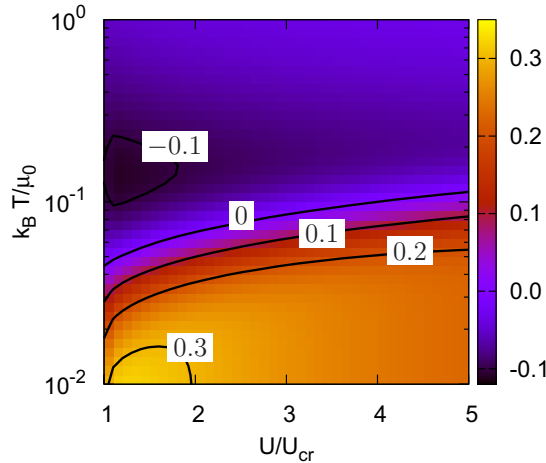


Figure 7.5: Anisotropic χ as a function of $k_B T/\mu_0$, and U/U_{cr} , for an homogeneous ^{52}Cr BEC with $n_{-3} = 10^{14}$ particles/cm 3 . The black lines describe configurations with the same anisotropy, the corresponding χ values are indicated.

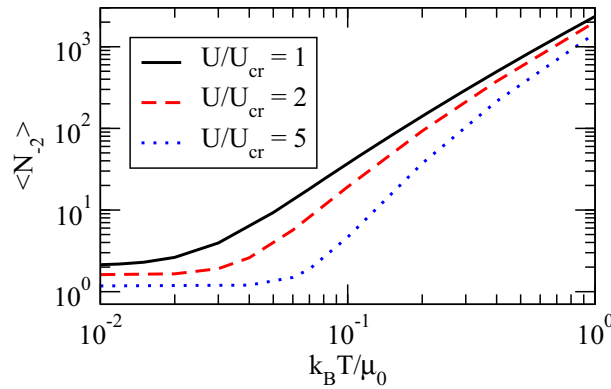


Figure 7.6: Number of chromium atoms in $m = -2$ as a function of $k_B T/\mu_0$ for different values of U/U_{cr} , for the case discussed in the text.

potential. Once the density profile of the $m = -3$ atoms is determined one can calculate the number of $m = -2$ atoms produced, due to the thermal spin fluctuations, by using the LDA, i.e., by integrating the local production of $m = -2$ atoms over the density profile of the trap, in a similar way as in Eq. (7.19).

Fig. 7.6 shows $\langle N_{-2} \rangle$ as a function of temperature for several values of the U/U_{cr} , for the specific case of a ^{52}Cr BEC with $N = 10^5$ in $m = -3$ in a spherical trap of frequency $\omega = 2\pi \times 50\text{Hz}$, where U_{cr} is determined by the central density $n(0,0) = 5.33 \cdot 10^{13}\text{cm}^{-3}$. Note that $a_{dd} = 0.894\text{nm} \ll a_{\text{h.o.}} = 1.97\mu\text{m}$, and hence well within the limits of the LDA. Close to U_{cr} populations of $\langle N_{-2} \rangle = 10$ may be attained below $0.1\mu_0/k_B$. Hence, as for the spin-1 case, Fig. 7.6 shows clearly that one may employ the population in $m = -2$ (combined with an abrupt jump into instability, as discussed for spin-1) for thermometry purposes. Finally, we should note that as for the case of spin-1 isotropic curves bend towards lower T when approaching U_{cr} , and hence also for chromium an adiabatic reduction of U/U_{cr} may allow for an interesting cooling mechanism.

Chapter 8

Summary and conclusions

In this thesis, we have studied the Josephson effect with BJJ formed by single-component, binary mixture and spinor Bose-Einstein condensates. We have used both a mean-field framework, based on the Gross-Pitaevskii equation, and a quantum approach through the two-site Bose-Hubbard model. Moreover, we also have studied temperature effects in spinor condensates. The main results and conclusions are summarized below.

Single-component BJJ: mean field

- First, we have reviewed the two-mode approximations, both S2M and I2M, and have discussed the different regimes that can appear in this configuration, i.e. Josephson oscillations, and macroscopic quantum self-trapping.
- We have performed numerical calculations of the TDGPE for the particular setup of the experiments reported in Ref. [70]. We have found a large amount of phase coherence and localization at each side of the potential barrier for both components, supporting the use of two-mode approximations.
- The comparisons between the two-mode models and the numerical solutions of the TDGPE show an excellent agreement for conditions close to the stable stationary regimes predicted by the two-mode models. As we depart from those stable points, the S2M fails to provide a quantitative agreement with the results obtained with the TDGPE equations. The range of validity of the I2M is much broader, fully capturing the dynamics for a larger set of initial conditions.
- The predictions of the two most commonly employed dimensional reductions of the TDGPE, the 1D-TDGPE and NPSE, have been shown to differ substantially, being the NPSE clearly in much better agreement with the original 3D dynamics in a broader set of conditions. In general, the 1D-TDGPE describes essentially the correct physics but is quantitatively far from the TDGPE predictions. Also, for self-trapped cases, it departs earlier from the two-mode behavior than the 1D-TDGPE or the NPSE.
- The validity of the two-mode approximation when atom-atom interactions are increased has also been studied. We have demonstrated the possibility of exciting

higher modes of the effective double-well potential through the dynamics. We have considered an initially imbalanced population and have shown that for a broad range of interaction energies the system remains self-trapped but not due to the dynamics between the two lower states of the Gross-Pitaevskii equation, as usually accepted, but due to another mechanism involving a third state. This transition from the coupling between the first two (1,2) to the next two (2,3) states can be well characterized and understood by analyzing the static properties of the effective potential (including interactions) which due to the fact that the system remains self-trapped does not vary substantially with time.

Single-component BJJ: beyond mean field

- The static properties of a single-component BJJ described by a two-site Bose-Hubbard model have been studied, focusing on the structure of the ground state.
- We have proposed a variational analytical approach to the ground state of the two-site Bose-Hubbard model that gives a useful insight in the physical nature of the ground state. We have carefully studied the limitations of the mean-field description strongly linked to the presence of fragmentation of the condensate and quantum fluctuations. The new proposed variational wave function is able to describe rather well the exact wave function and reproduces the energy, the one-body density matrix and the fragmentation of the state which are the main signatures that we have used to characterize the ground state. We have also compared the spectral decomposition of the exact ground state with the variational wave function obtaining a good agreement with the new proposed wave function. The wave function $|\Psi_{\text{var}}\rangle_{\text{min}}$, which parameters are obtained by minimizing the energy, can be used for any number of particles. Even when the number of particles can make the exact calculation more involved. This wave function, incorporates from the very beginning, $\Lambda \neq 0$, quantum correlations beyond the mean field and reproduces very well the fragmentation induced by these correlations which become larger in the cat-state region.
- We have discussed the dynamical properties of the system, taking an initial state that was fully condensed and completely localized on the left well. We have seen how the dynamics changes from Josephson oscillations to self-trapping as a function of Λ , and have observed the decreasing of the condensed fractions in time, which was more pronounced for smaller number of particles.
- The semi-classical limit has also been discussed, where one recovers the mean-field S2M equations. These equations predict a bifurcation on the population imbalance of the ground state when changing the atom-atom interactions. As discussed, this bifurcation is related to a ground state that is strongly-correlated.
- In order to provide more insight into the physical nature of the ground state, we have reviewed a $1/N$ approximation. We have compared both the energies and the density profiles predicted by this approximation with the ones obtained by exact diagonalization of the Bose-Hubbard model.

Binary mixture BJJ: mean field

- We have reviewed the S2M equations describing the dynamics of a binary mixture in the BJJ and have derived the corresponding I2M equations. We have shown the different dynamical regimes that can appear, i.e. Josephson oscillations, self-trapping and double self-trapping, and discussed the stability of the stationary solutions predicted by the S2M equations.
- The numerical calculations of the TDGPE have been done for an extension of the experiments [70]: the case of a binary mixture made by populating two of the Zeeman states of an $F = 1$ ^{87}Rb condensate. We have seen that each species preserves a large amount of phase coherence and localization at each side of the potential barrier, supporting the use of two-mode approximations.
- We have compared the TDGPE with the two-mode approximations, both the S2M and the I2M. Similar to the scalar case, these models show an excellent agreement for conditions close to the stable stationary regimes predicted by the two-mode models. The I2M has a range of validity much larger than the S2M, when leaving those stable points.
- The extension of the 1D-TDGPE and the NPSE to binary mixtures are compared with the TDGPE. Contrary to what happens with the 1D-TDGPE, the agreement between the NPSE and the full 3D dynamics is astonishingly good for this binary mixture, where the intra- and inter-species are very similar and the NPSE equations are particularly easy to handle. This agreement is not only seen on fully integrated magnitudes, for instance population imbalances, but also on the density profiles predicted along the direction hosting the barrier.
- We have also considered two situations where the two-mode approximation fails. This is naturally associated with the excitation of higher modes. Two different cases have been described, first the excitation of modes in the direction of the barrier and secondly, excitation of modes in the transverse direction. The NPSE has been shown to capture perfectly the excitations along the barrier direction, reproducing the integrated density profiles obtained with the TDGPE. The second case has been studied in a simulation performed with different intra- and inter-species interactions, which can be achieved in principle experimentally through Feshbach resonance modulation of the scattering lengths. In this case, the dynamics of the less populated component in each side of the trap departs notably from the two-mode with clear excitations of transverse modes, seen already in the density profiles along a transverse direction.

Spinor BJJ

- We have obtained the mean-field two-mode equations, which conform a system of eight coupled nonlinear differential equations relating the independent variables of the problem.

- For small population imbalances and small phase differences, we have discussed the decoupling of the exchange of populations from the Josephson dynamics. Specifically, we have identified the different time scales and the role of the population transfer in the stability of the Josephson oscillations. In addition, we have proposed an alternative way of determining the scattering lengths that characterize the atom-atom interactions.
- We have focused in the study of the ground state properties, and we have found that, for both the mean-field two-mode and the two-site BH descriptions, the number of particles in each component only depends on the sign of the spin-dependent interaction, U_2 .
- Furthermore, we have analyzed the problem of spatial symmetry breaking driven by the spin. For $\mathcal{M} = 0$, when $U_2 < 0$ the dependence of the bifurcation with the interactions is well understood and characterized by the mean-field theory. However, when $U_2 > 0$ the BH model shows a dependence with U_2 that the mean-field does not capture. This bifurcation is related to the creation of spin singlets, which drives the symmetry breaking in the system. We have derived an effective Hamiltonian for the interaction and tunneling of the spin singlets, that describes accurately this transition and relates it to the total population imbalance and its dispersion.

Use of spinor condensates as thermometers

- The thermal activation of spin excitations in spinor condensates has been analyzed. The stability of the system has been studied by considering the Bogoliubov spectrum for the homogeneous case.
- For the case of spin-1 condensates, an stable $m = 0$ condensate presents a non-negligible thermally activated population of $m = \pm 1$ due to spin-changing collisions.
- For the case of a stable chromium BEC in $m = -3$ dipole-induced spin-relaxation leads as well to thermal activation of the $m = -2$ population, which contrary to the spin-1 case, acquires an intriguing temperature-dependent anisotropy.
- For both cases we have shown that the spin population may be employed at very low temperatures, $T \ll \mu/k_B$ as a possible mechanism for ultralow-temperature thermometry.
- We have shown as well that an external adiabatic variation of the magnetic field may be employed to obtain an adiabatic cooling mechanism.

Appendix A

Imaginary time step method

The imaginary time step method is a numerical method used to find the lowest energy state of a Hamiltonian H [158]. In some cases, and using symmetry properties, it can also be used to find an excited state. In this thesis, we will use it to obtain the two lowest energy stationary solutions of the Gross-Pitaevskii equation, which are used 1) to build the initial states with a given population imbalance and phase difference and 2) to compute the parameters of the two-mode reductions.

Let us consider the basis of non-degenerate eigenfunctions of H , $\{|\varphi_n\rangle\}$, that fulfill

$$H |\varphi_n\rangle = E_n |\varphi_n\rangle , \quad (\text{A.1})$$

with E_n the energy of the state $|\varphi_n\rangle$. The ground state energy E_0 is, by definition, the lowest value of the set $\{E_n\}$.

A given state $|\phi\rangle$ can be expanded in terms of these basis vectors as

$$|\phi\rangle = \sum_n c_n |\varphi_n\rangle , \quad (\text{A.2})$$

with $c_n = \langle \varphi_n | \phi \rangle$. The time-evolution of this state is governed by the Hamiltonian H through the unitary evolution operator $U(t) = e^{-iHt/\hbar}$,

$$|\phi(t)\rangle = U(t) |\phi(0)\rangle = e^{-iHt/\hbar} \sum_n c_n |\varphi_n\rangle = \sum_n e^{-iE_n t/\hbar} c_n |\varphi_n\rangle . \quad (\text{A.3})$$

The imaginary time step method consists in considering an imaginary time $t \in \Im$ [158]. The evolution of the state $|\phi\rangle$, defining the real time $\tau = it \in \Re$, results in

$$|\phi(\tau)\rangle = \sum_n e^{-E_n \tau/\hbar} c_n |\varphi_n\rangle . \quad (\text{A.4})$$

Notice that this transformation gives a non-unitary operator $U(t)$, and therefore, the norm will not be preserved. In the limit of $\tau \rightarrow \infty$, due to the exponential character of the prefactors, only the contribution of the lowest energy E_0 survives in the evolution of the state $|\phi\rangle$. In this limit one can write

$$\lim_{\tau \rightarrow \infty} |\phi(\tau)\rangle \propto e^{-E_0 \tau/\hbar} c_0 |\varphi_0\rangle . \quad (\text{A.5})$$

Notice that the proportionality relation is due to the loss of norm in the time-evolution. Moreover, the former relation is only true when the initial state $|\phi(0)\rangle$ has some overlap with the lowest energy state $|\varphi_0\rangle$, i.e. $c_0 \neq 0$. Interestingly, this fact can be used to find one excited state. For instance, if initially $c_0 = 0$ and $c_1 \neq 0$, in the limit $\tau \rightarrow \infty$ one has,

$$\lim_{\tau \rightarrow \infty} |\phi(\tau)\rangle \propto e^{-E_1\tau/\hbar} c_1 |\varphi_1\rangle . \quad (\text{A.6})$$

In the double well problem, the ground state is symmetric and the first excited antisymmetric, i.e. even or odd under parity transformation. Therefore, if one takes an initial state $|\phi\rangle$ antisymmetric, the overlap with the ground state will be zero, $c_0 = 0$.

Because of the loss of norm during the imaginary time evolution, the algorithm has to be implemented using small time steps τ and renormalizing after each step. If the initial wave function is correctly normalized $|\phi_0\rangle$, after propagating a small time step $\delta\tau$ and considering up to first order, one has,

$$|\phi_1\rangle = e^{-H\delta\tau/\hbar} |\phi_0\rangle = \sum_{k=0}^{\infty} \frac{(-1)^k}{k!} \left(\frac{H\delta\tau}{\hbar} \right)^k |\phi_0\rangle \simeq \left[1 - \frac{H\delta\tau}{\hbar} \right] |\phi_0\rangle . \quad (\text{A.7})$$

At this point, the state $|\phi_1\rangle$ has to be renormalized: if $\mathcal{N}^2 = \langle \phi_1 | \phi_1 \rangle$, the normalized state is $|\phi_1\rangle / \mathcal{N}$. When this process is repeated many times, the state $|\phi_n\rangle$ converges to the ground state $|\varphi_0\rangle$. However, the time step $\delta\tau$ has to be small enough in order to ensure convergence of the algorithm, but large enough for the algorithm to be efficient.

Appendix B

Scalar BH: estimation of the bifurcation point

The scalar two-site BH model for N particles is

$$H = -J \left(\hat{a}_L^\dagger \hat{a}_R + \hat{a}_R^\dagger \hat{a}_L \right) + U_0 \hat{n}_R (\hat{n}_R - \hat{n}) + \frac{U_0 \hat{n}}{2} (\hat{n} - 1), \quad (\text{B.1})$$

where the last term can be considered as a constant since it commutes with the whole Hamiltonian. The Hilbert space is spanned by the complete basis

$$|n_R\rangle |n_L\rangle = |n_R\rangle |N - n_R\rangle, \quad (\text{B.2})$$

which, being labeled by only one quantum number, can be denoted as

$$|\nu\rangle = |n_R\rangle |N - n_R\rangle, \quad (\text{B.3})$$

with $\nu = n_R = 0, 1, \dots, N$. In terms of these states, the Hamiltonian reads

$$H = \sum_{\nu=0}^N \left[T_s(\nu) (|\nu-1\rangle \langle \nu| + |\nu\rangle \langle \nu-1|) + D_s(\nu) |\nu\rangle \langle \nu| \right], \quad (\text{B.4})$$

with

$$D_s(\nu) = U_0 \left[\nu(\nu - N) + \frac{N}{2} (N - 1) \right], \quad (\text{B.5})$$

$$T_s(\nu) = -J \sqrt{\nu(N + 1 - \nu)}, \quad (\text{B.6})$$

For $U_0 < 0$ there is a bifurcation point where the ground state starts to be self trapped. Here we give a raw estimation of the value of this point. To start with, since the bifurcation occurs for $|U_0| \ll J$, we consider the free particle case with the interaction treated as a perturbation.

For $U_0 = 0$, the energy of the ground state is

$$E_0 = -JN, \quad (\text{B.7})$$

and the interaction can be added perturbatively

$$E_1 = U_0 \frac{N(N-1)}{4}. \quad (\text{B.8})$$

In the other limit, $J = 0$, the ground state is degenerate with energy

$$\epsilon_0 = \frac{U_0 N}{2} (N-1), \quad (\text{B.9})$$

with a zero correction in the first order in J . Bifurcation is expected to occur when

$$E_0 + E_1 \simeq \epsilon_0. \quad (\text{B.10})$$

So, the bifurcation condition is given by

$$\frac{(N-1)|U_0|}{4J} \simeq 1. \quad (\text{B.11})$$

For $N \rightarrow \infty$, the bifurcation occurs also for an infinitesimal value of U_0 .

List of publications

Spinor Bose-Einstein condensates in a double-well: Population transfer and Josephson oscillations

B. Juliá-Díaz, M. Melé-Messeguer, M. Guilleumas and A. Polls
Phys. Rev. A **80**, 043622 (2009).

Josephson tunneling of binary mixtures of spinor BECs

M. Guilleumas, B. Juliá-Díaz, M. Melé-Messeguer and A. Polls
Laser Physics **20**, Issue 5, 1163-1168 (2010).
Proceedings of the 18th International Laser Physics Conference

Beyond standard two-mode dynamics in bosonic Josephson junctions

B. Juliá-Díaz, J. Martorell, M. Melé-Messeguer and A. Polls
Phys. Rev. A **82**, 063626 (2010).

Weakly linked binary mixtures of $F = 1$ ^{87}Rb Bose-Einstein condensates

M. Melé-Messeguer, B. Juliá-Díaz, M. Guilleumas, A. Polls and A. Sanpera
New J. Phys. **13**, 033012 (2011).

Two component bosonic Josephson junctions in elongated traps

M. Melé-Messeguer, B. Juliá-Díaz, M. Guilleumas and A. Polls
Molecular Physics **109**, Issue 23-24, 2763-2771 (2011).
Special issue in honor of Prof. Luciano Reatto

Improved variational approach to the two-site Bose-Hubbard model

M. Melé-Messeguer, B. Juliá-Díaz, and A. Polls
J. Low. Temp. Phys. **165**, Issue 5-6, 180-194 (2011).

Dynamic generation of spin-squeezed states in bosonic Josephson junctions

B. Juliá-Díaz, T. Zibold, M. K. Oberthaler, M. Melé-Messeguer, J. Martorell, and A. Polls
Phys. Rev. A **86**, 023615 (2012).

Spin-driven spatial symmetry breaking of spinor condensates in a double well

M. Melé-Messeguer, S. Paganelli, B. Juliá-Díaz, A. Sanpera, and A. Polls
Phys. Rev. A **86**, 053626 (2012).

Thermal spin fluctuations in spinor Bose-Einstein condensates

M. Melé-Messeguer, B. Juliá-Díaz, A. Polls, and L. Santos
Phys. Rev. A **87**, 033632 (2013).

Bibliography

- [1] A. Einstein, “Quantentheorie des einatomigen idealen gases,” *Sitzungsber. Preuss. Akad. Wiss.*, p. 261, 1924.
- [2] A. Einstein, “Quantentheorie des einatomigen idealen gases (zweite abhandlung),” *Sitzungsber. Kgl. Preuss. Akad. Wiss.*, vol. 1, p. 3, 1925.
- [3] S. N. Bose, “Plancks gesetz und lichtquantenhypothese,” *Z. Phys.*, vol. 26, p. 178, 1924.
- [4] C. J. Pethick and H. Smith, *Bose-Einstein condensation in dilute gases*. Cambridge University Press, 2008.
- [5] A. J. Leggett, “Bose-Einstein condensation in the alkali gases: Some fundamental concepts,” *Rev. Mod. Phys.*, vol. 73, p. 307, 2001.
- [6] C. Cohen-Tannoudji and D. Guéry-Odelin, *Advances in atomic physics. An overview*. World Scientific Publishing Co. Pte. Ltd., 2011.
- [7] P. Kapitza, “Viscosity of liquid helium below the λ -point,” *Nature*, vol. 141, p. 74, 1938.
- [8] J. F. Allen and A. D. Misener, “Flow phenomena in liquid helium II,” *Nature*, vol. 142, p. 643, 1938.
- [9] F. London, “The λ -phenomenon of liquid helium and the Bose-Einstein degeneracy,” *Nature*, vol. 141, p. 643, 1938.
- [10] F. London, “On the Bose-Einstein condensation,” *Phys. Rev.*, vol. 54, p. 947, 1938.
- [11] H. Glyde, *Excitations in liquid and solid helium*. Clarendon Press, Oxford, 1994.
- [12] C. E. Hecht, “The possible superfluid behaviour of hydrogen atom gases and liquids,” *Physica*, vol. 25, p. 1159, 1959.
- [13] W. C. Stwalley and L. H. Nosanow, “Possible ‘new’ quantum systems,” *Phys. Rev. Lett.*, vol. 36, p. 910, 1976.
- [14] I. F. Silvera and J. T. M. Walraven, “Stabilization of atomic hydrogen at low temperature,” *Phys. Rev. Lett.*, vol. 44, p. 164, 1980.

-
- [15] H. F. Hess, “Evaporative cooling of magnetically trapped and compressed spin-polarized hydrogen,” *Phys. Rev. B*, vol. 34, p. 3476, 1986.
- [16] T. W. Hänsch and A. L. Schawlow, “Cooling of gases by laser radiation,” *Optics communications*, vol. 13, p. 68, 1975.
- [17] S. Chu, C. Cohen-Tannoudji, and W. D. Phillips, *Nobel Lectures, Physics 1996-2000*. World Scientific Publishing Co., 2002.
- [18] Nobelprize.org, *Advanced information on the Nobel Prize in Physics 2001*. http://www.nobelprize.org/nobel_prizes/physics/laureates/2001/advanced.html, 2013.
- [19] E. A. Cornell and C. E. Wieman, “Nobel lecture: Bose-Einstein condensation in a dilute gas, the first 70 years and some recent experiments,” *Rev. Mod. Phys.*, vol. 74, p. 875, 2002.
- [20] E. L. Raab, M. Prentiss, A. Cable, S. Chu, and D. E. Pritchard, “Trapping of neutral sodium atoms with radiation pressure,” *Phys. Rev. Lett.*, vol. 59, p. 2631, 1987.
- [21] S. L. Cornish and D. Cassettari, “Recent progress in Bose-Einstein condensation experiments,” *Phil. Trans. R. Soc. Lond. A*, vol. 361, p. 2699, 2003.
- [22] M. H. Anderson, J. R. Ensher, M. R. Matthews, C. E. Wieman, and E. A. Cornell, “Observation of Bose-Einstein condensation in a dilute atomic vapor,” *Science*, vol. 269, p. 198, 1995.
- [23] K. B. Davis, M.-O. Mewes, M. R. Andrews, N. J. van Druten, D. S. Durfee, D. M. Stamper-Kurn, and W. Ketterle, “Bose-Einstein condensation in a gas of sodium atoms,” *Phys. Rev. Lett.*, vol. 75, p. 3969, 1995.
- [24] W. Ketterle, “Nobel lecture: When atoms behave as waves: Bose-Einstein condensation and the atom laser,” *Rev. Mod. Phys.*, vol. 74, p. 1131, 2002.
- [25] C. C. Bradley, C. A. Sackett, J. J. Tollet, and R. G. Hulet, “Evidence of Bose-Einstein condensation in atomic gas with attractive interactions,” *Phys. Rev. Lett.*, vol. 75, p. 1687, 1995.
- [26] W. Ketterle, “Experimental studies of Bose-Einstein condensation,” *Physics Today*, vol. 52, p. 30, 1999.
- [27] E. P. Gross, “Structure of a quantized vortex in boson systems,” *Nuovo Cimento*, vol. 20, p. 454, 1961.
- [28] L. P. Pitaevskii, “Vortex lines in an imperfect Bose gas,” *Sov. Phys. JETP*, vol. 13, p. 451, 1961.
- [29] R. Gati, *Bose-Einstein condensates in a single double-well potential*. PhD thesis, Heidelberg university, 2007.

-
- [30] M. R. Andrews, C. G. Townsend, H.-J. Miesner, D. S. Durfee, D. M. Stamper-Kurn, and W. Ketterle, "Observation of interference between two Bose condensates," *Science*, vol. 275, p. 637, 1997.
- [31] M. R. Matthews, B. P. Anderson, P. C. Haljan, D. S. Hall, C. E. Wieman, and E. A. Cornell, "Vortices in a Bose-Einstein condensate," *Science*, vol. 269, p. 198, 1995.
- [32] K. W. Madison, F. Chevy, W. Wohlleben, and J. Dalibard, "Vortex formation in a stirred Bose-Einstein condensate," *Phys. Rev. Lett.*, vol. 84, p. 806, 2000.
- [33] J. R. Abo-Shaeer, C. Raman, J. M. Vogels, and W. Ketterle, "Observation of vortex lattices in Bose-Einstein condensates," *Science*, vol. 292, p. 496, 2001.
- [34] D. G. Fried, T. C. Killian, L. Willmann, D. Landhuis, S. C. Moss, D. Kleppner, and T. J. Greytak, "Bose-Einstein condensation of atomic hydrogen," *Phys. Rev. Lett.*, vol. 81, p. 3811, 1998.
- [35] S. L. Cornish, N. R. Claussen, J. L. Roberts, E. A. Cornell, and C. E. Wieman, "Stable ^{85}Rb Bose-Einstein condensates with widely tunable interactions," *Phys. Rev. Lett.*, vol. 85, p. 1795, 2000.
- [36] A. Robert, O. Sirjean, A. Browaeys, J. Poupard, S. Nowak, D. Boiron, C. I. Westbrook, and A. Aspect, "A Bose-Einstein condensate of metastable atoms," *Science*, vol. 292, p. 461, 2001.
- [37] F. Pereira Dos Santos, J. Léonard, J. Wang, C. J. Barrelet, F. Perales, E. Rasel, C. S. Unnikrishnin, M. Leduc, and C. Cohen-Tannoudji, "Bose-Einstein condensation of metastable helium," *Phys. Rev. Lett.*, vol. 86, p. 3459, 2001.
- [38] G. Modugno, G. Ferrari, G. Roati, R. J. Brecha, A. Simoni, and M. Inguscio, "Bose-Einstein condensation of potassium atoms by sympathetic cooling," *Science*, vol. 294, p. 1320, 2001.
- [39] T. Weber, J. Herbig, M. Mark, H.-C. Nägerl, and R. Grimm, "Bose-Einstein condensation of cesium," *Science*, vol. 299, p. 232, 2003.
- [40] Y. Takasu, K. Maki, K. Komori, T. Takano, K. Honda, M. Kumakura, T. Yabuzaki, and Y. Takahashi, "Spin-Singlet Bose-Einstein Condensation of Two-Electron Atoms," *Phys. Rev. Lett.*, vol. 91, p. 040404, 2003.
- [41] A. Griesmaier, J. Werner, S. Hensler, J. Stuhler, and T. Pfau, "Bose-Einstein condensation of chromium," *Phys. Rev. Lett.*, vol. 94, p. 160401, 2005.
- [42] T. Fukuhara, S. Sugawa, and Y. Takahashi, "Bose-Einstein condensation of an ytterbium isotope," *Phys. Rev. A*, vol. 76, p. 051604, 2007.
- [43] T. Fukuhara, S. Sugawa, Y. Takasu, and Y. Takahashi, "All-optical formation of quantum degenerate mixtures," *Phys. Rev. A*, vol. 79, p. 021601(R), 2009.

- [44] S. Kraft, F. Vogt, O. Appel, F. Riehle, and U. Sterr, “Bose-Einstein condensation of alkaline earth atoms: ^{40}Ca ,” *Phys. Rev. Lett.*, vol. 103, p. 130401, 2009.
- [45] S. Stellmer, M. K. Tey, B. Huang, R. Grimm, and F. Schreck, “Bose-Einstein condensate of strontium,” *Phys. Rev. Lett.*, vol. 103, p. 200401, 2009.
- [46] Y. N. M. de Escobar, P. G. Mickelson, M. Yan, B. J. DeSalve, S. B. Nagel, and T. C. Killian, “Bose-Einstein condensation of ^{84}Sr ,” *Phys. Rev. Lett.*, vol. 103, p. 200402, 2009.
- [47] M. Lu, N. Q. Burdick, S. H. Youn, and B. L. Lev, “Strongly dipolar Bose-Einstein condensate of dysprosium,” *Phys. Rev. Lett.*, vol. 107, p. 190401, 2011.
- [48] K. Aikawa, A. Frisch, M. Mark, S. Baier, A. Rietzler, R. Grimm, and F. Ferlaino, “Bose-Einstein condensation of erbium,” *Phys. Rev. Lett.*, vol. 108, p. 210401, 2012.
- [49] C. Chin, R. Grimm, P. Julienne, and E. Tiesinga, “Feshbach resonances in ultracold gases,” *Rev. Mod. Phys.*, vol. 82, pp. 1225–1286, 2010.
- [50] S. Inouye, M. R. Andrews, J. Stenger, H.-J. Miesner, D. Stamper-Kurn, and W. Ketterle, “Observation of Feshbach resonances in a Bose-Einstein condensate,” *Nature*, vol. 392, p. 151, 1998.
- [51] S. Giovanazzi, A. Gorlitz, and T. Pfau, “Tuning the dipolar interaction in quantum gases,” *Phys. Rev. Lett.*, vol. 89, p. 130401, 2002.
- [52] T. Lahaye, C. Menotti, L. Santos, M. Lewenstein, and T. Pfau, “The physics of dipolar bosonic quantum gases,” *Rep. Prog. Phys.*, vol. 72, p. 126401, 2009.
- [53] T.-L. Ho, “Spinor Bose condensates in optical traps,” *Phys. Rev. Lett.*, vol. 81, p. 742, 1998.
- [54] T. Ohmi and K. Machida, “Bose-Einstein condensation with internal degrees of freedom in alkali atom gases,” *J. Phys. Soc. Jpn.*, vol. 67, p. 1822, 1998.
- [55] J. Stenger, S. Inouye, D. Stamper-Kurn, H.-J. Miesner, A. Chikkatur, and W. Ketterle, “Spin domains in ground-state Bose-Einstein condensates,” *Nature*, vol. 396, p. 345, 1998.
- [56] H. Pu and N. P. Biegelow, “Properties of two-species Bose condensates,” *Phys. Rev. Lett.*, vol. 80, pp. 1130–1133, 1997.
- [57] G. Modugno, M. Modugno, F. Riboli, G. Roati, and M. Inguscio, “Two atomic species superfluid,” *Phys. Rev. Lett.*, vol. 89, p. 190404, 2002.
- [58] I. Bloch, M. Greiner, O. Mandel, T. W. Hänsch, and T. Esslinger, “Sympathetic cooling of ^{85}Rb and ^{87}Rb ,” *Phys. Rev. A*, vol. 64, p. 021402(R), 2001.
- [59] C. J. Myatt, E. A. Burt, R. W. Ghrist, E. A. Cornell, and C. E. Wieman, “Production of two overlapping Bose-Einstein condensates by sympathetic cooling,” *Phys. Rev. Lett.*, vol. 78, p. 586, 1997.

- [60] S. Burger, K. Bongs, S. Dettmer, W. Ertmer, K. Sengstock, A. Sanpera, G. V. Shlyapnikov, and M. Lewenstein, “Dark solitons in Bose-Einstein condensates,” *Phys. Rev. Lett.*, vol. 83, p. 5198, 1999.
- [61] J. Denschlag, J. E. Simsarian, D. L. Feder, C. W. Clark, L. A. Collins, J. Cubizolles, L. Deng, E. W. Hagley, K. Helmerson, W. P. Reinhardt, S. L. Rolston, B. I. Schneider, and W. D. Phillips, “Generating solitons by phase engineering of a Bose-Einstein condensate,” *Science*, vol. 287, p. 97, 2000.
- [62] M. Lewenstein, A. Sanpera, and V. Ahufinger, *Ultracold atoms in optical lattices. Simulating quantum many-body systems*. Oxford University Press, Oxford, 2012.
- [63] B. D. Josephson, “Possible new effects in superconductive tunneling,” *Phys. Lett.*, vol. 1, pp. 251–253, 1962.
- [64] P. L. Anderson and J. W. Rowell, “Probable observation of the Josephson superconducting tunnel effect,” *Phys. Rev. Lett.*, vol. 10, p. 230, 1963.
- [65] S. Saphiro, “Josephson currents in superconducting tunneling: The effect of microwaves and other observations,” *Phys. Rev. Lett.*, vol. 11, p. 80, 1963.
- [66] J. Javanainen, “Oscillatory exchange of atoms between traps containing Bose condensates,” *Phys. Rev. Lett.*, vol. 57, pp. 3164–3166, 1986.
- [67] R. Gati and M. K. Oberthaler, “A bosonic Josephson junction,” *J. Phys. B: At. Mol. Opt. Phys.*, vol. 40, pp. R61–R89, 2007.
- [68] A. Smerzi, S. Fantoni, S. Giovanazzi, and S. R. Shenoy, “Quantum coherent atomic tunneling between two trapped Bose-Einstein condensates,” *Phys. Rev. Lett.*, vol. 79, p. 4950, 1997.
- [69] F. S. C. S. Burger, C. Fort, P. Maddaloni, F. Minardi, A. Trombettoni, A. Smerzi, and M. Inguscio, “Josephson junction arrays with Bose-Einstein condensates,” *Science*, vol. 293, p. 843, 2001.
- [70] M. Albiez, R. Gati, J. Fölling, S. Hunsmann, M. Cristiani, and M. K. Oberthaler, “Direct observation of tunneling and nonlinear self-trapping in a single bosonic Josephson junction,” *Phys. Rev. Lett.*, vol. 95, p. 010402, 2005.
- [71] S. Levy, E. Lahoud, I. Shomroni, and J. Steinhauer, “The a.c. and d.c. Josephson effects in a Bose-Einstein condensate,” *Nature*, vol. 449, p. 579, 2007.
- [72] S. Raghavan, A. Smerzi, S. Fantoni, and S. R. Shenoy, “Coherent oscillations between two weakly coupled Bose-Einstein condensates: Josephson effects, π oscillations, and macroscopic quantum self-trapping,” *Phys. Rev. A*, vol. 59, pp. 620–633, 1999.
- [73] D. Ananikian and T. Bergeman, “Gross-pitaevskii equation for Bose particles in a double-well potential: Two-mode models and beyond,” *Phys. Rev. A*, vol. 73, p. 013604, 2006.

-
- [74] M. P. A. Fisher, P. B. Weichman, G. Grinstein, and D. S. Fisher, “Boson localization and the superfluid-insulator transition,” *Phys. Rev. B*, vol. 40, p. 546, 1989.
- [75] H. J. Lipkin, N. Meshkov, and A. J. Glick, “Validity of many-body approximation methods for a solvable model: (i). exact solutions and perturbation theory,” *Nucl. Phys.*, vol. 62, p. 188, 1965.
- [76] J. Estève, C. Gross, A. Weller, S. Giovanazzi, and M. K. Oberthaler, “Squeezing and entanglement in a bose-einstein condensate,” *Nature*, vol. 455, pp. 1216–1219, 2008.
- [77] M. Kitagawa and M. Ueda, “Squeezed spin states,” *Phys. Rev. A*, vol. 47, p. 5138, 1993.
- [78] J. K. Korbicz, J. I. Cirac, and M. Lewenstein, “Spin squeezing inequalities and entanglement of n qubit states,” *Phys. Rev. Lett.*, vol. 95, p. 120502, 2005.
- [79] C. Gross, T. Zibold, E. Nicklas, J. Estève, and M. K. Oberthaler, “Atomic homodyne detection of continuous-variable entangled twin-atom states,” *Nature*, vol. 464, p. 1165, 2010.
- [80] J. Maa, X. Wanga, C. P. Suna, and F. Nori, “Quantum spin squeezing,” *Phys. Rep.*, vol. 509, p. 89, 2011.
- [81] B. Juliá-Díaz, T. Zibold, M. K. Oberthaler, M. Melé-Messeguer, J. Martorell, and A. Polls, “Dynamic generation of spin-squeezed states in bosonic Josephson junctions,” *Phys. Rev. A*, vol. 86, p. 023615, 2012.
- [82] B. Juliá-Díaz, E. Torrontegui, J. Martorell, J. G. Muga, and A. Polls, “Fast generation of spin-squeezed states in bosonic Josephson junctions,” *Phys. Rev. A*, vol. 86, p. 063623, 2012.
- [83] G. J. Milburn, J. Corney, E. M. Wright, and D. F. Walls, “Quantum dynamics of an atomic Bose-Einstein condensate in a double-well potential,” *Phys. Rev. A*, vol. 55, p. 4318, 1997.
- [84] J. Javanainen and M. Y. Ivanov, “Splitting a trap containing a Bose-Einstein condensate: Atom number fluctuations,” *Phys. Rev. A*, vol. 60, p. 2351, 1999.
- [85] B. Juliá-Díaz, D. Dagnino, M. Lewenstein, J. Martorell, and A. Polls, “Macroscopic self-trapping in Bose-Einstein condensates: Analysis of a dynamical quantum phase transition,” *Phys. Rev. A*, vol. 81, p. 023615, 2010.
- [86] M. Olshanii, “Atomic scattering in the presence of an external confinement and a gas of impenetrable bosons spin-3 chromium Bose-Einstein condensates,” *Phys. Rev. Lett.*, vol. 81, pp. 938–941, 1998.
- [87] L. Salasnich, A. Parola, and L. Reatto, “Effective wave equations for the dynamics of cigar-shaped and disk-shaped Bose condensates,” *Phys. Rev. A*, vol. 65, p. 043614, 2002.

- [88] S. Giovanazzi, A. Smerzi, and S. Fantoni, “Josephson effects in dilute Bose-Einstein condensates,” *Phys. Rev. Lett.*, vol. 84, p. 4521, 2000.
- [89] B. Juliá-Díaz, J. Martorell, M. Melé-Messeguer, and A. Polls, “Beyond standard two-mode dynamics in bosonic Josephson junctions,” *Phys. Rev. A*, vol. 82, p. 063626, 2010.
- [90] S. Ashhab and C. Lobo, “External Josephson effect in Bose-Einstein condensates with a spin degree of freedom,” *Phys. Rev. A*, vol. 66, p. 013609, 2002.
- [91] M. Melé-Messeguer, B. Juliá-Díaz, M. Guilleumas, A. Polls, and A. Sanpera, “Weakly linked binary mixtures of $F = 1$ ^{87}Rb Bose-Einstein condensates,” *New J. Phys.*, vol. 13, p. 033012, 2011.
- [92] M. Guilleumas, B. Juliá-Díaz, M. Melé-Messeguer, and A. Polls, “Josephson tunneling of binary mixtures of spinor BECs,” *Laser Physics*, vol. 20, pp. 1163–1168, 2010.
- [93] M. Melé-Messeguer, B. Juliá-Díaz, M. Guilleumas, and A. Polls, “Two component bosonic Josephson junctions in elongated traps,” *Molecular Physics*, vol. 109, pp. 2763–2771, 2011.
- [94] M. Melé-Messeguer, B. Juliá-Díaz, and A. Polls, “Improved variational approach to the two-site Bose-Hubbard model,” *J. Low. Temp. Phys.*, vol. 165, pp. 180–194, 2011.
- [95] Ö. E. Müstecaplıoğlu, W. Zhang, and L. You, “Quantum dynamics of a spin-1 condensate in a double-well potential,” *Phys. Rev. A*, vol. 75, p. 023605, 2007.
- [96] A. Wagner, C. Bruder, and E. Demler, “Spin-1 atoms in optical superlattices: Single-atom tunneling and entanglement,” *Phys. Rev. A*, vol. 84, p. 063636, 2011.
- [97] B. Juliá-Díaz, M. Melé-Messeguer, M. Guilleumas, and A. Polls, “Spinor Bose-Einstein condensates in a double-well: Population transfer and Josephson oscillations,” *Phys. Rev. A*, vol. 80, p. 043622, 2009.
- [98] M. Melé-Messeguer, S. Paganelli, B. Juliá-Díaz, A. Sanpera, and A. Polls, “Spin-driven spatial symmetry breaking of spinor condensates in a double well,” *Phys. Rev. A*, vol. 86, p. 053626, 2012.
- [99] M. Melé-Messeguer, B. Juliá-Díaz, A. Polls, and L. Santos, “Thermal spin fluctuations in spinor Bose-Einstein condensates,” *Phys. Rev. A*, vol. 87, p. 033632, 2013.
- [100] B. L. Hammond, W. A. Lester, and P. J. Reynolds, *Monte Carlo Methods in ab initio quantum chemistry*. World Scientific, 1994.
- [101] E. P. Gross, “Hydrodynamics of a superfluid condensate,” *Journal of Mathematical Physics*, vol. 4, p. 195, 1963.

-
- [102] F. Dalfovo, S. Giorgini, L. Pitaevskii, and S. Stringari, “Theory of Bose-Einstein condensation in trapped gases,” *Rev. Mod. Phys.*, vol. 71, p. 463, 1999.
- [103] F. Dalfovo, L. Pitaevskii, and S. Stringari, “The condensate wave function of a trapped atomic gas,” *J. Res. Natl. Inst. Stand. Technol.*, vol. 101, p. 537, 1996.
- [104] M. Albiez, *Observation of nonlinear tunneling of a Bose-Einstein condensate in a single Josephson junction*. PhD thesis, University of Heidelberg, 2005.
- [105] T. Zibold, E. Nicklas, C. Gross, and M. K. Oberthaler, “Classical bifurcation at the transition from Rabi to Josephson dynamics,” *Phys. Rev. Lett.*, vol. 105, p. 204101, 2010.
- [106] A. I. Streltsov, O. E. Alon, and L. S. Cederbaum, “General variational many-body theory with complete self-consistency for trapped bosonic systems,” *Phys. Rev. A*, vol. 73, p. 063626, 2006.
- [107] D. Masiello, S. B. McKagan, and W. P. Reinhardt, “Multiconfigurational Hartree-Fock theory for identical bosons in a double well,” *Phys. Rev. A*, vol. 72, p. 063624, 2005.
- [108] A. Tonel, J. Links, and A. Foerster, “Behaviour of the energy gap in a model of Josephson coupled Bose-Einstein condensates,” *J. Phys A: Math. Gen.*, vol. 38, pp. 6879–6891, 2005.
- [109] D. R. Dounas-Frazer, A. M. Hermundstad, and L. Carr, “Ultracold bosons in a tilted multilevel double-well potential,” *Phys. Rev. Lett.*, vol. 99, p. 200402, 2007.
- [110] L. Carr, D. Dounas-Frazer, and M. Garcia-March, “Dynamical realization of macroscopic superposition states of cold bosons in a tilted double well,” *EPL*, vol. 90, p. 10005, 2010.
- [111] P. Cheinet, S. Trotzky, M. Feld, U. Schnorrberger, M. Moreno-Cardoner, S. Fölling, and I. Bloch, “Counting atoms using interaction blockade in an optical superlattice,” *Phys. Rev. Lett.*, vol. 101, p. 090404, 2008.
- [112] F. Meier and W. Zwerger, “Josephson tunneling between weakly interacting Bose-Einstein condensates,” *Phys. Rev. A*, vol. 64, p. 033610, 2001.
- [113] K. Sakmann, A. I. Streltsov, O. E. Alon, and L. S. Cederbaum, “Exact quantum dynamics of a bosonic Josephson junction,” *Phys. Rev. Lett.*, vol. 103, p. 220601, 2009.
- [114] Y.-J. Lin, K. Jiménez-García, and I. B. Spielman, “Spin-orbit-coupled Bose-Einstein condensates,” *Nature*, vol. 471, p. 83, 2011.
- [115] S. B. Papp, J. M. Pino, and C. E. Wieman, “Tunable miscibility in a dual-species Bose-Einstein condensate,” *Phys. Rev. Lett.*, vol. 101, p. 040402, 2008.

-
- [116] F. V. Pepe, P. Facchi, G. Florio, and S. Pascazio, “Domain wall suppression in trapped mixtures of Bose-Einstein condensates,” *Phys. Rev. A*, vol. 86, p. 023629, 2012.
- [117] L. Wen and J. Li, “Tunneling dynamics between two-component Bose-Einstein condensates,” *Phys. Lett. A*, vol. 369, p. 307, 2007.
- [118] X.-Q. Xu, L.-H. Lu, and Y.-Q. Li, “Stability and dynamical property for two-species ultracold atoms in double wells,” *Phys. Rev. A*, vol. 78, p. 043609, 2008.
- [119] G. Mazzaella, M. Moratti, L. Salasnich, M. Salerno, and F. Toigo, “Atomic Josephson junction with two bosonic species,” *J. Phys. B: At. Mol. Opt. Phys.*, vol. 42, p. 125301, 2009.
- [120] Ö. E. Müstecaplıođlu, W. Zhang, and L. You, “An effective quasi-one-dimensional description of a spin-1 atomic condensate,” *Phys. Rev. A*, vol. 71, p. 025603, 2005.
- [121] L. Salasnich and B. A. Malomed, “Vector solitons in nearly one-dimensional Bose-Einstein condensates,” *Phys. Rev. A*, vol. 74, p. 053610, 2006.
- [122] I. I. Satija, R. Balakrishnan, P. Naudus, J. Heward, M. Edwards, and C. W. Clark, “Symmetry-breaking and symmetry-restoring dynamics of a mixture of Bose-Einstein condensates in a double well,” *Phys. Rev. A*, vol. 79, p. 033616, 2009.
- [123] G. Mazzaella, M. Moratti, L. Salasnich, and F. Toigo, “Nonlinear quantum model for atomic Josephson junctions with one and two bosonic species,” *J. Phys. B: At. Mol. Opt. Phys.*, vol. 43, p. 065303, 2010.
- [124] B. Juliá-Díaz, M. Guilleumas, M. Lewenstein, A. Polls, and A. Sanpera, “Josephson oscillations in binary mixtures of $F = 1$ spinor Bose-Einstein condensates,” *Phys. Rev. A*, vol. 80, p. 023616, 2009.
- [125] W. Wang, “Self-trapping and dynamical stability of two-component Bose-Einstein condensates in a double-well potential,” *J. Phys. Soc. Japan*, vol. 78, p. 094002, 2009.
- [126] H. T. Ng, C. K. Law, and P. Leung, “Quantum-correlated double-well tunneling of two-component Bose-Einstein condensates,” *Phys. Rev. A*, vol. 68, p. 013604, 2003.
- [127] E. G. M. van Kempen, S. J. J. M. F. Kokkelmans, D. J. Heinzen, and B. J. Verhaar, “Interisotope determination of ultracold rubidium interactions from three high-precision experiments,” *Phys. Rev. Lett.*, vol. 88, p. 093201, 2002.
- [128] K. W. Mahmud, H. Perry, and W. P. Reinhardt, “Quantum phase-space picture of Bose-Einstein condensates in a double well,” *Phys. Rev. A*, vol. 71, p. 023615, 2005.
- [129] M. Jääskeläinen and P. Meystre, “Dynamics of Bose-Einstein condensates in double-well potentials,” *Phys. Rev. A*, vol. 71, p. 043603, 2005.

-
- [130] B. Juliá-Díaz, J. Martorell, and A. Polls, “Bose-Einstein condensates on slightly asymmetric double-well potentials,” *Phys. Rev. A*, vol. 81, p. 063625, 2010.
- [131] J. I. Cirac, M. Lewenstein, K. Mølmer, and P. Zoller, “Quantum superposition states of Bose-Einstein condensates,” *Phys. Rev. A*, vol. 57, p. 1208, 1998.
- [132] V. S. Shchesnovich and M. Trippenbach, “Fock-space WKB method for the boson Josephson model describing a Bose-Einstein condensate trapped in a double-well potential,” *Phys. Rev. A*, vol. 78, p. 023611, 2008.
- [133] N. N. Bogoliubov, “On the theory of superfluidity,” *J. Phys. (USSR)*, vol. 11, p. 23, 1947.
- [134] M. Holthaus and S. Stenholm, “Coherent control of the self-trapping transition,” *Eur. Phys. J. B*, vol. 20, p. 451, 2001.
- [135] A. Micheli, D. Jaksch, J. I. Cirac, and P. Zoller, “Many-particle entanglement in two-component Bose-Einstein condensates,” *Phys. Rev. A*, vol. 67, p. 013607, 2003.
- [136] D. M. Stamper-Kurn, M. R. Andrews, A. P. Chikkatur, S. Inouye, H.-J. Miesner, J. Stenger, and W. Ketterle, “Optical confinement of a Bose-Einstein condensate,” *Phys. Rev. Lett.*, vol. 80, p. 2027, 1998.
- [137] H. Saito and M. Ueda, “Spontaneous magnetization and structure formation in a spin-1 ferromagnetic Bose-Einstein condensate,” *Phys. Rev. A*, vol. 72, p. 023610, 2005.
- [138] S. R. Leslie, J. Guzman, M. Vengalattore, J. D. Sau, M. L. Cohen, and D. M. Stamper-Kurn, “Amplification of fluctuations in a spinor Bose-Einstein condensate,” *Phys. Rev. A*, vol. 79, p. 043631, 2009.
- [139] J. Mur-Petit, M. Guilleumas, A. Polls, A. Sanpera, and M. Lewenstein, “Dynamics of $F = 1$ ^{87}Rb condensates at finite temperatures,” *Phys. Rev. A*, vol. 73, p. 013629, 2006.
- [140] M. Moreno-Cardoner, J. Mur-Petit, M. Guilleumas, A. Polls, A. Sanpera, and M. Lewenstein, “Predicting spinor condensate dynamics from simple principles,” *Phys. Rev. Lett.*, vol. 99, p. 020404, 2007.
- [141] W. Zhang, D. L. Zhou, M.-S. Chang, M. S. Chapman, and L. You, “Dynamical instability and domain formation in a spin-1 Bose-Einstein condensate,” *Phys. Rev. Lett.*, vol. 95, p. 180403, 2005.
- [142] J. Mur-Petit, “Spin dynamics and structure formation in a spin-1 condensate in a magnetic field,” *Phys. Rev. A*, vol. 79, p. 063603, 2010.
- [143] J. Kronjäger, C. Becker, P. Soltan-Panahi, K. Bongs, and K. Sengstock, “Spontaneous pattern formation in an antiferromagnetic quantum gas,” *Phys. Rev. Lett.*, vol. 105, p. 090402, 2010.

- [144] C. K. Law, H. Pu, and N. P. Biegelow, “Quantum spins mixing in spinor Bose-Einstein condensates,” *Phys. Rev. Lett.*, vol. 81, p. 5257, 1998.
- [145] J. Mur-Petit, *Many-body studies on atomic quantum systems*. PhD thesis, University of Barcelona, 2005.
- [146] S. Yi, Ö. E. Müstecaplıoğlu, C. P. Sun, and L. You, “Single-mode approximation in a spinor-1 atomic condensate,” *Phys. Rev. A*, vol. 66, p. 011601, 2002.
- [147] Y. Wu, “Simple algebraic method to solve a coupled-channel cavity QED model,” *Phys. Rev. A*, vol. 54, p. 4534, 1996.
- [148] A. de-Shalit and I. Talmi, *Nuclear Shell Theory*. Mineola, New York, 2004.
- [149] C. Cohen-Tannoudji, J. Dupont-Roc, and G. Grynberg, *Atom-photon interactions: Basic processes and applications*. Wiley, New York, 1992.
- [150] R. Gati, B. Hemmerling, J. Fölling, M. Albiez, and M. K. Oberthaler, “Noise thermometry with two weakly coupled Bose-Einstein condensates,” *Phys. Rev. Lett.*, vol. 96, p. 130404, 2006.
- [151] B. Pasquiou, E. Maréchal, L. Vernac, O. Gorceix, and B. Laburthe-Tolra, “Thermodynamics of a Bose-Einstein condensate with free magnetization,” *Phys. Rev. Lett.*, vol. 108, p. 045307, 2012.
- [152] F. Deuretzbacher, G. Gebreyesus, O. Topic, M. Scherer, B. Lücke, W. Ertmer, J. Arlt, C. Klempt, and L. Santos, “Parametric amplification of matter waves in dipolar spinor Bose-Einstein condensates,” *Phys. Rev. A*, vol. 82, p. 053608, 2010.
- [153] A. Griesmaier, T. Koch, M. Fattori, T. Pfau, S. Giovanazzi, P. Pedri, and L. Santos, “Observation of dipole-dipole interaction in a degenerate quantum gas,” *Phys. Rev. Lett.*, vol. 95, p. 150406, 2005.
- [154] D. H. J. O’Dell, S. Giovanazzi, and C. Eberlein, “Exact hydrodynamics of a trapped dipolar BEC,” *Phys. Rev. Lett.*, vol. 92, p. 250401, 2004.
- [155] C. Eberlein, S. Giovanazzi, and D. H. J. O’Dell, “Exact solution of the Thomas-Fermi equation for a trapped BEC with dipole-dipole interactions,” *Phys. Rev. A*, vol. 71, p. 033618, 2005.
- [156] L. Santos and T. Pfau, “Spin-3 chromium Bose-Einstein condensates,” *Phys. Rev. Lett.*, vol. 96, p. 190404, 2006.
- [157] A. Einstein and W. J. de Hass, “Experimenteller nachweis der ampereschen molekularströme,” *Verhandl. Deut. Physik Ges.*, vol. 17, p. 152, 1915.
- [158] M. L. Chiofalo, S. Succi, and M. P. Tosi, “Ground state of trapped interacting Bose-Einstein condensates by an explicit imaginary-time algorithm,” *Phys. Rev. E*, vol. 62, p. 7438, 2000.

